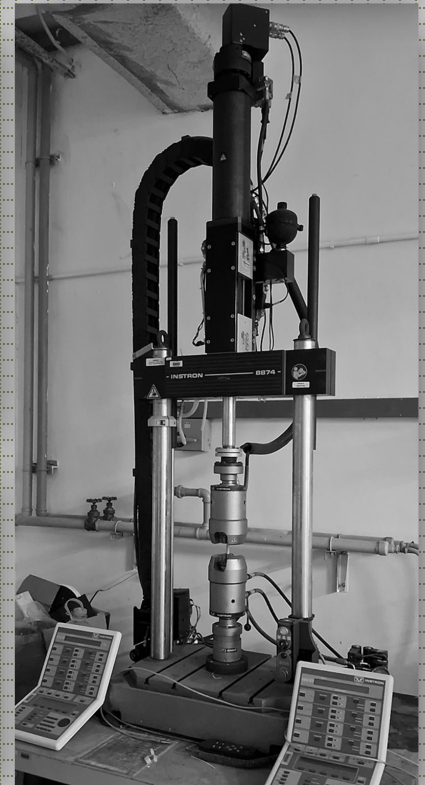
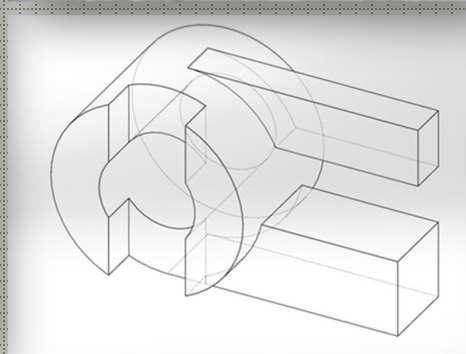
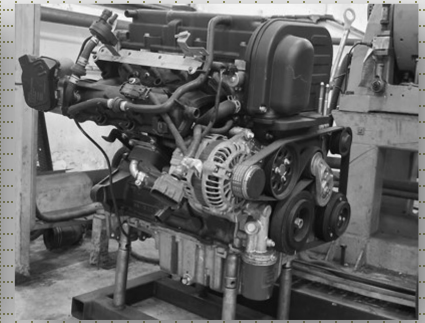
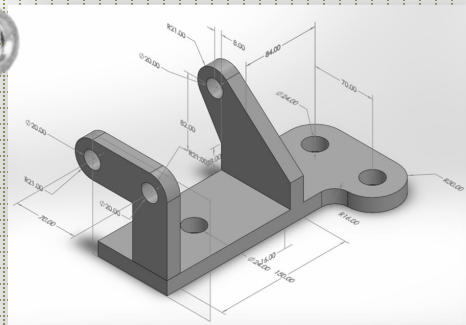
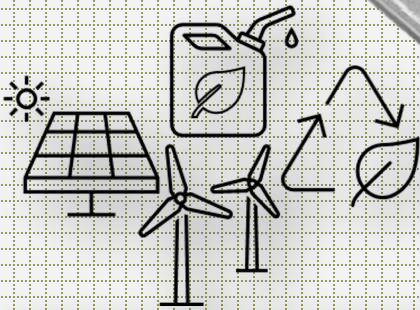


MECHANICAL ENGINEERING INSIGHTS

HIGHLIGHTS FROM FINAL YEAR PROJECTS

2024



EDITORS

SHAIFULAZUAR BIN ROZALI

CHEAH MEI YEE

MOHD.FADZIL BIN JAMALUDIN



FAKULTI KEJURUTERAAN
Faculty of Engineering

Editors

SHAIFULAZUAR BIN ROZALI

CHEAH MEI YEE

MOHD.FADZIL BIN JAMALUDIN

MECHANICAL ENGINEERING INSIGHTS

Highlights from Final Year Projects 2024

MECHANICAL ENGINEERING INSIGHTS HIGHLIGHTS FROM FINAL YEAR
PROJECTS 2024

Copyright by Fakulti Kejuruteraan Universiti Malaya, 2024

All rights reserved. No part of this publication may be reproduced or transmitted in any form or by any means, electronic or mechanical, recording or any information storage and retrieval system, without permission in writing from the publisher. The publisher, the authors and the editors are safe to assume that the advice and information in this book are believed to be true and accurate at the date of publication. Neither the publisher nor the authors or the editors give a warranty, express or implied, with respect to the material contained herein or for any errors or omissions that may have been made.

Published in Malaysia by:

Fakulti Kejuruteraan Universiti Malaya
Pejabat Timbalan Dekan Penyelidikan
Fakulti Kejuruteraan
Universiti Malaya
50603, Kuala Lumpur
MALAYSIA

eISBN NUMBER : 978-967-2182-45-0

TABLE OF CONTENTS

Foreword from the Head of Department..... **i**
Associate Professor Dr. Nurin Wahidah binti Mohd Zulkifli

Foreword from the Dean..... **ii**
Professor Ir. Dr. Nik Nazri bin Nik Ghazali

THEME: MECHANICAL

Development of an IoT Sensory Devices for Aquaponic System..... **2**
Shaarvesvaran A/L Murugiah and Ahmad Saifizul bin Abdullah

Development of a Motorized Ball Valve for Automated Aquaponic System..... **9**
Muhammad Hafizzudin bin Kamaluddin and Ahmad Saifizul bin Abdullah

A Study on the Repurposing Abandoned Building into Urban Farms..... **14**
Stephanie William Mogindol and Farazila binti Yusof

Microstructural and Tribological Analysis of Fe-based Amorphous Laser Cladded Coatings on AISI52100 under Various Lubrication Conditions..... **17**
Hussam Yahya Mohammed Al-Haddi and Nurin Wahidah binti Mohd Zulkifli

Tribological Analysis of Modified Palm Oil Lubricant using Nano Additives as Transmission Fluid for Electric Vehicle..... **22**
Yuvvaraj A/L Balan and Nurin Wahidah binti Mohd Zulkifli

Development of Visual Based Machinery Faults Diagnostics System using Phased-Based Motion Magnification and Displacement Extraction..... **27**
Syahirah Binti Mazhairul and Ong Zhi Chao

Development of IoT Vibration Sensor-based Machinery Health Monitoring and Faults Diagnostics System for Predictive Maintenance..... **33**
Muhammad Shahril Bin Zainol Abidin and Ong Zhi Chao

Development of Embedded System for Automatic Tracking Intelligent Umbrella... **39**
Tan Seng Kiat and Mohammed Abdo Hashem Ali

A Novel Robust Dew Point Evaporative Cooler..... **44**
Shum Choy Kit and Mohd Nashrul bin Mohd Zubir

Development of a Novel Sunlight Delivery System for Algae Photosynthesis in an Indoor Recirculating Aquaculture System (I-RAS)..... **48**
Goh Hong Sheng and Mohd Nashrul bin Mohd Zubir

Development of software for laboratory equipment at faculty of engineering, Universiti Malaya by implementing database system and website application..... **54**
Muhammad Syaiful Bin Lokman and Mohd Zamri bin Zainon @ Baharom

| | |
|--|------------|
| Nature Algorithms for Optimizing Coil Spring Design in Mechanical System..... | 59 |
| <i>Chua Kai Yang and Sabariah binti Julai @ Julaihi</i> | |
| Development of In-Pipe Water Turbine for Low Head Condition in Wastewater Treatment Plant..... | 65 |
| <i>Ilham Bin Syukri and Sabariah binti Julai @ Julaihi</i> | |
| Optimization of Linkage-based Suspension Layout Considering Vehicle Suspension Application..... | 70 |
| <i>Chew Boon Kheng and Soong Ming Foong</i> | |
| Time-frequency analysis on financial instruments..... | 74 |
| <i>Lee Ming Hooi and Soong Ming Foong</i> | |
| Design and Fabrication of Floating Vertical Wind-Wave Turbine: A Comprehensive Study on Prototype Structures with Hybrid Harvesting Systems for Sustainable Energy Ecosystems..... | 78 |
| <i>Mohamad Kamal Fahmi bin Yasman and Norhafizan bin Ahmad</i> | |
| Finite Element Simulation of Knee Loading During Driving..... | 82 |
| <i>Omar Ihab Mohamed Abdelwahab Mohamed and Andri Andriyana</i> | |
| Pressure Loss and Heat Transfer Analysis of Drag Reducing Additives..... | 87 |
| <i>Aayez Ahmad Virk and Kazi Md Salim Newaz</i> | |
| Application of Carbon Structured Nanofluids from Biomass for the Enhanced Performance of Flat Plate Solar Thermal Collector..... | 92 |
| <i>Mifzal bin Salihin and Kazi Md. Salim Newaz</i> | |
| Investigation of a Thermoelectric Cooling System Utilising Multichannel Duct Nozzle..... | 97 |
| <i>Muhammad Faisal bin Abdul Muis and Mohd Faizul bin Mohd Sabri</i> | |
| Fire Simulation and Analysis of Mechanical Jet Fans Ventilation System in an Underground Car Park Using CFD..... | 102 |
| <i>Nur Syahirah binti Abdul Rahman and Nik Nazri bin Nik Ghazali</i> | |
| Numerical Simulation of Heat Dispersion Around the Engineering Tower due to Condenser Installation..... | 107 |
| <i>Mohammad Iqbal Haqim bin Mohamad Robi and Nik Nazri bin Nik Ghazali</i> | |
| Computational Study of Two-phase Flow (Mixture of Water-air) in Venturi Nozzle Structure..... | 113 |
| <i>Adli Al-Wafi bin Mohd. Normarzuki and Poo Balan Ganesan</i> | |

THEME: MANUFACTURING

| | |
|--|------------|
| Investigating Sustainable Behaviour of UM Community Towards Sustainable Development Goals (SDGs)..... | 117 |
| <i>Nur Aimi Shazliana binti Md Samil and Salwa Hanim binti Abdul Rashid</i> | |
| Process Parameter Optimization of Selective Laser Melting (SLM) Ti-6Al-4V Using Density Control & Defect Prevention Criterion by Analytical Approach..... | 120 |
| <i>Muhammad Lutfi bin Mohd Salleh and Mohd Sayuti Ab Karim</i> | |
| Grading of Wooden Products based on Defect Detection and Classification using You Only Look Once (YOLO) Method..... | 124 |
| <i>Athirah binti Ridzuan and Azuddin bin Mamat</i> | |
| An Exploratory Research of Electrospinning with Multi-nozzles and Multiplane configuration: Effects of Jets Working Parameter on Nanofiber Production Rate.... | 130 |
| <i>Muhammad Shafiz Danial bin Ismadi and Edzrol Niza bin Mohamad</i> | |
| Development of Last-Mile Vaccine Delivery System for Government Health Clinics in Selangor – A Vehicle Routing Study..... | 136 |
| <i>Muhammad Syazani bin Muhammad Nizam and Siti Nurmaya binti Musa</i> | |
| Lightweight Design and Fabrication of Water Bottle Replenishing Tool..... | 142 |
| <i>Naim bin Nasri and Tan Chin Joo</i> | |
| Design & Development of Laboratory Scale Hydraulic Press for Recycling Metal Chips..... | 146 |
| <i>Muhammad Haziq Iqbal bin Adnan and Tuan Zaharinie binti Tuan Zahari</i> | |
| SolidWorks Training Module for Technicians..... | 153 |
| <i>Ahmad Faris Afham bin Sahari and Aznijar bin Ahmad Yazid</i> | |
| Universiti Malaya Student Residence Audit: Student Satisfaction Towards Facilities Management..... | 158 |
| <i>Muhammad Amir Arif bin Mohamed Maliki and Aznijar bin Ahmad Yazid</i> | |
| Design and Fabrication of a Prototype Floating Structure for Integrated Solar, Wind, and Wave Energy Harvesting..... | 161 |
| <i>Fauzan Ariff bin Shahrizal and Norhafizan bin Ahmad</i> | |
| Design and Development of a Gamified Augmented Reality-based Teaching and Learning System for Industrial Robot..... | 166 |
| <i>Lucy Sii Leh Ting and Yap Hwa Jen</i> | |
| Development of Image Guided Positioner for Robot Drilling in the Aerospace Manufacturing Industries..... | 172 |
| <i>Wong Pui Teng and Yap Hwa Jen</i> | |

THEME: MATERIALS

| | |
|--|-----|
| Fabrication and Testing of Nanofiber Reinforced Composite..... | 178 |
| <i>Lim Jia Chen and Amalina binti Muhammad Afifi</i> | |
| Microstructural Characterisation of Labu Sayong and Implications on Cooling Action..... | 182 |
| <i>Muhammad Nur Asyraf bin Norwan Chik and Hendrik Simon Cornelis Metselaar</i> | |
| Silicon Nitride (Si ₃ N ₄) for Carbon Capture..... | 187 |
| <i>Liang Ai Lin and Hendrik Simon Cornelis Metselaar</i> | |
| Microwave Carbonization of Oil Palm Kernel Shell (OPKS) using Activated Carbon as Absorber..... | 192 |
| <i>Muhammad Ariffuddin bin Mohd Sabari and Shaifulazuar bin Rozali</i> | |
| Effect of Catalyst on Carbonization of Oil Palm Empty Fruit Bunch (EFB)..... | 197 |
| <i>Amsyar bin Khairom and Shaifulazuar Rozali</i> | |
| Simulation and Analysis of IMC Behaviour in SAC305/Nano-Fe Solder under Mechanical Loading and Temperature Variations..... | 201 |
| <i>Ben Lee How Yin and Goh Yingxin</i> | |
| Assessment of Creep Resistant Materials and Low-Quality Steam Impact on Steam Turbine Blade..... | 207 |
| <i>Noor Amnan bin Hijattulah and Mohd Zamri bin Zainon</i> | |
| Giving a Second Life to Campus Waste Paper..... | 210 |
| <i>Amar Fikry bin Mohd Aznan and Muhammad Khairi Faiz bin Ahmad Hairuddin</i> | |
| Characterising Shear State Mechanical Properties and Thermomechanical Finite Element Analysis of SAC305 Solder..... | 215 |
| <i>Chan Wei Juan and Muhammad Khairi Faiz bin Ahmad Hairuddin</i> | |
| Corrosion Inhibition for Carbon Steel in Alkaline Environment by Addition of Andrographis Paniculata Extract..... | 219 |
| <i>Asrul Faiq bin Fazli and Nazatul Liana binti Sukiman</i> | |
| Andrographis Paniculata Leaves Extract as a Sustainable Additive in Epoxy Coating for Anti-Corrosion Protection of Carbon Steel..... | 224 |
| <i>Mohammad Iffat Zakwan bin Noorulkhairi and Nazatul Liana binti Sukiman</i> | |
| Polymer added with MgO for Remineralize and Removal of Heavy Metals in Contaminated Water..... | 227 |
| <i>Dhaneish Kumar and Nor Ishida binti Zainal Abidin</i> | |
| UV-Curable Urethane Acrylate from Palm Oil for Waterproof Coating..... | 232 |
| <i>Shaatish Rao A/L Jeeva and Nor Ishida binti Zainal Abidin</i> | |

| | |
|--|------------|
| Development of Bioplastic from Food Waste..... | 237 |
| <i>Jeslin Yew Wei Chen and Suriani Binti Ibrahim</i> | |
| Development of Poly (Ethylene Oxide) Based Solid Polymer Electrolytes Thin Films for Sodium Battery..... | 242 |
| <i>Nur Farzana binti Jaafar and Suriani binti Ibrahim</i> | |
| Recycled Aluminium Alloy Casting Process: An Investigation on the Effects of Annealing Parameters..... | 248 |
| <i>Nur Sakinah binti Zainol and Tuan Zaharinie binti Tuan Zahari</i> | |
| New Way of Sustaining Paintings on The Wall at The Engineering Faculty..... | 252 |
| <i>Muhammad Faris bin Mohd Anuar and Bushroa binti Abd Razak</i> | |
| Breaking Barriers in Solar Cells: Synthesis of Mesoporous Titanium Dioxide using Template Free Method..... | 255 |
| <i>Lew Sheau Wenn and Tan Chou Yong</i> | |
| Enhancing Supercapacitor Performance with Hydrothermally Synthesized Mesoporous Nickel-Based Nanostructure..... | 261 |
| <i>Leong Sze Xun and Tan Chou Yong</i> | |
| Warpage Analysis of Flip Chip Semiconductor Packages..... | 266 |
| <i>Sam Yong Pin and Wong Yew Hoong</i> | |
| Development of Fire-Retardant Nanocomposite Thin Films for Building Applications..... | 269 |
| <i>Tan Wei Kang and Wong Yew Hoong</i> | |
| INDEX | 273 |

FOREWORD FROM THE HEAD OF DEPARTMENT



Associate Professor Dr. Nurin Wahidah binti Mohd Zulkifli
Head of Mechanical Engineering Department
Faculty of Engineering
Universiti Malaya

The Department of Mechanical Engineering proudly presents “Mechanical Engineering Insights: Highlights from Final Year Project 2024” - a carefully curated collection of outstanding Final Year Projects from our graduating students. These projects represent not merely the culmination of four years of rigorous engineering education, but also embody the innovation, dedication, and technical excellence that our department strives to instill in every student.

This compilation is divided into three fundamental themes: Mechanical, Manufacturing, and Materials, representing the core domains of mechanical engineering. The Mechanical theme showcases our students' prowess in applying theoretical knowledge to practical engineering solutions. Their projects showcase advanced applications of IoT-based sensing technologies, tribological studies, system control and automation, as well as mechanical design and performance optimization. These developments directly address crucial industrial challenges, from enhancing food security to optimizing machinery performance, in addition to improving operational safety. The analysis and practical applicability of these projects reflects our program's emphasis on developing solutions for tangible industrial needs. In the Manufacturing theme, our students have embraced the transformative potential of Industry 4.0. Their projects exemplify the integration of smart manufacturing principles with sustainable development goals (SDGs). The scope ranges from process optimization and prototype development to innovative diagnostic systems and waste recycling solutions. Enhancing production efficiency while maintaining a strong commitment to environmental sustainability is a balance that modern engineering must strike. The Materials theme underscores our department's commitment to advancing material engineering and its applications. The projects in this section demonstrate comprehensive studies in material development, reinforcement techniques, and innovative recycling methods. Our students' work in this domain reflects their understanding that material selection and development are fundamental to product effectiveness and environmental responsibility.

The projects listed here represent countless hours of research, experimentation, and dedication. I extend my heartfelt congratulations to all contributing students and express my gratitude to our faculty members whose guidance has been instrumental in bringing these projects to fruition. This compilation not only documents outstanding academic achievement but also serves as a bridge between university education and industrial innovation.

FOREWORD FROM THE DEAN



Professor Ir. Dr. Nik Nazri bin Nik Ghazali
Dean, Faculty of Engineering
Universiti Malaya

This compilation of final year projects from the Department of Mechanical Engineering “Mechanical Engineering Insights: Highlights from Final Year Project 2024” features the efforts of the graduating batch of 2024. These projects showcase what our students can achieve after four years of hard work and learning. Each project reflects their creativity and technical skills, showing how they can solve real-world problems with practical and sustainable solutions.

From developing efficient systems to optimizing manufacturing processes and exploring sustainable materials, our students have demonstrated exceptional ingenuity in tackling complex industrial problems. Each project selected for this publication represents a significant contribution to engineering knowledge, showcasing original approaches that push the boundaries of what's possible in mechanical engineering. The breadth of work presented here spans critical areas including process optimization, IoT-based systems, advanced materials research, and system performance enhancement. What stands out is not just the technical excellence of these projects, but also their practical applicability and environmental consciousness. Our students have consistently demonstrated their ability to bridge the gap between theoretical understanding and real-world implementation, developing solutions that are both technically sophisticated and sustainably minded.

This compilation reflects the faculty's unwavering commitment to preparing industry-ready graduates who can excel in today's dynamic engineering landscape. To the graduating batch of 2024, congratulations on reaching this milestone. Your hard work, resilience, and ingenuity are evident in these projects, which set a high standard for future cohorts. I trust that this compilation will serve as an inspiration for readers and a proud reminder of your achievements as you embark on your professional journeys.

THEME : MECHANICAL

Development of an IoT Sensory Device for Aquaponic Systems

Shaarvesvaran A/L Murugiah^a and Ahmad Saifizul bin Abdullah^{b*}

Department of Mechanical Engineering,
Faculty of Engineering, Universiti Malaya,
50603, Kuala Lumpur, Malaysia

Email: ^amshaarvesvaran@gmail.com, ^bsaifizul@um.edu.my

*Corresponding author

ABSTRACT

Global food security challenges are increasing due to population growth and rapid urbanization. Aquaponics offers resource-efficient urban farming solutions but faces obstacles like high commitment. To overcome this, a robust IoT Sensory Device for Aquaponic Systems is proposed. The research aims to develop an automated monitoring system using IoT, design a user-friendly interface, and establish a disease risk index based on water parameter impacts on fish health. Hardware selection, sensor calibration, and circuitry design were conducted. A ThingSpeak dashboard displays real-time values, with an email alert system for threshold breaches. A Telegram update system was added for user-friendly real-time information. A Fish Disease Index was established to gauge water parameter severity. Overall, the IoT monitoring system aims to enhance efficiency, sustainability, and user commitment in aquaponics.

Keywords: Aquaponics; IoT; Monitoring; Sensor; Sustainability

1. INTRODUCTION

Recent statistics from multiple sources indicate that food security challenges are on the rise globally. Aquaponics, an integrated system that comprises an aquaculture system and a hydroponic system, is an approach to addressing food security [1]. However, aquaponics also has its own challenges, including high commitment and time consumption. Additionally, water parameters are crucial to guaranteeing the success of an aquaponic system.

To address this, a robust Internet of Things (IoT) Sensory Device for Aquaponic Systems is proposed. This integration can help enhance the sustainability and reliability of the aquaponic system. Moreover, to further enhance the success of this system, fish health and its correlation with water parameters will also be studied. The objectives of this research are (1) to develop a reliable automated monitoring system using IoT for an aquaponic setup, (2) to design an interface to facilitate remote monitoring with an alerting system, and (3) to study the impact of water parameters on fish health and establish a fish disease risk index.

2. METHODOLOGY

After conducting a thorough literature review, threshold levels for water parameters (Temperature, pH, DO, Ammonia, and Turbidity) were established and ranked based on their severity towards fish health. The table below shows the thresholds for one of the parameters.

Table 1. Temperature Threshold Table

| Parameter | Optimum Range | Thresholds | |
|-------------|---------------|------------|-----------|
| Temperature | 25 – 30 | ≤ 15 | High Risk |
| | | 16 – 23 | Low Risk |
| | | 25 – 30 | Optimum |
| | | 32 – 35 | Low Risk |
| | | ≥ 38 | High Risk |

Besides, to accommodate outdoor use, an enclosure box was designed to house the electronics, with design criteria listed below.

Table 2. Enclosure Box Design Criteria

| Criteria | Justification |
|--------------|--|
| Waterproof | Water from rainfall should not be able to leak into the box. |
| Air Flow | Hence, proper airflow is required to prevent overheating. |
| Inlet/Outlet | There needs to be a passage to be able to facilitate wires. |
| UV Resistant | Direct sunlight should not degrade the material of the box over time. |
| Mounting | Should be able to be mounted and dismantled easily at aquaponics site for maintenance. |

Similarly, a sensor housing was designed to protect delicate sensors from fish and debris, based on the criteria listed below.

Table 3. Sensor Housing Design Criteria

| Criteria | Justification |
|------------------|---|
| Material | The material should not degrade over prolonged immersion in water and should not pose any toxic harm to the fishes. |
| Water Flow | The housing should facilitate water exchange with the surroundings to prevent stagnation of water in the housing. |
| Ease of Cleaning | The housing should be easy to be cleaned. |
| Inlet | An inlet should facilitate the wires from the sensors. |

ThingSpeak was selected to display real-time sensor readings for water quality parameters. An alert system via email was also developed to notify users when thresholds are exceeded or sensors malfunction. However, recognizing that users may not continuously monitor the dashboard or check emails regularly, a Telegram Update System was developed to provide continuous and effortless real-

time information access. Next, to enhance sensor reliability, calibration was carried out, followed by a second round of customized calibration.

Moreover, the proposed sensor system measures ammonia levels using a method based on the relationship between ammonia equilibrium, pH, and temperature, as documented by the Florida Department of Environmental Protection (FDEP). The equations used are shown below.

$$pK_a = \frac{0.0901821 + 2729.92}{T_k}$$

$$f = \frac{1}{(10^{pK_a - pH} + 1)}$$

A Fish Disease Index (FDI) was proposed to be established. This index is for users to gage on how severe the situation is when thresholds are exceeded. The equation used to establish the FDI is shown below.

$$Index = \frac{|Measured Value - Average Optimum Value|}{Average Optimum Value}$$

3. RESULTS AND DISCUSSION

The sensor calibration outcome is shown below.

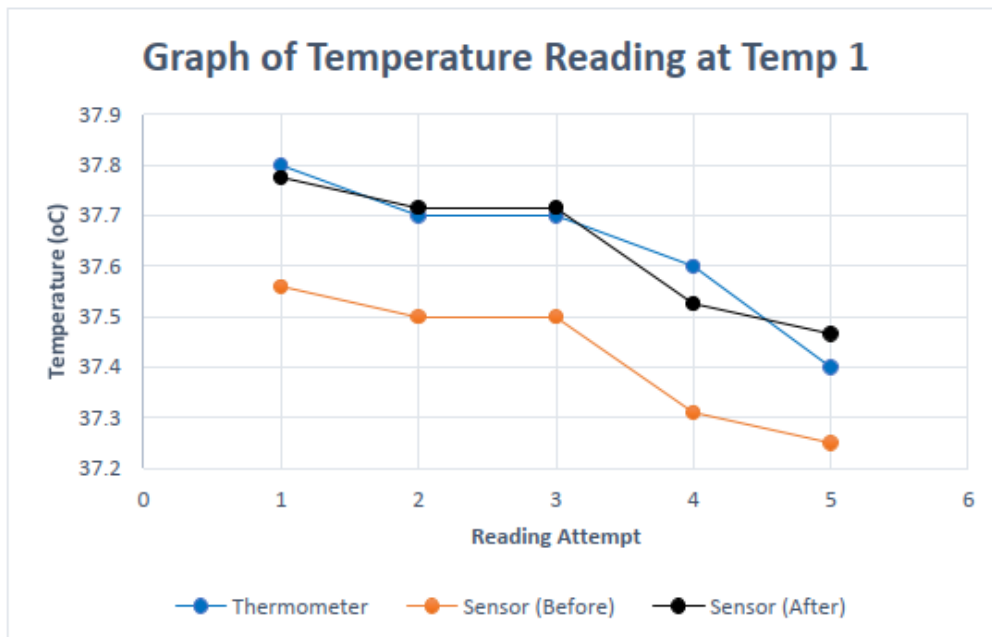


Figure 1. Temperature Calibration Graph

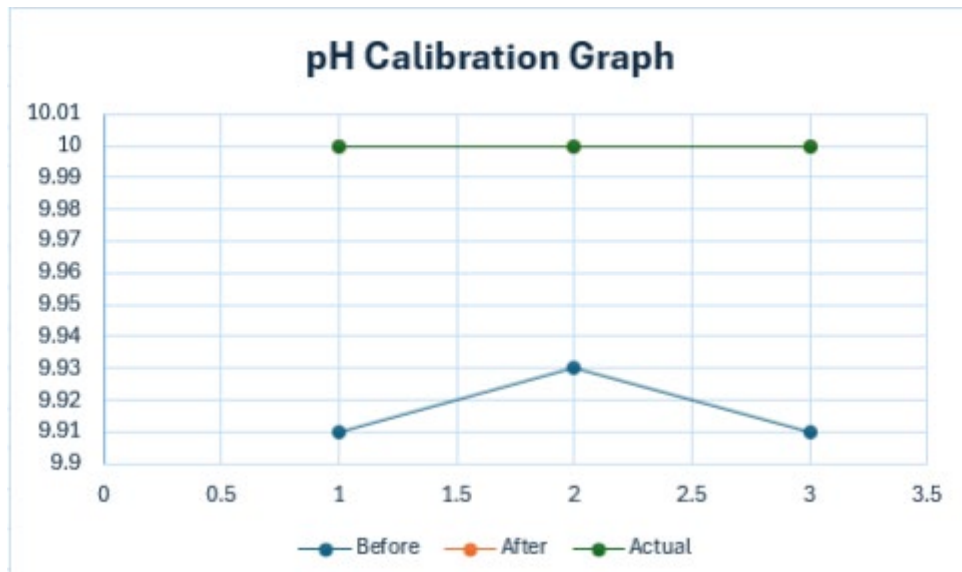


Figure 2. Temperature Calibration Graph

Table 4. Dissolved Oxygen Calibration values in mg/L

| Theoretical | Before Cal (Avg) | After Cal (Avg) |
|-------------|------------------|-----------------|
| 7.71 | 7.00 | 7.70 |

The turbidity sensor initially operated using the manufacturer's equation, which proved erroneous. A new method using best-fit graphing based on voltage points from the sensor datasheet was developed:

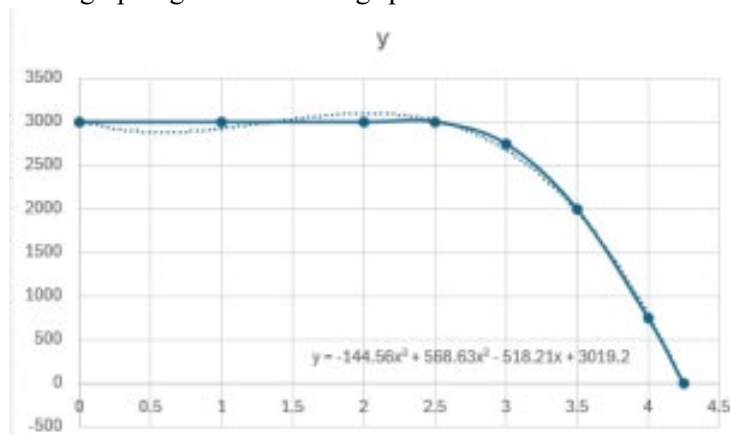


Figure 3. Turbidity sensor modelling to obtain equation

Following the methodology, the Fish Disease Index (FDI) was calculated for all water parameters. Table below shows an example of FDI.

Table 5. FDI for temperature

| Category | Threshold | | Index | |
|------------------------------|-------------|-------------|-------------|-------------|
| | Lower Limit | Upper Limit | Lower Limit | Upper Limit |
| High Risk | 0 | 15 | 1.00 | 0.45 |
| Low Risk | 16 | 23 | 0.42 | 0.16 |
| Optimum | 24 | 30 | 0.13 | 0.09 |
| Low Risk | 32 | 35 | 0.16 | 0.27 |
| High Risk | 38 | 50 | 0.38 | 0.82 |
| Average Optimum Value = 27.5 | | | | |

Based on design criteria, the enclosure box, sensor housing, and circuit were developed and tested, then assembled at UM Aquaponics, Block L, Level 4.

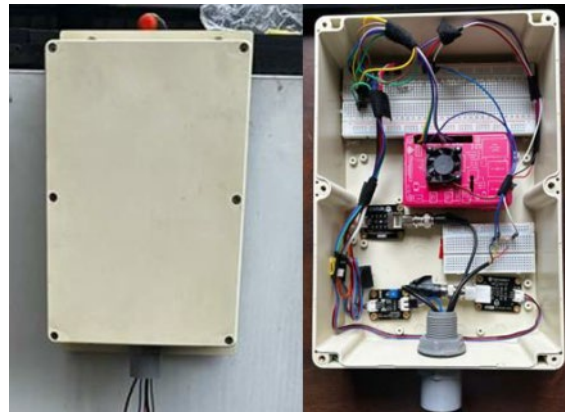


Figure 4. Interior and exterior view of enclosure box



Figure 5. Sensor Housing



Figure 6. IoT Monitoring System installed at site

The ThingSpeak dashboard was also developed as shown in the figure below:



Figure 7. ThingSpeak dashboard snippet

Email alerts and a Telegram Update System were developed to notify users of water condition changes and sensor malfunctions. This system provides effortless, real-time updates, allowing users to receive important information instantly without the need to constantly check the dashboard or email.

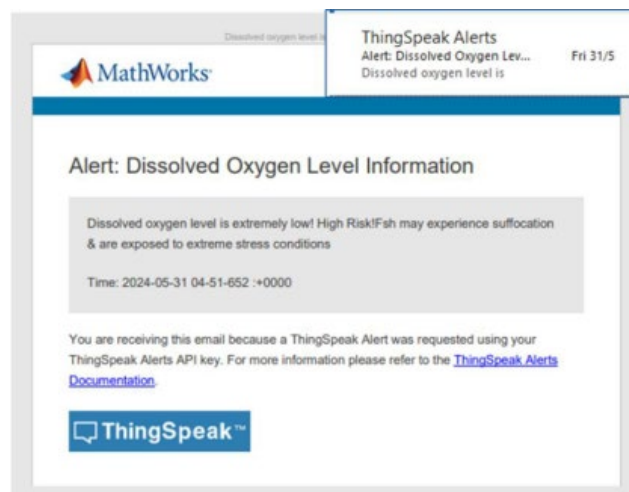


Figure 8. Email Alerts

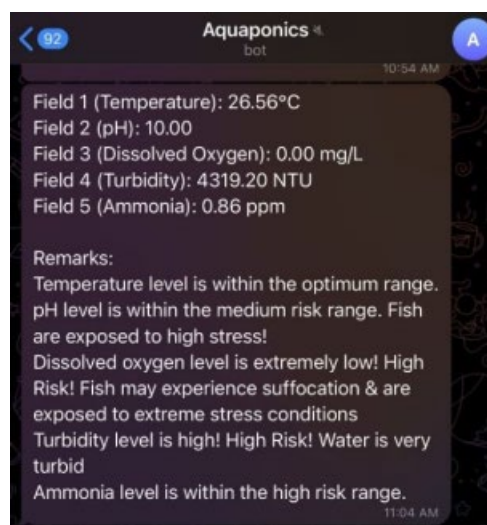


Figure 9: Telegram Update System

4. CONCLUSION

This project successfully developed a user- friendly IoT monitoring system for aquaponic setups, integrating sensors for crucial water parameters. Deployed at the University Malaya aquaponic site, it supports optimal plant and fish growth. A user-friendly ThingSpeak dashboard allows remote monitoring, with an alert system providing timely notifications. The project also established a Fish Disease Index (FDI) for early health risk detection. Overall, this system enhances efficiency, sustainability, and ease of maintenance in urban farming practices.

REFERENCES

- [1] Pattillo, D. A. (2017). An Overview of Aquaponic Systems: Aquaculture Components. Technical Bulletin of North Central Regional Aquaculture Center, 124.
https://lib.dr.iastate.edu/cgi/viewcontent.cgi?article=1019&context=ncrac_techbulletins

Development of Motorized Ball Valve for Automated Aquaponics System

Muhammad Hafizzudin bin Kamaluddin^a and Ahmad Saifizul bin Abdullah^{b*}

Department of Mechanical Engineering,
Faculty of Engineering, Universiti Malaya,
50603, Kuala Lumpur, Malaysia

Email: ^a hafizzudink187@gmail.com, ^b saifizul@um.edu.my

*Corresponding author

ABSTRACT

This research aims to understand and improve the activation behaviour of a bell siphon in an aquaponics setup at Block L, Level 4, Faculty of Engineering. The study investigates the impact of varying water flow rates on the siphon's performance and develops a model of the water circulation system to design an effective controller using MATLAB. Key methodologies included the development of a lab-scale aquaponic prototype with acrylic bell siphon, creation of specific test metrics to study flow rate variations and modelling the system using transfer functions. PID tuner command in MATLAB was used to design controller for new design requirements of the system which are 20% overshoot percentage and under 15 seconds settling time. Visual observations of the bell siphon's behaviour, particularly issues with activation and deactivation, informed the study. The terms used are “siphon not stopping” and “siphon not starting”. Among P, PI, PD, and PID controllers, the PID controller proved to be the most effective in achieving the desired system response.

Keywords: Automated Aquaponics; Bell Siphon; Water Flow Control; PID Controller; Sustainable Farming

1. INTRODUCTION

Urban farming improves food security and sustainability by using 50% less water and land than traditional agriculture and reducing transportation energy and packaging waste. In aquaponics, Media-Filled Grow Beds use gravel and a bell siphon for water circulation and nutrient uptake. The bell siphon regulates the water circulation in system, essential for plant growth and water quality. Water control systems with sensors and actuators balance water levels and nutrient flow. PID Control models enhance stability and productivity. This study uses control theory to optimize water management in aquaponics, integrating system modelling to improve the bell siphon's efficiency and advance aquaponic technology.

2. METHODOLOGY

A lab-scale prototype of basis aquaponic system was built to ease experiment purpose. The prototype consists of a fish tank, grow bed, acrylic bell siphon, submersible water pump and simple piping configuration. Figure 1 shows the prototype.



Figure 1. Lab-scale Aquaponic Setup

The physical model used in this application to solve the problem is motorized ball valve. The control valve actuated by controlling the position angle of the ball valve (1) and water dynamic tank for water flowing in grow bed (2).

$$\left[\frac{R_a}{K_t} (J_m s + D_m) + K_b \right] \theta_m(t) = V(t) \quad (1)$$

$$\dot{h} = XQ_{in} - Y\sqrt{h_1} \quad (2)$$

(2) is non-linear system. Linearization required starting with setting operating point, trimming and Taylor series solution.

(1) and (2) were changed to frequency domain through Laplace transform.

$$G_1(s) = \frac{\theta_m(s)}{V(s)} = \frac{K_t/R_a J_m}{s \left[s + \frac{1}{J_m} \left(D_m + \frac{K_t K_b}{R_a} \right) \right]} \quad (3)$$

$$G_2(s) = \frac{h(s)}{\theta_m(s)} = \frac{0.1759X}{s + \frac{Y}{2\sqrt{h_1}}} \quad (4)$$

The overall system modelling is $G(s) = G_1(s)G_2(s) = \frac{h(s)}{V(s)}$

$$G(s) = \left(\frac{K_t/R_a J_m}{s \left[s + \frac{1}{J_m} \left(D_m + \frac{K_t K_b}{R_a} \right) \right]} \right) \left(\frac{X}{s + \frac{Y}{2\sqrt{h_1}}} \right) \quad (5)$$

PID tuner was used for design controller and compared between P, PI, PD, PID.

3. RESULTS AND DISCUSSION

The siphon's behaviour was observed through the acrylic bell siphon.



Figure 2. Siphon Effect

A few flow variations were studied and analysed based on the parameters such time taken, number of cycles, fill up and discharge rate and siphon start-stop behaviour.

Table 1. Raw Data

| Valve opening angle (%) | Time taken to fill up grow bed until opening standpipe (s) | | | | Time Taken for siphoning effect (s) | | | | Time taken to discharge water out of grow bed (s) | | | |
|-------------------------|--|-----|-----|-----|-------------------------------------|----|----|-----|---|------|------|--------|
| | 1 | 2 | 3 | Avg | 1 | 2 | 3 | Avg | 1 | 2 | 3 | Avg |
| 100 | 160 | 157 | 158 | 158 | 12 | 10 | 11 | 11 | 1200 | 1200 | 1200 | 1200++ |
| 75 | 202 | 199 | 202 | 201 | 12 | 17 | 18 | 16 | 1200 | 1200 | 1200 | 1200++ |
| 50 | 251 | 262 | 255 | 256 | 15 | 17 | 18 | 17 | 495 | 442 | 430 | 456 |
| 25 | 410 | 370 | 380 | 387 | 25 | 22 | 21 | 23 | 250 | 275 | 260 | 262 |
| 10 | 600 | 620 | 615 | 612 | 60 | 60 | 60 | 60 | 0 | 0 | 0 | 0 |

Table 2 shows the comparison of siphoning effects for different valve opening angle. Number of cycles was taken for each valve opening condition ranging from 5% to 100%.

Table 2. Valve opening vs number of cycles

| Valve opening angle (%) | 3 cycles | |
|-------------------------|-----------------|-----------------|
| | Siphon starting | Siphon stopping |
| 100 | / | X |
| 75 | / | X |
| 50 | / | / |
| 25 | / | / |
| 20 | / | / |
| 15 | / | / |
| 10 | X | X |
| 5 | X | X |

The overall transfer function that represents the whole system for both water control and water dynamic tank is:

$$G(s) = \frac{4.722}{s^3 + 2.299s^2 + 0.921s} \quad (6)$$

Time response based on equation is represented using MATLAB:

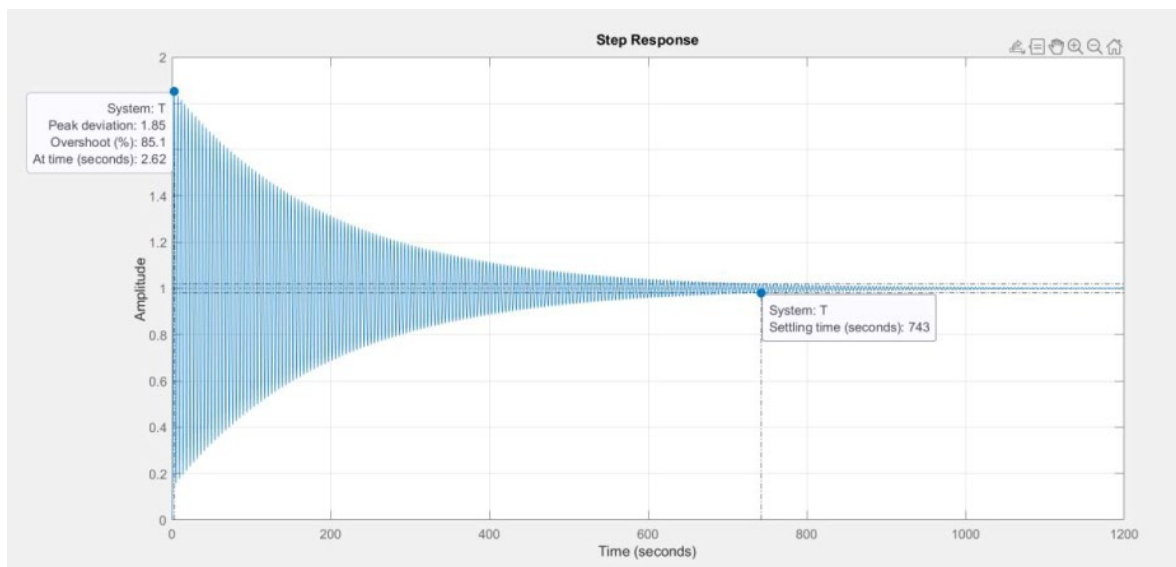


Figure 3. Time Response System

PID tuner is used to design controller to meet new desired requirement:

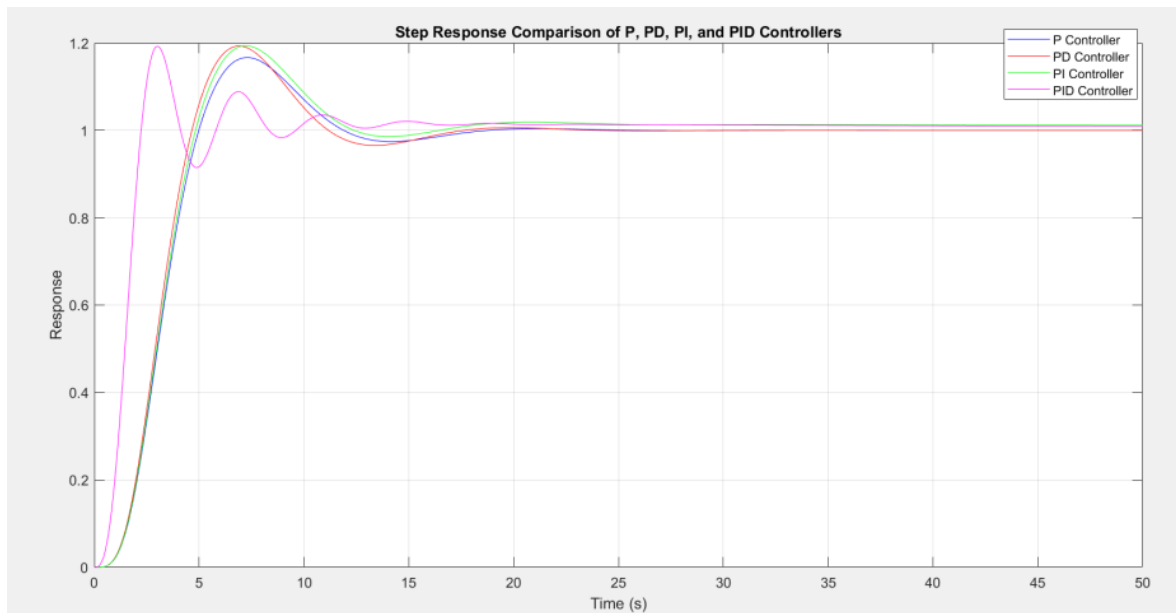


Figure 4. Tuned Response

4. CONCLUSION

The project investigated the bell siphon activation behavior in an aquaponics system, using an acrylic bell siphon to visually understand water flow and identify issues like siphon activation failures. Through extensive testing and validation, correlations were established between various parameters, and the water circulation system was successfully modeled, resulting in the development of a transfer function. A PID controller was designed to meet the new requirements, significantly improving system response and providing a foundation for future development.

REFERENCES

- [1] Cui, B., Lin, Z., Zhu, Z., Wang, H., & Ma, G. (2017). Influence of opening and closing process of ball valve on external performance and internal flow characteristics. *Experimental Thermal and Fluid Science*, 80, 193–202. <https://doi.org/10.1016/j.expthermflusci.2016.08.022>
- [2] Goddek, S., Joyce, A., Kotzen, B., & Burnell, G. M. (Eds.). (2019). *Aquaponics Food Production Systems*. Springer International Publishing. <https://doi.org/10.1007/978-3-030-15943-6>
- [3] Hossain, A. F. M. A., & Afzal, M. H. B. (2013). Management of irrigation and drainage systems using mathematical modelling. *Journal of Applied Water Engineering and Research*, 1(2), 129–136. <https://doi.org/10.1080/23249676.2013.876371>

A Study on the Repurposing of Abandoned Buildings into Urban Farms

Stephanie William Mogindol^a and Farazila binti Yusof^{b*}

Department of Mechanical Engineering,
Faculty of Engineering, Universiti Malaya,
50603, Kuala Lumpur, Malaysia

Email: ^a stephmogindol@gmail.com, ^b farazila@um.edu.my

*Corresponding author

ABSTRACT

Urbanization, a global phenomenon, offers numerous benefits but also leads to issues like building abandonment, which is prevalent in Malaysia. This study explores repurposing abandoned buildings for urban farming to extend their use and provide green solutions for climate change and food insecurity. Despite its potential, converting buildings into urban farms is challenging due to the lack of a standardized approach and tools to assess feasibility. Additionally, the process is hindered by risks and uncertainties regarding costs and returns. This research introduces the FLEX 4.0 VERTICAL FARMING (F4VF) program, aimed at urban farmers and developers. The program uses a two-step approach: evaluating the building's adaptive capacity and assessing the feasibility of vertical farms in specific spaces. The goal is to facilitate the transformation of abandoned buildings into thriving vertical farms, promoting sustainable agriculture and urban revitalization. This framework seeks to unlock the potential of neglected buildings, turning them into sustainable agricultural hubs.

Keywords: Abandoned Buildings; FLEX 4.0; Sustainability; Urban Farms; Vertical Farming

1. INTRODUCTION

In contemporary urban landscapes, the abundance of abandoned buildings presents an underutilized resource with immense potential: the conversion into urban vertical farms. The challenge lies in the lack of an approach to assess the feasibility of this conversion. Hence, this study introduces the 'FLEX 4.0 for Vertical Farms' (F4VF) tool designed to assess this feasibility.

Research Objectives:

- To investigate the adaptive capacity of abandoned buildings based on FLEX 4.0.
- To create a tool to assess the viability of converting an abandoned building into a vertical farm in terms of its adaptive capacity and production payoff.
- To validate the proposed holistic approach of assessing the regeneration of an abandoned building into an urban vertical farm through a case study comparison.

2. METHODOLOGY

The F4VF tool includes a two-step process:

2.1 FLEX 4.0 (Geraedts, 2016)

FLEX 4.0 [1] is an existing framework providing various parameters that can be used to describe the feasibility of an abandoned building to be regenerated. These parameters are defined by 44 flexibility key performance indicators with default weighting factors and are classed into five categories or 'layers', namely the site, structure, skin, facilities, and space plan.

2.2 VF Configuration (CityFarm, 2024)

Computes the feasibility of constructing a VF within an abandoned space, given desired dimensional parameters. This study referenced the commercial vertical farming units by CityFarm Malaysia [2]. Output parameters of this computation include total unit purchase price, monthly power usage, monthly cost, and monthly produce that would be incurred.

For validation, the created program will be used on a case study of the Plantagon project [3].

3. RESULTS AND DISCUSSION

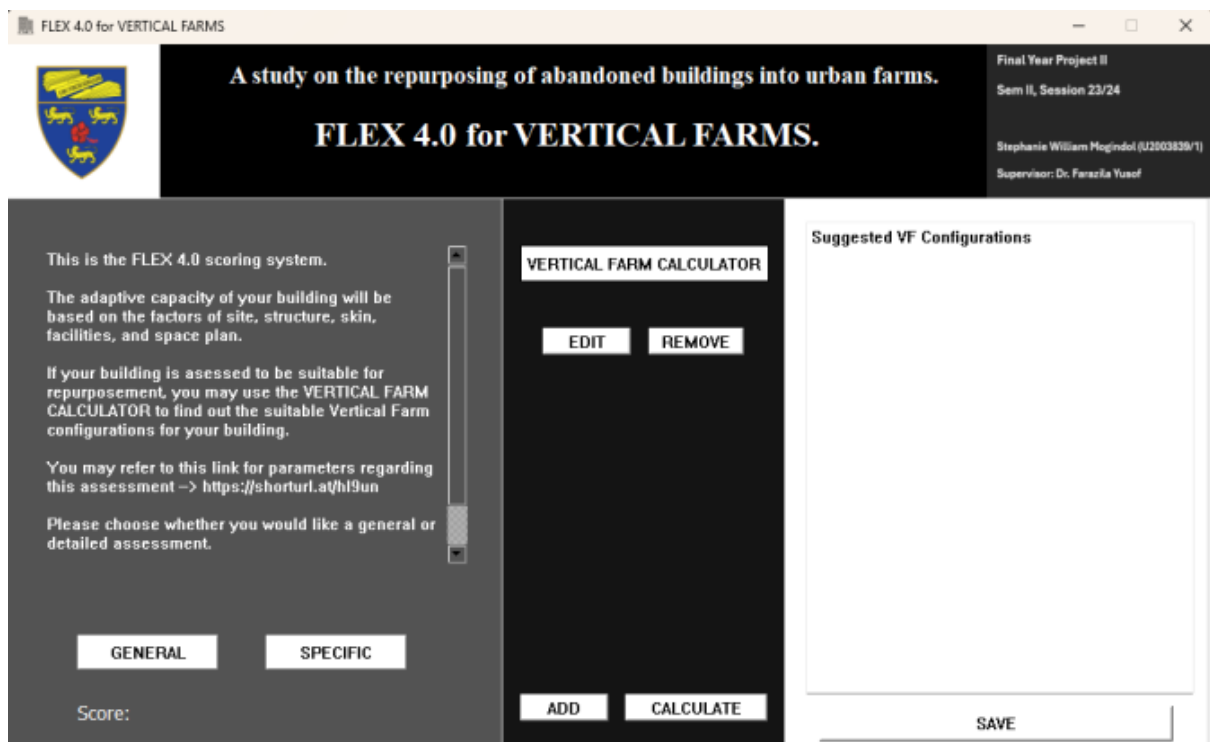


Figure 1. User interface of the F4VF tool.

3.1 FLEX 4.0 & VF Configuration assessment pilot run on the F4VF tool:

A general and specific assessment was carried out with specified sample parameters. The output generated matched the hypothetical calculated results.

3.2 Validation with the Plantagon Case Study:

The parameters of Plantagon used in this validation were:

Table 1. Plantagon vertical farm data.

| | |
|----------------------|--|
| Growing area | approx. 48437.6 ft ² = 220.0854 ft by 220.0854 ft |
| Height | 11.5 ft |
| Annual yield | 500,000 kg of vegetables |
| Monthly yield | 500,000 kg/12 months = 41,666.67 kg |

This data was input into the F4VF tool, where the output yielded the results:

```
Suggested VF Configurations:  
  
Room 1 ..... 302  
  
Total unit purchase price = RM9060000  
Monthly power usage = 240996kWh  
Monthly cost = RM124137.1  
Monthly produce = 26274kg
```

Figure 2. Final values of the F4VF tool the Plantagon project.

When comparing the F4VF program output with the actual results, a 36.94% percentage difference was computed. The large gap in both values were determined to be:

- Higher innovative technology used by Plantagon such as a helix conveying system and a heat turbulence management system.
- Multiple stakeholders managing the system.
- Large-scale of the farm operation

4. CONCLUSION

Abandoned urban buildings present opportunities for sustainable redevelopment through vertical farming. This research developed the FLEX 4.0 Vertical Farming (F4VF) tool to assess and facilitate this process. The F4VF tool combines evaluating a building's flexibility with an analysis of vertical farming feasibility, ensuring a thorough assessment. It addresses the lack of specialized tools for converting abandoned buildings into farms, empowering stakeholders to navigate the complexities of such projects. Although validation showed discrepancies with real-world data, the tool's strength lies in providing a comprehensive initial assessment. This research contributes to sustainable urban development and the revitalization of neglected spaces.

REFERENCES

- Geraedts, R. (2016). FLEX 4.0, a practical instrument to assess the adaptive capacity of buildings. *Energy Procedia* 96 (2016) 568 – 579. DOI: <https://doi.org/10.1016/j.egypro.2016.09>
- CityFarm Malaysia. (2024). All Kits & Systems. CityFarm Malaysia. <https://cityfarm.my/collections/all-hydroponic-setup>
- Fahim, R. A. (2021). Exploring the potentials and challenges of transforming vacant buildings in dense urban areas into an indoor vertical farm. Ain Shams University, Faculty of Engineering. Cairo, Egypt.

Microstructural and Tribological Analysis of Fe-based Amorphous Laser Cladded Coatings on AISI 52100 under Various Lubrication Conditions

Hussam Yahya Mohammed Al-Haddi ^a and Nurin Wahidah binti Mohd Zulkifli ^{b*}

Department of Mechanical Engineering,
Faculty of Engineering, Universiti Malaya,
50603, Kuala Lumpur, Malaysia

Email: ^a hussam.alhaddi@gmail.com, ^b nurinmz@um.edu.my

*Corresponding author

ABSTRACT

This study addresses the limitations of AISI 52100 steel, specifically its wear and corrosion susceptibility, by developing Fe-based amorphous coatings through laser cladding. The research focuses on optimizing laser cladding parameters, maximizing amorphous content, and evaluating the microstructural and tribological properties of the coatings. Experimental methods include laser cladding of FeCrMoCB on AISI 52100 substrates, followed by characterization tests using XRD, SEM, and 3D optical profilometry. Based on initial characterization tests, two laser cladding parameters were found to be optimal, the parameters for S6 and S7 were subsequently called P1 and P2. Tribological and corrosion tests under various conditions done on P1 and P2 samples demonstrated significant improvements. Coatings showed an amorphous phase content of 33.2%-53.2%, with uniform deposition thickness ranging from 16.61 to 33.27 μm . Under dry sliding conditions, polished steel exhibited the highest CoF of 0.141, while P1 and P2 coatings demonstrated reduced values of 0.104 and 0.127. Corrosion tests revealed that uncoated polished steel had the highest corrosion rate of 0.061 mm/y, whereas P1 and P2 coatings showed significantly lower rates of 0.022 mm/y and 0.035 mm/y. Results indicate that Fe-based amorphous coatings effectively enhance the tribological and corrosion resistance of AISI 52100 steel in severe environments.

Keywords: AISI 52100 Steel; Fe-Based Amorphous Coatings; Laser Cladding; Tribological Properties; Corrosion Resistance

1. INTRODUCTION

AISI 52100 steel is a metal used in harsh environments. Solutions are needed to increase its lifespan and reduce wear and corrosion. Among these solutions, laser cladding is particularly effective, offering precise control, high-quality coatings, and minimal heat-affected zones [1]. Fe-based amorphous coatings applied using laser cladding provide significant advantages due to their amorphous structure, which lacks grain boundaries, enhancing wear and corrosion resistance. Fe-based coatings are cost-effective and readily available, making them ideal for industrial applications [2]. This research aims to develop Fe-based amorphous coatings on AISI 52100 steel through laser cladding, optimizing parameters like laser power, scan speed, and overlap rate to achieve the best coating properties.

Objectives include evaluating the microstructural and tribological properties of the coatings and investigating their performance under various lubrication testing conditions.

2. METHODOLOGY

2.1 Coating Deposition

Substrates undergo surface preparation then 0.75g of FeCrMoCB powders were then deposited by laser cladding under varying parameters (laser power, scan speed, overlap rate). Post-coating processes included polishing to achieve a uniform surface for precise characterization.

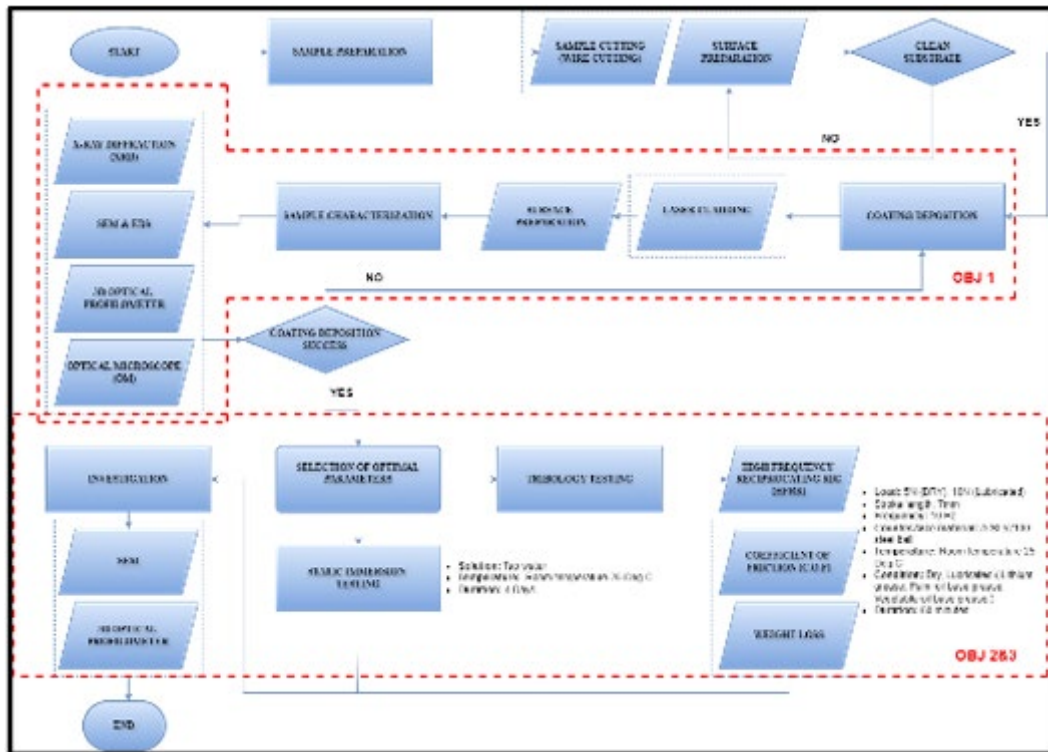


Figure 1. Research flowchart

2.2 Coating Characterization

Characterization tests included X-ray diffraction (XRD) to measure amorphous content, scanning electron microscopy (SEM) for microstructure analysis, and 3D optical profilometry for surface roughness. The amorphous content was calculated using the formula:

$$\text{AmorphousContent}(AC) = \frac{\text{Area under the amorphous background}}{\text{Total area under the XRD pattern}}$$

2.3 Tribological Testing

Tribological testing assessed wear resistance and frictional behavior under dry and lubricated conditions using a High Frequency Reciprocating Rig (HFRR), Lubrications used were Commercial grease, and two biodegradable greases. The coefficient of friction (CoF) was determined using:

$$\mu = \frac{F}{P}$$

2.4 Corrosion Testing

Corrosion testing involved immersion tests, with the corrosion rate calculated by:

$$\text{Corrosion Rate} = \frac{\Delta W \times 87.6}{A \times t \times \rho}$$

Where:

- ΔW = Weight loss (mg)
- A = Surface area cm²
- t = Time (Hours)
- ρ = Density (g/cm³)

3. RESULTS AND DISCUSSION

3.1 Initial Characterization and Development of Laser Cladding Parameters

X-ray diffraction (XRD) analysis confirmed the amorphous nature of FeCrMoCB powder, characterized by broad, diffuse peaks. Among the nine samples, S6 and S7 showed 46.3% and 42.97% amorphous content, respectively, indicating rapid solidification. The highest amorphous content was found in S8 at 53.19% (Fig. 2). The coatings exhibited a combination of crystalline and amorphous phases, with Fe-Cr, Fe₂₃B₆, FeN_{0.0499}, and B_{0.3}C_{1.3}N_{0.3} being common phases. These results suggest that the laser cladding process was effective in producing a significant amorphous phase, crucial for enhancing wear and corrosion resistance.

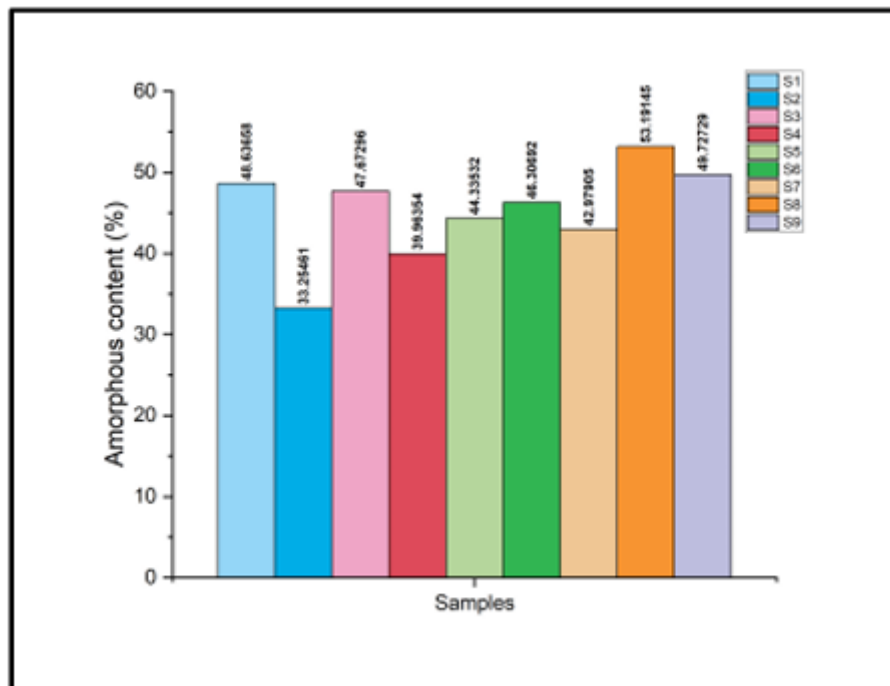


Figure 2. Amorphous content

The thickness of the coatings varied based on laser parameters, with S6 and S7 measuring 31.26 μm and 30.72 μm , respectively. Thicker coatings generally resulted from higher laser power and appropriate scan speeds and overlap percentages. Consistent thickness is essential for uniform protection and mechanical stability of the coatings, indicating optimal laser cladding parameters were used.

3.2 Tribological Performance

Under dry conditions, polished steel had the highest CoF at 0.141, while P1 and P2 showed lower values at 0.104 and 0.127, respectively. With commercial lithium based grease, CoF reduced for polished steel to 0.131, and for P1 and P2 to 0.099 and 0.117, respectively. Palm oil-based grease further reduced CoF, with polished steel at 0.128 and P1 and P2 at 0.072 and 0.111. Vegetable oil-based grease showed a slight increase in CoF for polished steel to 0.130, while P1 and P2 were at 0.084 and 0.113. These results demonstrate that Fe based coatings significantly reduce friction, especially when combined with biodegradable lubricants.

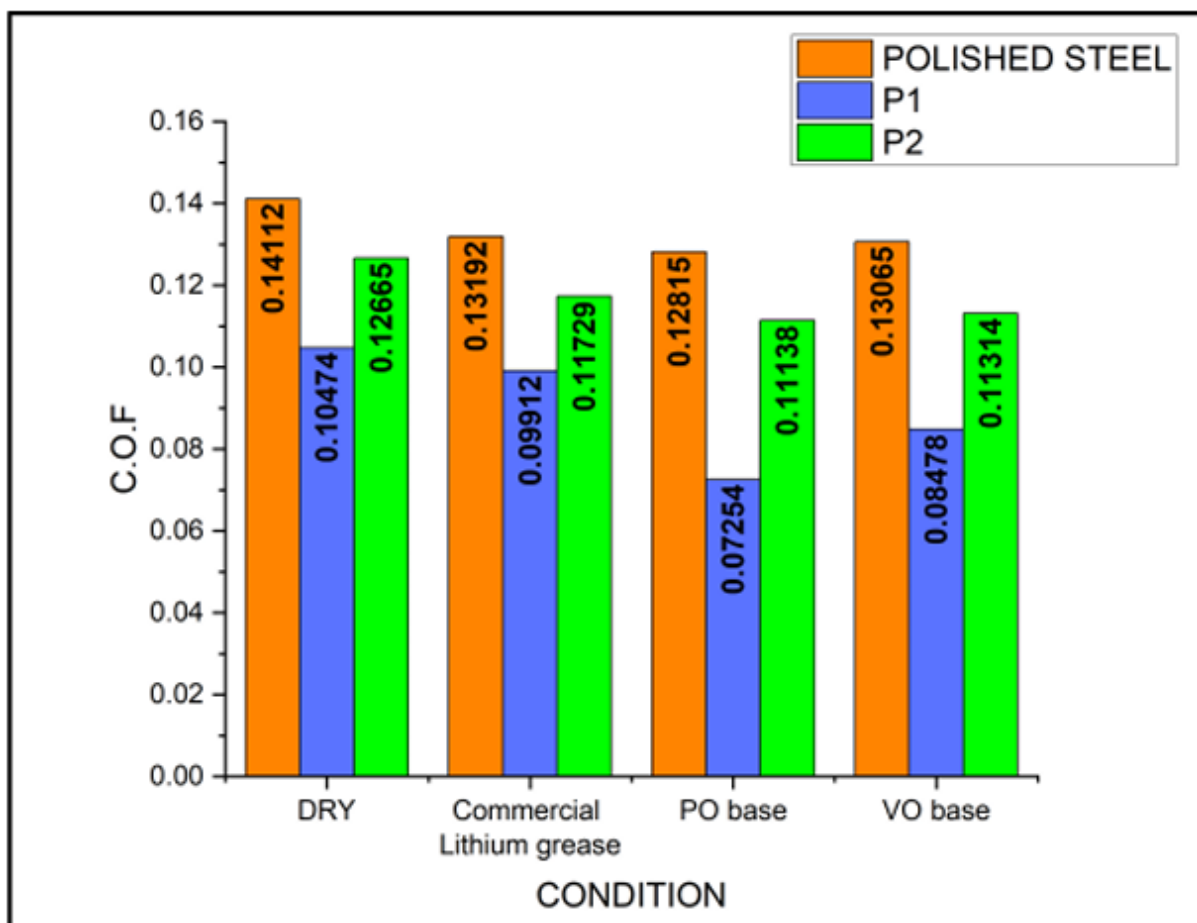


Figure 3. Average CoF

3.3 Corrosion Evaluation

Corrosion Rate: Polished steel had the highest corrosion rate at 0.061 mm/y, whereas P1 (using S6 parameters) had a corrosion rate of 0.022 mm/y and P2 (using S7 parameters) had a rate of 0.035 mm/y. This significant reduction in corrosion rate for the coated samples indicates enhanced corrosion resistance provided by the Fe-based amorphous coatings.

SEM analysis showed significant corrosion damage on polished steel with numerous pits and a rough texture. In contrast, P1 and P2 exhibited fewer pits and smoother surfaces, indicating higher corrosion resistance. The smoother surfaces and fewer pits in the coated samples further confirm the effectiveness of the coatings in providing enhanced protection against corrosive environments.

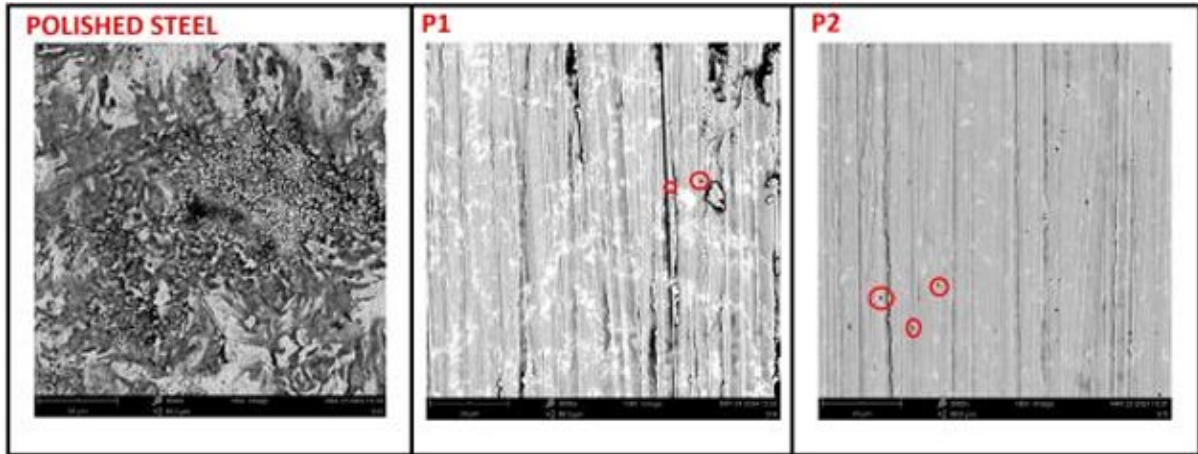


Figure 4. SEM images of corroded samples

4. CONCLUSION

This study demonstrated the effectiveness of Fe-based amorphous coatings developed through laser cladding in enhancing the tribological and corrosion resistance of AISI 52100 steel. The characterization phase identified two optimal samples, S6 and S7, based on their significant amorphous content and consistent coating thickness. Higher laser power and appropriate scan speeds were crucial for rapid solidification and uniform deposition, while moderate overlap rates minimized porosity and thermal stress.

Tribological testing showed that the coated samples, P1 and P2, had lower coefficients of friction and reduced wear rates compared to uncoated steel, with P1 exhibiting the best performance. Lubrication further improved results, with biodegradable lubricants, especially palm oil-based grease, reducing friction and wear more effectively than commercial lithium-based grease.

Corrosion testing indicated that the coatings significantly enhanced corrosion resistance, with coated samples showing fewer pits and smoother surfaces than uncoated steel. These findings underscore the potential of Fe-based amorphous coatings, particularly when used with environmentally friendly lubricants, to improve the durability and lifespan of components in harsh environments.

REFERENCES

- [1] Jiang, R. S., Wang, Y. T., Tang, J., Xu, G., & De Liu, Z. (2016). Microstructure and Properties of Fe-Based Amorphous Composite Coating Prepared by Pulse Laser. *Materials Science Forum*, 849, 642-646. <https://doi.org/10.4028/www.scientific.net/msf.849.642>
- [2] Yu, J., Qiao, C., Zhang, S., Liu, Z., & Wróblewski, P. (2023). Tribological properties of laser-cladded Fe-based amorphous composite coatings under dry and lubricated sliding. *Optics & Laser Technology/Optics and Laser Technology*, 166, 109583. <https://doi.org/10.1016/j.optlastec.2023.109583>

Tribological Analysis of Modified Palm Oil Lubricant using Nano Additives as Transmission Fluid for Electric Vehicle

Yuvvaraj A/L Balan^a and Nurin Wahidah binti Mohd Zulkifli^{b*}

Department of Mechanical Engineering,
Faculty of Engineering, Universiti Malaya,
50603, Kuala Lumpur, Malaysia

Email: ^a yuvvaraj2708@gmail.com, ^b nurinmz@um.edu.my

*Corresponding author

ABSTRACT

Lubricants are essential for the optimal performance of electric vehicle (EV) mechanical systems, prompting a shift from conventional mineral oils to bio-based alternatives due to environmental concerns. This study examines the physicochemical and tribological properties of pure palm base oil enhanced with hexagonal boron nitride (h-BN) and polytetrafluoroethylene (PTFE). Friction tests at 40°C, 60°C, and 80°C, along with a copper strip test for corrosion resistance, were conducted. The formulations were compared to commercial ATF Premium Automatic Transmission Fluid (PETRON) and G-III base oil. Using a DUCOM Four Ball Tester TH-30H and SEM, the 0.5 wt% PTFE + 0.7 wt% h-BN nano lubricant showed the lowest friction and wear scar diameter at 80°C, and highest corrosion resistance. It also demonstrated a stable viscosity index with high dynamic and kinematic viscosities, making it ideal for transmission gear components. This study supports the development of eco-friendly lubricants for EVs.

Keywords: Additives, Bio-based, Corrosion, Lubricants, Tribological

1. INTRODUCTION

The global shift towards environmentally friendly lubricants and the adoption of nanotechnology is reshaping the mineral-oil-based lubricants market. However, mineral-based lubricants pose environmental risks, leading to soil and water contamination. Bio-based lubricants, including sustainable biofuels, offer a viable solution by significantly reducing carbon emissions. In tribology, the study of friction, wear, and lubrication is vital for the efficient operation of electric vehicle (EV) transmission systems. Effective lubrication reduces friction, protects gears and bearings, and ensures thermal stability, preventing overheating under varying conditions (Abdel-Rehim et al., 2021; Ali et al., 2022) [1,2].

Bio-lubricants, particularly biodegradable nano-lubricants, enhance lubrication, reduce friction, and align with sustainability goals (Hund et al., 1994; Gulzar, 2018) [7]. Despite their benefits, challenges like stability and system compatibility require further research. Vegetable oils, while promising, suffer from poor thermal oxidation stability and inadequate low-temperature performance, limiting their use (Erhan, Sharma, & Perez, 2006) [6]. Palm oil, with its adaptable fatty acid profile, presents a potential solution. Its viscosity can be optimized with additives, and nanoparticles offer unique properties that enhance performance (Jongschaap et al., 2007; Thapa et al., 2018) [8,12].

Our research aims to address gaps in EV transmission fluid studies by analyzing bio-based nano lubricants at elevated temperatures. We focus on combining polytetrafluoroethylene (PTFE) and hexagonal boron nitride (h-BN) with palm oil to reduce friction and improve corrosion resistance, bridging existing research gaps (Del Río et al., 2022; Opia, Abdollah, & Amiruddin, 2023) [5,11].

2. METHODOLOGY

This study investigates the physicochemical and tribological properties of bio-based lubricants using palm oil enhanced with varying concentrations of polytetrafluoroethylene (PTFE) and hexagonal boron nitride (h-BN). Samples were prepared with different h-BN percentages, while maintaining the same volume of palm oil and PTFE. A commercial ATF Premium Automatic Transmission Fluid (PETRON) served as a baseline. Metal specimens were polished to assess oxidation in the oil samples.

Four samples were prepared: pure palm oil, and three with nano-additives (0.5 wt% PTFE + 0.5 wt% h-BN, 0.5 wt% PTFE + 0.6 wt% h-BN, and 0.5 wt% PTFE + 0.7 wt% h-BN). Oleyl sarcosine (0.5 wt%) was added as a corrosion inhibitor and stabilizer. Additives were dispersed through 4 hours of ultrasonication after blended using a magnetic hot plate stirrer at 40°C and 600 rpm for 1 hour. Polished metal specimens were prepared for corrosion testing.

A DUCOM four-ball tester TR-30H series evaluated the frictional properties and wear resistance of the lubricants. Tests followed the ASTM D2266 method, with conditions including a 40 kg load, 1200 ± 50 rpm speed, and temperatures of 40°C, 60°C, and 80°C. The coefficient of friction (COF) was calculated using the IP-239 Standard of 1986, while wear scar diameter was measured using SEM.

The calculation of COF can be achieved using the following formula:

$$\mu = \frac{T\sqrt{6}}{3Wr}$$

The corrosion resistance test was simulated using a test rig following ASTM D4636-99 standards. A three-neck flask contained the oil sample, maintained at 240°C and stirred at 500 rpm. Airflow simulated oxidation, with a condenser preventing evaporation and a thermometer monitoring temperature. Copper plates were used to assess lubricant corrosion resistance. SEM, using a Hitachi TM-3030 microscope, examined corrosion resistance in the surface morphology of the copper plate. The copper plates were polished and went through corrosion testing before SEM analysis. Images compared corrosion morphology across different samples, using a magnification range of 15x to 30000x.

3. RESULTS AND DISCUSSION

The primary objectives include evaluating sedimentation, viscosity properties, friction and wear characteristics, and metal degradation. Figures 1 and 2 illustrate the oil samples before and after being undisturbed for three weeks, revealing minimal sedimentation. Formulated nano lubricants with PTFE and hexagonal boron nitride (h-BN) showed effective particle dispersion. The sample with 0.5 wt% PTFE + 0.7 wt% h-BN exhibited the most sedimentation, likely due to oversaturation. Stability over two weeks suggests effective stabilizing agents. This aligns with Ali et al. (2022) [2] on titanium dioxide and oleyl sarcosine inhibiting sedimentation.



Figure 1. Nano lubricants after the formulation process



Figure 2. Nano lubricants after 3 weeks undisturbed

Specifically, the 0.5 wt% PTFE + 0.7 wt% h-BN sample showed the highest kinematic viscosity and viscosity index, indicating better performance over a range of temperatures. Soleimani et al. (2018) [12] support these findings, noting that nano additives improve lubricity and stability. FTIR spectra for various formulations, identifying functional groups like CHO aldehyde, O-H stretch, and N-H amines. The presence of these groups suggests oxidation reactions and self-lubricating properties. The 0.5 wt% PTFE + 0.7 wt% h-BN sample exhibited superior lubricity, consistent with findings from Arumugam et al. (2018) [3] and Yamane et al. (2006) [14].

Figures 3 and 4 shows the related data indicate that the 0.5 wt% PTFE + 0.7 wt% h-BN sample demonstrated the best performance with an 18.72% decrease in the coefficient of friction (COF) and the smallest wear scar diameter (WSD) at 40°C, 60°C and 80°C. Enhanced lubricity is attributed to strong bonds formed by high polarity ester groups and the fatty acid molecules in bio-based lubricants. Findings align with Beckford et al. (2016) [4] and Del Río et al. (2020) [5].

Surface damage analysis showed that ATF Premium Automatic Transmission Fluid caused the most severe corrosion, while pure palm oil exhibited better performance, attributed to its fatty acid polymers forming protective tribo-films. Nano lubricants with PTFE and h-BN, especially the 0.5 wt% PTFE + 0.7 wt% h-BN formulation, showed superior thermal stability and minimal oxidation, indicating excellent protective qualities. This aligns with Moreno et al. (2021) [10] and Li et al. (2018) [9]. In summary, the study demonstrates that nano lubricants with PTFE and h-BN significantly improve lubricity, stability, and corrosion resistance compared to traditional lubricants. The 0.5 wt% PTFE +

0.7 wt% h-BN formulation is particularly effective, maintaining stable physical properties and offering superior protection against wear and corrosion, making it a promising candidate for practical applications.

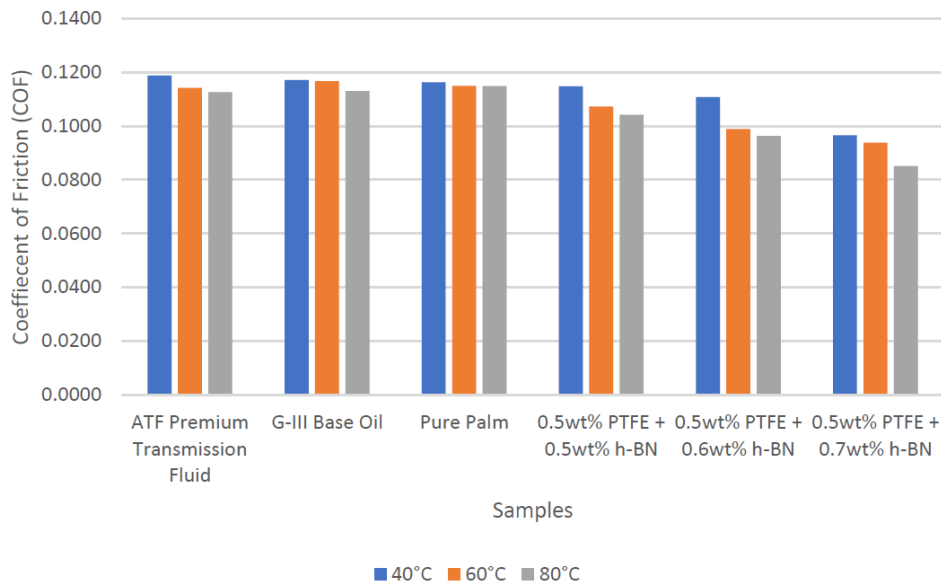


Figure 3. Coefficient of Frictions (COF) for samples at different working temperatures

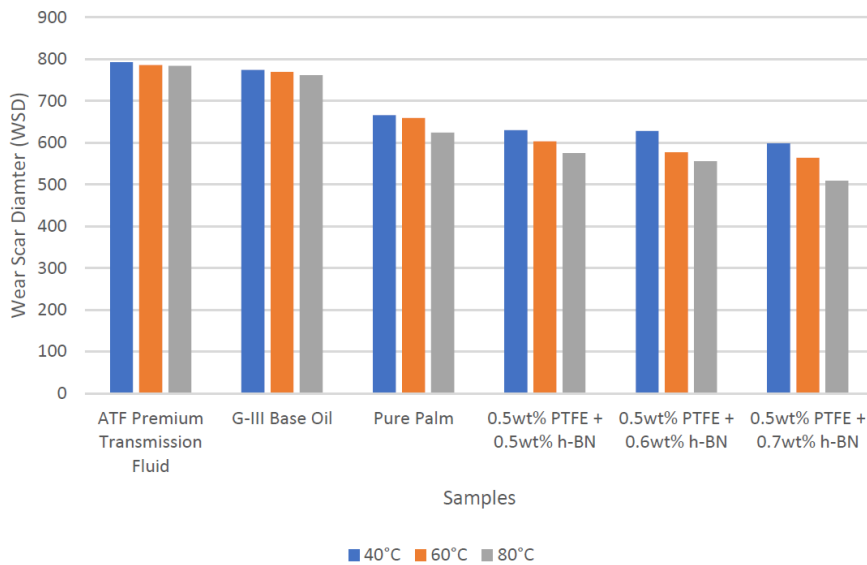


Figure 4. WSD values for samples at different working temperatures (μm)

4.0 CONCLUSION

In conclusion, this research investigated the physicochemical and tribological properties of TMP ester and pure palm oil with varying percentages of PTFE and h-BN additives. The formulation with 0.5wt % PTFE + 0.7wt% h-BN exhibited the highest viscosity index (198.3) and dynamic viscosity, indicating superior stability and lubrication across temperatures. FTIR spectra confirmed the presence of functional groups enhancing lubricant properties. This formulation also demonstrated the lowest coefficient of friction (0.0825) and wear scar diameter (509μm) at 80°C, significantly outperforming

pure palm oil and AT Premium Transmission Fluid. Additionally, it showed the least corrosiveness, indicating effective corrosion reduction. Overall, the 0.5wt% PTFE + 0.7wt% h-BN lubricant excelled in maintaining viscosity, reducing friction and wear, and providing superior corrosion resistance, making it the most effective formulation tested.

REFERENCES

1. Abdel-Rehim, A. A., Akl, S. Y., & Elsouady, S. (2021). Investigation of the tribological behavior of mineral lubricant using copper oxide nano additives. *Lubricants*, 9(2), 16. <https://doi.org/10.3390/>
2. Ali, M. K. A., Abdelkareem, M. a. A., Elagouz, A., & Hou, X. (2022). Nanolubricant additives. In Elsevier eBooks (pp. 675–711). <https://doi.org/10.1016/b978-0-323-90524-4.00032-3>
3. Arumugam, S., Ellapan, R., & Sriram, G. (2021). Degradation of engine components upon exposure to chemically modified vegetable oil - based automotive lubricant. *Journal of the Indian Chemical Society*.
4. Beckford, S., Cai, J., Fleming, R. A., & Zou, M. (2016). The effects of graphite filler on the tribological properties of Polydopamine/PTFE coatings. *Tribology Letters*, 64(3). <https://doi.org/10.1007/s11249-016-0777-5>
5. Del Río, J. M. L., Alba, A. B., Guimarey, M. J., Prado, J. I., Amigo, A., & Fernández, J. (2023). Surface tension, Wettability and Tribological Properties of a Low Viscosity Oil Using CaCO₃ and CeF₃ Nanoparticles as Additives. *Journal of Molecular Liquids*, 391, 123188. <https://doi.org/10.1016/j.molliq.2023.1112318>
6. Erhan, S. Z., Sharma, B. K., & Perez, J. M. S. (2006). Oxidation and low temperature stability of vegetable oil-based lubricants. *Industrial Crops and Products*, 24(3), 292–299. <https://doi.org/10.1016/j.indcrop.2006.06.008>
7. Gulzar, M. (2018). Literature review. In Springer theses (pp. 7-61). https://doi.org/10.1007/978-981-10-8294-8_2
8. Jongschaap, R., Corré, W., & Bindraban, P. (2007). Claims and facts on *Jatropha Curcas*L. ResearchGate. https://www.researchgate.net/publication/254137539_Claims_and_Facts_on_Jatropha_curcasL
9. Li, W., Jiang, C., Xu, N., Ma, R., & Wang, X. (2018). Tribological properties of polyolester based lubricants and their influence on oxidation stability. *Journal of Engineering Tribology*, 1-8.
10. Moreno, K. J., Teresa Hernandez-Sierra, M., Baez, J. E., Rodriguez-deLeon, E., Daniel Aguilera-Camacho, L., & Garcia-Miranda, J. (2021). On the tribological and oxidation study of xanthophylls as natural additives in castor oil for green lubrication. *Materials*.
11. Opia, A. C., Abdollah, M. F. B., & Amiruddin, H. Tribological Performance of Modified *Jatropha* lubricant Under Reciprocating NANOVEA T 50 Tribometer for Electric Vehicles.
12. Soleimani, M., Dehabadi, L., D. Wilson, L., & G. Tabil, L. (2018). Antioxidants classification and applications in lubricants. In D. W. Johnson, *Tribology, lubricants and additives*. doi:10.5772/intechopen.72621
13. Thapa, S., Indrawan, N., & Bhoi, P. (2018). An overview on fuel properties and prospects of *Jatropha* biodiesel as fuel for engines. *Environmental Technology and Innovation*, 9, 210–219. <https://doi.org/10.1016/j.eti.2017.12.00>
14. Yamane, K., Kawasaki, K., Sone, K., Hara, T., & Prakoso, T. (2006). Unsaturated fatty acid methyl esters and thermal oxidation characteristics. *Rev. Automotive Eng.*, 593-600.

Development of Visual Based Machinery Faults Diagnostic System using Phase-Based Motion Magnification and Displacement Extraction

Syahirah Binti Mazhairul^a and Ong Zhi Chao^{b*}

Department of Mechanical Engineering,
Faculty of Engineering, Universiti Malaya,
50603, Kuala Lumpur, Malaysia

Email: ^a syahirahmj8@gmail.com, ^b alexongzc@um.edu.my

*Corresponding author

ABSTRACT

Rotating machinery is widely used in industries, but it can fail unexpectedly, causing significant financial losses. Traditional methods for diagnosing machinery faults use sensors, which can be expensive and difficult to implement in large machines. This thesis presents a new, low-cost method using visual-based techniques to diagnose machinery faults. The proposed system uses videos of machinery to detect and magnify small movements that are hard to see with the naked eye. By analyzing these magnified movements, potential faults in the machinery can be identified and measured. Tests were conducted on various machines, including a guitar string, a lab test rig, and an industrial motor, to demonstrate the effectiveness of this method. Results show that the visual-based approach can produce reliable data for diagnosing faults and can work alongside traditional sensor-based approach. This method offers a cost-effective solution for monitoring machinery, providing a wider field of view and reducing overall costs. The thesis also discusses the benefits and limitations of this visual-based diagnostic system, suggesting it is a useful algorithm and tool for maintaining machinery in the industry.

Keywords: Displacement Extraction; Fault Diagnostics; Machinery; Motion Magnification; Visual-Based Monitoring.

1. INTRODUCTION

Rotating machinery is crucial in many industries but can suffer from unexpected failures, leading to costly downtime and repairs. Traditional fault diagnosis systems rely on sensors, such as accelerometers, which are effective but can be expensive and challenging to implement on large-scale machine [1]. Recent research has explored the potential of visual-based techniques as a cost-effective alternative for diagnosing machinery faults. The visual-based approach involves using video footage to detect and magnify subtle movements. This method leverages advancements in phase-based motion magnification and displacement extraction to provide detailed analysis of machinery [3].

Several key research papers have influenced this thesis. Wu et al. introduce the Eulerian Video Magnification (EVM) framework, which serves as a foundation for visual motion magnification techniques [4]. Improvement on EVM method have resulting with the Phase-Based Motion Magnification (PBMM) method using a Complex Steerable Pyramid (CSP) as shown in Fig. 1, which significantly improves noise handling and amplification of subtle motion [3]. In term of phase-based

displacement extraction [2], it's the advancement have continuously enhance the accuracy and applicability in various industrial settings. This research aims to develop a reliable, low-cost visual-based machinery fault diagnostic system by implementing PBMM and displacement extraction. Tests conducted on a guitar string, lab test rig, and industrial motor to demonstrate the effectiveness of this method in identifying and quantifying faults.

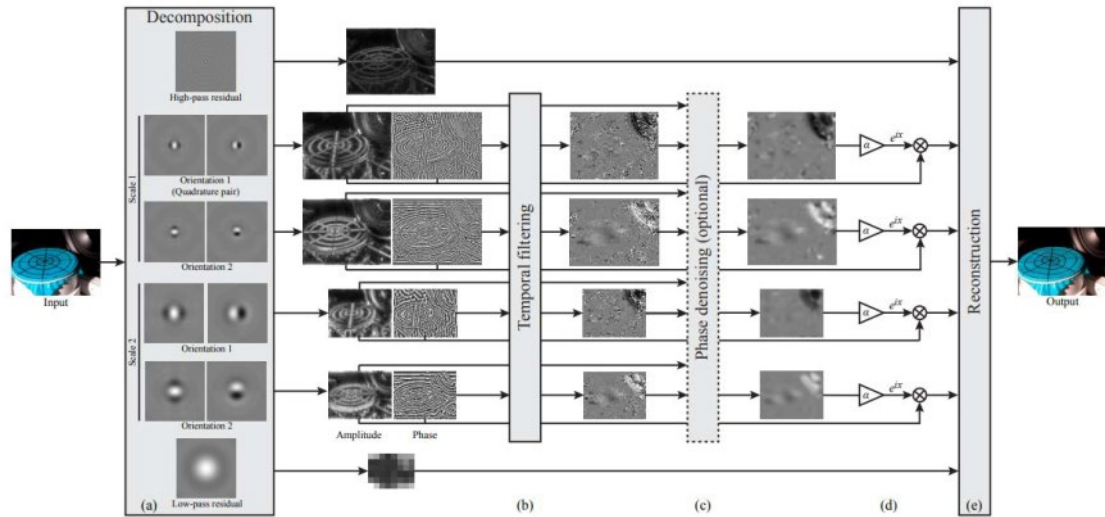


Figure 1. Overview CSP for Phase-Based Motion Magnification (Wadhwa et. al., 2013)

2. METHODOLOGY

The methodology is divided into three main stages. Firstly, the PBMM is implemented using Python, with essential libraries installed to support the process. Key Parameters such as maximum frame number (MaxFr.), window size (β), frame rate (FPS), magnification factor (α) and frequency range (Freq.) are set based on the parameters of device camera, video footages to achieve clear magnified motion which are stated in Table 1. Some videos which are being tested on are guitar, baby, column, test rig and industrial motor to ensure effective magnification.

Table 1. Parameters to magnify motion for each designated video.

| Video | MaxFr. | β | FPS | Freq. (Hz) | α |
|------------------|--------|---------|------|------------|----------|
| Baby | 300 | 30 | 30 | 0.4 - 3 | 10 |
| Guitar | 300 | 30 | 600 | 72-92 | 20 |
| Column | 600 | 100 | 1500 | 222-230 | 100 |
| Test Rig | 240 | 30 | 240 | 20-30 | 20 |
| Industrial Motor | 300 | 7 | 333 | 40-60 | 50 |

Secondly, the displacement extraction procedure involves decomposing videos into different levels to capture varying scales of detail. Based on research paper by [2], during the extraction, subband orientation of settings are being set based on the desired type of motion analysis. Subband [0] which is the 0° orientation is for analyzing x-motion and Subband [1] is represented as 90° orientation for analyzing y-motion.

During extraction of phases at each level for desired motion analysis, there is also computation of phase difference and phase gradients to calculate displacement. Computation in equations (1), (2) and (3) are made for y-motion analysis, the same flow progress computation are made for x-motion analysis. $\Delta\phi$ refers to phase difference, D is the denominator, $\frac{\partial\phi}{\partial y}$ is phase gradient y, Δy is the displacement of y direction.

$$\Delta\phi = \phi(y, t) - \phi(y, 0) \quad (1)$$

$$D = \{(\text{real}_y)^2 + (\text{imag}_y)^2\} + (1 \times 10^{-8})$$

$$\frac{\partial\phi}{\partial y} = \{(\text{real}_y) \cdot (\text{Grad_imag}_y) - (\text{imag}_y) \cdot (\text{Grad_real}_y)\} / D \quad (2)$$

$$\Delta y = \left(\frac{\partial\phi}{\partial y}\right)^{-1} \times (\Delta\phi) \quad (3)$$

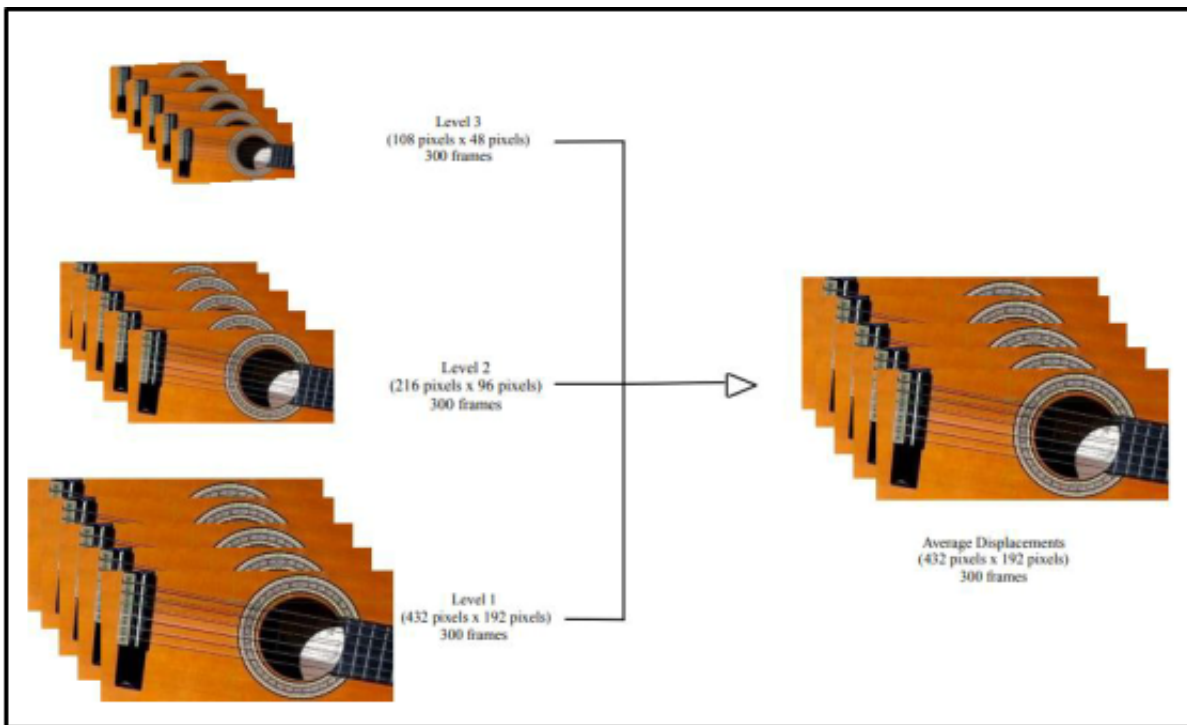



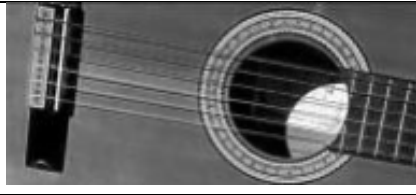








Figure 2. Graphical view of process pixel wise averaging.

The displacement y will be obtained for all Maximum No. Frame for each levels. Each of these levels have different dimensions, therefore pixel wise averaging is needed to compute the average displacement of each frame in each level to have output of average displacement across all frames. Fig 2. shows the graphical process of pixel wise averaging. The data from average displacement are used to be build Time Domain series and Fast Fourier Transform (FFT) Spectrum for analysis process.

3. RESULTS AND DISCUSSION

Results obtained for PBMM are obtained successfully and are shown in Table 2. All magnified videos are in grayscale for better visualizing of magnified subtle motions. Note that Test Rig video was taken using mobile phone

Table 2. Comparison of original and magnified video.

| Original Video | Magnified Videos |
|---|--|
|  |  |
|  |  |
|  |  |
|  |  |
|  |  |

For better analysis during phase extraction on each level, observation can be made on the phase maps, phase gradient maps and displacement maps. Fig 3 is consisting of phase maps & phase gradient maps and displacement map for test rig.

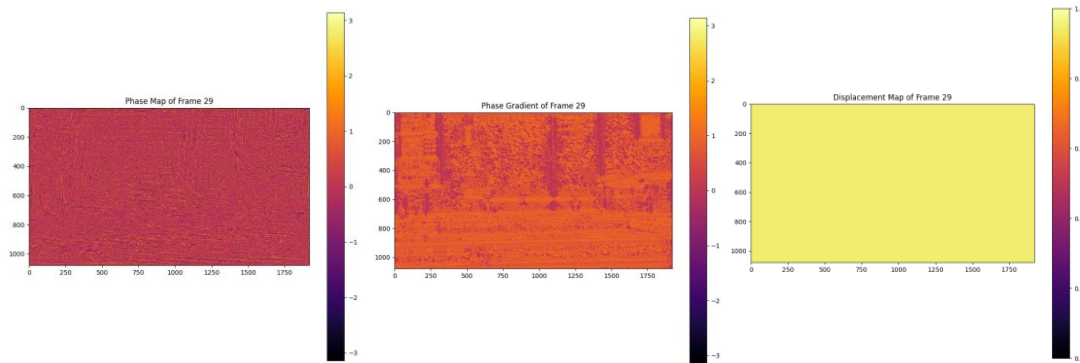


Figure 3. Phase maps, Phase Gradient maps & Displacement map at Level 1

With the displacement extraction & pixel wise averaging completed, chosen pixel to analyze for test rig is (150, 731) and graph Average Y Displacement against Frame No. is shown in Fig 4. The analysis can be further done in time domain series and FFT spectrum as shown in Fig 5.

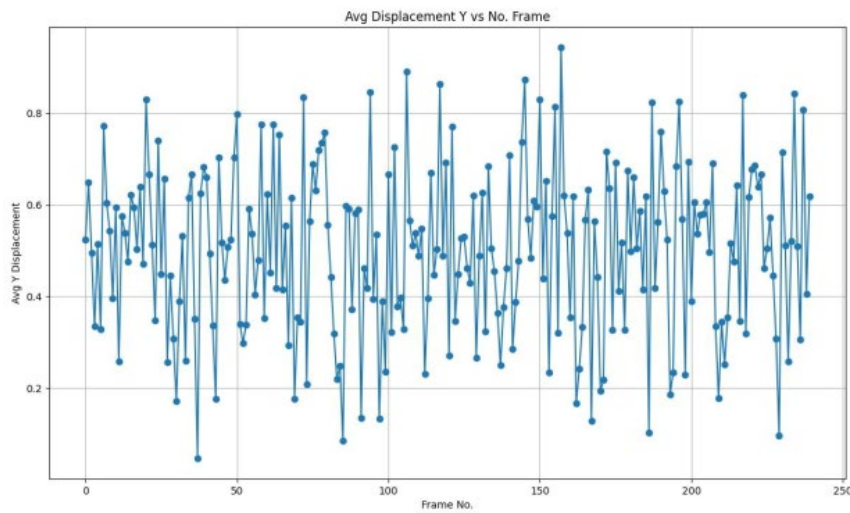


Figure 4. Graph Average. Displacement Y vs Frame No.

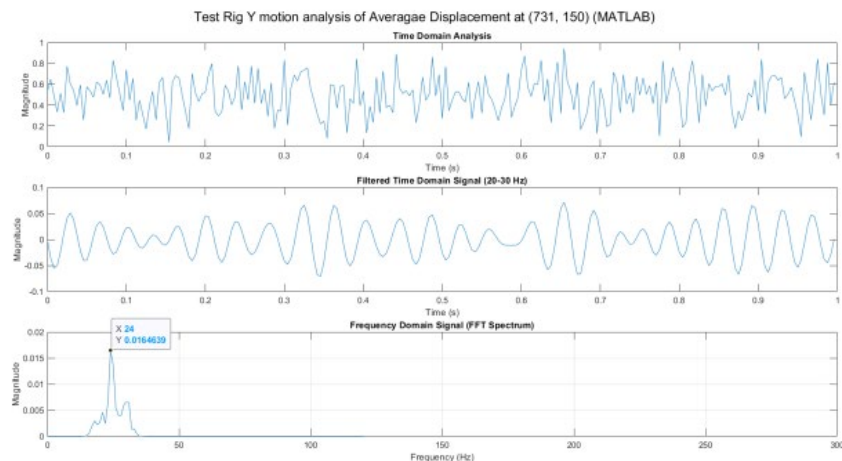


Figure 5. Time domain & FFT of Test Rig (Visual-based)

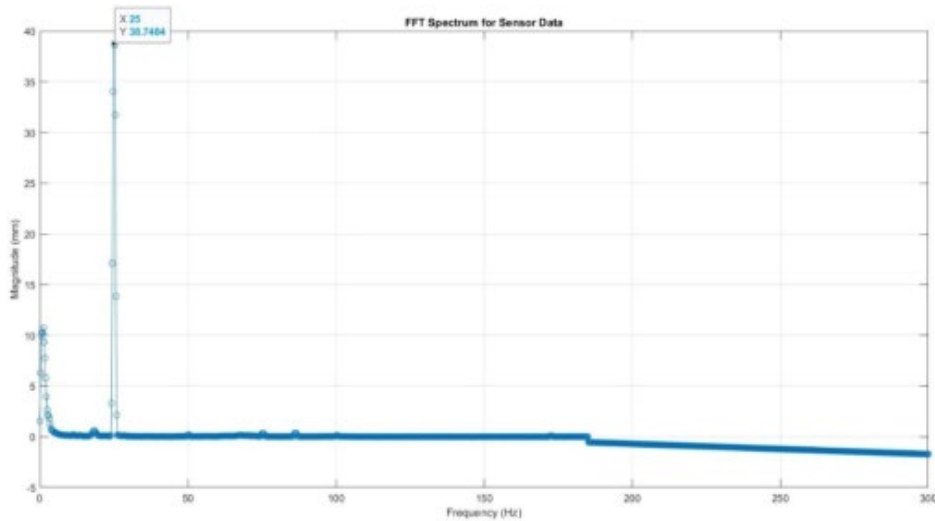


Figure 6. FFT spectrum of data from sensor.

Peak at 24Hz in Fig 5 indicate the test rig is having static imbalance issue. Comparing peak in Fig 5 and Fig 6 which is obtain using sensor, there is about 4% error for visual-based approach.

4.0 CONCLUSION

The PBMM method has proven to be able to magnify subtle motions for all videos tested. As shown in the quality magnification and phase maps produced. The phase-based displacement extraction approach also produces sufficient data which proves the method to be reliable and able to achieve using low-cost camera.

REFERENCES

- Carden, E. P., & Fanning, P. (2004). Vibration Based Condition Monitoring: A Review. *Structural Health Monitoring*, 3(4), 355-377.
- Collier, S., & Dare, T. (2022). Accuracy of phase-based optical flow for vibration extraction. *Journal of Sound and Vibration*, 535, 117112.
- Wadhwa, N., Rubinstein, M., Durand, F., & Freeman, W. T. (2013). Phase- based video motion processing. *ACM Trans. Graph.*, 32(4), Article 80.
- Wu, H.-Y., Rubinstein, M., Shih, E., Guttag, J., Durand, F., & Freeman, W. (2012). Eulerian video magnification for revealing subtle changes in the world. *ACM Trans. Graph.*, 31(4), Article 65.

Development of IoT Vibration Sensor-based Machinery Health Monitoring and Fault Diagnostics System for Predictive Maintenance

Muhammad Shahril Bin Zainol Abidin^a and Ong Zhi Chao^{b*}

Department of Mechanical Engineering,
Faculty of Engineering, Universiti Malaya,
50603, Kuala Lumpur, Malaysia

Email: ^a 17205720@siswa.um.edu.my, ^b alexongzc@um.edu.my

*Corresponding author

ABSTRACT

This project presents the design, development, and evaluation of an IoT-based vibration sensor system for machinery health monitoring and fault diagnostics, aimed at enhancing predictive maintenance. Utilizing an ADXL1002 MEMS accelerometer, AD7175-2 ADC, and ESP32-S2 microcontroller, the system captures high-resolution vibration data, processed and transmitted wirelessly to a cloud database using Firebase. Sensitivity calibration aligned the developed system with a reference industrial accelerometer, achieving precise measurements with a recalibrated sensitivity of 35 mV/g. Despite higher noise levels due to electrical grounding issues in the ADC module, the system successfully identified bearing faults through envelope analysis and spectral kurtosis. Additionally, a 2D-CNN model achieved 96.5% accuracy in classifying bearing conditions based on grayscale image representations of vibration signals. Future work includes optimizing noise reduction, enhancing real-time data processing, integrating predictive analytics, and extensive field testing to validate and improve the system's performance for broader industrial applications.

Keywords: ADXL1002; IoT; Predictive Maintenance; Vibration Analysis; Wireless

1. INTRODUCTION

Predictive maintenance is crucial in modern industrial operations to prevent machinery failures and reduce downtime. Traditional strategies, such as reactive and preventive maintenance, often lead to higher costs and inefficiencies (Randall & Antoni, 2011). Predictive maintenance, leveraging advanced monitoring and data analytics, optimizes maintenance schedules and reduces operational costs (Rayes & Salam, 2017). Vibration analysis, particularly effective for detecting bearing faults, is widely used for machinery health monitoring (Randall & Antoni, 2011). The advent of IoT and AI technologies has further enhanced predictive maintenance systems by enabling real-time data acquisition, remote monitoring, and advanced fault diagnostics. This research focuses on developing an IoT-based vibration sensor system that integrates these technologies to provide a robust solution for machinery health monitoring.

2. METHODOLOGY

2.1 Hardware Selection

The system's core components include the ADXL1002 MEMS accelerometer, AD7175-2 ADC, and ESP32-S2 micro-controller. The ADXL1002 accelerometer provides high-resolution vibration data, which is converted to digital format by the AD7175-2 ADC and processed by the ESP32-S2 micro-controller. The micro-controller also handles wireless data transmission to a cloud database using Wi-Fi with UDP protocols (Gomez et al., 2012; Postel, 1980).

2.2 System Design

The vibration data acquisition system was designed to measure vibrations from rotating machinery in a production line. The analog signal from the accelerometer, ranging from 0V to 5V, is digitized by the ADC with 24-bit quantization. The digital data is transmitted wirelessly to a computer, where it is processed and visualized in real-time. An alert system is integrated to notify users of high vibration levels, enabling prompt maintenance actions.

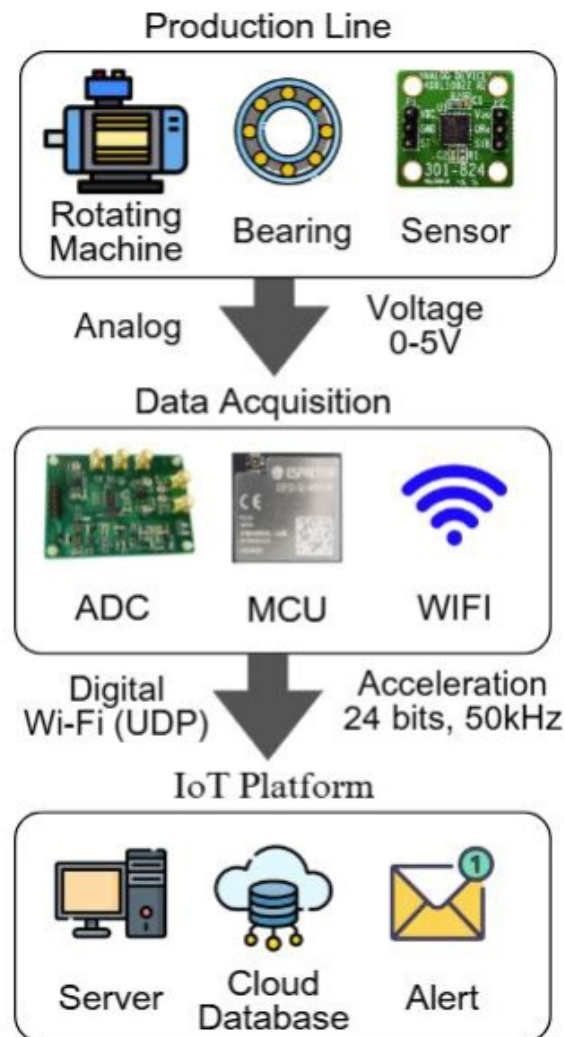


Figure 1. Architecture of the IoT Vibration Monitoring System

2.3 Performance Analysis

The system's performance was evaluated through sensitivity calibration, noise analysis, and bearing fault diagnostics. Sensitivity calibration involved comparing the system's measurements with a reference industrial accelerometer, adjusting the sensitivity to achieve accurate readings. Noise analysis assessed the noise density of the system's signal. Bearing fault diagnostics used envelope analysis and spectral kurtosis to identify characteristic vibration signatures of various bearing faults.

2.4 Deep Learning Implementation

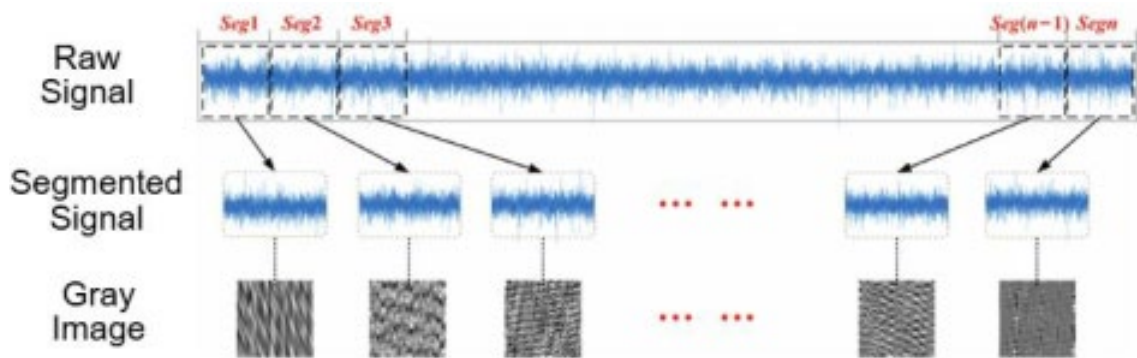


Figure 2. FFT spectrum of noise signal

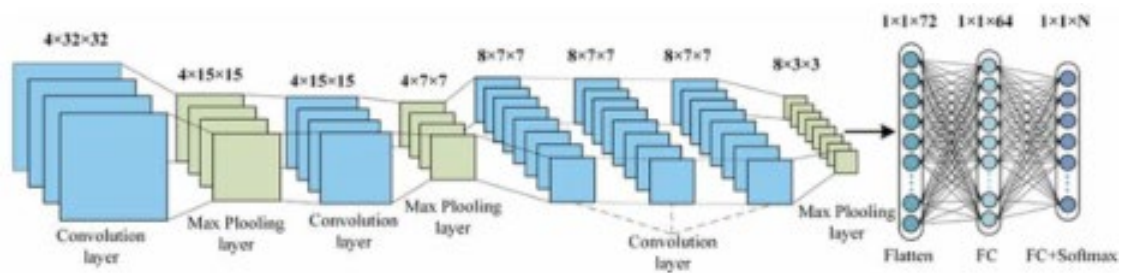


Figure 3. FFT spectrum of noise signal

A 2D-Convolutional Neural Network (2D-CNN) model was developed to classify bearing conditions based on grayscale image representations of vibration signals. The model was trained and evaluated using data collected from a test rig.

3. RESULTS AND DISCUSSION

3.1 Performance Analysis

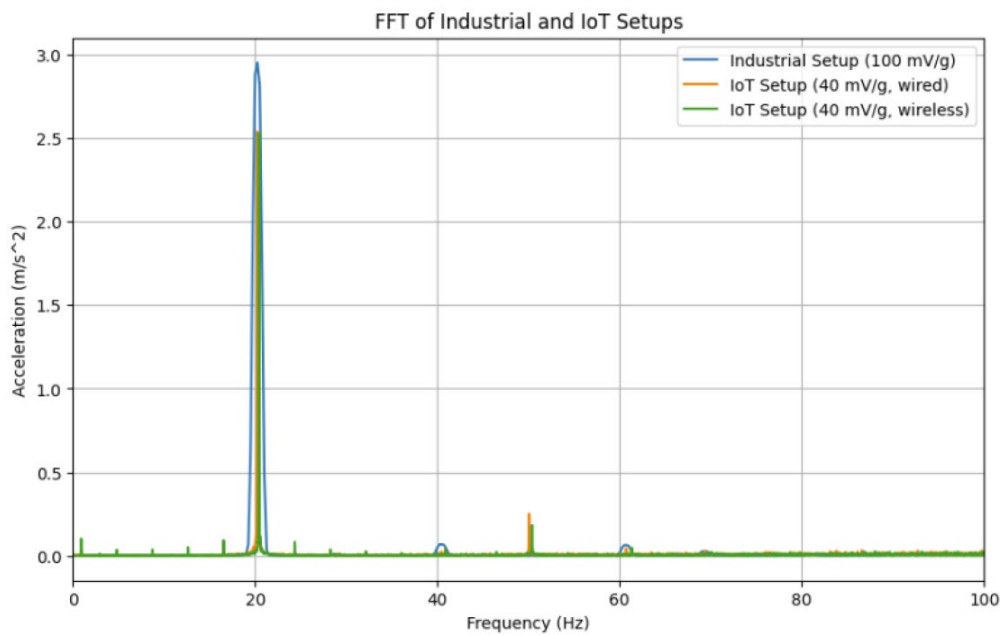


Figure 4. Calibrated sensitivity (35 mV/g)

The developed system successfully captured high-resolution vibration data and transmitted it wirelessly for real-time processing and analysis. Sensitivity calibration improved the system's accuracy, aligning its measurements with those of a reference industrial accelerometer. The calibrated sensitivity of 35 mV/g ensured precise vibration measurements across various motor speeds.

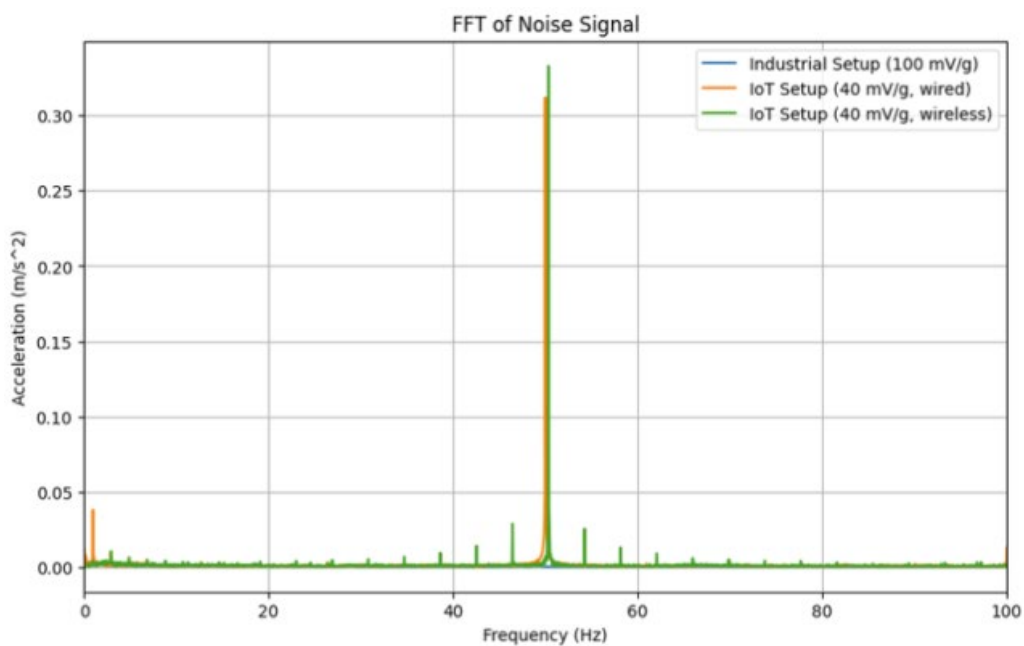


Figure 5. FFT spectrum of noise signal

The noise analysis revealed a significant noise issue, with the system's noise density being substantially higher than that of the reference accelerometer. The primary cause was identified as electrical grounding issues within the ADC module, with a prominent noise frequency at 50 Hz corresponding to the local power line frequency. Despite this, the system was able to capture accurate vibration signals for fault diagnostics.

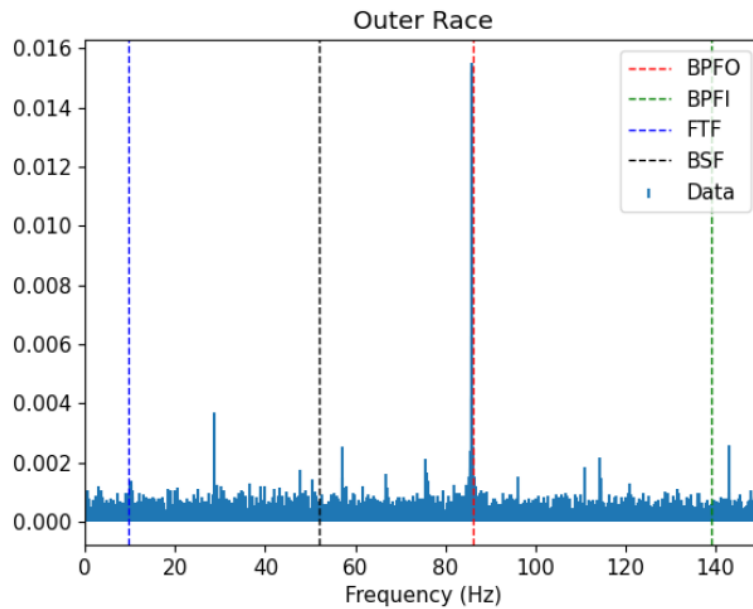


Figure 6. Envelope analysis of outer race defect

Envelope analysis successfully identified bearing faults. For instance, the outer race defect data showed an increase in kurtosis after preprocessing, with clear peaks at characteristic fault frequencies in the FFT spectrum as in Fig 6. Similar results were obtained for other bearing conditions, confirming the system's effectiveness in fault diagnostics.

3.2 Deep Learning Model Evaluation

The 2D-CNN model achieved a mean accuracy of 96.5% in classifying bearing conditions as shown in Fig 7. The model's performance was validated using a t-SNE plot, which showed clear clustering of the different fault types, indicating that the model effectively learned to distinguish between them. However, it is noted that both training and test data were collected from the same test rig, and further validation in real-world industrial environments is necessary to ensure the model's robustness and generalizability.

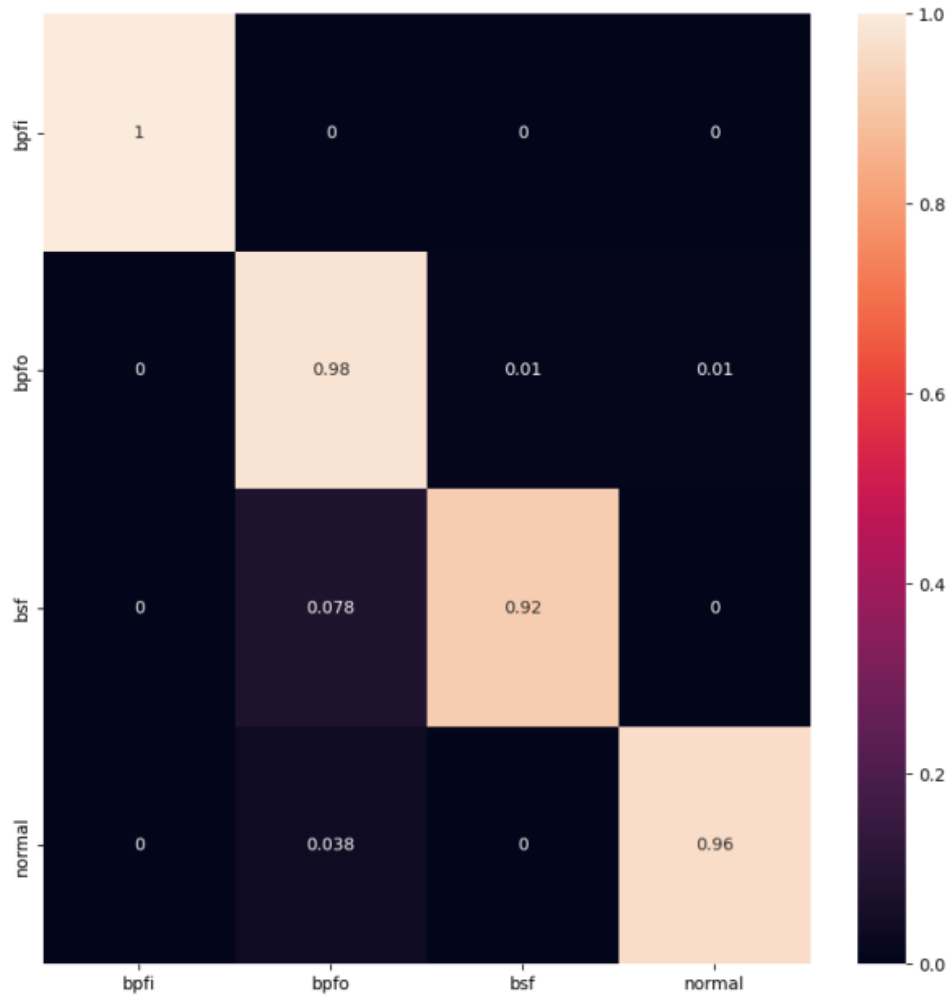


Figure 7. Confusion matrix of model testing

4. CONCLUSION

This project successfully developed and evaluated an IoT-based vibration sensor system for machinery health monitoring and fault diagnostics. The integration of the ADXL1002 MEMS accelerometer, AD7175-2 ADC, and ESP32-S2 micro-controller provided accurate and reliable vibration measurements, despite some noise issues. The system demonstrated effective fault diagnostics through envelope analysis and spectral kurtosis, and the 2D-CNN model achieved high accuracy in classifying bearing conditions.

REFERENCES

- [1] Gomez, C., Oller, J., & Paradells, J. (2012). Overview and evaluation of Bluetooth Low Energy: An emerging low-power wireless technology. *Sensors*, 12(9), 11734-11753.
- [2] Postel, J. (1980). User Datagram Protocol. RFC 768.
- [3] Randall, R. B., & Antoni, J. (2011). Rolling element bearing diagnostics—A tutorial. *Mechanical Systems and Signal Processing*, 25(2), 485-520.
- [4] Rayes, A., & Salam, S. (2017). *Internet of Things From Hype to Reality: The Road to Digitization*. Springer.

Development of Embedded System for Automated Tracking Intelligent Umbrella

Tan Seng Kiat ^a and Mohammed Abdo Hashem Ali ^{b*}

Department of Mechanical Engineering,
Faculty of Engineering, Universiti Malaya,
50603, Kuala Lumpur, Malaysia

Email: ^a kiattua0907@gmail.com, ^b hashem@um.edu.my

*Corresponding author

ABSTRACT

The "Development of Embedded System for Automatic Tracking Intelligent Umbrella (ATIUI)" project addresses the limitations of traditional umbrella designs, which require manual handling and pose challenges for individuals with upper limb disabilities and the elderly. This research integrates Unmanned Aerial Vehicle (UAV) technology to create a hands-free, autonomous umbrella. Four ultrasonic sensors and a fuzzy logic tracking algorithm ensure the UAV maintains close proximity to the user. The system features 3D- printed mounts for the umbrella and sensors, a Remote-Controlled Umbrella Deployment System to minimize aerodynamic resistance during take-off and landing, and an IoT remote control interface via Blynk. Preliminary tests demonstrated a tracking accuracy of 70%, with identified challenges including wind interference and altitude control issues. Recommendations for improvement include stronger drones, advanced sensors, and refined algorithms. This innovative approach aims to redefine umbrella functionality, offering enhanced usability and convenience.

Keywords: Autonomous Umbrella; Embedded System; Fuzzy Logic; IoT; UAV Tracking.

1. INTRODUCTION

Traditional umbrellas require manual handling, posing significant challenges for elderly individuals and those with upper limb disabilities, leading to discomfort and fatigue [1]. The "Development of Embedded System for Automatic Tracking Intelligent Umbrella (ATIUI)" project addresses these issues by integrating UAV technology to create a hands-free, autonomous umbrella. This innovative solution uses ultrasonic sensors and advanced tracking algorithms to maintain proximity to the user, providing continuous protection without manual intervention. By combining GPS, ultrasonic technology, and IoT remote control via smartphones, the ATIUI offers user-friendly operation and enhanced safety. The embedded system processes sensor data to guide the UAV, enabling automatic tracking, obstacle avoidance, and controlled landing. This research aims to revolutionize umbrella functionality, improving the quality of life for users and redefining the umbrella's role in daily life

2. METHODOLOGY

The intelligent umbrella system utilizes a UAV with a remotely controlled umbrella deployment mechanism, ensuring efficient operation through a rack and pinion design as shown in Figure 1. The mount design prioritizes balanced weight distribution and aerodynamics, using CAD and simulation tools to optimize stability and performance. Ultrasonic sensors and GPS are integrated for precise user

tracking and UAV positioning. Ultrasonic sensors, chosen for their reliability, are positioned to detect user movements in all directions. Data from these sensors is processed to ensure accurate and responsive tracking.

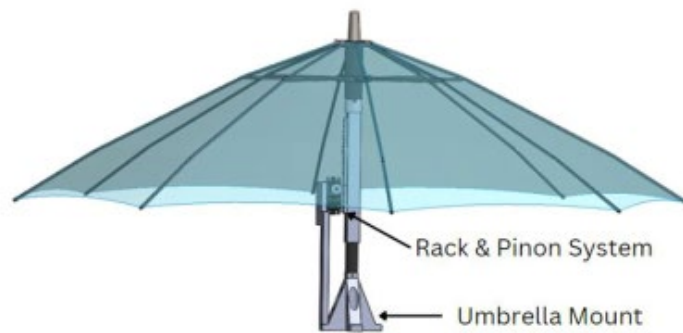


Figure 1. Remote-Controlled Umbrella System Design

The beam angle of HC-SR04 sensor's 15-degree and is countered by a 13-degree offset in sensors mounting design. This angling minimizes ultrasonic beams hitting unintended objects, improving accuracy in detecting the user's movement and position relative to the drone.

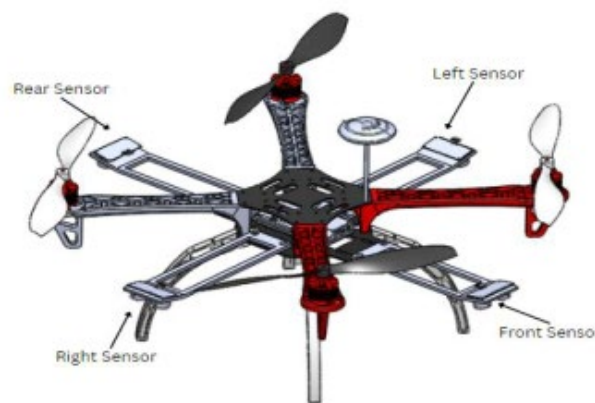


Figure 2. Planned orientation of the ultrasonic sensors

The sensors are oriented towards the ground to ensure accurate detection. When the user moves, for example, forward, the front sensor's signal is blocked while the others remain pointed at the ground. This blockage indicates a "close" reading in the fuzzy logic membership function, while the unblocked sensors read "far," enabling precise tracking of the user's movement as shown in Figure 3.

The user directions tracking system employs a fuzzification interface with four inputs (front, back, left, and right distances) to determine the UAV's positional relationship with the user. Each input has two membership functions: Close and Far. When a specific distance is "Near" and others are "Far," the UAV adjusts its movement accordingly (forward, backward, left, or right). Defuzzification translates these inputs into two outputs: pitch (Forward, Neutral, Backward) and roll (Left, Neutral, Right), ensuring the UAV accurately follows the user's movements.

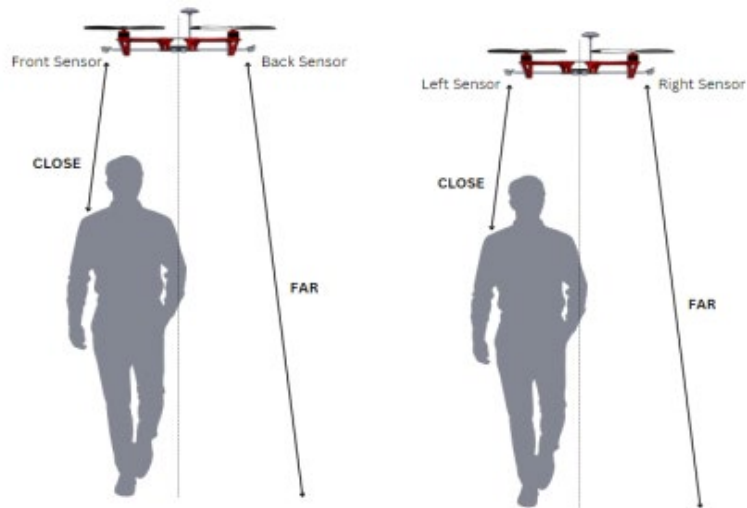


Figure 3. Data acquisition for tracking system

The fuzzy logic system is developed using MATLAB as shown in Figure 4 & 5.

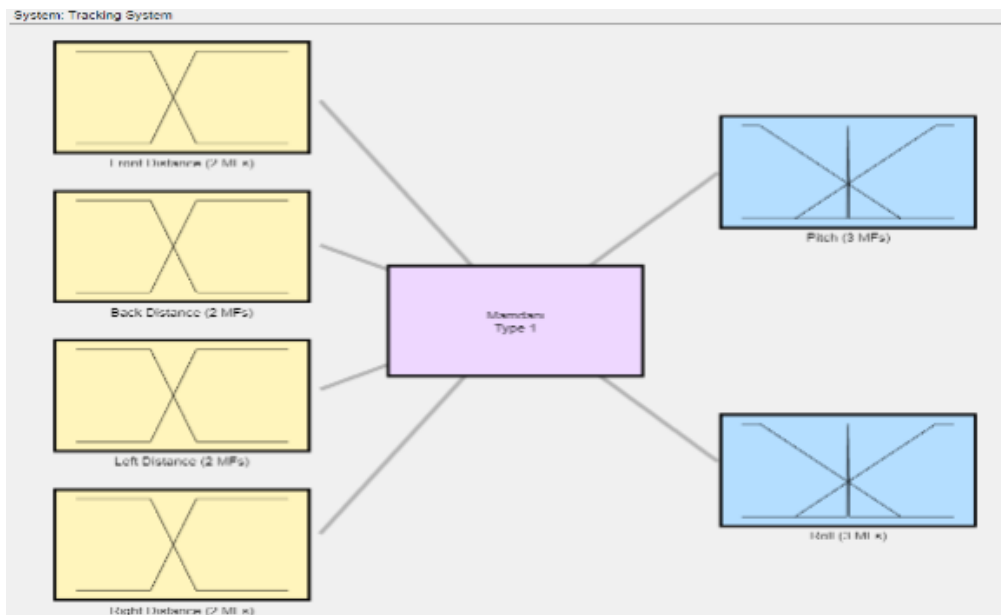


Figure 4. Fuzzy Logic System

| Rule | Weight | Name |
|--|--------|--------|
| 1 If Front Distance is Close and Back Distance is Far and Left Distance is Far and Right Distance is Far then Pitch is Forward, Roll is Neutral | 1 | rule1 |
| 2 If Front Distance is Far and Back Distance is Close and Left Distance is Far and Right Distance is Far then Pitch is Backward, Roll is Neutral | 1 | rule2 |
| 3 If Front Distance is Far and Back Distance is Far and Left Distance is Close and Right Distance is Far then Pitch is Neutral, Roll is Left | 1 | rule3 |
| 4 If Front Distance is Far and Back Distance is Far and Left Distance is Far and Right Distance is Close then Pitch is Neutral, Roll is Right | 1 | rule4 |
| 5 If Front Distance is Far and Back Distance is Far and Left Distance is Far and Right Distance is Far then Pitch is Neutral, Roll is Neutral | 1 | rule5 |
| 6 If Front Distance is Close and Back Distance is Close and Left Distance is Far and Right Distance is Far then Pitch is Neutral, Roll is Neutral | 1 | rule6 |
| 7 If Front Distance is Close and Back Distance is Far and Left Distance is Close and Right Distance is Far then Pitch is Neutral, Roll is Neutral | 1 | rule7 |
| 8 If Front Distance is Close and Back Distance is Far and Left Distance is Far and Right Distance is Close then Pitch is Neutral, Roll is Neutral | 1 | rule8 |
| 9 If Front Distance is Far and Back Distance is Close and Left Distance is Close and Right Distance is Far then Pitch is Neutral, Roll is Neutral | 1 | rule9 |
| 10 If Front Distance is Far and Back Distance is Far and Left Distance is Close and Right Distance is Close then Pitch is Neutral, Roll is Neutral | 1 | rule10 |

Figure 5. Fuzzy Rules

3. RESULTS AND DISCUSSION

The UAV umbrella prototype setup as shown in Figure 6 & 7 involved mounting sensors and an umbrella on the drone, developing a remote-controlled umbrella deployment system, and implementing an IoT remote control interface. This setup enabled the drone to reduce aerodynamic resistance during take-off and landing by closing the umbrella, thereby enhancing stability and performance.



Figure 6. Sensors Mounting



Figure 7. Full Setup

Initial flight tests revealed that using a normal adult-sized umbrella caused instability and control issues due to excessive weight and aerodynamic resistance. Switching to a smaller umbrella resolved these issues, suggesting that a more powerful drone would be needed for larger umbrellas.

Dynamic tracking tests demonstrated a 70% accuracy rate across 20 trials. The system successfully tracked user movements most of the time, but environmental factors like wind and altitude variations caused tracking errors. Improving the drone's stability, incorporating advanced sensors, and refining the tracking algorithm could enhance overall accuracy and reliability. Figure 8 shows two examples of unidirectional tracking test.



Figure 8. Unidirectional Tracking Test

Figure 9 shows the multidirectional loop tracking test in the flight path map.



Figure 9. Loop Tracking Test

4. CONCLUSION

The development of the Automatic Tracking Intelligent Umbrella (ATIU) system showcased its potential to aid elderly and disabled individuals with an intelligent, hands-free umbrella solution. The project successfully created a UAV prototype equipped with ultrasonic sensors, a remote-controlled deployment system, and an IoT interface. The fuzzy logic tracking algorithm achieved high accuracy in controlled tests, though dynamic tracking tests highlighted challenges such as wind interference, resulting in a 70% accuracy rate. These findings indicate the feasibility and promise of the ATIU system, with further improvements needed for enhanced reliability in real-world conditions.

REFERENCES

- Holding an umbrella can cause physical discomfort while traveling; what to do? (2023, February 14). Issuu. https://issuu.com/huriiaproducts/docs/holding-an-umbrella-can-cause-physical-discomfort-#google_vignette
- Ultrasonic Range Sensor (HC-SR04). (n.d.). Pi-Shop.ch. <https://www.pi-shop.ch/ultrasonic-range-sensor-hc-sr04#:~:text=Please%20Note.,to%20the%20nearest%200.3cm>.

A Novel Robust Dew Point Evaporative Cooler

Shum Choy Kit^a and Mohd Nashrul Bin Mohd Zubir^{b*}

Department of Mechanical Engineering,
Faculty of Engineering, Universiti Malaya,
50603, Kuala Lumpur, Malaysia

Email: ^a choykitshum@gmail.com, ^b nashrul@um.edu.my

*Corresponding author

ABSTRACT

Conventional space cooling technologies are energy demanding and pose significant environmental challenges, such as global warming. Dew point evaporative cooling (DPEC), also known as M-Cycle cooling, provides an energy-efficient and natural alternative by using water as a coolant. DPEC has limitations of large geometrical size and lower efficiency in its heat and mass exchanger, compared to other cooling systems. Wet channel heat transfer is hindered by conventional wicking material. This research aims to investigate the effects of incorporating fins design and hydrophilic coating materials to enhance the overall performance of DPEC heat and mass exchangers. Six channel designs: in-line full, in-line partial, in-line intermittent, staggered full, staggered partial and staggered intermittent fins were evaluated using flow simulation and ANSYS heat simulation. Channel design with in-line and full fin arrangement in the dry channel was selected with an overall thermal performance of 1.544. The wettability of anodized, polished, and Titanium Dioxide coated aluminium were measured. Titanium Dioxide coated aluminium was found to exhibit hydrophilic properties, characterized by a low contact angle (48.5°). This can enhance the wet channel wettability and improve the performance of heat and mass exchangers.

Keywords: Dew Point Evaporative Cooler; Fins; Heat Exchanger; Titanium Dioxide; Wettability

1. INTRODUCTION

The energy demand is significant for space cooling. Heating, Ventilation, and Air Conditioning (HVAC) systems are the highest contributor, consuming up to 38% of a building's total energy usage [1, 2] With such energy demand, there is a need for energy-efficient space cooling solutions. Dew point evaporative cooling, an energy-efficient cooling alternative, but face limitations of bulkier, less efficient heat and mass exchangers and lower wettability of wet channel surfaces. This research aims to investigate the performance of the heat and mass exchanger with added fins in the dry channel and wettability of Titanium Dioxide (TiO_2) coating on aluminium. The findings could contribute to more sustainable and effective cooling solutions.

2. METHODOLOGY

2.1 SOLIDWORKS Flow Simulation

The CAD models of six channel designs were created using SOLIDWORKS. The designs have different combinations of fin arrangement (in-line or staggered) and placement (full, partial, intermittent). Flow simulation was conducted to evaluate velocity and pressure distribution, in the heat and mass exchanger channel. The boundary condition of the flow simulation uses an inlet velocity of 2.4 m/s, temperature 293.2 K and 101.3 kPa for both supply and exhaust air outlets.

2.2 ANSYS Heat Simulation

Further investigation of air temperature is conducted using ANSYS Fluent. The analysis is based on a laminar model, with boundary conditions of inlet velocity 2.4 m/s, ambient temperature 30°C, constant heat flux $-393 \text{ W/m}^2\text{K}$. Overall thermal performance, η compares the performance of the reference model (no fins) and the proposed design, it is calculated using Nusselt number and pressure drop as shown in the following equations:

$$\eta = \frac{Nu/Nu_0}{\left(\Delta P/\Delta P_0\right)^{\frac{1}{3}}}$$

$$Nu = \frac{hL_c}{k}$$

2.3 Contact Angle Measurement

Three samples of aluminium sheets of dimensions 5cm x 5cm with different anodized, polished and TiO_2 surface finish are measured for their contact angle of water. Contact angle is measured using an optical tensiometer by dropping 5 μ l of water onto the surface and measure using SCA20 software. Three repeated readings are taken on each sample, and the average value was taken as the final value of the contact angle of water.

3. RESULTS AND DISCUSSION

3.1 Flow and Heat Simulation

Velocity, pressure and temperature distributions are evaluated. Flow simulation shows staggered intermittent design has good velocity distribution and low pressure drop. High air velocity stream with low-pressure drop is required to ensure air travels to its desired destination. Taking account of temperature, instead in-line full design shows better overall thermal performance in heat simulation.

Table 1 below shows the calculated overall thermal performance. In-line full fins have a high Nusselt number of 193. Although it has high pressure drop, the overall thermal performance (1.544) shows that it has good convective heat transfer ability, sufficient to use as final design. It is highest among the other channel designs.

Table 1. Overall thermal performance calculation

| Channel design | Temperature drop, ΔT (°C) | HTC. h (W/m^2K) | Nusselt Number, Nu | Pressure drop, ΔP (Pa) | η |
|----------------|-----------------------------------|---------------------|--------------------|--------------------------------|-------------|
| No fins | 4.58 | 85.718 | 28.512 | 24.00 | (reference) |
| In-line full | 2.03 | 193.355 | 64.114 | 74.13 | 1.544 |
| In-line part. | 2.95 | 133.092 | 44.175 | 57.00 | 1.161 |
| In-line int. | 2.42 | 162.612 | 53.963 | 59.00 | 1.402 |
| Stag. full | 2.22 | 177.229 | 58.787 | 65.65 | 1.474 |
| Stag. partial | 3.95 | 99.539 | 33.034 | 51.84 | 0.896 |
| Stag. int. | 3.74 | 105.062 | 34.867 | 51.56 | 0.948 |

3.2 Titanium Dioxide Wettability on Aluminium

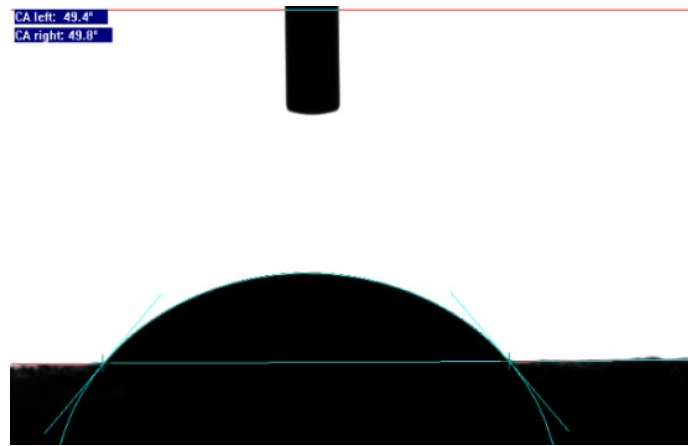


Figure 1. Contact Angle of Water of Titanium Dioxide Coated Aluminium

TiO_2 coated aluminium has the lowest contact angle and is the most hydrophilic compared to anodized, polished finishes. This is due to TiO_2 having high surface energy, which attracts water molecules. The measurement data is shown in Table 2.

Table 2. Contact Angle Measurement Results

| Sample | Average Contact Angle (°) |
|--------------------------|---------------------------|
| Anodized Aluminium | 124.9 |
| Polished Aluminium | 103.2 |
| TiO_2 coated Aluminium | 48.5 |

4.0 CONCLUSION

The proposed heat and mass exchanger design includes circular fins in the dry channel and hydrophilic Titanium Dioxide in the wet channel. The optimization of fins with different arrangements and placement was evaluated by conducting flow simulation and heat simulation. Simulation results yield the final selection of the channel design, in-line fin arrangement, with full fin placement. The selected design exhibits the highest overall thermal performance of 1.54 among the channel designs with a Nusselt number of 64.14. The wettability of the coating made from Titanium Dioxide nanoparticles was

investigated. The coating exhibits hydrophilic properties with low contact angle of 48.5°. This coating is suitable to be used to improve the wettability of the heat and mass exchanger.

REFERENCES

S. Abdullah et al., "Technological development of evaporative cooling systems and its integration with air dehumidification processes: A review," *Energy and Buildings*, vol. 283, p. 112805, 2023/03/15/2023, doi: <https://doi.org/10.1016/j.enbuild.2023.112805>.

M. González-Torres, L. Pérez- Lombard, J. F. Coronel, I. R. Maestre, and D. Yan, "A review on buildings energy information: Trends, end-uses, fuels and drivers," *Energy Reports*, vol. 8, pp. 626-637, 2022/11/01/2022, doi: <https://doi.org/10.1016/j.egy.2021.11.280>.

Development of a Novel Sunlight Delivery System for Algae Photosynthesis in an Indoor Recirculating Aquaculture System (I-RAS)

Goh Hong Sheng ^a and Mohd Nashrul bin Mohd Zubir ^{b*}

Department of Mechanical Engineering,
Faculty of Engineering, Universiti Malaya,
50603, Kuala Lumpur, Malaysia

Email: ^a hsheng0614@gmail.com, ^b nashrul@um.edu.my

*Corresponding author

ABSTRACT

This research investigates the development of a sustainable sunlight delivery system for indoor Recirculating Aquaculture Systems (RAS) to enhance microalgae growth. The methodology involves designing a Plano Convex Optic Fiber system that captures and transports natural sunlight to indoor environments, optimizing Photosynthetically Active Radiation (PAR) levels for microalgae photosynthesis. Experimental results demonstrated that the system achieved PAR values ranging from 40-400 $\mu\text{molm}^{-2}\text{s}^{-1}$, with peak efficiency at noon and a maximum of 28.16% efficiency observed. A second experiment showcased the system's robustness by maintaining higher and more stable luminance levels compared to direct sunlight exposure, even under varying sun positions and weather conditions. The standard deviation for the prototype was significantly lower than direct exposure, indicating consistent and reliable illumination. This study provides a cost-effective, sustainable solution for indoor aquaculture, promoting optimal algae growth and improved ammonia control, thereby advancing sustainable practices in the industry.

Keywords: Sustainable Sunlight Delivery; Indoor Aquaculture; Plano Convex Optic Fiber; Microalgae Growth; Photosynthetically Active Radiation

1. INTRODUCTION

Aquaculture, the cultivation of aquatic organisms, is the fastest-growing sector in global food production. Recirculating Aquaculture Systems (RAS), shown in Fig.1, represent a major advancement, offering controlled environments that enhance water quality and sustainability. However, indoor RAS face challenges in providing adequate light for microalgae photosynthesis, crucial for bio-filtration and nutrient recycling. Traditional artificial lighting systems are energy-intensive and costly, raising operational expenses and environmental impact. To address this, the current project focuses on designing a sunlight delivery system for indoor environments, leveraging Malaysia's abundant year-round sunshine. The system uses a solar collector to capture and concentrate sunlight, which is then transmitted through optical fibers to the indoor aquatic environment. This reduces reliance on artificial lighting, cutting energy consumption and operational costs, while enhancing sustainability by utilizing renewable energy. The project aims to replace artificial light sources in RAS with a sustainable alternative, developing a framework to evaluate the system's performance.

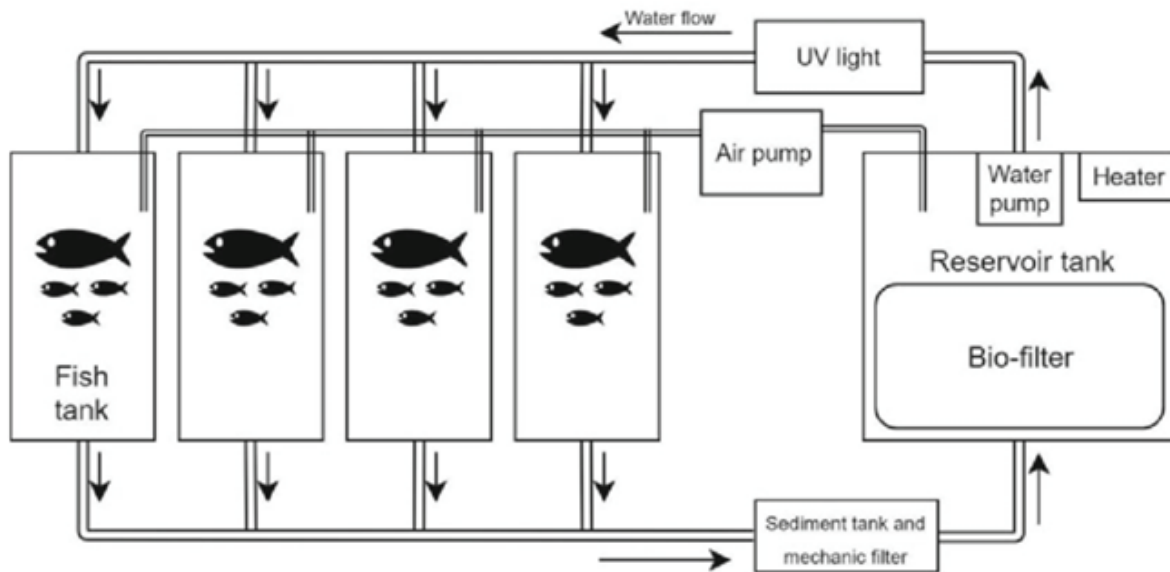


Figure 1. RAS General Flowchart

Key components include selecting appropriate materials like optical fibers and luminary materials to ensure efficiency and cost-effectiveness. This approach aligns with global sustainability goals, promoting green practices in aquaculture. This research seeks to create a low-cost, efficient daylighting system tailored for microalgae cultivation in indoor RAS, enhancing sustainability and economic viability in the aquaculture industry.

2. METHODOLOGY

A cost-effective Plano Convex Optical Fiber light collecting system was designed. This system replaces expensive Fresnel lenses and complex collimators with a basic plano-convex lens to concentrate sunlight onto optical fibers positioned at the lens's focal point motivated by [4]. The prototype was fabricated by cutting PMMA end-glow optical fibers into 40-50 cm lengths and ensuring their tips were smooth for efficient light transmission. A plano-convex lens with a diameter of 22 mm and a focal length of 24 mm was used to focus sunlight. The optical fibers were secured in a 3D-printed holder with an M5 screw mechanism, allowing precise alignment with the lens's focus, as shown in Figures 3 & 4.

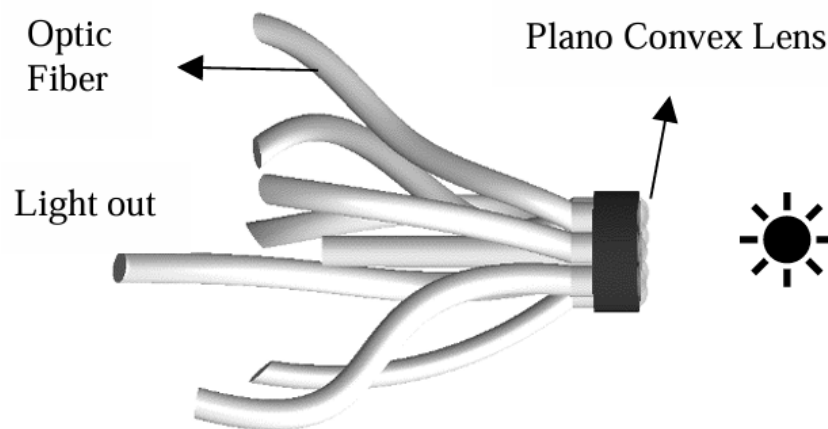


Figure 2. SolidWorks 3D Assembly Concept



Figure 3. Actual Prototype

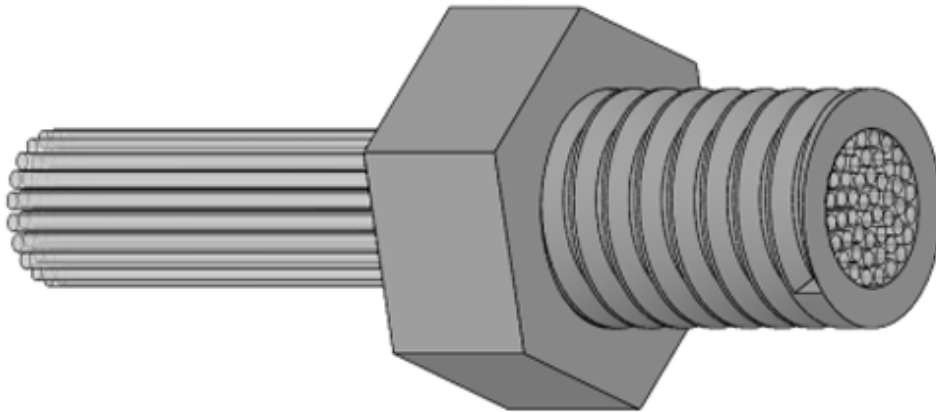


Figure 4. Fibre Holder

Two experiments were conducted to assess the sunlight delivery system. In Experiment 1, the system's efficiency was determined by comparing Photosynthetically Active Radiation (PAR) values between sunlight and light transmitted into a dark room by the prototype, using a PAR Meter.

$$Efficiency = \frac{PAR \text{ in the dark room}}{PAR \text{ at open area (Sunlight)}} \times 100\%$$

Experiment 2 aimed to demonstrate the system's uniformity and consistency by measuring luminance inside identical dark boxes hourly at multiple locations over three days. The standard deviation of these measurements was calculated to confirm the system's ability to maintain steady and uniform light intensity across various positions :

$$\sigma = \sqrt{\frac{1}{N} \sum_{i=1}^N (x_i - \mu)^2}$$

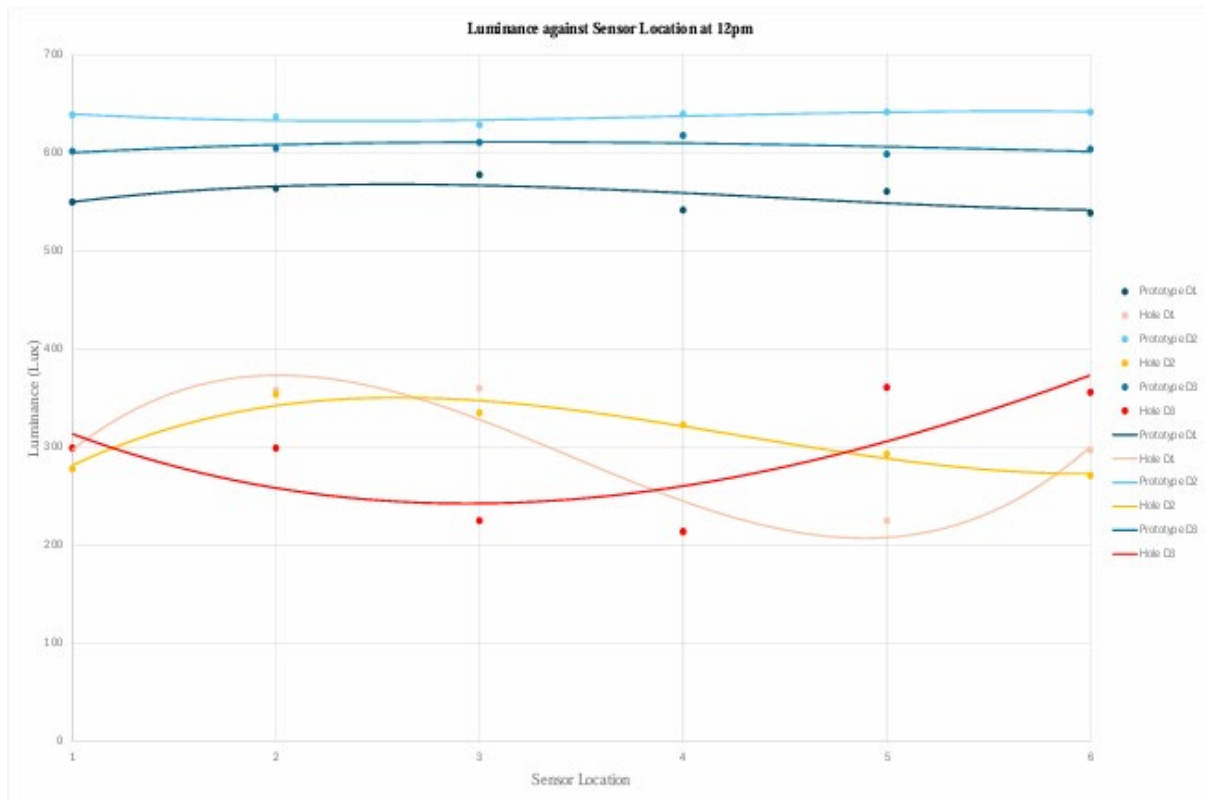


Figure 5. Illuminance against sensor locations

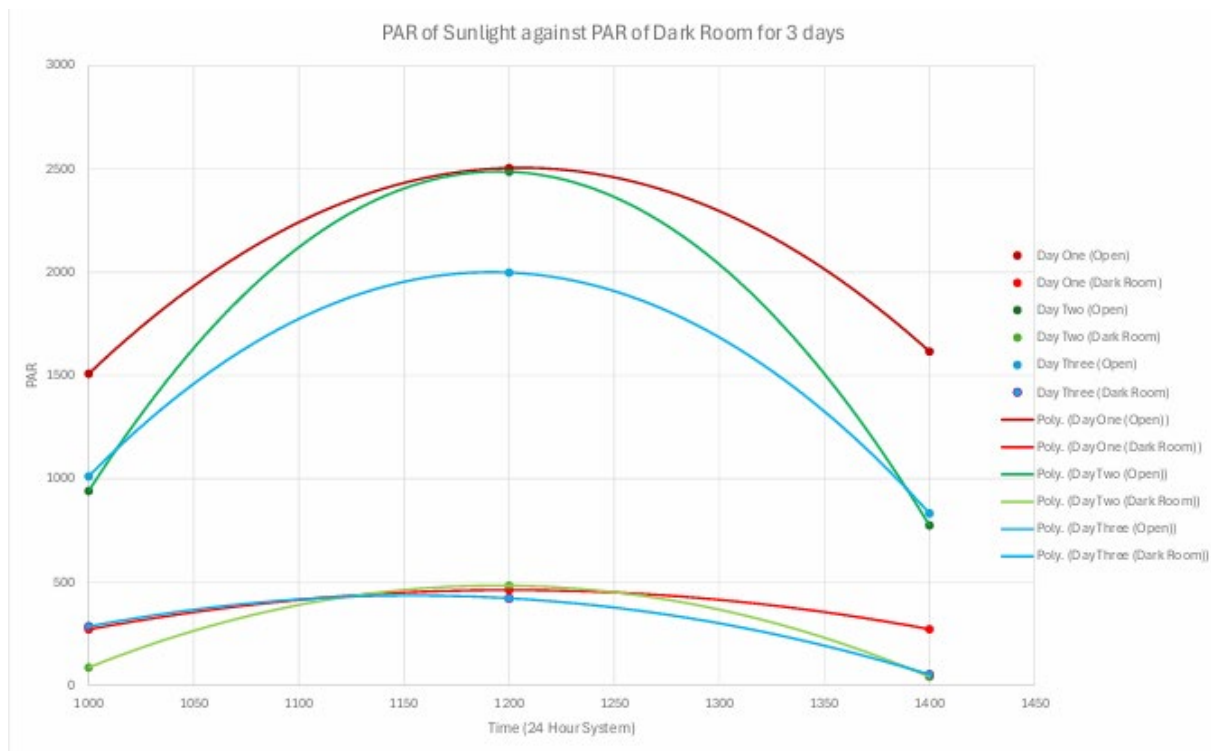


Figure 6. PAR of sunlight against PAR of darkroom

3. RESULTS AND DISCUSSION

The results of Experiment One revealed a correlation between sunlight's Photosynthetically Active Radiation (PAR) and the PAR recorded within the experimental setup. While sunlight typically ranged between $271\text{-}2486 \mu\text{molm}^{-2}\text{s}^{-1}$ the prototype collected PAR values of $40\text{-}400 \mu\text{molm}^{-2}\text{s}^{-1}$ s, sufficient for algae's photosynthesis [2][3] but lacking uniformity and stability. Experiment Two focused on comparing luminance levels between direct exposure and the prototype. The prototype demonstrated higher and more stable luminance levels, as evidenced by lower standard deviations ranging from 4.27 to 24.75 compared to direct exposure's 6.87 to 80.97. However, the illuminance value is considered low compared to normal light exposure level. Reasons for these discrepancies were identified, including limited optic fiber quantity, material selection, assembly precision, chromatic aberration, spot size considerations, sunlight direction variability, and surface imperfections. These findings underscore the need for improvements to enhance the prototype's performance in capturing consistently and efficiently.

4. CONCLUSION

This research successfully achieved its objectives of designing and fabricating a novel sunlight delivery system tailored for algae photosynthesis, effectiveness by evaluating its comparing Photosynthetically Active Radiation (PAR) with natural sunlight and demonstrating its flexibility in illuminating various positions. The developed prototype exhibited promising results, albeit with room for improvement in areas such as optic fiber quantity, material selection and lens quality, refining these aspects will enhance the system's performance and contribute to sustainable aquaculture practices by providing a cost-effective and efficient solar-based lighting solution.

REFERENCES

- [1] Ahmed, N., & Turchini, G. M. (2021). Recirculating aquaculture systems (RAS): Environmental adaptation. *Journal of Cleaner Production*, 297, 126604. <https://doi.org/10.1016/j.jclepro.2021.126604>
- [2] Ashley. (2021, June 15). Microalgae Growth Light Spectrum - Industrial Plankton. *Industrial Plankton*. <https://industrialplankton.com/2021/05/15/microalgae-light-spectrum/>
- [3] Metsoviti, M. N., Papapolymerou, G., Karapanagiotidis, I. T., & Katsoulas, N. (2019). Effect of Light Intensity and Quality on Growth Rate and Composition of *Chlorella vulgaris*. *Plants*, 9(1), 31. <https://doi.org/10.3390/plants9010031>
- [4] Ullah, I., Lv, H., Whang, A. J., & Su, Y. (2017). Analysis of a novel design of uniformly illumination for Fresnel lens-based optical fiber daylighting system. *Energy and Buildings*, 154, 19–29. <https://doi.org/10.1016/j.enbuild.2017.08.066>

Development of Software for Laboratory Equipment at Faculty of Engineering, Universiti Malaya by Implementing Database System and Website Application

Muhammad Syaiful Bin Lokman^a and Mohd Zamri bin Zainon @ Baharom^{b*}

Department of Mechanical Engineering,
Faculty of Engineering, Universiti Malaya,
50603, Kuala Lumpur, Malaysia

Email: ^a muhdsyaiful.lkmn@gmail.com, ^b zzainonum.edu.my

*Corresponding author

ABSTRACT

This report presents a through plan of action for solving issues with the Faculty of Engineering's traditional lab equipment management system. To improve accessibility, automate data administration, and enhance overall laboratory operating efficiency, the suggested solution combines effective database system with user-friendly website application. The concerns that have been highlighted, including the lack of transaction records, the vulnerability to human error, and the frequent losing of equipment, demand a transition to new technologies. With that, the goal of the research includes replacing manual systems with the technological application, reducing costs and paperwork, and ensuring quick data access. The system's capability is shown by the effective integration of data into MySQL database and the website application. Overall, the goal of this project is to provide a useful tool for documenting, arranging, and retrieving data on lab equipment, setting the basis for a productive, dependable, and modern laboratory environment.

Keywords: Database, Equipment, Management, Software, Website

1. INTRODUCTION

In traditional inventory management systems, records and information are typically stored in Excel files. Unfortunately, these files can be corrupted or accidentally deleted. Using Excel also presents disadvantages such as limited scalability, difficulty in managing large datasets, and increased risk of human error. For an institution like the Faculty of Engineering, which houses significant equipment and components for teaching and learning, an efficient inventory management system is crucial [1]. Maintaining a systematic laboratory equipment management system is essential for managing assets, research, and education effectively.

Implementing a database can enhance accessibility, optimize data administration, and increase the overall effectiveness of laboratory operations. A database management system provides a practical and efficient way to define, store, and retrieve data. Additionally, integrating a user-friendly website application facilitates accessibility and user engagement with laboratory equipment. This system allows users to conveniently access, update, and retrieve information, ensuring effective and flexible laboratory equipment management

2. METHODOLOGY

2.1 Requirement for the System

The Laboratory Equipment Management System has specific functional requirements for different user roles. Asset Managers gain all access such as update profiles, manage lab equipment, view and print reports, and access equipment details. Lecturers and students on the other hand, can register, update profiles, and search for and view equipment. Non-functional requirements emphasize a user-friendly interface, faster performance than manual systems, accurate data for decision-making, and robust security measures, including login protection and regular data backups.

2.2 Design of the System

The design phase of the Laboratory Equipment Management System uses UML for visual representation as shown in Fig.1, which is then translated into source code. PHP and MySQL are used for the backend, and Bootstrap 5, CSS, and HTML for the frontend. The ER diagram organizes database components and interactions. The relational database model includes tables for Asset Manager, Lab Equipment, Lab Equipment View, Lab Equipment User, and Lab Equipment Location, with foreign keys indicated. Use case diagrams and descriptions outline key functionalities for Asset Managers, Lecturers, and Students, including login, profile updates, equipment management, and report generation.

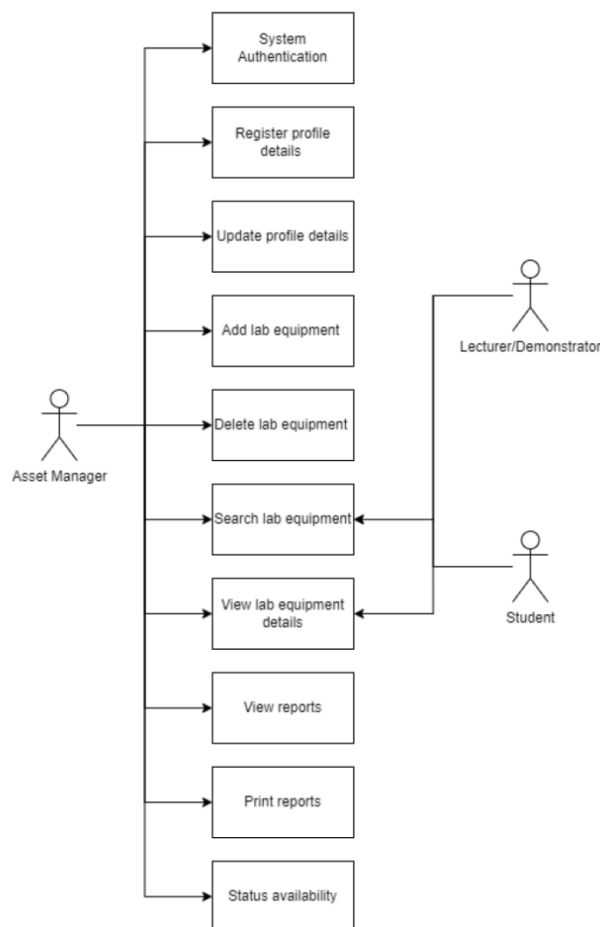


Figure 1. UML use case diagram

2.3 Development of the Database

The database development process involves connecting MySQL with Python using MySQL Connector. This connection is established by providing necessary parameters like host, username, password, and database. Once connected, tables are created within the MySQL database by defining column parameters based on the ER diagram. Data insertion is managed efficiently by importing data directly from Excel files using MySQL Workbench, which accelerates the process and ensures accuracy when dealing with large datasets.

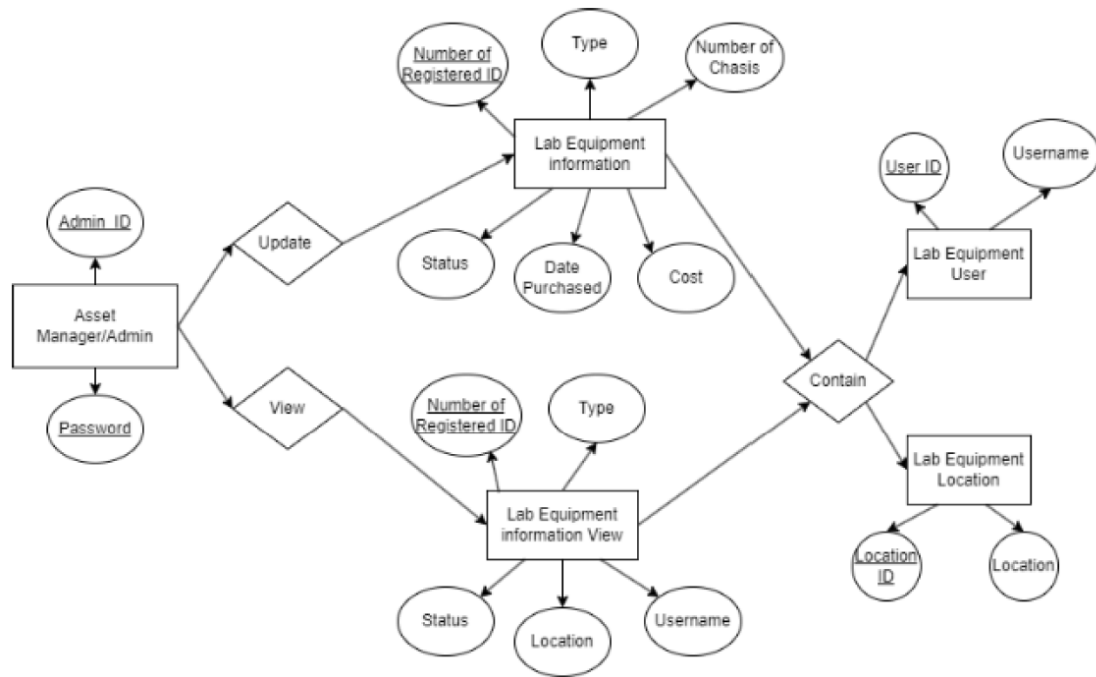


Figure 2. ER Diagram

2.4 Development of the Website

The website development uses XAMPP for a local web server environment and Visual Studio Code as the IDE. Connecting PHP to MySQL is crucial for data retrieval and storage. The website's creation involves identifying necessary pages, coding each separately as PHP files for modularity, and implementing functionalities like system authentication, profile registration, equipment management, and report generation. This structured approach ensures easier maintenance and debugging, resulting in a dynamic and efficient laboratory equipment management system.

3. RESULTS AND DISCUSSIONS

The project involved developing a comprehensive database and website for managing laboratory equipment. The database development phase focused on creating tables for equipment information, user data, and location details, with special IDs for efficient data management. The MySQL database integration was successful, allowing for dynamic data handling and secure storage.



Figure 3. Main page (Login)

The website development phase utilized tools like XAMPP and Visual Studio Code, with PHP and MySQL for backend operations and Bootstrap 5, CSS, and HTML for frontend design. The website provided functionalities such as user authentication, equipment management, and report generation, enhancing data accessibility and manipulation. From Fig.4, this is a page designed for administrators, granting them access to perform all the functions mentioned above.

Comparing the new system with the existing Excel-based system highlighted significant improvements. The new system offered enhanced data management, data integrity, user access control, and a user-friendly interface. It addressed issues like data duplication, security vulnerabilities, and data consistency, providing a more reliable and efficient platform for managing laboratory equipment.

| Register ID | Equipment Type | Check Number | Cost | Location | User Name | Purchase Date | Availability | Action |
|-------------|---------------------------|--------------|--------|--|--------------------------------|---------------|--------------|---------------------------------|
| K-000024 | CNC MACHINE | 295-041025 | 110.00 | 101004/02/02/02/03/04/05/06/07/08/09/10/11/12/13/14/15/16/17/18/19/20/21/22/23/24/25/26/27/28/29/30/31/32/33/34/35/36/37/38/39/40/41/42/43/44/45/46/47/48/49/50/51/52/53/54/55/56/57/58/59/60/61/62/63/64/65/66/67/68/69/70/71/72/73/74/75/76/77/78/79/80/81/82/83/84/85/86/87/88/89/90/91/92/93/94/95/96/97/98/99/100 | MOHD FUZDI BIN SABRI (3013) | 10/10/18 | Available | Update Delete View Report |
| K-000194 | CNC MACHINE | 0 | 270.00 | 14011004/02/03/04/05/06/07/08/09/10/11/12/13/14/15/16/17/18/19/20/21/22/23/24/25/26/27/28/29/30/31/32/33/34/35/36/37/38/39/40/41/42/43/44/45/46/47/48/49/50/51/52/53/54/55/56/57/58/59/60/61/62/63/64/65/66/67/68/69/70/71/72/73/74/75/76/77/78/79/80/81/82/83/84/85/86/87/88/89/90/91/92/93/94/95/96/97/98/99/100 | MOHD SWALIM AB SALIM | 10/11/18 | Available | Update Delete View Report |
| K-000055 | LATHING MACHINE (MACHINE) | 0544 | 250.00 | 101004/02/03/04/05/06/07/08/09/10/11/12/13/14/15/16/17/18/19/20/21/22/23/24/25/26/27/28/29/30/31/32/33/34/35/36/37/38/39/40/41/42/43/44/45/46/47/48/49/50/51/52/53/54/55/56/57/58/59/60/61/62/63/64/65/66/67/68/69/70/71/72/73/74/75/76/77/78/79/80/81/82/83/84/85/86/87/88/89/90/91/92/93/94/95/96/97/98/99/100 | MANSUR BIN MANSUR | 10/10/18 | Available | Update Delete View Report |
| K-001254 | HYDRAULIC PRESS | 1023 | 1900 | 140110/02/03/04/05/06/07/08/09/10/11/12/13/14/15/16/17/18/19/20/21/22/23/24/25/26/27/28/29/30/31/32/33/34/35/36/37/38/39/40/41/42/43/44/45/46/47/48/49/50/51/52/53/54/55/56/57/58/59/60/61/62/63/64/65/66/67/68/69/70/71/72/73/74/75/76/77/78/79/80/81/82/83/84/85/86/87/88/89/90/91/92/93/94/95/96/97/98/99/100 | ZURRIE BINTI SASM | 10/10/18 | Available | Update Delete View Report |

Figure 4. Admin page

4. CONCLUSION

The development of the laboratory equipment management software marks a significant advancement in addressing key issues within the existing system. Through a robust database and web application, it effectively tackles challenges such as missing transaction records, human errors, misplaced equipment, inefficient data collection, lack of real-time information, misuse of equipment logs, and incidents of equipment loss. The software achieves its objectives by replacing manual methods with automation, offering a systematic design for monitoring, reducing costs and paperwork, and providing easy access to equipment availability data. This integration of technology enhances equipment management, productivity, data accuracy, and real-time accessibility, paving the way for a more efficient and accountable laboratory environment.

REFERENCES

Rahman, F. Y. A., Kasuan, N., Dzulkifli, M. R., Saat, E. H. M., Dahari, M. F., & Saidi, M. A. (2016, 8-8 Aug. 2016). Development of FKE UiTM Kampus Pasir Gudang lab equipment web database. 2016 7th IEEE Control and System Graduate Research Colloquium (ICSGRC)

Nature Algorithms for Optimizing Coil Springs Design in Mechanical System

Chua Kai Yang ^a and Sabariah binti Julai @ Julaihi ^{b*}

Department of Mechanical Engineering,
Faculty of Engineering, Universiti Malaya,
50603, Kuala Lumpur, Malaysia

Email: ^a chuakaiyang.cky@gmail.com, ^b sabszum.edu.my

*Corresponding author

ABSTRACT

Coil springs are vital in various sectors, yet their design often receives inadequate attention. Optimizing coil spring design can enhance performance, cost efficiency, and sustainability by minimizing material waste. This study employs metaheuristic algorithms to optimize coil spring design for minimum mass while satisfying axial load, deflection, and surge wave frequency requirements. Key variables include wire diameter, mean coil diameter, and the number of active coils. Algorithms such as Particle Swarm Optimization (PSO), Genetic Algorithm (GA), Firefly Algorithm (FA), Teaching-Learning-Based Optimization (TLBO), and Biogeography-Based Optimization (BBO) are utilized and compared against benchmark studies. Each algorithm's stability and convergence are analyzed across different populations and iterations using MATLAB 2023A. Results indicate that PSO and BBO achieve the best solutions, with BBO being more efficient in computational time. A comparative analysis with Tzanetos and Blondin (2023) highlights the efficiency and high performance of PSO and BBO for this optimization problem.

Keywords: Coil Spring Optimization; Metaheuristic Algorithms; Particle Swarm Optimization; Biogeography-Based Optimization; Computational Efficiency

1. INTRODUCTION

Coil springs are crucial for storing and releasing mechanical energy, making them essential in many mechanical systems. They are used in vibration isolation systems to absorb and dampen vibrations, impacting performance in industrial machinery and aerospace. Optimizing coil spring design enhances performance, stability, and load-carrying capacity. Reducing the weight of coil springs is vital for waste management, and cost reduction. Lighter springs lead to minimizing material usage and improved resource efficiency. Optimized designs with less material result in increased durability and reduced maintenance (Herrmann et al., 2018), contributing to lower manufacturing costs and reduced environmental impact (Branowski et al., 2019).

This study employs various optimization algorithms to refine coil spring design. Particle Swarm Optimization (PSO), Genetic Algorithms (GA), Firefly Algorithm (FA), Teaching-Learning-Based Optimization (TLBO), and Biogeography Based Optimization (BBO) will be used as they have not been reviewed and validated in the paper by Tzanetos & Blondin (2023). By employing these advanced

optimization methods, the study aims to enhance the functionality and efficiency of coil springs while addressing sustainability objectives.

2. METHODOLOGY

This optimization task is to design a coil spring the minimum possible mass to carry a given axial load without material failure while satisfying the following performance requirements:

- Deflection of the spring is at least Δ
- Attaining a frequency of surge waves higher than ω_0

To design the mathematical model, four constraints are considered. The coil spring, illustrated in Figure 1, uses design variables including mean coil diameter (D), wire diameter (d), and the number of active coils (N).

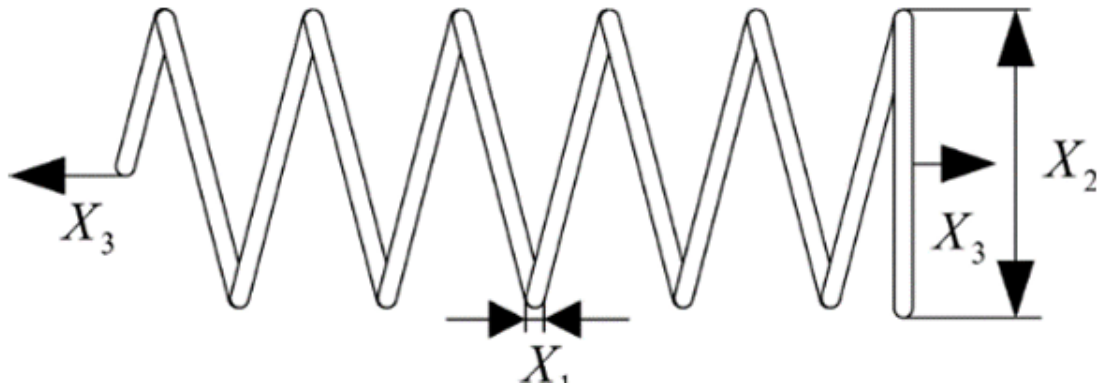


Figure 1. Coil Spring design problem (Li et al., 2022)

The decision variables are defined as x_1 , x_2 , and x_3 , corresponding to d , D , and N , respectively. Applying the values of the parameters as shown in Fig. 2 to (1) that will be expanded, the objective function is formulated as (2):

$$Mass = \left(\frac{\pi}{4}d^2\right)[(N + Q)\pi D]\rho \quad (1)$$

$$f(x) = (x_3 + 2)x_2 x_1^2 \quad (2)$$

Where the constraints of the problem to form the objective function equation is:

$$g_1(x) = 1 - \frac{x_2^3 x_3}{71875 x_1^4} \leq 0$$

$$g_2(x) = 1 - \frac{140.45 x_1}{x_2^3 x_3} \leq 0$$

$$g_3(x) = \frac{x_1 + x_2}{1.5} - 1 \leq 0$$

$$g_4(x) = \frac{4x_2^2 - x_1 x_2}{12566(x_2 x_1^3 - x_1^4)} + \frac{1}{5108 x_1^2} \leq 0$$

| Explanation | Symbol | value/measure |
|-------------------------------------|------------|--|
| Deflection along the axis of spring | δ | in |
| Mean coil diameter | D | in |
| Wire diameter | d | in |
| Number of active coils | N | |
| Gravitational constant | g | 386 in/s ² |
| Frequency of surge waves | ω | Hz |
| Weight density of spring material | γ | 0.285 lb/in ³ |
| Shear modulus | G | (1.15 × 10 ⁷) lb/in ² |
| Mass density of material | ρ | (7.38342 × 10 ⁻⁴) lb – s ² /in ³ |
| Allowable shear stress | τ_a | 80,000 lb/in ² |
| Number of inactive coils | Q | 2 |
| Applied load | P | 10 lb |
| Minimum spring deflection | Δ | 0.5 in |
| Lower limit on surge wave frequency | ω_0 | 100 Hz |
| Limit on outer diameter of coil | D_0 | 1.5 in |

Figure 2. Parameters and variables of the coil spring design (Arora, 2011)

PSO, GA, FA, TLBO, and BBO are developed and implemented in MATLAB 2023A, with parameters such as population size and number of iterations carefully tuned to find the optimal configuration for each algorithm. These algorithms were then compared based on their ability to converge to optimal solutions efficiently and effectively.

3. RESULTS AND DISCUSSION

The evaluation considers the best solution achieved by each algorithm, along with the mean value across all runs. As shown in Table 1 and Figure 3, PSO and BBO consistently produced the best solutions with cost functions of 0.012689 and 0.012694, respectively. FA and TLBO performed reasonably well but did not match PSO and BBO's optimality. GA was less effective in producing the best solution but showed good consistency across trials. These results underscore the importance of choosing the right algorithm based on the specific characteristics and requirements of the optimization problem.

Table 1. Simulation results for 5 algorithms methods

| Method | x_1 | x_2 | x_3 | Best Solution |
|--------|--------|--------|--------|---------------|
| PSO | 0.0519 | 0.3614 | 11.039 | 0.012689 |
| GA | 0.0579 | 0.5225 | 5.6840 | 0.013480 |
| FA | 0.0500 | 0.3174 | 14.067 | 0.012741 |
| TLBO | 0.0500 | 0.3173 | 14.073 | 0.012748 |
| BBO | 0.0520 | 0.3651 | 10.839 | 0.012694 |

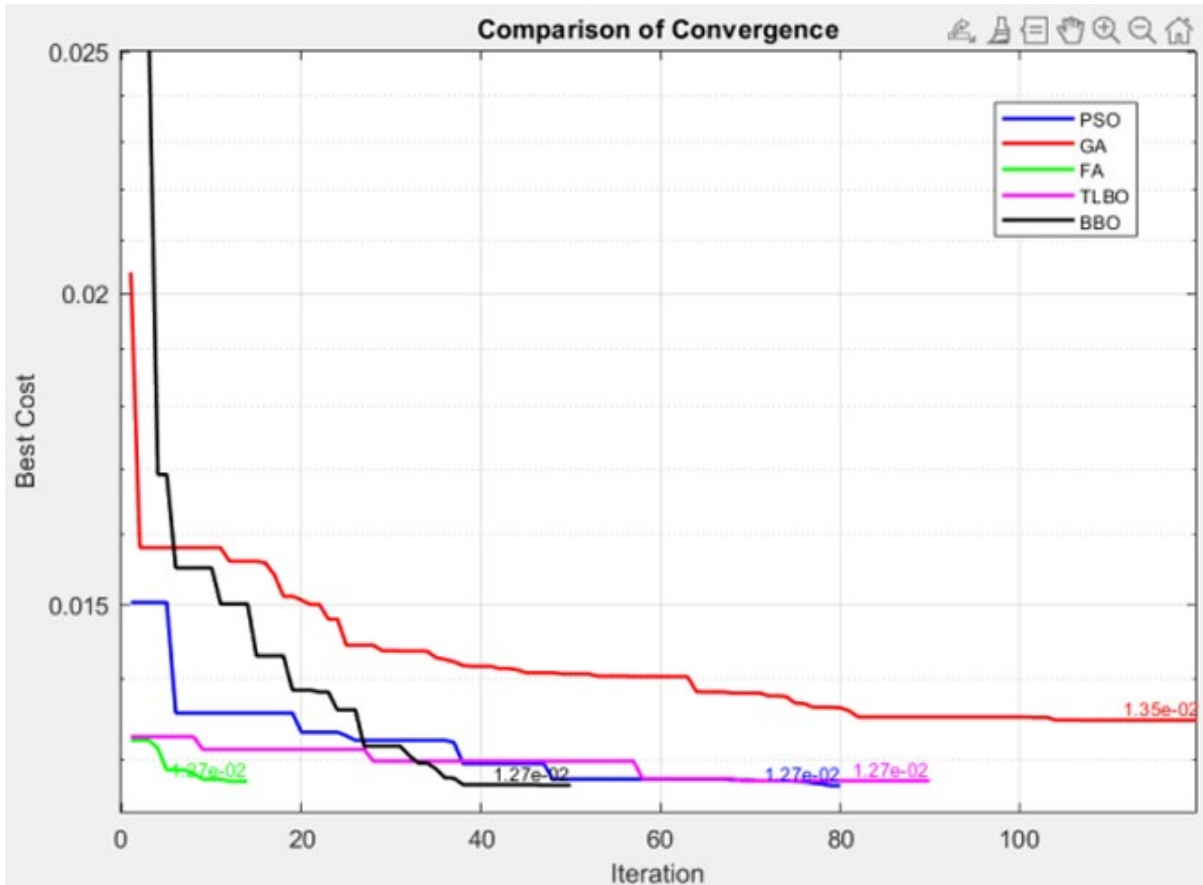


Figure 3. Comparison of convergence graph

As compared to the top four algorithms that had the best results for the spring coil design in Table 2, the closest results from our findings are from BBO and PSO. They did not surpass them but demonstrated highly competitive and reliable results. FA, TLBO, and GA still need refinement for a better performance in spring coil design optimization.

Table 2. Top 4 algorithm methods validated

| Method | x_1 | x_2 | x_3 | Best Solution |
|--------|--------|-------|-------|---------------|
| CSS | 0.0517 | 0.358 | 11.16 | 0.0126384 |
| WEO | 0.0516 | 0.356 | 11.29 | 0.0126650 |
| TEO | 0.0516 | 0.356 | 11.29 | 0.0126650 |
| TSO | 0.0517 | 0.357 | 11.22 | 0.0126650 |

Table 3: Analysis of computational time

| Method | Populations | Iterations | Time |
|--------|-------------|------------|-----------|
| PSO | 600 | 80 | 1.039981 |
| GA | 400 | 120 | 1.156383 |
| FA | 40 | 11 | 0.5045816 |
| TLBO | 400 | 90 | 0.922588 |
| BBO | 400 | 50 | 0.48422 |

Based on Table 3, for different algorithm methods, each has its own optimal configuration system due to their different unique strategies. Each algorithm was tested with different sets of populations and iterations to find their optimal configuration.

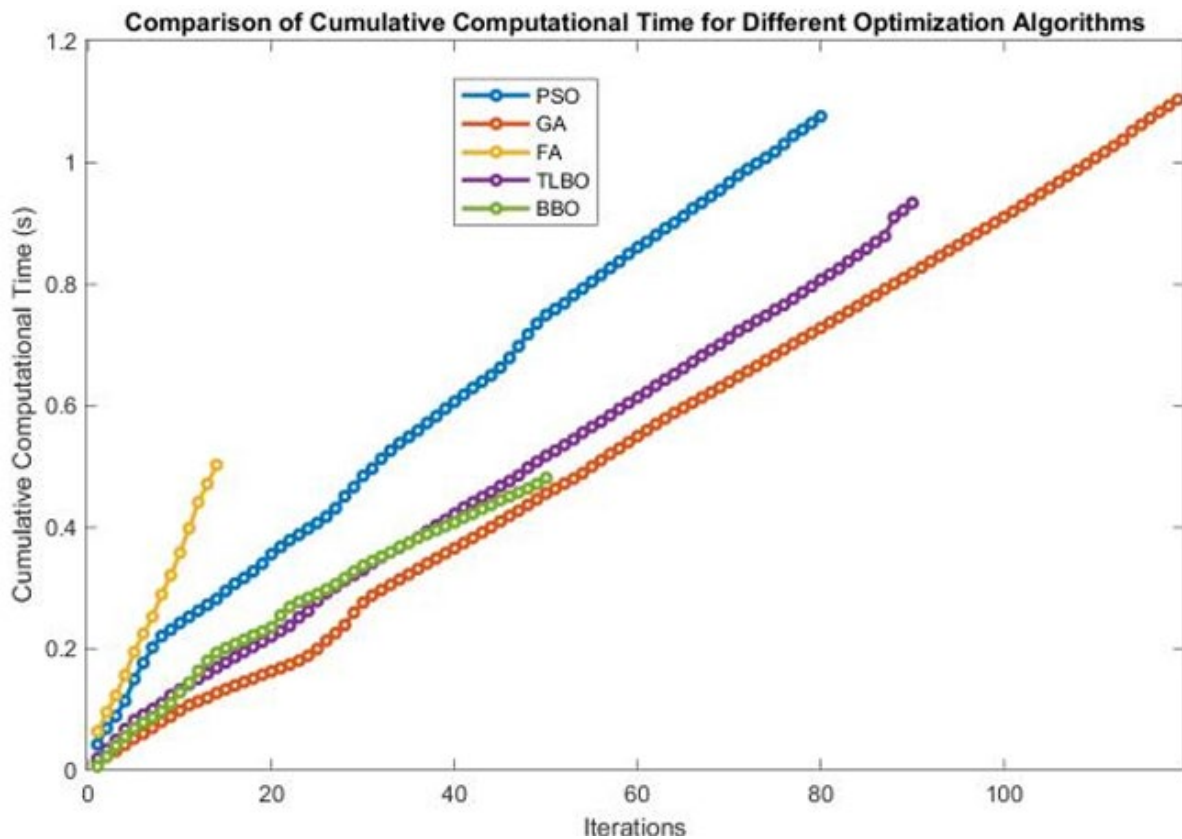


Figure 4. Computational Time for 5 methods

Based on Figure 4, BBO has the fastest average computational time at 0.48422 seconds. Despite its speed, BBO does not compromise on the mean cost function. Comes in 2nd is FA but with a weaker result. PSO which yields the best results took a double time of BBO which makes BBO outperform the other four algorithms, showcasing its efficiency for real-time and resource-constrained applications.

This is extremely important for real-time and resource-constrained applications, where minimizing computational time is crucial without sacrificing solution quality.

4. CONCLUSION

In conclusion, this study evaluated metaheuristic algorithms for optimizing coil spring design, including PSO, GA, FA, TLBO, and BBO which not been reviewed and validated. Results showed PSO and BBO consistently outperformed other algorithms, achieving superior solutions for reducing spring mass while meeting performance requirements. Computational efficiency emerged as a crucial factor, with BBO notably excelling in solution quality and computational time reduction. This suggests that BBO is a promising algorithm for optimizing coil spring design, particularly in scenarios requiring quick and efficient solutions. Future research should focus on refining these algorithms and addressing limitations to enhance their performance further.

Overall, this study provides valuable insights into the optimal use of metaheuristic algorithms in coil spring design optimization, contributing to advancements in mechanical system design.

REFERENCES

- [1] Arora, J. S. (2004). Introduction to Optimum design. In Elsevier eBooks. <https://doi.org/10.1016/b978-0-12-064155-0.x5000-9>
- [2] Branowski, B., Zabłocki, M., & Sydor, M. (2019). The Material Indices Method in the Sustainable Engineering Design Process: a review. *Sustainability*, 11(19), 5465. <https://doi.org/10.3390/su11195465>
- [3] Herrmann, C., Dewulf, W., Hauschild, M. Z., Kaluza, A., Kara, S., & Skerlos, S. (2018). Life cycle engineering of lightweight structures. *CIRP Annals*, 67(2), 651–672. <https://doi.org/10.1016/j.cirp.2018.05.008>
- [4] Tzanetos, A., & Blondin, M. J. (2023). A qualitative systematic review of metaheuristics applied to tension/compression spring design problem: Current situation, recommendations, and research direction. *Engineering Applications of Artificial Intelligence*, 118, 105521. <https://doi.org/10.1016/j.engappai.2022.105521>

Development of In-Pipe Water Turbine for Low Head Condition in Wastewater Treatment Plant

Ilham Bin Syukri ^a and Sabariah binti Julai @ Julaihi ^{b*}

Department of Mechanical Engineering,
Faculty of Engineering, Universiti Malaya,
50603, Kuala Lumpur, Malaysia

Email: ^ailhamsyukri1410@gmail.com, ^bsabsz@um.edu.my

*Corresponding author

ABSTRACT

This research paper presents the design of a low-head in-pipe hydropower system that generates energy from water flow within pipes. At the In-Pipe Hydropower Laboratory, Universiti Malaya, a specialized testing rig simulates low head conditions using variable speed drive (VSD) to adjust the water pump speed. The system targets conditions with heads below 5.1 meters. The turbine blades and nozzle are designed using SolidWorks and then fabricated using a 3D printer with PLA Pro materials. A nozzle with a diameter ratio of 0.5 is chosen by experimenting with the selection of the diameter ratio, adjusting the VSD to 14 Hz, and ensuring stable flow at 0.5 bar pressure and a 4.019 l/s flow rate. Various parameters, including rotational speed, pressure, and velocities, are measured to assess mechanical and hydraulic power. Experimental results indicate system efficiency peaks at 92.55% with a 5.724 l/s flow rate. Optimal torque and angular velocity are 1.49 Nm and 140.67 RPM, respectively.

Keywords: In-Pipe Hydropower; Low-Head Energy Generation; Turbine Design; Hydraulic Power Efficiency; 3D Printed Turbine

1. INTRODUCTION

The pursuit of renewable energy has led to the development of in-pipe hydropower systems, which harness the kinetic and potential energy of water flowing through pipes using compact hydroelectric turbines. These systems are focused on low-head conditions, such as those found in wastewater treatment plants. In-pipe hydropower is advantageous because it is cost-effective and can be integrated into existing infrastructure without requiring large new structures.

This system is versatile, suitable for applications including irrigation, water cleaning, and powering homes and businesses. The primary goal of this research is to enhance the efficiency of in pipe hydropower systems used in low-head conditions. Since this in-pipe hydropower system will use the concept of a Pelton-like turbine, which is more suitable for high head and low flow rates, it will be challenging to adapt the Pelton-like turbine to low-head conditions.

The study aims to enhance the performance of Pelton-like in-pipe hydropower systems in low-head conditions, which will reduce energy costs and carbon emissions while providing a reliable renewable energy source. Key components include the nozzle, which increases water pressure and flow speed, and the turbine blades, which convert kinetic energy into mechanical power. Overall, in-pipe hydropower systems represent a promising solution for sustainable energy generation.

2. METHODOLOGY

2.1 Experimental Setup

The In-Pipe Hydropower Lab in Block Q of the Engineering Department Faculty hosts experiments requiring a 1 bar maximum pressure, utilizing a 3-inch-wide PVC pipe with reservoirs at inlet and outlet. To determine the stagnation pressure, it is necessary to use a pressure gauge while closing the system. A variable speed drive (VSD) controls water flow, monitored by a pressure gauge and ultrasonic flow sensor. The hydropower system, encased in carbon steel, features a turbine runner with 24 bolt points, accommodating up to 12 blades. The setup of the new test rig is shown in Figure 1.



Figure 1. Setup of the test rig

2.2 Design of Nozzle

The shape and design of a nozzle have significant impacts on the effectiveness of a hydropower system. Therefore, before starting developing a nozzle, it is important to determine which type of nozzle will perform the best in the low head condition. The diameter ratio is set in advance to find the nozzle's outlet diameter. For this experiment, a nozzle with a diameter ratio of with the range of 0.5 to 0.8 will be selected which will be shown in Table 1.

Table 1. Different diameter ratio of nozzles

| Inlet Diameter (mm) | Outlet Diameter (mm) | Diameter Ratio |
|--------------------------------|---------------------------------|-----------------------|
| 77 | 38.5 | 0.5 |
| 77 | 46.2 | 0.6 |
| 77 | 53.9 | 0.7 |
| 77 | 61.6 | 0.8 |

2.3 Turbine Blade Design

In this turbine system, the blade plays a crucial role in capturing and directing the water jet from the nozzle effectively. Designing a blade for a low-head in-pipe hydropower system is challenging due to the limited head for power generation. Optimizing torque is essential for capturing energy more efficiently. Key design elements include curved blades and openings at the blade end. Curved blades promote smooth water flow, minimizing turbine water flow disruptions. Blade openings enhance water flow dynamics. The turbine blade design aims to closely match the angle for perpendicular impact to maximize torque generation. Figure 2 shows the turbine blade used for this project.



Figure 2. Turbine blade

2.4 Mechanical Power

Mechanical energy is harvested using turbines in pipe hydro systems, which rotate in response to the flow of water. To measure mechanical power, the angular velocity and torque of the system must be calculated first. The angular velocity of a given system can be determined by using a digital tachometer and torque can be calculated by using equation (2.1).

$$Torque = Density \times Diameter (Jet Velocity - Turbine Velocity) \quad (2.1)$$

Based on research done by Aima Mariaty Ahmad, Sabariah Julai, Iswadi Jauhari and Norfazila Mohd Sultan in 2023, mechanical power can be obtained by using the equation (2.2)

$$Mechanical Power [W] = Torque [Nm] \times Angular velocity \left[\frac{rad}{s} \right] \quad (2.2)$$

2.5 Hydraulic Power and Efficiency

Hydraulic power from water refers to the energy extracted from the movement or force of water. To measure hydraulic power, certain parameters such as flow rate and jet velocity from the experiment are required which are shown in the equation (2.3).

$$Hydraulic Power [W] = 1/2 \times Density \left[\frac{kg}{m^3} \right] \times Flowrate \left[\frac{m}{s} \right] \times Jet velocity \left[\frac{m^3}{s} \right] \quad (2.3)$$

When both the value of the mechanical power and the hydropower is obtained, the efficiency of turbine is calculated by using equation (2.4).

$$\text{Turbine Efficiency} = \frac{\text{Mechanical Power}}{\text{Hydraulic Power}} \times 100\% \quad (2.4)$$

3. RESULTS AND DISCUSSION

As is known, angular rotation results from the turbine blades starting to rotate due to the force and velocity from the nozzle. Mechanical power is calculated by using equation 2.2, which illustrated in Table 2.

Table 2. Experimental Data for Mechanical Power with Turbine

| Flowrate (1/s) | Angular Velocity (rpm) | Torque (Nm) | Mechanical Power (W) |
|----------------|------------------------|-------------|----------------------|
| 0 | 0 | 0 | 0.000 |
| 1.838 | 0.395 | 1.579 | 2.894 |
| 2.791 | 0.599 | 2.398 | 6.672 |
| 3.458 | 0.743 | 2.971 | 10.242 |
| 3.946 | 0.847 | 3.390 | 13.337 |
| 4.479 | 0.962 | 3.848 | 17.183 |
| 4.931 | 1.059 | 4.236 | 20.826 |
| 5.381 | 1.155 | 4.623 | 24.801 |
| 5.724 | 1.229 | 4.918 | 28.063 |
| 6.057 | 1.301 | 5.208 | 31.424 |

As the flow rate increases in an in-pipe hydropower system, it is expected that both the mechanical power and hydraulic power will increase. This is because higher flow rates result in a larger volume of water passing through the turbine, which leads to more power being available for conversion.

Table 3. Experimental Data for Mechanical Power with Turbine

| Hydraulic Power (W) | Efficiency (%) | Mechanical Power (W) |
|---------------------|----------------|----------------------|
| 0.000 | 0.000 | 0.000 |
| 2.285 | 0.000 | 0.000 |
| 7.999 | 81.656 | 6.532 |
| 15.214 | 87.701 | 13.342 |
| 22.606 | 90.532 | 20.466 |
| 33.060 | 91.129 | 30.127 |
| 44.113 | 91.686 | 40.445 |
| 57.326 | 92.151 | 52.826 |
| 69.001 | 92.550 | 63.861 |
| 81.758 | 92.548 | 75.666 |

The torque produced for the low head application (0.5 bar) is 1.945 Nm, with an angular velocity of 100.5 RPM. However, the optimal torque value is 1.49 Nm with an angular velocity of 140.67 RPM in order to improve both mechanical power and system efficiency, as illustrated in Table 4.

Table 4. Minimum, Maximum, Optimum and Achieve Torque with respective Turbine Velocity

| | Torque (Nm) | Turbine Velocity (m/s) | Angular Velocity | Mechanical Power (W) |
|-----------------------|--------------------|-------------------------------|-------------------------|-----------------------------|
| Torque Max | 2.97 | 0.00 | 0.00 | 0.000 |
| Torque Achieve | 1.945 | 1.173 | 100.5 | 20.467 |
| Torque Optimum | 1.49 | 1.70 | 140.67 | 21.906 |
| Torque Min | 0.00 | 3.390 | 281.33 | 0.000 |

4. CONCLUSION

The experiment successfully demonstrated the feasibility of a low-head in-pipe hydropower system for energy generation. Using a specially designed and 3D-printed nozzle and turbine blades, the system was tested under various flow conditions in a controlled laboratory setup. The VSD effectively simulated low-head conditions, and key performance parameters were measured. The results showed that the system achieved a peak efficiency of 92.55% at a flow rate of 5.724 l/s, with optimal torque and angular velocity recorded for 0.5 bar at 1.49 Nm and 140.67 RPM, respectively. These findings indicate that such a system can efficiently recover energy from low-head water flows, offering a sustainable solution for energy recovery.

REFERENCES

- [1] Ahmad, A. M., Julai, S., Jauhari, I., & Sultan, N. M. (2023). In-pipe hydropower vertical axis parallel turbines prototype: performance and workability testing. *Energy Sources, Part A: Recovery, Utilization, and Environmental Effects*, 45(1), 2317–2329. <https://doi.org/10.1080/15567036.2023.2187098>

Optimization of Linkage-based Suspension Layout Considering Vehicle Suspension Application

Chew Boon Kheng ^a and Soong Ming Foong ^{b*}

Department of Mechanical Engineering,
Faculty of Engineering, Universiti Malaya,
50603, Kuala Lumpur, Malaysia

Email: ^a chewkheng428@gmail.com, ^b mfsoong@um.edu.my

*Corresponding author

ABSTRACT

The vehicle suspension system is a crucial aspect of the automobile industry, balancing comfort, stability, and safety by maintaining tire-road contact, absorbing road imperfections, and preventing the transfer of vertical energy. Conventional suspension systems with fixed parameters compromise performance in varied driving conditions, impacting consistent road contact. This research aims to determine optimal characteristics of linkage-based suspension layouts and compare their performance with conventional systems. The scope involves optimizing linkage-based layouts under different conditions, assessing ride comfort, handling, and tire load distribution, and validating results through experiments. Equations for linkage-based suspension are derived, then Simulink model and MATLAB optimization code are developed for comprehensive analysis. The study includes 3D models of the linkage-based suspension and suspension test rig for visualization. Practical implementation involves fabricating the linkage-based suspension and test rig. Finally, an experiment will be conducted to validate the performance of linkage-based suspension.

Keywords: Vehicle Suspension System; Linkage-Based Suspension; Ride Comfort; Tire Load Distribution; Simulink Model

1. INTRODUCTION

The suspension system of a vehicle is vital for balancing ride comfort, handling stability, and safety. Conventional suspension systems use fixed spring constants and damping coefficients, which may not provide optimal performance under varying driving conditions and loads. These systems often compromise between ride comfort and handling stability, leading to issues like inconsistent road contact during sudden braking, sharp corners, or on uneven surfaces, thereby increasing accident risk. This research aims to determine the optimum characteristics of a linkage-based suspension layout and compare its performance to conventional suspension systems.

2. METHODOLOGY

Theoretical equation for linkage-based suspension was derived:

$$k_{eq} = k \cot^2 \theta \text{ or } k \frac{\cos^2 \theta}{\sin^2 \theta} \text{ or } k \left(\frac{a^2}{b^2} \right)$$

Simulink model of the linkage-based suspension was developed, and optimization was done by using MATLAB. The parameters of optimization for linkage-based suspension are below:

Table 1. Parameters of vehicle

| | |
|---------------------------------------|------------|
| Sprung Mass | 317.5 kg |
| Unsprung Mass | 45.4 kg |
| Tire elasticity constant | 192000 N/m |
| Suspension spring constant | 22000 N/m |
| Suspension damping coefficient | 1500 Ns/m |

The optimization was also done by using parameters of truck to validate the versatility of the design in different applications.

Table 2. Parameters of truck [1]

| | |
|---------------------------------------|------------|
| Sprung Mass | 1350 kg |
| Unsprung Mass | 335 kg |
| Tire elasticity constant | 760000 N/m |
| Suspension spring constant | 270000 N/m |
| Suspension damping coefficient | 16800 Ns/m |

Static load Hooke's Law experiment was conducted to validate the performance of linkage-based suspension. Weights are placed on the test rig and the compression of suspension measured and recorded. By applying Hooke's law, the spring constant of the suspension can be calculated.

3. RESULTS AND DISCUSSION

Figures 1 and 2 show that linkage-based suspension offers a broader Pareto front range compared to conventional suspension, allowing for more varied suspension settings. While linkage-based suspension achieves lower car body acceleration, it results in higher dynamic tire loads. According to Eq. 1, the equivalent spring constant depends on the vertical length and horizontal length of the linkage. As the suspension is compressed, lower the equivalent spring constant. This reduction lowers car body acceleration but increases dynamic tire load. The linkage-based suspension effectively isolates the car body from road disturbances, absorbing and dissipating vibrations within the linkage structure. However, this isolation leads to higher dynamic loads on the tires.

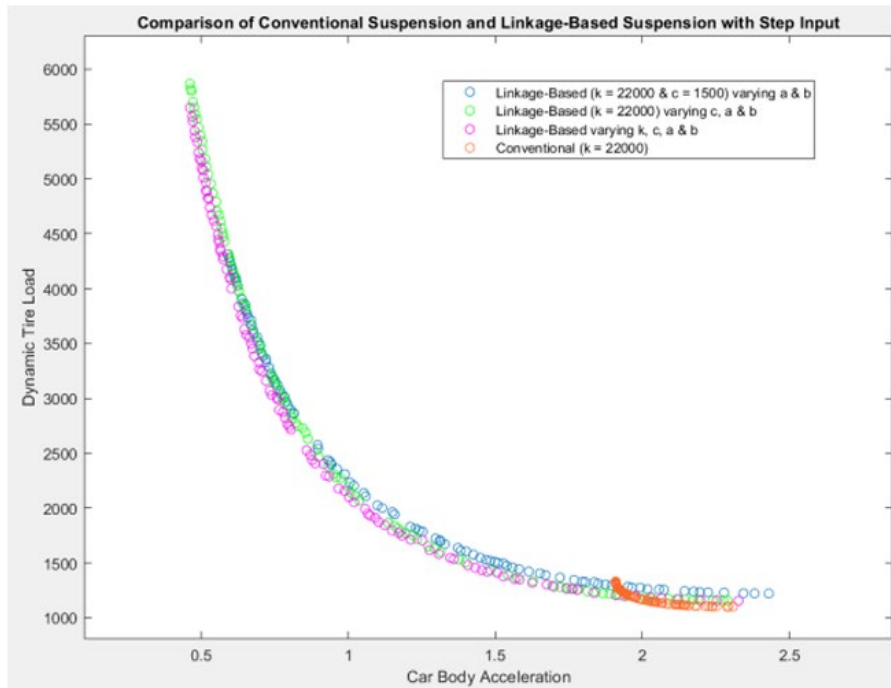


Figure 1. Comparison of Conventional Suspension and Linkage-Based Suspension with Step Input Pareto Front

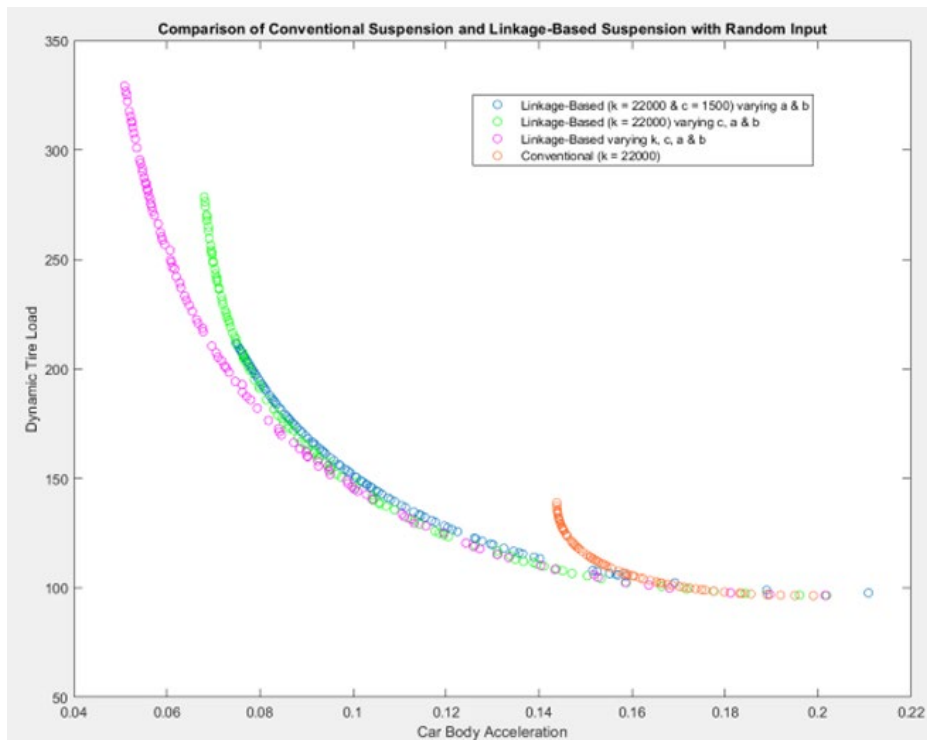


Figure 2. Comparison of Conventional Suspension and Linkage-Based Suspension with Random Input Pareto Front

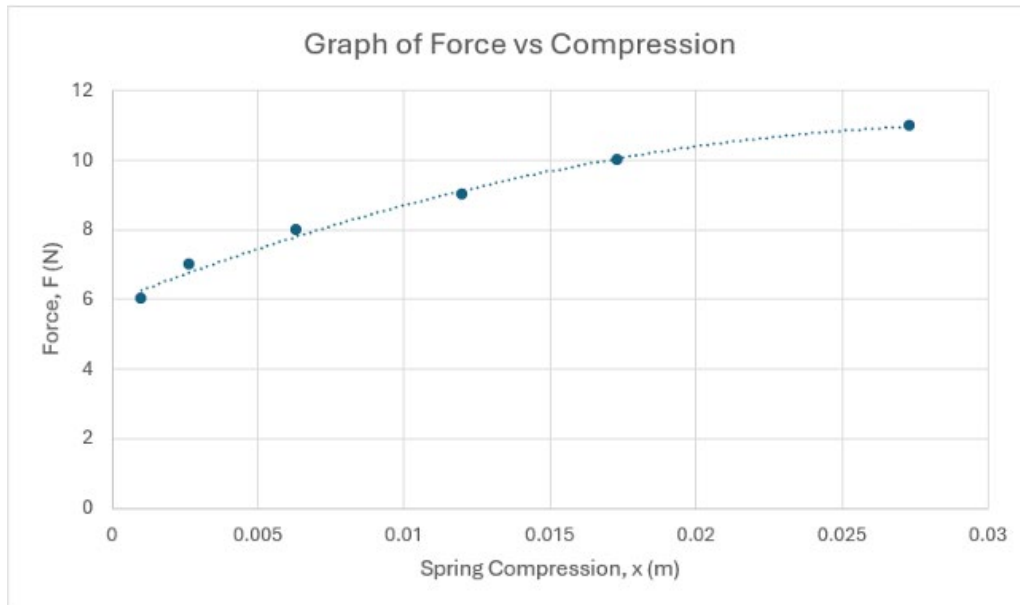


Figure 3. Graph of Force vs Compression

Based on Graph 3, we can observe that the gradient of the graph is decreasing. According to Hooke's Law, the gradient of the graph refers to the spring constant, which means that as we increase the load or compress the spring, the spring constant is decreased. The experiment results match Eq. 1. and simulation results, validate that the linkage-based suspension is having variable spring constant.

4. CONCLUSION

Simulation results indicate that linkage-based suspension offers a greater range of suspension settings compared to conventional suspension. The equivalent spring constant of the linkage-based suspension depends on the vertical length and horizontal length of the linkage. As the suspension is compressed, lower the equivalent spring constant. This reduced spring constant results in lower car body acceleration but higher dynamic tire load. Static load experiments using Hooke's Law support these findings, validating that linkage-based suspension has a variable spring constant, unlike conventional suspension which has a fixed spring constant.

REFERENCES

- [1] Di Mascio, P., Loprencipe, G., Moretti, L., Puzzo, L., & Zoccali, P. (2017). Bridge Expansion Joint in Road Transition Curve: Effects Assessment on Heavy Vehicles. *Applied Sciences*, 7(6), 599. <https://doi.org/10.3390/app7060599>

Time-Frequency Analysis on Financial Instruments

Lee Ming Hooi ^a and Soong Ming Foong ^{b*}

Department of Mechanical Engineering,
Faculty of Engineering, Universiti Malaya,
50603, Kuala Lumpur, Malaysia

Email: ^a leehooigor@gmail.com, ^b mfsoongum.edu.my

*Corresponding author

ABSTRACT

This study explores the application of time-frequency analysis on financial instruments using Fourier and Wavelet transforms to quantitatively assess market dynamics. Utilizing data from January 1, 2000, to May 30, 2024, sourced through Python yfinance library, the research employs Fourier and Wavelet transforms to uncover underlying trends and predict financial crises such as the 2008 Global financial crisis. Fourier Transform analysis revealed dominant lower frequency components, indicating long-term trends in financial instruments. In contrast, Wavelet Analysis provided a 2D visualization of time-frequency signals, highlighting significant cyclical behaviors with high wavelet magnitudes at lower frequencies. The study also developed a Python-based GUI integrating time-frequency and fundamental analysis methods, enhancing the practical application of the findings. Overall, this approach transforms qualitative financial assessments into quantitative, data-driven insights, offering a profound understanding of the cyclical nature of markets.

Keywords: Time-Frequency Analysis; Financial Instruments; Fourier Transform; Wavelet Analysis; Market Dynamics

1. INTRODUCTION

This research draws parallels between time frequency analysis used in engineering for detecting machinery defects, and its application to financial markets, particularly in understanding and predicting market dynamics. The time-frequency analysis seeks to transform qualitative investment strategies into quantitative, data-driven insights for investors to foresee major financial crisis.

By using Fourier Transform and Wavelet Transform analysis, this study aims to uncover patterns in financial time series that are not visible through conventional time-domain analyses. The project specifically investigates the potential of Fourier Series analysis and Continuous Wavelet Transform analysis to predict major financial crises, such as the 2008 Global Financial Crisis, by identifying the sudden spike in low frequency coefficient that may signify impending market downturns. [1]

2. METHODOLOGY

This research project employs Fourier Transform and Wavelet Transform analyses to delve into the time-frequency dynamics of financial instruments, aiming to predict significant financial downturns like the 2008 Global Financial Crisis. Data collection for this study spans from January 1, 2000, to May

30, 2024, involving securities such as S&P500, Malaysia Index, Microsoft, Starbucks, and Bitcoin, using Python and the 'yfinance' library for data retrieval. Preprocessing includes cleaning data with a dropna() function to ensure continuity and applying a Hamming window to minimize spectral leakage (for Fourier Transform only). [2]

The methodology transitions from time domain analysis, visualizing stock prices and returns to identify trends, to frequency domain analysis using FFT to detect dominant cycles. The Fourier series analysis is particularly focused on low frequency components to anticipate major market shifts, while Continuous Wavelet Transform analysis provides a 2D visualization of time-frequency signals, highlighting significant market events with high wavelet magnitudes. A GUI developed using Python's Tkinter library integrates these analyses, offering users interactive tools for detailed examination and comparison of financial data, enhancing the practical application of theoretical financial models as shown in Figure 1.

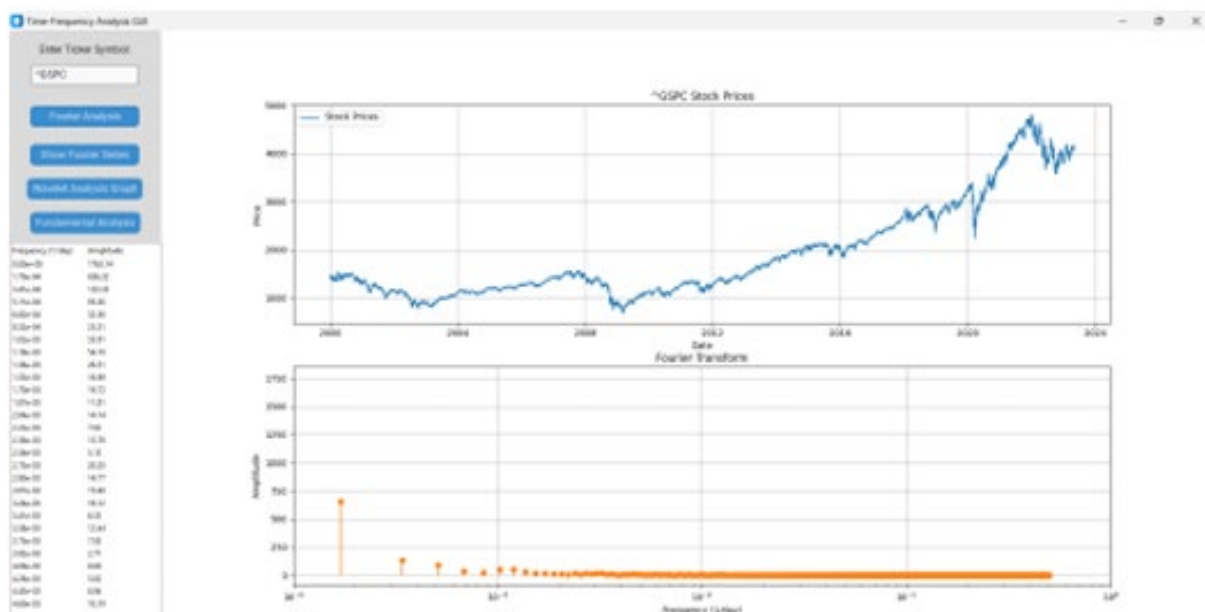


Figure 1. Time-Frequency Analysis GUI

3. RESULTS AND DISCUSSION

Figure 2 demonstrates that the non-zero lowest frequency (1.70×10^{-4}) has the highest amplitude, 656.32 of Fourier Coefficient, suggesting that the S&P 500 is predominantly influenced by long-term investment trends. Similarly, other financial instruments such as MSFT, SBUX, and the KLSE index show a comparable non-zero peak frequency to that of the S&P 500. In contrast, BTC-USD displays a greatest non-zero dominant frequency at (3.18×10^{-4}), underscoring its highest fluctuation characteristics.

Figure 3 clearly illustrates a significant increase in the C1 coefficient, which represents the frequency of one cycle per year, during the financial crisis for the S&P 500 index. This sudden spikes during Dec 2007 & Sept 2008 in the C1 coefficient suggest that the S&P 500 index can provide a warning signal during the 2007-2008 global financial crisis.

The Continuous Wavelet Transform graph of the S&P 500 monthly returns, shown in Figure 4, clearly demonstrates sudden increases in wavelet magnitude, indicated by prominent red regions in the low-frequency areas during periods of financial crises (2008 and 2020)

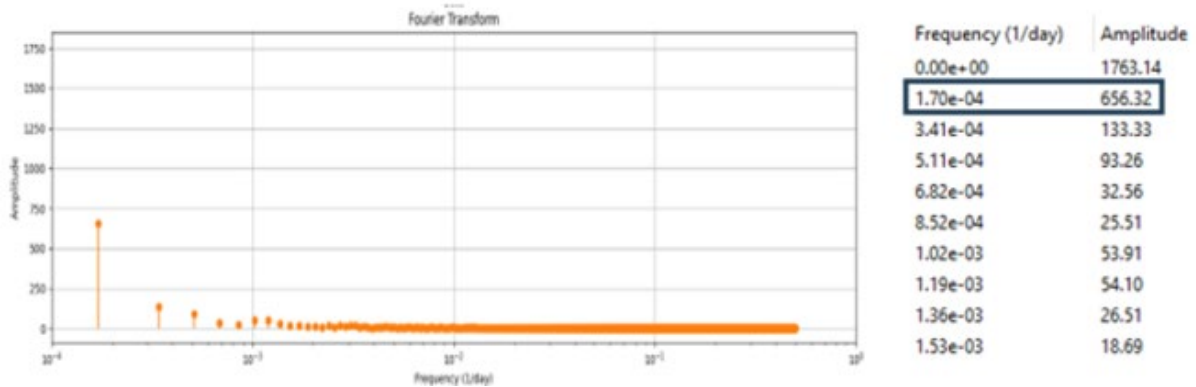


Figure 2. Fourier Transform on S&P500

| Date | C1 | C2 | C3 | C4 | Return(%) |
|------------|------|------|------|------|-----------|
| 2007-10-31 | 0.68 | 1.84 | 2.92 | 1.01 | 1.48 |
| 2007-11-30 | 0.96 | 2.14 | 2.75 | 0.89 | -4.40 |
| 2007-12-31 | 1.90 | 3.28 | 1.72 | 0.81 | -0.86 |
| 2008-01-31 | 2.03 | 3.33 | 1.87 | 0.89 | -6.12 |
| 2008-02-29 | 2.09 | 3.15 | 2.06 | 0.63 | -3.48 |
| 2008-03-31 | 2.11 | 3.22 | 2.11 | 0.59 | -0.60 |
| 2008-04-30 | 1.86 | 3.12 | 1.87 | 0.85 | 4.75 |
| 2008-05-31 | 0.92 | 4.04 | 2.86 | 0.51 | 1.07 |
| 2008-06-30 | 1.27 | 3.72 | 2.73 | 0.87 | -8.60 |
| 2008-07-31 | 1.26 | 3.72 | 2.72 | 0.87 | -0.99 |
| 2008-08-31 | 1.53 | 2.12 | 2.95 | 2.74 | 1.22 |
| 2008-09-30 | 4.60 | 0.96 | 5.85 | 2.27 | -9.08 |
| 2008-10-31 | 5.06 | 1.34 | 5.75 | 1.76 | -16.94 |

Figure 3. Fourier Series Analysis on S&P500 during 2007-2008 Global Financial Crisis

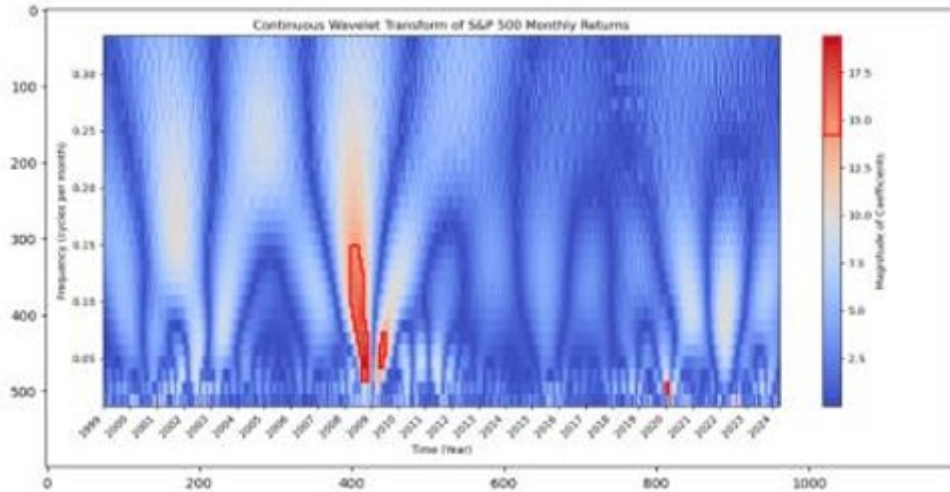


Figure 4. Continuous Wavelet Graph for S&P500

4. CONCLUSION

This study successfully established a comprehensive framework for the time frequency analysis of financial instruments using Fourier and Wavelet transform. The Fourier Transform method excelled in pinpointing dominant frequencies in financial instruments, while Fourier Series successfully captured major downturns in stocks and indices, though less effective in volatile instruments like Bitcoin. Wavelet Transform analysis further enhanced the detection of crises by visually emphasizing high magnitude wavelet coefficients during turbulent periods. Lastly, the development of a user-friendly CustomTkinter enabled GUI using interactive exploration of financial data, integrating time-frequency analysis methods with fundamental analysis tools.

REFERENCES

- [1] Jun, D., et al., Signal analysis of global financial crises using Fourier series. *Physica A: Statistical Mechanics and its Applications*, 2019. 526: p. 121015.
- [2] Olbrys, J. and M. Mursztyn, Measuring stock market resiliency with Discrete Fourier Transform for high frequency data. *Physica A: Statistical Mechanics and its Applications*, 2019. 513: p. 248-256.

Design and Fabrication of Floating Vertical Wind-Wave Turbine: A Comprehensive Study on Prototype Structures with Hybrid Harvesting Systems for Sustainable Energy Ecosystems

Mohamad Kamal Fahmi bin Yasman ^a and Norhafizan bin Ahmad ^{b*}

Department of Mechanical Engineering,
Faculty of Engineering, Universiti Malaya,
50603, Kuala Lumpur, Malaysia

Email: ^a kamalfahmi115@gmail.com, ^b mfsoongum.edu.my

*Corresponding author

ABSTRACT

This project explores a hybrid system combining wind and wave energy for consistent and reliable renewable power. We developed a vertical turbine merging Darrieus and Savonius blades, along with an Oscillating Water Column (OWC) for wave energy capture. The system includes a Wells turbine structure and a gearbox for enhanced energy conversion efficiency. The approach involved a thorough review of existing technologies and careful material selection, using aluminum and stainless steel for durability in marine environments. The project focused on measuring the fabricated design against the CAD model, revealing minor discrepancies within acceptable tolerances. Future efforts will involve rigorous measurement and validation of the design, ensuring it meets energy needs effectively. This includes detailed assessments of the vertical wind turbine, gearbox systems, Wells turbine structure, and OWC to optimize integration and performance.

Keywords: floating vertical wind-wave turbine; renewable energy integration; hybrid energy systems; CAD modeling and fabrication; offshore energy solutions.

1. INTRODUCTION

The project focuses on developing a floating vertical wind-wave turbine to harness both wind and wave energy efficiently. [1] focus on the advantages of integrating offshore wind and wave farms in terms of power stabilization and decreased operational interruptions compared to standalone solutions. Technically, it requires sophisticated control systems to manage the different characteristics of wind and wave energy [2]. The hybrid approach aims to address this by integrating wind and wave energy harvesting mechanisms in a single unit, promising enhanced efficiency, consistent power output, and reduced environmental impact [3].

This innovative turbine is designed to operate effectively in diverse environmental conditions, bridging the gap between lab-based models and real-world applications. [4] focus on integrating green power: use experiments and software simulations to find out how well wave, solar, and wind energies can work

together. By fabricating and testing the prototype in actual offshore environments, we aim to ensure its structural integrity, durability, and functionality [5]. This project contributes significantly to the precision and accuracy of measurement analysis between CAD models and fabrication designs in renewable energy technologies. By ensuring that the fabricated structures closely adhere to their digital blueprints, we support the global effort to reduce reliance on non-renewable energy and combat climate change. Accurate measurement of fabrication tolerances helps in maintaining the structural integrity and performance of the final prototype [6].

2. METHODOLOGY

The design and fabrication of the floating vertical wind-wave turbine begins with detailed CAD modeling using SolidWorks software. Each component of the hybrid system is meticulously designed to incorporate necessary features for functionality and assembly, ensuring precise dimensions and material properties to analyze stress and strain. The CAD models are integrated into an assembly to form a cohesive system, with simulation capabilities used to analyze the operational dynamics under various conditions. This process ensures that the final design is robust, reliable, and ready for fabrication, minimizing errors and discrepancies during the manufacturing phase.

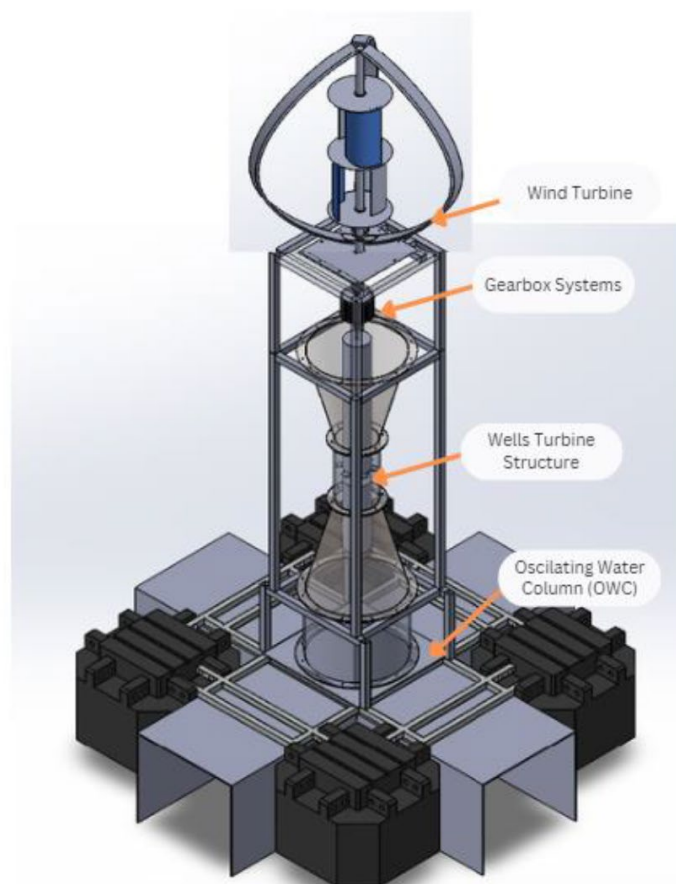


Figure 1. Final design of hybrid harvester system in SolidWorks.

The fabrication process involves selecting materials and components suitable for marine environments, such as T-slot aluminium extrusions, aluminium square tubes, and stainless steel for their durability and corrosion resistance. Key components like the oscillating water column structure, Wells turbine, and rotor blades are designed for optimal performance and integrated into a modular support structure. The

assembly process ensures structural integrity and ease of maintenance. Measurement analysis between the CAD Model and the fabricated design ensures that the prototype adheres to the specified dimensions, with laser distance meters used to capture precise measurements and verify tolerances.\

3. RESULTS AND DISCUSSIONS

The results of this project indicate that the fabricated hybrid wind-wave turbine structure closely adheres to the dimensions specified in the CAD model, with most measurements falling within acceptable tolerance levels. Minor discrepancies were observed in dimensions such as base length and height, but these variations are typical in fabrication processes and do not significantly impact the overall performance or structural integrity of the turbine.

This alignment also validates our comprehensive planning and execution approach, emphasizing the importance of precision in both design and fabrication stages. Moving forward, the focus will be on optimizing the integration of the vertical wind turbine, gearbox systems, Wells turbine structure, and oscillating water column to ensure seamless operation and enhanced energy conversion efficiency, ultimately contributing to the advancement of sustainable energy solutions.

Table 1 shows overall height and measurement of the base of hybrid wind-wave model that creates a comparison between Cad Model and fabricated design. The details of measurement analysis for each component are shown in the report. The table also shows the deviations and percentage difference and discuss the reason of the deviations and how to improve the tolerance.

Table 1. Comparison of overall height and dimension of the base for hybrid wind-wave structure.

| Component | Measurement value (mm) | | Difference (mm) | Error Percentage (%) |
|----------------|------------------------|-------------------|-----------------|----------------------|
| | CAD Model | Fabricated Design | | |
| Overall height | 5701 | 6114 | 413 | 7.24 |
| Base length | 2920 | 3040 | 120 | 4.11 |
| Base Width | 2917.5 | 3032 | 114.5 | 3.92 |
| Base Height | 1175 | 1265 | 90 | 7.66 |

The structure's overall height shows a deviation of 413 mm (7.24%) from the CAD model, primarily due to assembly issues that may impact balance and performance. The base dimensions also exhibit significant deviations: the length differs by 120 mm (4.11%), width by 114.5 mm (3.92%), and height by 90 mm (7.66%). These discrepancies suggest potential assembly issues that need to be addressed to improve precision.

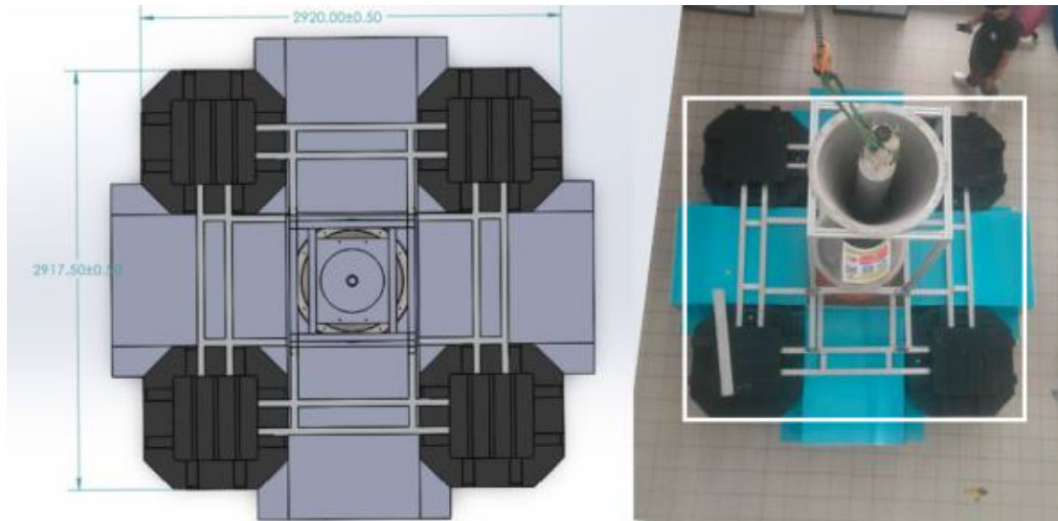


Figure 2. Comparison between CAD Model and fabricated design of the base.

4. CONCLUSIONS

The measurement analysis between the CAD model and the fabricated hybrid vertical wind-wave turbine structure showed that the fabricated design closely matches the specified dimensions, with minor discrepancies within acceptable tolerance levels. Critical dimensions like overall height, base dimensions, and turbine shaft diameter exhibited minimal differences, unlikely to affect performance or structural integrity. While slight variations in base length and height suggest areas for improvement in future fabrication efforts, the overall process was successful in translating the CAD model into a high-fidelity physical prototype. This validation underscores the importance of precise measurement and comparison for reliable and efficient renewable energy systems.

REFERENCES

1. Astariz, S., & Iglesias, G. (2015). Enhancing wave energy competitiveness through co-located wind and wave energy farms. A review on the shadow effect. *Energies*, 8(7), 7344–7366. <https://doi.org/10.3390/en8077344>
2. Moghimi, M., Derakhshan, S., & Motawej, H. (2018, November 22). *A mathematical model development for assessing the engineering and economic improvement of wave and Wind Hybrid Energy System - Iranian Journal of Science and Technology, Transactions of Mechanical Engineering*. SpringerLink. <https://link.springer.com/article/10.1007/s40997-018-0272-8>
3. Maksoud, M. A. (n.d.). *Substantial research secures the Blue Future for our Blue Plant*. Renewable Energy and Sustainable Development. <http://apc.aast.edu/ojs/index.php/RESA/article/view/138>
4. Talaat, M., Farahat, M. A., & Elkholy, M. H. (2019). Renewable Power Integration: Experimental and simulation study to investigate the ability of integrating wave, solar and wind energies. *Energy*, 170, 668–682. <https://doi.org/10.1016/j.energy.2018.12.171>
5. Hassani, S., Vu, T. N., Rosli, N. R., Esmaeely, S. N., Choi, Y.-S., Young, D., & Nesic, S. (2014). Wellbore integrity and corrosion of low alloy and stainless steels in high pressure CO₂ Geologic Storage Environments: An experimental study. *International Journal of Greenhouse Gas Control*, 23, 30–43. <https://doi.org/10.1016/j.ijggc.2014.01.016>
6. Montgomery, D. C. (2012). *Design and Analysis of Experiments* (8th ed.). John Wiley & Sons.

Finite Element Simulation of Knee Loading During Driving

Omar Ihab Mohamed Abdelwahab Mohamed ^a and Andri Andriyana ^{b*}

Department of Mechanical Engineering,
Faculty of Engineering, Universiti Malaya,
50603, Kuala Lumpur, Malaysia

Email: ^a omarrehabb11@gmail.com, ^b andri.andriyana@um.edu.my

*Corresponding author

ABSTRACT

This study examines the influence of stress on the knee joint in driving positions by studying the viscoelastic properties of the meniscus. It compares the distribution of stress between models with viscoelastic and linear elastic properties and analyzes the disparities between good and bad driving positions. The knee model, derived from prior studies, is incorporated in ANSYS software, integrating bone structures, articular cartilage, menisci, and other components with different material properties. The application of finite element analysis is used to model stress under both constant and cyclic forces. The key findings indicate that the bad driving position leads to increased stress levels and highlight the importance of viscoelastic properties, especially in the meniscus. Suggested improvements involve optimizing the knee model, integrating muscle dynamics, and enhancing material characterization to enhance realism.

Keywords: biomechanics; driving; finite element analysis; knee; stress

1. INTRODUCTION

Following the COVID-19 pandemic, there is a greater focus on ergonomics to improve human well-being, considering the influence of modern lifestyles on health (Brown et al., 2021). The sedentary nature of work has raised concerns regarding the health of knee joints, which are further worsened by urban lifestyles (Robinson, 2018). However, there is a lack of comprehension regarding the dynamics of knee loading during activities such as driving, despite being aware of this issue. This study seeks to fill this void by investigating the stress on knee components during driving through the utilization of finite element simulations. The objective is to offer a profound understanding of knee well-being and formulate more precise models for real-life situations.

2. METHODOLOGY

The methodology details the process of creating and improving a model of a human knee joint for biomechanical simulation using finite element analysis (FEA) in ANSYS. The model incorporates bones, articular cartilage, tibial cartilage, and menisci, with each component being assigned material properties based on existing literature. Bones exhibit linear elastic behaviour, cartilages demonstrate neo-hookean hyperelastic behaviour, and menisci display viscoelastic behaviour. Another fully linear simulation will be conducted for comparison.

Table 1. Linear and nonlinear material properties.

| Component | Young's Modulus (MPa) | Poisson's Ratio | Density (ton/mm ³) |
|---------------------------------------|------------------------------------|---|--------------------------------|
| Bones | 17,400 | 0.3 | 1.708583E-9 |
| Cartilages | 10 | 0.4 | 1.26765E-9 |
| Menisci | 59 | 0.49 | 1.10231E-9 |
| Viscoelastic Properties for Meniscus | Relaxation Moduli (MPa): 7.2, 15.0 | Relaxation Time (s): 7.2, 49.9 | |
| Neo-Hookean Properties for Cartilages | Initial Shear Modulus (MPa): 6.8 | Incompressibility parameter (Pa-1): 1E-06 | |

The knee model obtained from (Chandran, 2021) based on a CT scan of a 24-years old woman was assembled in SolidWorks to simulate optimal and suboptimal driving positions with thigh to shinbone angles of 119° and 131° respectively.

A constant compressive force of 20N and a cyclic compressive force ranging from 0 to 20N simulate pedal forces during driving. For realism, the model has fixed hip support and Earth gravity. Young's modulus, Poisson's ratio, and density of bones, cartilage, and menisci are described. Cartilage uses neo-hookean hyperelastic parameters, while the menisci use relaxation moduli and times for viscoelasticity.

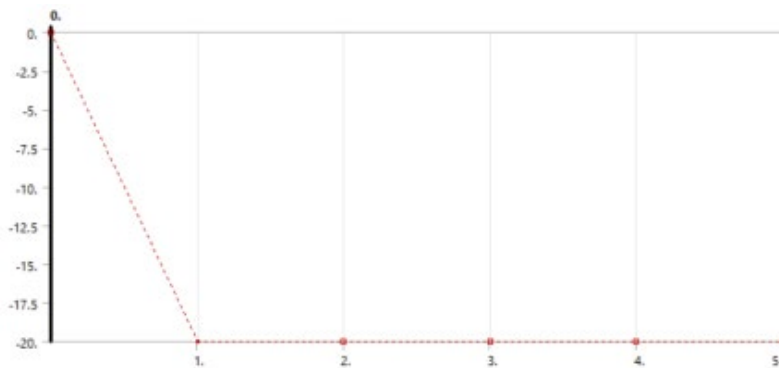


Figure 1. Constant force applied (20N)

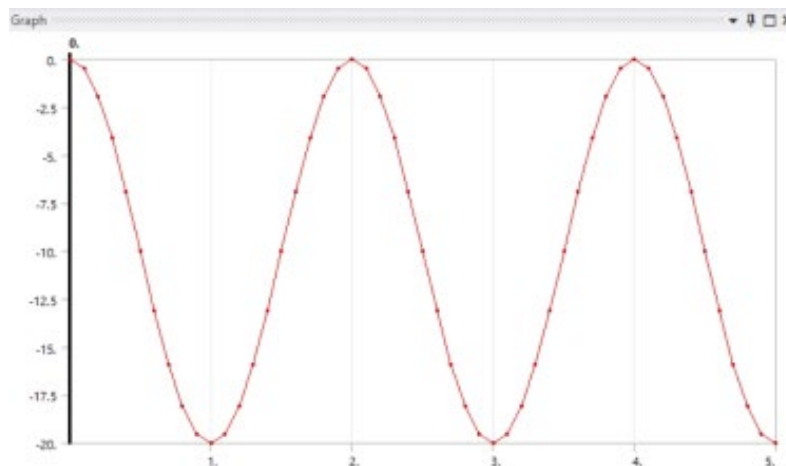


Figure 2. Cyclic force applied (0 to 20N).

3. RESULTS AND DISCUSSION

Comparison of constant and cyclic forces showed significant knee joint stress differences. The optimal knee position had an average meniscus stress of 147.790 KPa under constant force, compared to 376.890 KPa in the suboptimal position. During cyclic loading, the optimal position had a lower average meniscus stress of 174.690 KPa than the suboptimal position of 439.230 KPa.

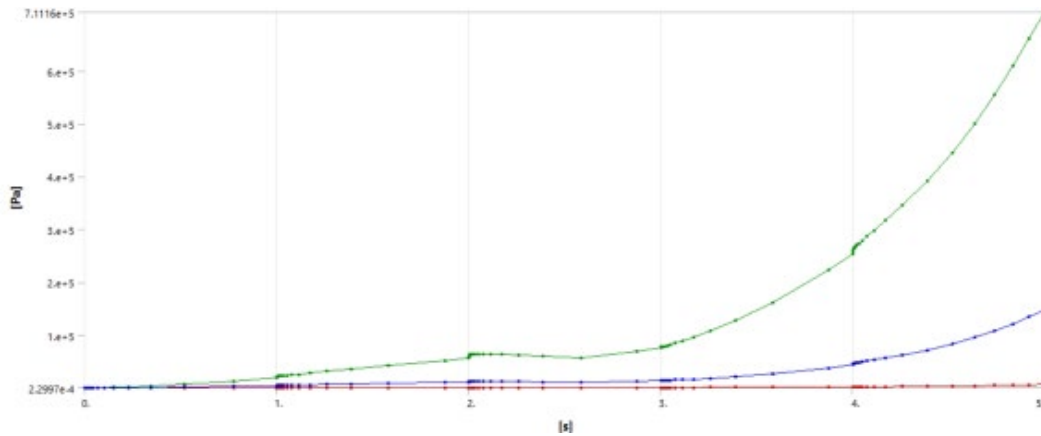


Figure 3. Stress on menisci, constant force, nonlinear.

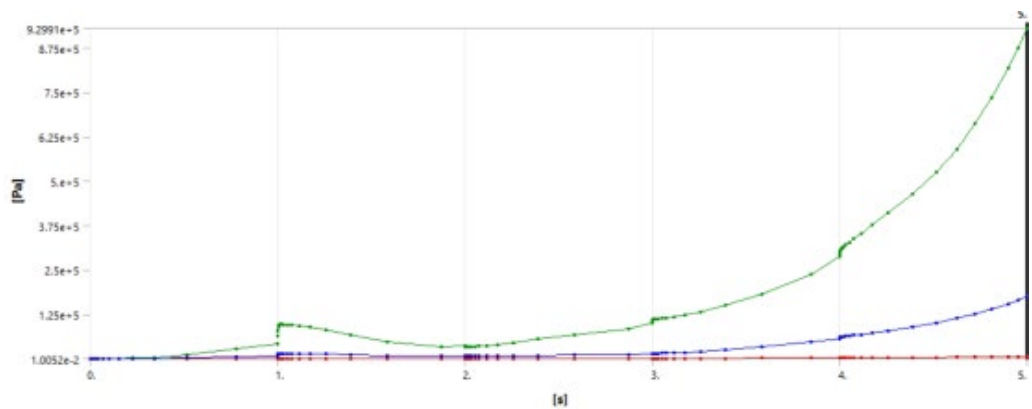


Figure 4. Stress on menisci, cyclic force, nonlinear.

Unlike constant force, cyclic loading in the nonlinear simulation deformed the meniscus more than the bottom of the femur.

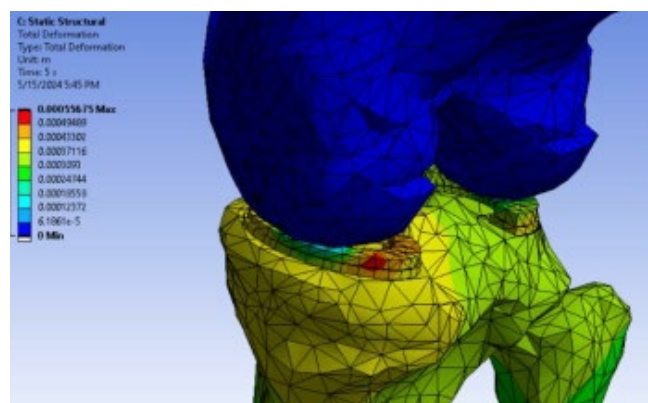


Figure 5. Deformation in good position, cyclic force with nonlinear simulation

The good driving position consistently had lower knee stress than the bad driving position under constant force. In the good position, articular cartilage had an average stress 1.557 KPa, compared to 28.381 KPa in the bad position. The good position's tibial cartilage had an average stress of 60.843 KPa, while the bad position had 479.870 KPa. In cyclic loading, the good driving position had lower knee component stress than the bad position. The good driving position reduced meniscus stress significantly, demonstrating the importance of proper alignment in knee joint stress reduction.

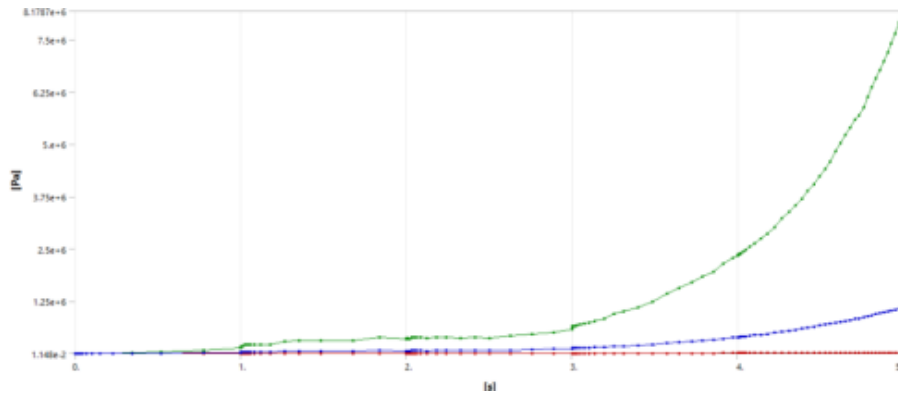


Figure 6. Stress on menisci, const. force, bad position

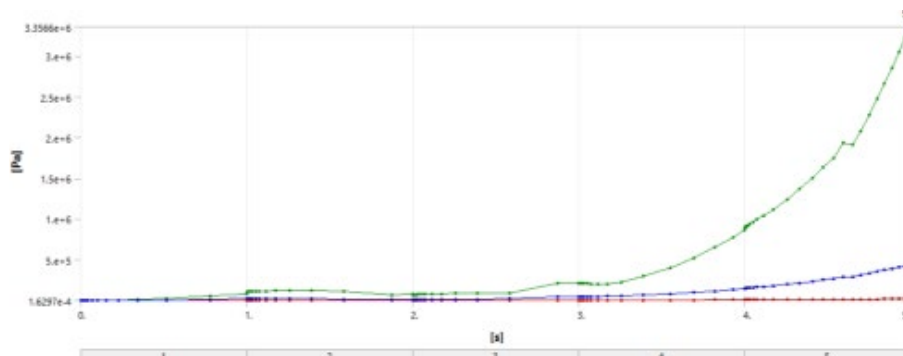


Figure 7. Stress on menisci, cyclic force, bad position

Comparing linear and non-linear simulations revealed how material properties affect stress distribution. Non-linear simulations produced higher stress concentrations than linear simulations in constant and cyclic force scenarios. In the constant force condition, the non-linear model had 174.690 KPa meniscus stress, compared to 18.625 KPa in the linear model. Tibial cartilage had an average stress of 75.316 KPa in the non-linear model and 5.5586 KPa in the linear model.

In addition, the non-linear simulation showed articular cartilage stress of 1.4467 KPa, while the linear model showed 0.6994 KPa. Viscoelastic properties are needed to accurately represent knee joint biomechanics, especially under dynamic loading conditions.

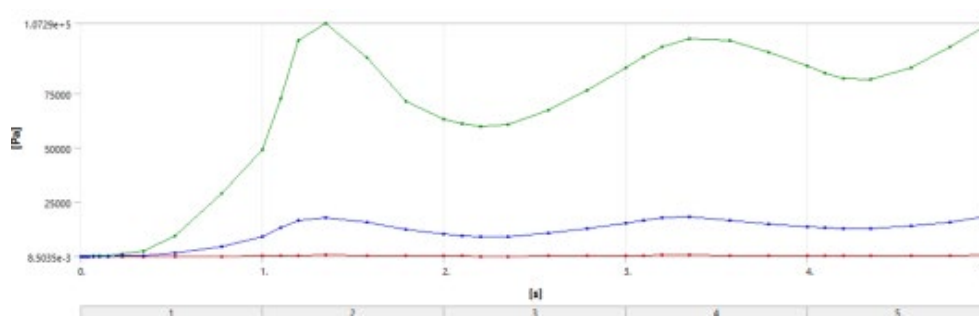


Figure 8. Stress on menisci, cyclic force, linear.

4. CONCLUSION

The study aimed to compare viscoelastic and hyperelastic material properties to linear elastic properties to determine how stress affects the knee joint under various driving conditions. Driving posture significantly affects knee joint stress, with improper alignment increasing stress in all knee components in both loading scenarios as resulted from the simulations. The nonlinear model consistently had higher stress than the linear model. Previous research has shown that soft tissues are viscoelastic and hyper elastic, requiring nonlinear simulations for future research. Thus, simulations with nonlinear material properties better represent knee biomechanics.

In addition, Viscoelastic simulations showed that the meniscus deformed most under cyclic loading, unlike linear models. To improve simulations and investigate how demographic factors affect knee joint stress, future research could focus on model improvements, muscle inclusion, advanced viscoelastic modeling, and experimental validation to further enhance the reliability of the results.

REFERENCES

- Brown, C., et al. (2021). "Knee Joint Function in Athletes." *International Journal of Sports Science*, 15(2), 123-136.
- Chandran, A. S., Trivedi, R., Modi, B., & Patel, R. (2021). Estimation of stress and strain of knee joint using finite element analysis. *Journal of Physics: Conference Series*, 2070(1), 012217. <https://doi.org/10.1088/1742-6596/2070/1/012217>
- Robinson, D. (2018). "The Impact of Sedentary Work on Knee Health." *Occupational Health Journal*, 30(4), 312-325.

Pressure Loss and Heat Transfer Analysis of Drag Reducing Additives

Aayez Ahmad Virk ^a and Kazi Md Salim Newaz ^{b*}

Department of Mechanical Engineering,
Faculty of Engineering, Universiti Malaya,
50603, Kuala Lumpur, Malaysia

Email: ^a aayezahmad@yahoo.com, ^b salimnewaz@um.edu.my

*Corresponding author

ABSTRACT

Biopolymers and surfactants can drastically change water flow in closed loop piping systems; thus, scientists are interested in using small quantities to induce improvements. Due to cost reductions and lower investment requirements, the food, pharmaceutical, petroleum, and agricultural industries use such additives as drag reduction agents. Concentration, salinity, and polarity of additives can disrupt turbulent flow in closed pipes. Since they are biodegradable and environmentally friendly, soluble polymers and surfactants are becoming more popular. Gum Arabic and cetyltrimethylammonium bromide were tested to minimize drag. Pressure drop, friction loss, drag reduction percentage, and heat transfer rate affect experimental outcomes. Cetyltrimethylammonium bromide and gum Arabic concentrations of 50, 100, 200, and 250 ppm and 0.5:0.5 hybrid solutions were used to obtain data. Using a certain concentration in the test rig will significantly reduce fluid pressure in the piping system. The pressure drops are summarized. However, heat transfer to additive-influenced water solutions will be assessed to determine heat loss or gain.

Keywords: Drag reduction; Surfactants; Biopolymers; Heat transfer; Pressure drop

1. INTRODUCTION

Normally pipelines are used to carry fluids in slurry, crude oil, refined petroleum, cooling, heating, agriculture industry and etc. Researchers investigate biopolymers and surfactants to reduce pipeline pressure drop and enhance heat transfer. High Reynold's number, Darcy friction factor, and pressure drop characterizes these adoptions. Pressure loss has been addressed in several ways. Pumping liquids with a stronger pump is a suitable example which is impractical due to its high cost. Polymers and surfactants of low concentrations minimize fluid turbulence friction [1]. Thus, drag-reducing agents reduce energy waste and fluid flow friction. Their cost effectiveness and drag reduction ability have made them attractive in the chemical industry. This research uses a surfactant as well as a biopolymer to reduce closed pipe flow drag and enhance heat transfer throughout the fluid flow. Drag reducers are thick, viscous, and viscoelastic like old honey. As hydrocarbon chains, pipeline and oil DRAs shouldn't affect refining procedures or products. DRA solvents are viscoelastic, time independent, shear degradable, and non-Newtonian [2]. In 1949, Toms introduced this approach. He found that polymers tend to lower fluid resistance in low-viscosity materials. Researchers have further worked on and researched on additives in search of drag loss mitigation [3].

2. METHODOLOGY

This section summarizes the methodology as well as the techniques used for conducting the experimental runs for coming up with the results.

2.1 Additive Concentrations Used

The additives used (CTAB and GA) are prepared at concentrations of 50, 100, 200 and 250 ppm. The experiment is run strictly at fluid inlet temperatures of 30°C.

2.2 Experimental Setup and Sample

Preparation

The components of the test rig are: Chiller, 100L tank, agitator motor, pump, inverter, magnetic flow transmitter, magnetic flow tube, pressure transducer, data logger and piping and insulation.

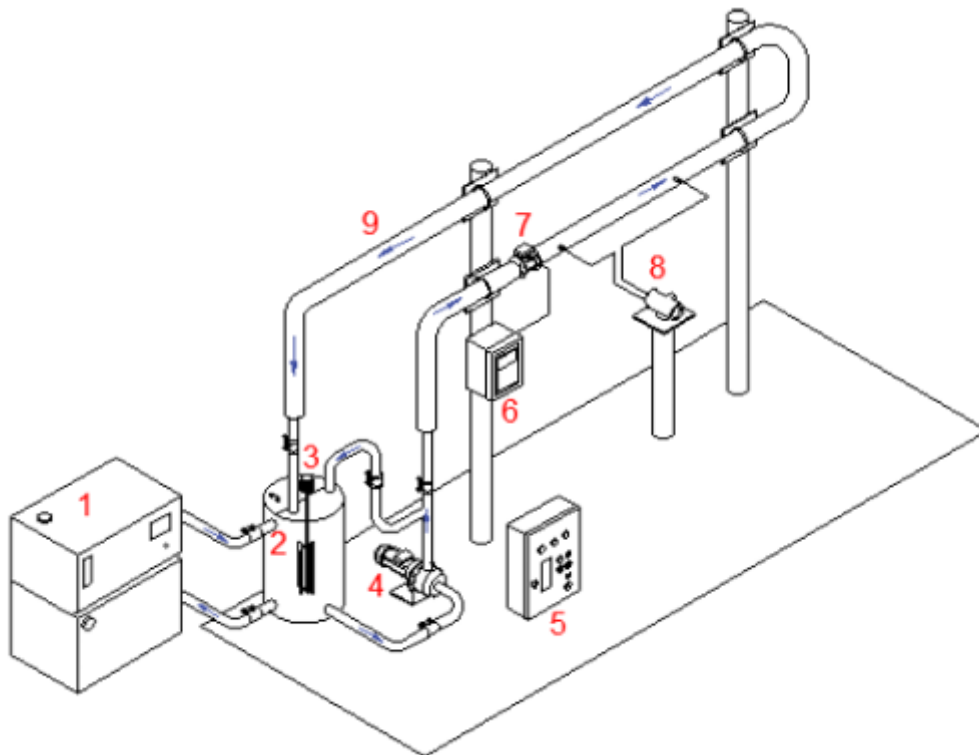


Figure 1. Isometric model of the Test rig

The sample is first weighed in the boat, added to the beaker and allowed to stir thoroughly for almost 15 minutes. Next, it is added to the 100L tank connected to the rig which is topped up with distilled water. The mixture is then allowed to agitate for another 2 hours in the tank. Lastly, the mixture is allowed to rest for 12 hours in order to achieve complete solubility and micellization of the additives before starting the experimental run. This process is repeated for every sample concentration. The mass conversion is done using the following equation:

$$1 \text{ ppm} = \frac{0.000998859 \text{ g}}{1L} \cdot 100 L = 0.0998859 \text{ g}$$



Figure 2. Sample preparation and addition

2.3 Thermophysical properties

The thermophysical properties of the samples such as the density, viscosities as well as the thermal conductivities are obtained using the viscometer and TPA respectively.

3. RESULTS AND DISCUSSION

This section includes results from the pressure drop and heat transfer coefficient of the samples under study. It was found that CTAB had the best drag reducing ability and GA has the best heat transfer ability. This is shown in the results plotted in the section.

3.1 CTAB Drag Reducibility

CTAB concentrations of 50, 100, 200 and 250 ppm prove to have excellent reduction in drag which accounts for: 3.88%, 4.03%, 14.93% and 26.89%. Higher concentrations tend to be better at reducing drag.

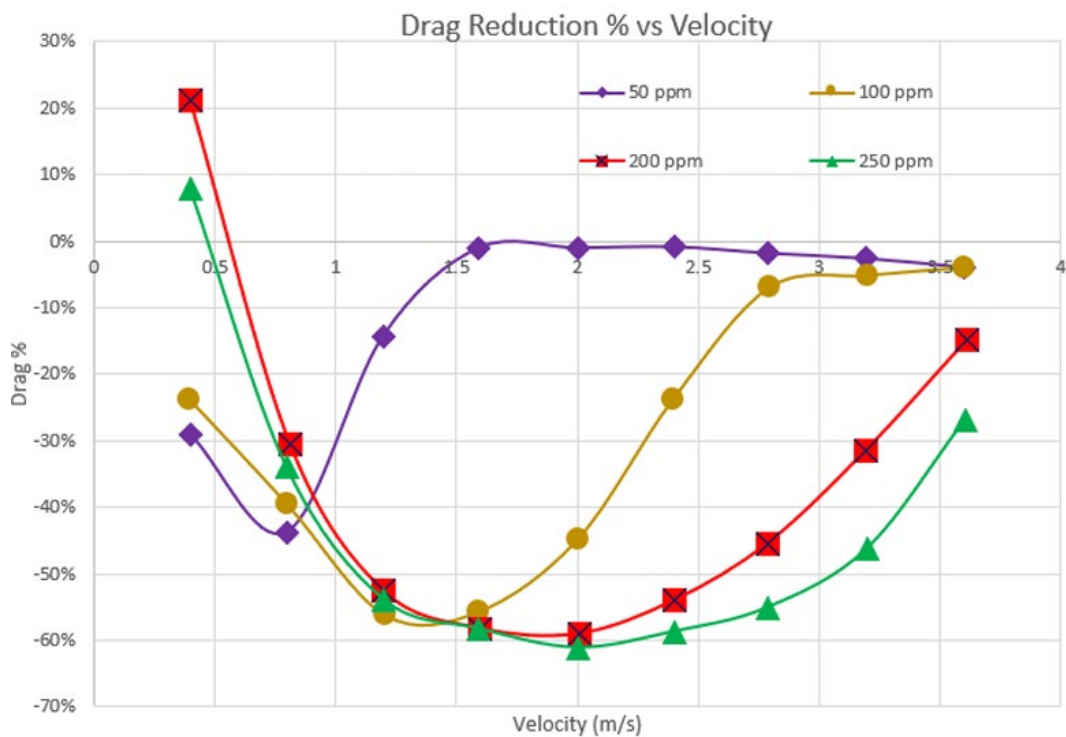


Figure 3. Drag Reduction % vs Velocity for CTAB

3.2 GA Heat Transferability

GA concentrations of 50, 100, 200 and 250 ppm prove to have excellent heat transfer rates which accounts for an increase compared to water by: 12.31%, 19.01%, 25.6% and 26.8%. Overall, we can say that higher concentrations of the biopolymer tend to be better at reducing drag.

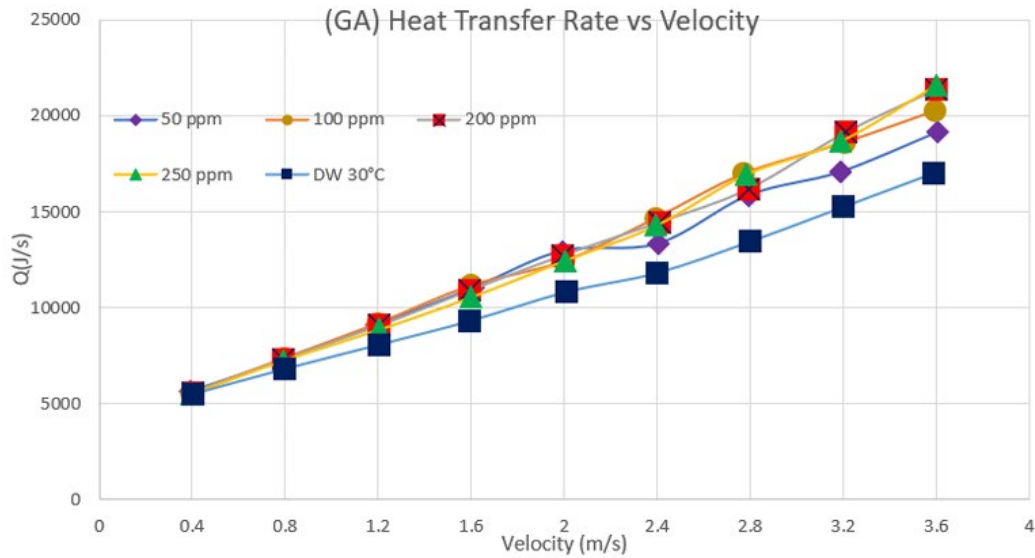


Figure 4. Heat Transfer Rate vs Velocity for GA

3.3 Hybrid Solution

Hybrid solution concentrations of 50, 100, 200 and 250 ppm prove to have excellent heat transfer rates which accounts for an increase compared to water by: 5.07%, 16.41%, 28.46% and 33.81%. Higher concentrations tend to be better at reducing drag.

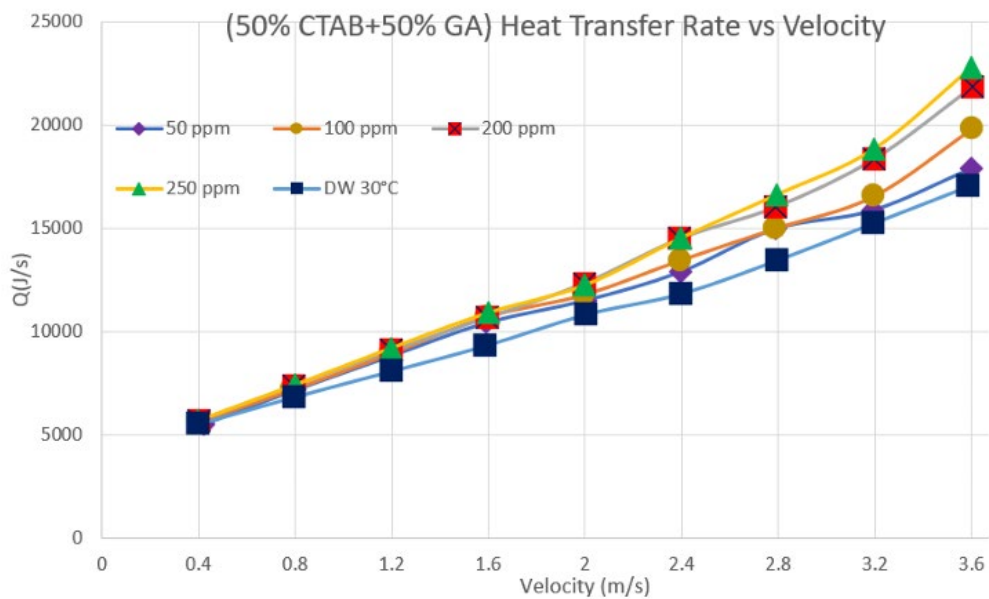


Figure 5. Heat Transfer Rate vs Velocity for (0.5 CTAB:0.5 GA

The hybrid additive concentrations of 50, 100, 200 and 250 ppm don't have very satisfying drag reduction properties. However, they do tend to have excellent heat transfer rates when compared to distilled water. The drag is seen to increase by 4.64%, 5.96% 3.22% and 2.23% respectively at 3.6 m/s in the case of the surfactant and biopolymer addition together.

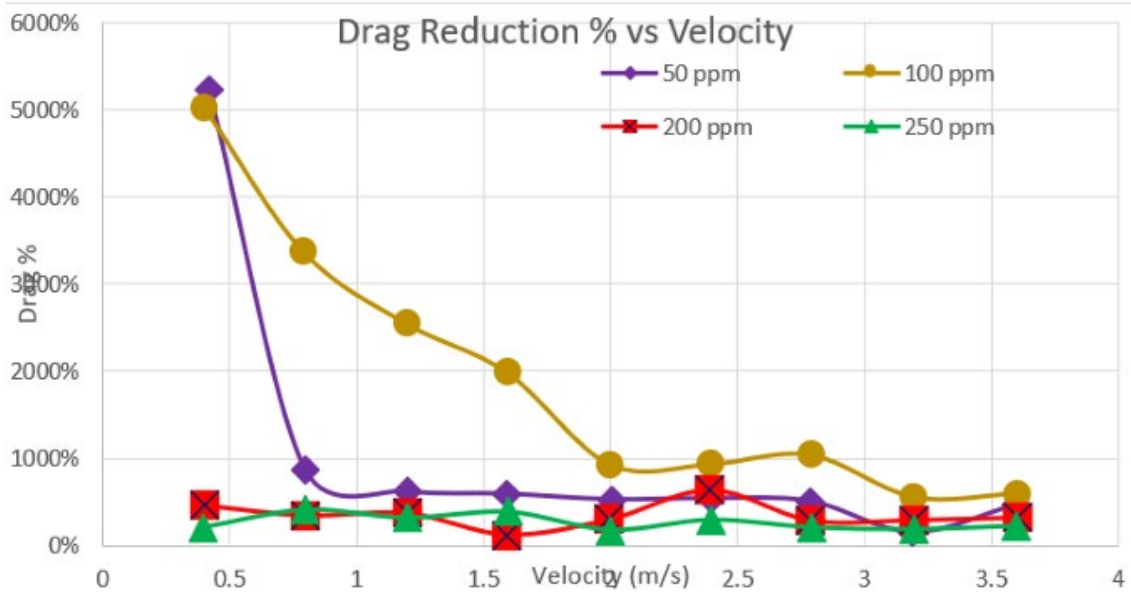


Figure 6. Drag Reduction vs Velocity for (0.5 CTAB:0.5 GA

4. CONCLUSION

Overall, lower amounts of pumping power are needed if CTAB is used as an additive. Almost 27% can be reduced for 250 ppm concentrations. However, the hybrid solution and gum Arabic biopolymer can help increase heat transfer rates by almost 34% and 27% respectively. This trend can be observed throughout an increase in additive concentration as well as an increase in fluid velocities.

REFERENCES

- [1] Hadri, F., Guillou, S. J. I. J. o. E. S., & Technology. (2010). Drag reduction by surfactant in closed turbulent flow. 2, 6876-6879.
- [2] Lester, C. J. O., & Journal, G. (1985). Drag reduction agents. 4, 51-56.
- [3] Toms, B. A. (1949). Some observations on the flow of linear polymer solutions through straight tubes at large Reynolds numbers. Paper presented at the Proc. 1st Intl Congr. Rheol

Application of Carbon Structured Nanofluids from Biomass for the Enhanced Performance of Flat Plate Solar Thermal Collector

Mifzal bin Salihin ^a and Kazi Md. Salim Newaz ^{b*}

Department of Mechanical Engineering,
Faculty of Engineering, Universiti Malaya,
50603, Kuala Lumpur, Malaysia

Email: ^a mifzal.salihin@gmail.com, ^b salimnewaz@um.edu.my

*Corresponding author

ABSTRACT

Conventional working fluids used in liquid flat plate solar thermal collector (FPSC) have low thermal performance and their synthesis often release harmful gases posing health and environmental risk. This study proposes a green alternative, Green Activated Carbon nanofluid derived from biomass, where activated carbon nanoparticles are dispersed in distilled water using the two-step method. The structural, thermophysical and thermal energy efficiency of FPSC using Activated Carbon – Distilled Water (AC/DW) nanofluid were examined and compared relative to distilled water. The test were conducted with AC/DW at weight concentrations of 0.05 wt.%, 0.10 wt.% and 0.15 wt.%, different flow rates 0.559 L/min, 0.84 L/min, 1.1 L/min and 1.4 L/min, heat flux intensities 700 W/m, 800 W/m, 900 W/m, 1000 W/m and inlet temperature of 30 °C, 35°C, 40°C and 45°C. Results showed a 9% increase in thermal conductivity of the AC/DW compared to distilled water at 30°C. The energy efficiency improvements for the FPSC relative to distilled water are 10.85%, 19.01% and 27.43% for 0.05 wt.%, 0.1 wt.% and 0.15 wt.% of AC/DW at flow rate of 1.4 L/min respectively. The max FPSC area reduction of 28.5% was accomplished at 0.1 wt.% at flow rate 1.1 L/min.

Keywords: Green Activated Carbon; Nanofluid; Solar Thermal Collector; Thermal Efficiency; Biomass

1. INTRODUCTION

The FPSC is vital for harnessing solar energy, transferring heat to working fluids for applications like heating and drying. Conventional working fluids like water and ethylene glycol have low thermal conductivity, limiting FPSC efficiency. Therefore, nanofluids, created by dispersion of nanoparticles in base fluid have been developed to improve thermal conductivity of fluid. These nanofluids can enhance the performance to up to 20-30% [1] showing significant improvement to the thermal performance of FPSC. However, the common nanofluid synthesis often uses hazardous chemicals, posing environmental and health risks[2]. The current work focuses on biomass derived carbon nanofluids which explored AC/DW nanofluids to improve FPSC efficiency and reduce solar collector area without environmental and health hazards, addressing a gap in current studies.

2. METHODOLOGY

2.1 Preparation of nanofluid

Activated carbon nanoparticles were produced from coconut husk by drying and pyrolyzing it in a nitrogen environment, then crushing the charcoal in a ball mill. The AC/DW nanofluid was prepared using the two-step method: combining activated carbon nanoparticles with distilled water, stirring, and ultrasonication at 75kHz for 1 hour. Nanofluids with concentrations of 0.05 wt.%, 0.1 wt.%, and 0.15 wt.% were prepared.

2.2 Experimental Setup

2.2.1 Characterization of thermophysical properties

Thermal conductivity was measured using a KD2 Pro analyzer, while density and viscosity were obtained with an Anton Paar rheometer. AC/DW at 0.05wt.%, 0.10wt.%, and 0.15wt.% were tested between 20 °C and 40 °C .

2.2.2 Thermal performance of FPSC

The heat flux intensity, flow rate, inlet temperature varies using the variable transformer, flow control valve, industrial chiller respectively. The inlet and outlet temperature are monitored by the data logger.

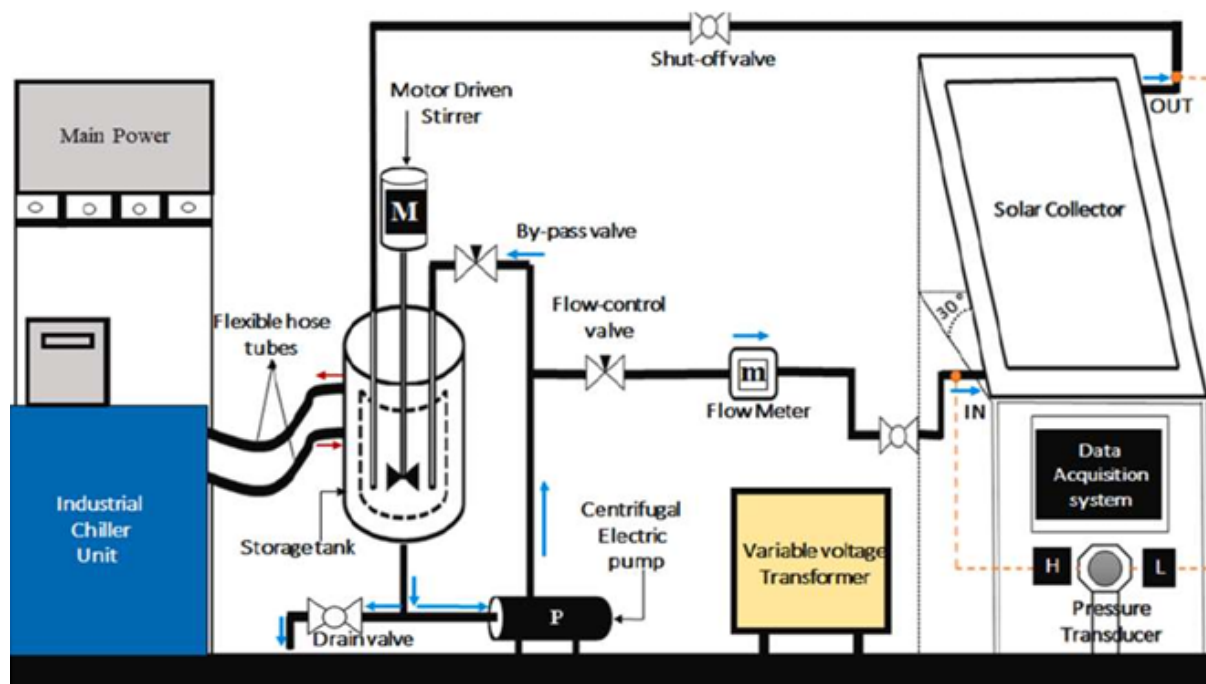


Figure 1. FPSC test rig

2.3 Mathematical Equations for efficiency calculations

To calculate efficiency, η the useful gain, Q area, A and solar irradiation, G needs to be computed.

$$Qu = \dot{m}Cp(T_{in} - T_{out}) \quad (1)$$

$$G = \frac{VI}{A} \quad (2)$$

$$\eta = \frac{Qu}{AG} \quad (3)$$

$$\text{Reduced temperature} = \frac{T_{in} - T_{ambient}}{G} \quad (4)$$

Cp specific heat capacity of nanofluid, T outlet temperature, T inlet temperature, V voltage of heater, I current of heater, A area of the panel.

$$(\rho Cp)_{nf} = (\rho Cp)_{nf}(\varphi) + (\rho Cp)_{bf}(1 - \varphi) \quad (5)$$

Specific heat capacity, c density, ρ and the concentration of nanoparticle, φ

$$Arc = \frac{\dot{m}cp(T_{out} - T_{ambient})}{G\eta} \quad (6)$$

3. RESULTS AND DISCUSSION

3.1 Thermal property of AC/DW nanofluid

Table 1. Thermophysical property of AC/DW vs. DW

| Aspects | DW | 0.05 wt. % | 0.10 wt. % | 0.15 wt. % |
|---|---------|------------|------------|------------|
| k (W/m. K) | 0.614 | 0.635 | 0.642 | 0.670 |
| Cp (J/g. K) | 4.1798 | 4.1941 | 4.1784 | 4.1779 |
| ρ (kg/m³) | 995.65 | 995.66 | 995.97 | 996.1 |
| μ (mPa. s) | 0.81742 | 0.82104 | 0.82467 | 0.83488 |
| V (mm²/s) | 0.82171 | 0.82719 | 0.82791 | 0.83826 |

3.2 Thermal performance of AC/DW nanofluid relative to distilled water

The thermal enhancement of AC/DW relative to distilled water ranges from 7.21% to 27.4% with 0.15 wt.% at different flow rates.

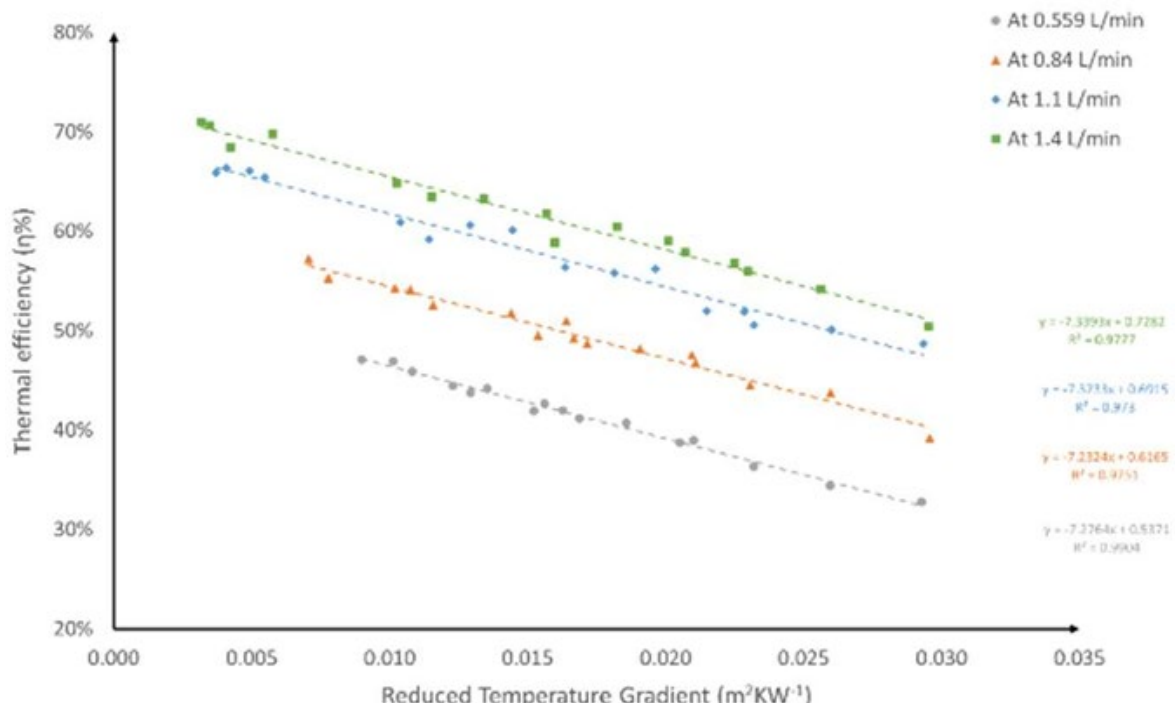


Figure 2. η vs. reduced temperature at 0.15wt.%

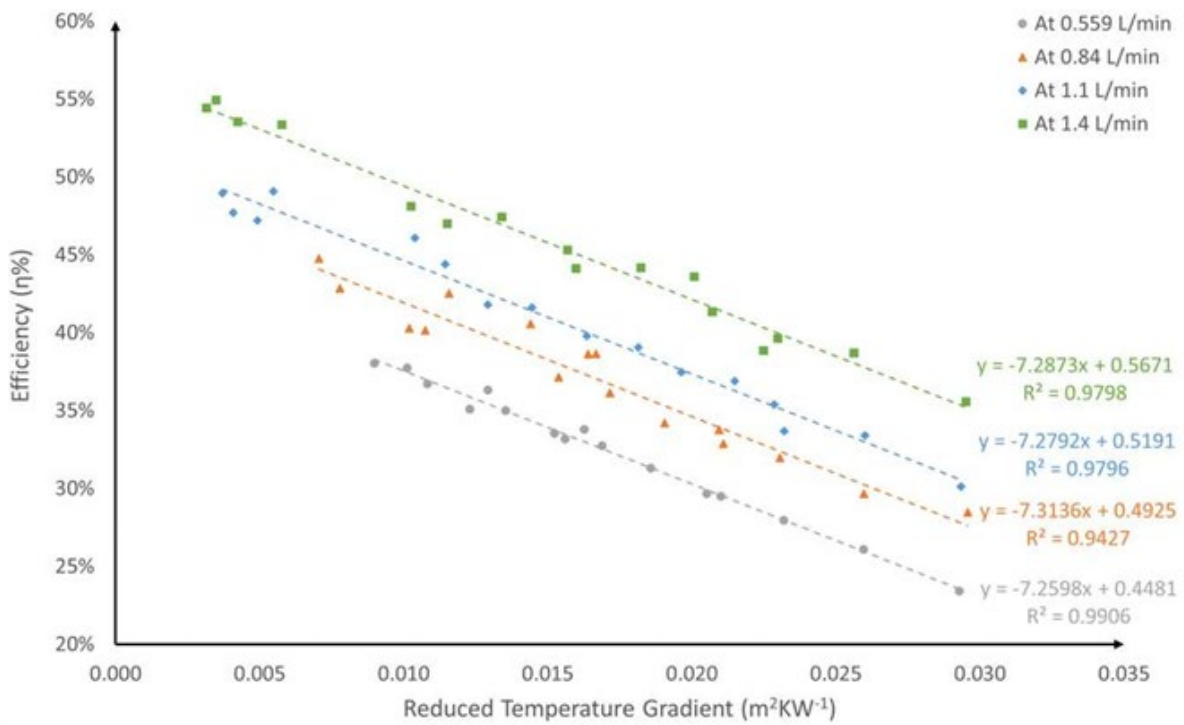


Figure 3. η vs. reduced temperature gradient of water

3.3 FPSC Area Reduction

The range of FPSC area reduction is from 5.26% to 28.5% respectively with a peak at 1.1 L/min at 0.1 wt.%.

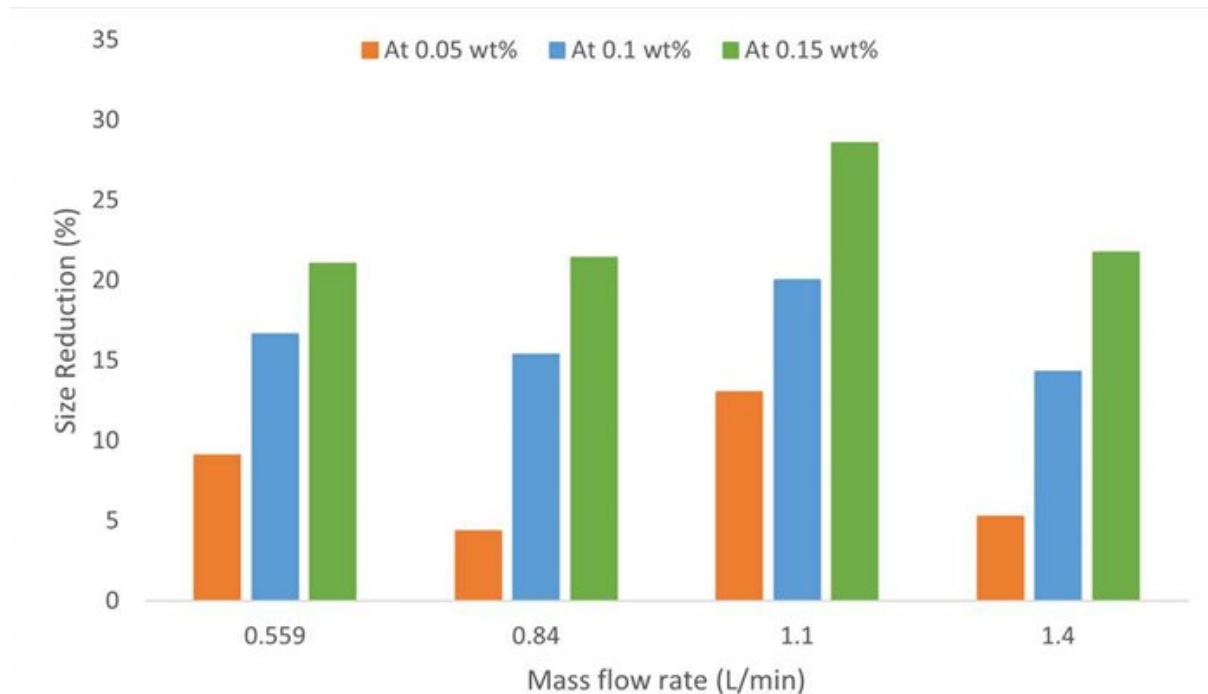


Figure 4. Size reduction against mass flow rate

4. CONCLUSION

Activated carbon nanofluids (0.05 wt.%, 0.10 wt.%, 0.15 wt.%) enhance FPSC efficiency. At 1.1 L/min, thermal improvement is 27.43% for 0.15 wt.%. At 1.4 L/min, performance boosts to 72.82%. The greatest FPSC area reduction, 28.5%, is with 0.15 wt.% AC/DW at 1.1 L/min.

REFERENCES

- [1] M. Amar et al., “Energy, exergy and economic (3E) analysis of flat-plate solar collector using novel environmentally friendly nanofluid,” *Sci Rep*, vol. 13, no. 1, Dec. 2023, doi: 10.1038/s41598-023 27491-w.
- [2] M. A. Alfellag et al., “Green synthesized clove-treated carbon nanotubes/titanium dioxide hybrid nanofluids for enhancing flat-plate solar collector performance,” *Appl Therm Eng*, vol. 246, Jun. 2024, doi: 10.1016/j.applthermaleng.2024.122982.

Investigation of a Thermoelectric Cooling System Utilising Multichannel Duct Nozzle

Muhammad Faisal bin Abdul Muis^a and Mohd Faizul bin Mohd Sabri^{b*}

Department of Mechanical Engineering,
Faculty of Engineering, Universiti Malaya,
50603, Kuala Lumpur, Malaysia

Email: ^a faisalmuis80@gmail.com, ^b faizul@um.edu.my

*Corresponding author

ABSTRACT

This study aimed to enhance the cooling performance of thermoelectric systems by using optimized duct nozzle designs. Thermoelectric cooling, efficient for small-scale uses, struggles with energy consumption and efficiency when scaled up. To tackle this, the research tested two 3D-printed duct nozzles: a conventional hollow duct and an innovative multichannel duct, both made from PLA filament using CAD models. The experimental setup included a Peltier module between two aluminium heat sinks, fans, and temperature sensors within an insulated enclosure. Cooling performance was assessed under three conditions: no nozzle, hollow nozzle, and multichannel nozzle, over a 60-minute period. Results showed the multichannel nozzle improved air cooling by 21.9%, outperforming the hollow nozzle's 8.4% improvement, due to better airflow distribution.

Keywords: Cooling efficiency; Duct nozzle; Multichannel duct; Thermoelectric cooling; Thermoelectric systems

1. INTRODUCTION

In today's world, efficient thermal management and energy conservation are critical. Nozzles and ducts, which guide and control fluid flow, are essential in addressing the challenges of rising energy consumption and environmental concerns. Industries demand better energy efficiency and effective thermal management to reduce carbon footprints and prevent overheating in various applications. Conventional duct nozzles often suffer from low cooling performance and high power consumption, leading to inefficiencies. By optimizing nozzle and duct designs, it's possible to enhance airflow distribution, improve cooling performance, and reduce energy use. This research focuses on developing advanced duct nozzle configurations, such as multichannel designs, to achieve better cooling efficiency in thermoelectric systems. These improvements aim to meet the contemporary needs for sustainable and energy-efficient solutions in industrial and technological applications.

2. METHODOLOGY

2.1 3D Printing Duct Nozzles

The design process began with creating two duct nozzles using SolidWorks: a hollow duct nozzle with a streamlined shape and a multichannel duct nozzle with multiple internal channels to optimize airflow. Both designs included features for mounting to the heat sink and fan. These models were then imported into FlashPrint slicing software, with PLA filament settings adjusted to ensure proper printing conditions. The G-code generated by the slicing software was used for printing on a Flashforge 3D printer. The printing process involved loading the PLA filament, preheating the extruder and bed, and closely monitoring the initial layers for proper adhesion. After printing, the duct nozzles were carefully removed, and any support structures were cleared.

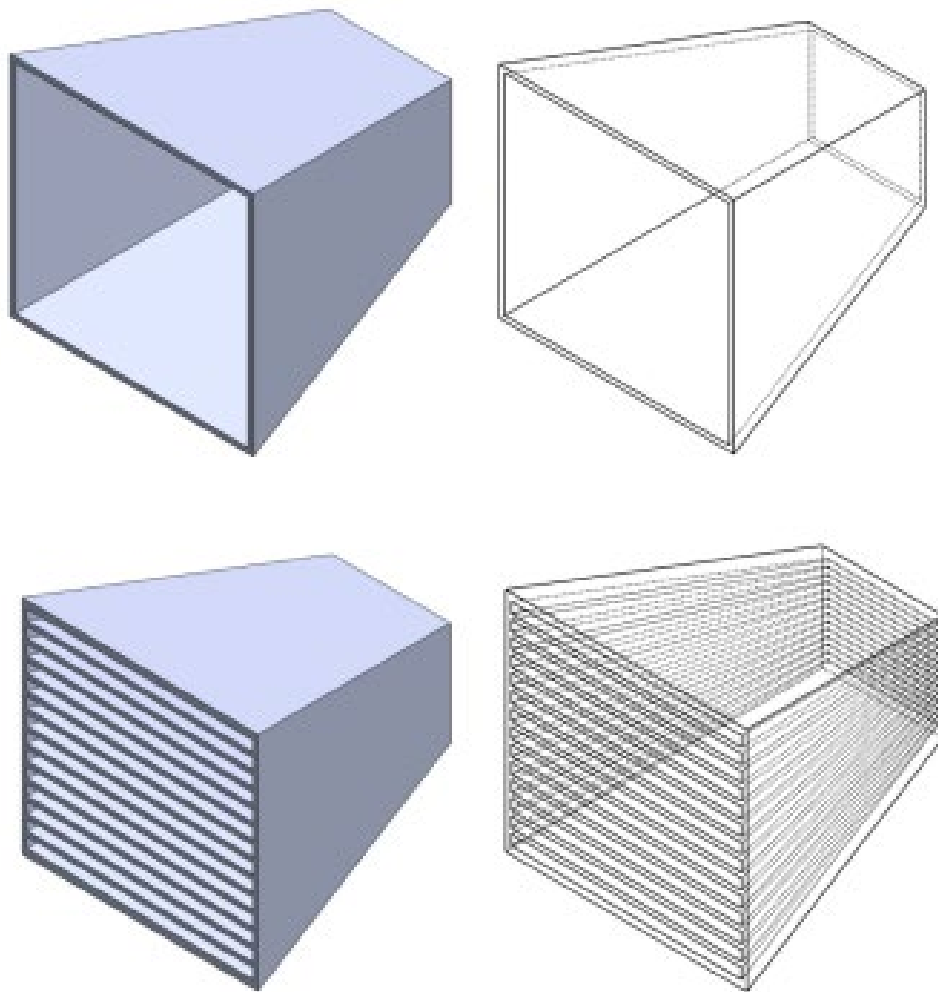


Figure 1. 3D Model of hollow and multichannel duct nozzle

2.2 Experimental Setup

The experimental setup aimed to investigate temperature variation using a thermoelectric cooling system. A Peltier module was placed between two aluminium heat sinks to facilitate heat dissipation, with two fans enhancing air circulation. The setup was housed in a Styrofoam box for thermal

insulation, and an aluminium block was positioned as a reference point for temperature measurements. Temperature data were acquired using a data logger connected to three K-type thermocouples placed at strategic points. The procedure involved assembling the setup, configuring the data logger, and recording temperature readings at specified intervals. The experiment was repeated with both the hollow and multichannel duct nozzles to assess their cooling performance under consistent conditions.

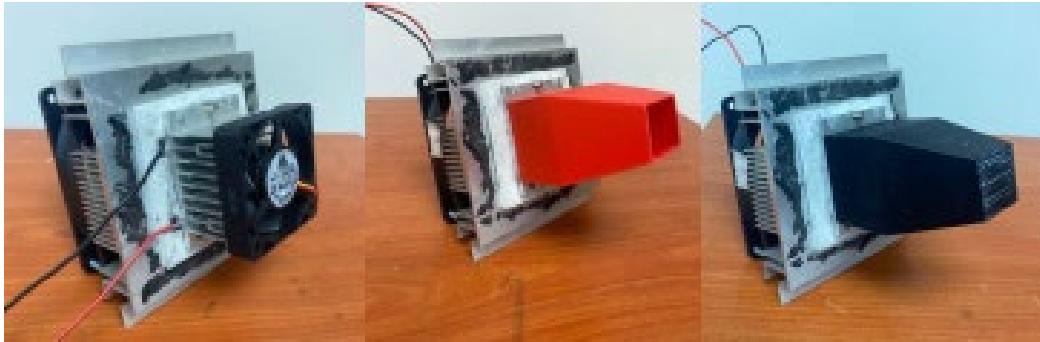


Figure 2. Thermoelectric cooling system without duct, with hollow duct and with multichannel duct

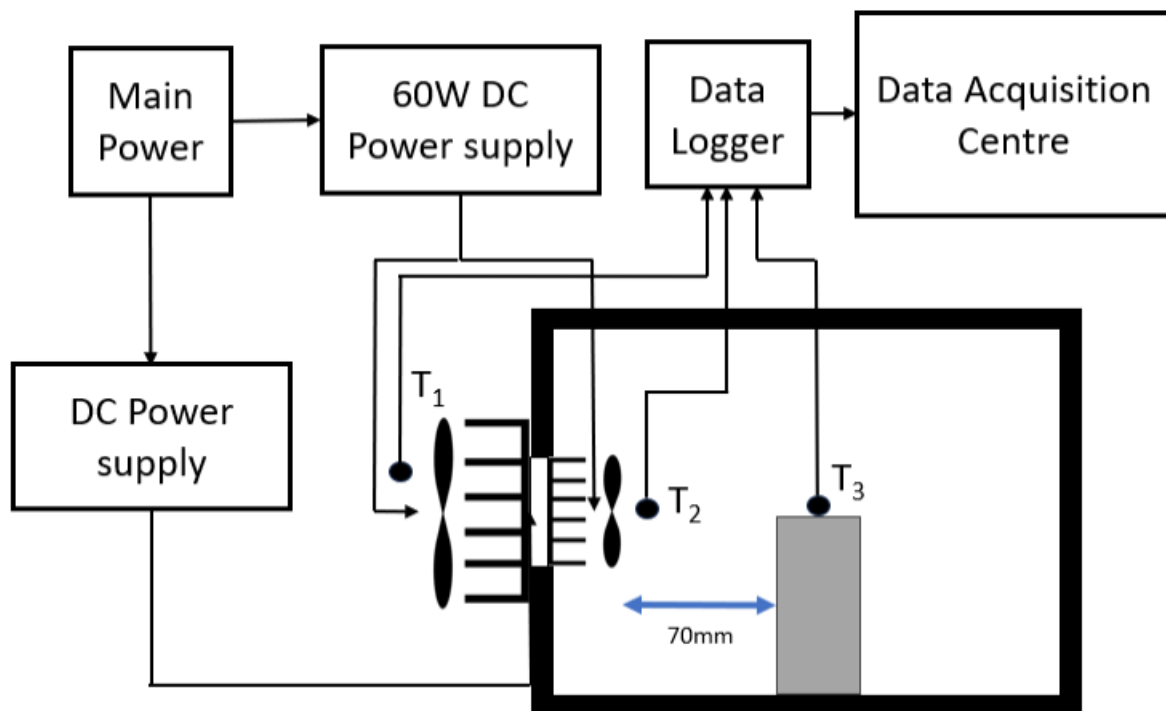


Figure 3. Experimental setup

3. RESULTS AND DISCUSSION

Based on the graph showing temperature cooling curves for different duct nozzle configurations, the multichannel duct nozzle exhibited the fastest cooling rate and achieved the lowest temperature among the three configurations tested, reaching approximately 13.17°C after 60 minutes. The hollow duct nozzle also showed improved cooling performance compared to the "no duct" case, reaching around 15.46°C at 60 minutes. In contrast, the configuration without a duct nozzle had the slowest cooling rate and remained at the highest temperature of approximately 16.87°C after 60 minutes.

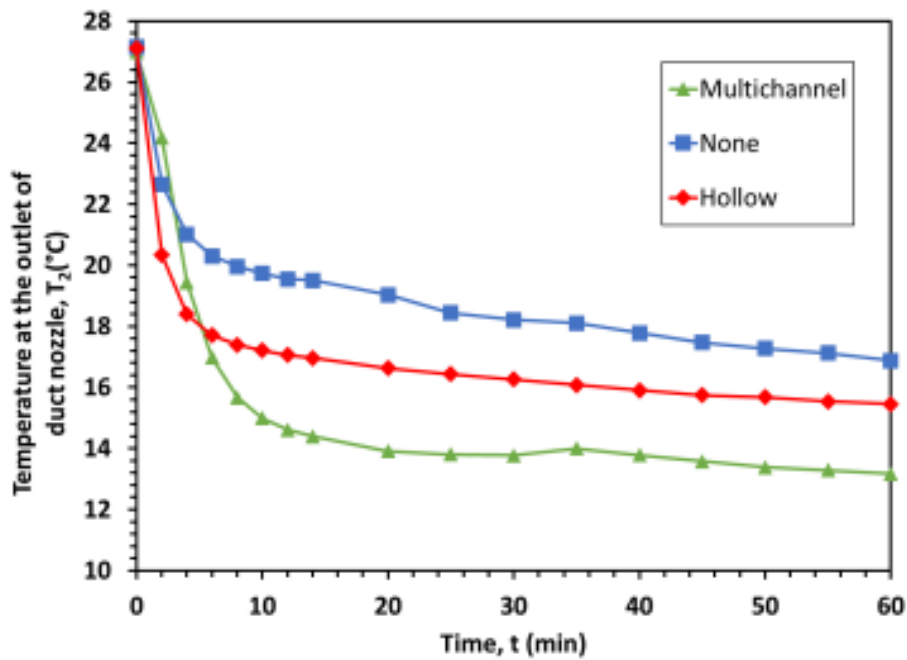


Figure 4. Graph of temperature at the nozzle outlet against time

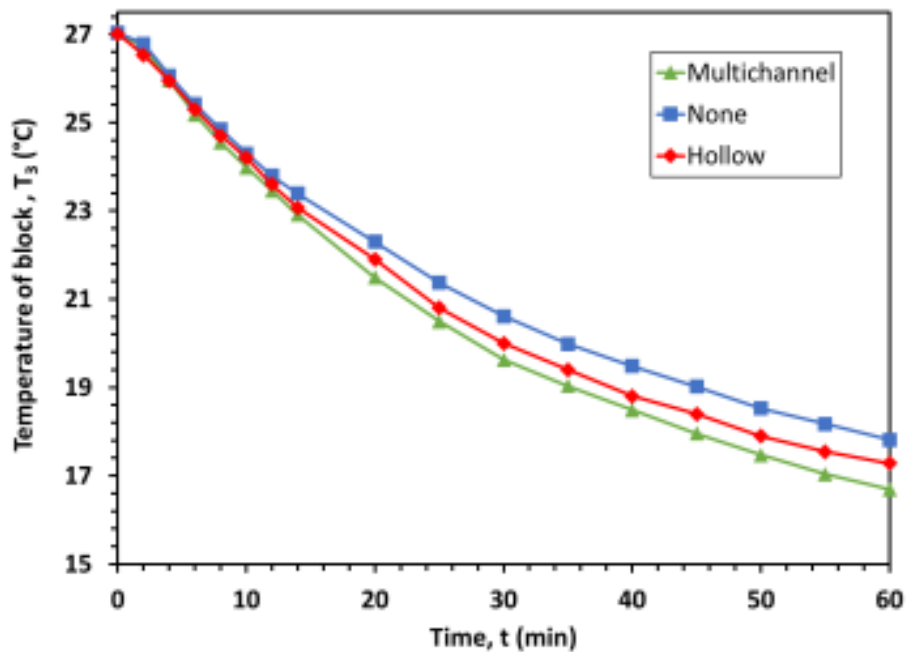


Figure 5. Graph of temperature of block against time

4. CONCLUSION

In conclusion, the research emphasizes the critical influence of duct nozzle design on cooling efficiency. The multichannel duct nozzle proved most effective, achieving a temperature of approximately 13.17°C after 60 minutes, marking a significant 21.9% improvement over the "no duct" scenario. This superiority is attributed to enhanced airflow distribution and increased surface area. While the hollow duct nozzle also improved cooling, reaching around 15.46°C (8.4%) after 60 minutes, its effectiveness was less than

the multichannel design due to a singular air channel. These findings highlight the importance of optimizing duct nozzle design for efficient cooling, with the multichannel approach showing promise for substantial temperature reduction.

REFERENCES

- [1] Chen, H., Sun, M., Xiong, D., Yang, Y., Wang, T., & Wang, H. (2023). Large eddy simulation of supersonic flow in ducts with complex cross-sections. *Theoretical and Applied Mechanics Letters*, 13(6). <https://doi.org/10.1016/j.taml.2023.100469>
- [2] Fukutani, K., & Shakouri, A. (2006). Design of bulk thermoelectric modules for integrated circuit thermal management. *IEEE Transactions on Components and Packaging Technologies*, 29(4), 750–757. <https://doi.org/10.1109/TCAPT.2006.885938>
- [3] Mishra, V. K., Panda, S. K., Sen, B., Maiya, M. P., & Rao, B. P. C. (2022). Performance of different duct-nozzle arrangement on heat removal from a nuclear fuel storage vault under regular operating conditions. *Nuclear Engineering and Design*, 395. <https://doi.org/10.1016/j.nucengdes.2022.111871>

Fire Simulation and Analysis of Mechanical Jet Fans Ventilation System in an Underground Car Park Using CFD

Nur Syahirah binti Abdul Rahman^a and Nik Nazri bin Nik Ghazali^{b*}

Department of Mechanical Engineering,
Faculty of Engineering, Universiti Malaya,
50603, Kuala Lumpur, Malaysia

Email: ^a nrsyahirahrahman@gmail.com, ^b nik_nazri@um.edu.my

*Corresponding author

ABSTRACT

This research uses Computational Fluid Dynamics (CFD) through the ANSYS software to analyze and optimize the jet fan ventilation system during a fire incident in an underground car park of 4777.58 m² area. The primary objective of this study is to analyze the current ventilation design, propose optimization ideas, and validate that the modified design improves the efficiency of ventilation and smoke dispersion. Two transient simulations were analyzed: a base case and a modified case, both simulating a virtual burning car. Key parameters for evaluating ventilation performance were temperature and airflow velocity distribution. Both cases reached a maximum temperature of 198.17°C. Modifications, including strategic jet fan placement and configuration, significantly improved ventilation by reducing hotspots and enhancing smoke clearance. The modified design showed less hot air coverage and resolved back-layering issues, efficiently directing hot air toward exits and facilitating safer evacuation routes. These findings validate the design modifications and highlight the importance of strategic ventilation planning for fire safety in underground car parks. This research provides valuable insights into optimizing ventilation systems using CFD, offering practical solutions with broad applicability.

Keywords: Computational Fluid Dynamics; Fire safety; Jet fans; Underground car park; Ventilation system

1. INTRODUCTION

A 2024 survey by [1] found that 73% of Malaysians own a car, increasing the demand for parking spaces. This leads developers to construct underground car parks due to limited land availability. Since these enclosed spaces require proper ventilation, especially in the event of a fire, traditional systems relying on costly, space-intensive ductwork [2] are being replaced by Impulse Ventilation Systems (IVS) with jet fans, which enhance airflow and remove contaminants more efficiently [3]. This system serves both daily and emergency fire ventilation [4]. Underground car parks pose significant fire risks, as synthetic materials in vehicles emit harmful gases during combustion, with temperatures often exceeding 815°C [5]. Fires also produce toxic gases like carbon monoxide (CO) [6]. The rise in electric vehicle (EV) usage further increases fire risk due to thermal runaway in lithium-ion batteries [7]. CFD aids in optimizing ventilation design by simulating airflow dynamics and evaluating various configurations, allowing precise calculations of fluid flow properties. fire safety, CFD assesses the efficacy of jet fan systems. This research leverages CFD to propose design improvements, offering practical solutions for enhanced fire safety for a specific underground car park design.

2. METHODOLOGY

2.1 Geometry Modelling in Ansys DesignModeler

An underground parking space of a residential building is chosen and modeled using ANSYS DesignModeler software.

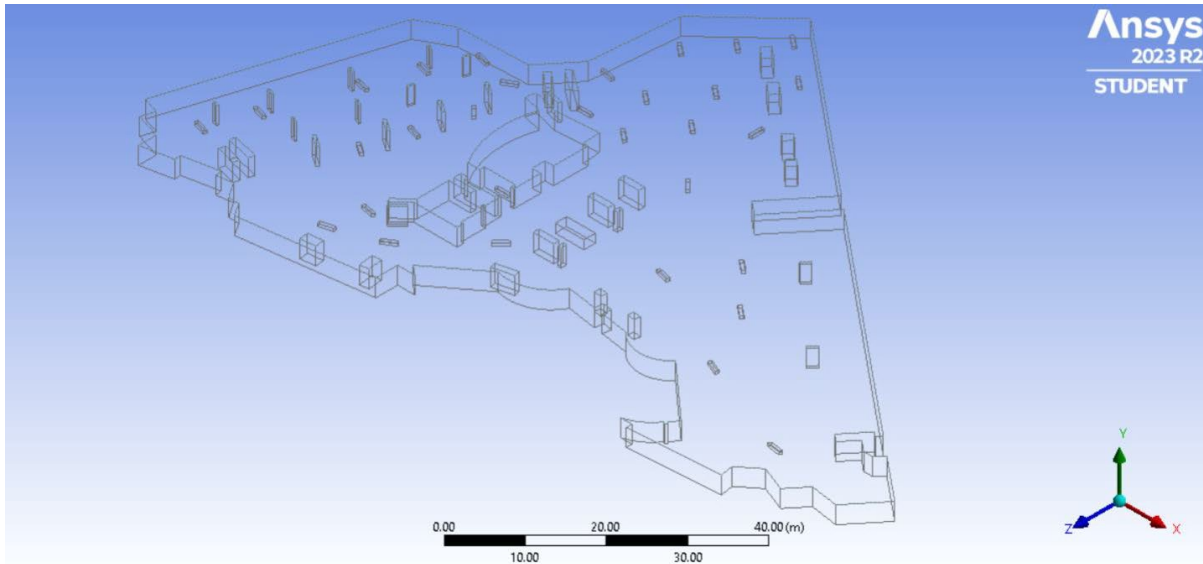


Fig. 1: 3D model of the base case design

2.2 Mesh Independence Study

Mesh resolution optimization was done by adjusting element sizes to create multiple resolutions, followed by conducting simulations. Key parameters are recorded and presented in Table 1.

Table 1. Meshing analysis

| Element size (m) | Number of elements | Maximum static temperature (°C) | Maximum airflow velocity |
|------------------|--------------------|---------------------------------|--------------------------|
| 0.2 | 576,158 | 198.17 | 40.39 |
| 0.25 | 355,613 | 193.98 | 37.65 |
| 0.3 | 257,550 | 187.01 | 37.06 |
| 0.5 | 86,106 | 187 | 31.97 |
| 1.0 | 27,026 | 187 | 24.94 |

The goal is to determine the optimum mesh size, defined as the largest size where parameters remain consistent. The key parameters show fluctuations, indicating unsteady recorded values for each element size. Consequently, the smallest one, 0.2 m, resulting in the finest mesh, is deemed the most optimum choice for this analysis.

2.3 Base Case Analysis and Design Optimization

In this simulation, an enclosed volume represents the air medium within the car park model, with structural elements treated as obstructions.

All boundary conditions, physics, and solver settings are configured in Ansys Fluent. This includes setting up the car fire source, supply and exhaust fans, and jet fan specifications. After the simulation is complete, the contours of maximum static temperature and airflow velocity are extracted using Ansys post-processing.

3. RESULTS AND DISCUSSION

The study involved two 5-minute transient simulations: for base and modified cases of the underground car park design. Temperature and airflow velocity distribution at plane $y = 2.7$ m became the parameters of interest and analyzed to evaluate on the model's ventilation performance.

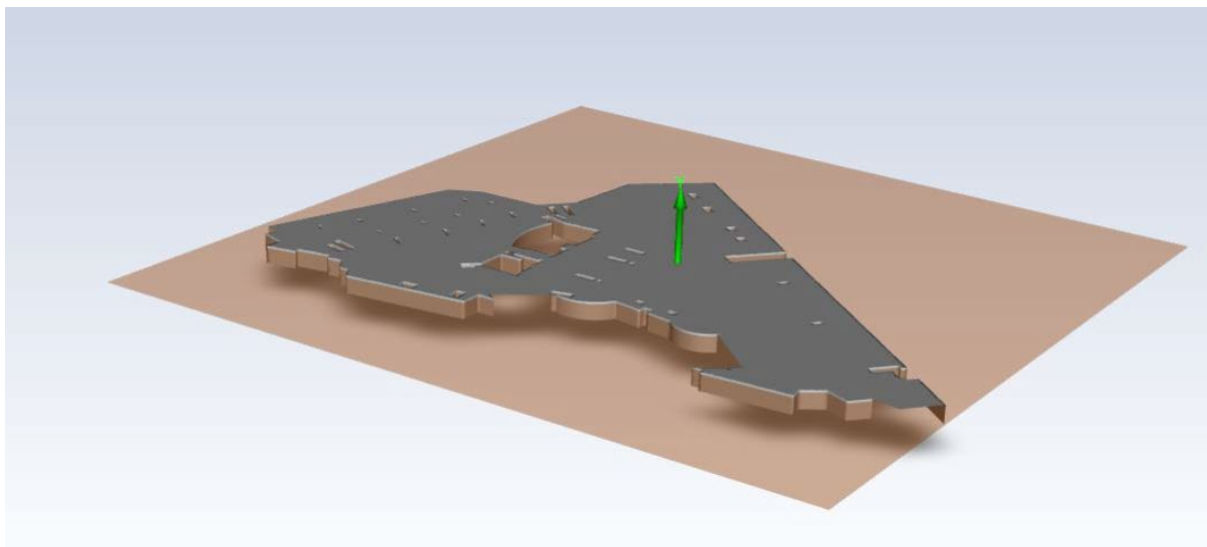
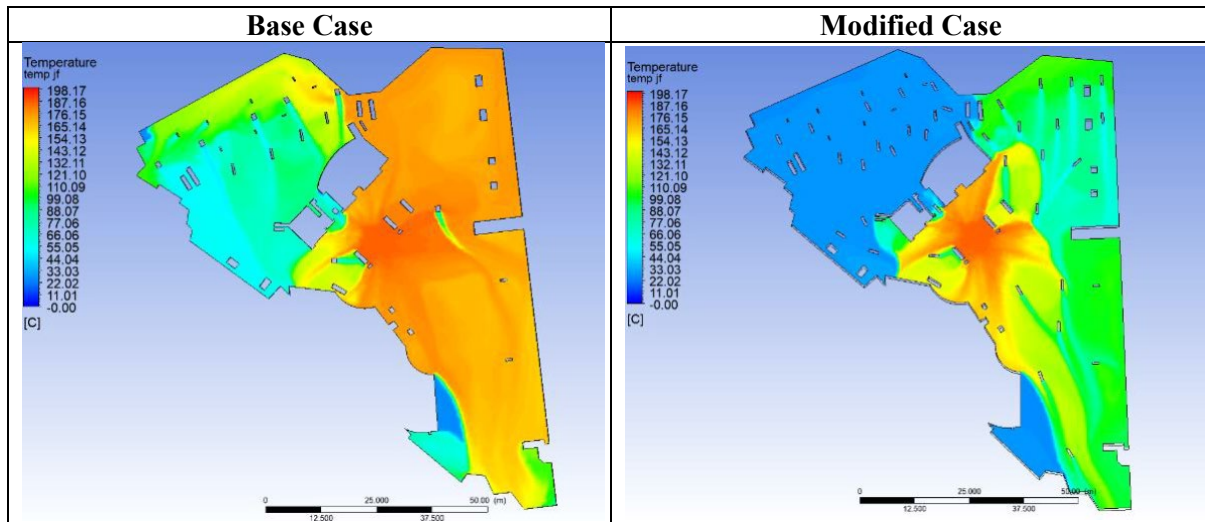


Figure 2. Location of plane $y = 2.7$ m

3.1 Temperature Distribution Contour

The modified design significantly reduces hotspots and improves temperature distribution. This demonstrates effective smoke clearance with less area covered by hot air. The addition of jet fans in the modified case has successfully directed airflow towards exits, enhancing smoke containment and evacuation safety by keeping areas near natural air inlets clear, particularly in the first five minutes of a fire.

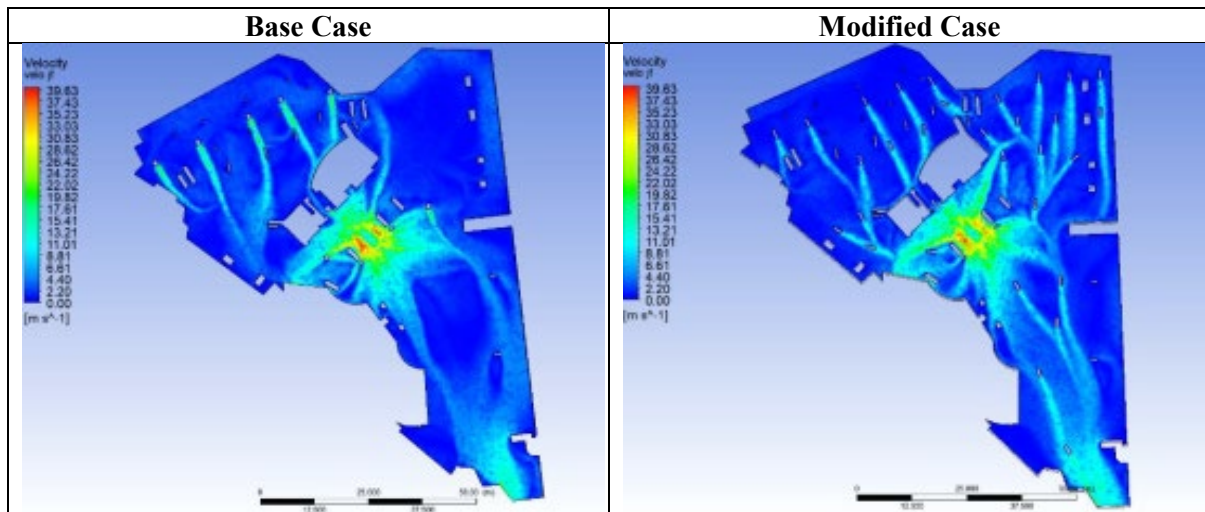
Table 2: Temperature distribution contour



3.2 Airflow Velocity Distribution

Airflow induced by the fire consistently directs towards the exhaust fans in both cases, aligning with the intended ventilation strategy. The jet fans significantly facilitate this flow.

Table 3: Airflow velocity contour



Comparing airflow velocity distribution between the base and modified cases reveals improvements in the modified design. The modified design exhibits a more uniform and clear airflow towards the exits, while the base case shows areas of undesirable back-layering.

This enhanced airflow correlates with the temperature distribution improvements shown in Table 2.

4. CONCLUSION

In conclusion, this study effectively optimized the jet fan mechanical ventilation system for an underground car park using CFD modelling. Initial design limitations, such as the potential for back-

layering and the spread of high temperatures to distant zones were identified. Through strategic modifications, including a staggered arrangement of jet fans, careful selection of jet fan specifications, and precise configuration, ventilation performance was significantly enhanced. These improvements resulted in reduced hotspots and improved smoke clearance. The findings emphasize the critical role of utilizing CFD to evaluate, modify, and enhance ventilation systems in underground car parks to uphold safety standards.

REFERENCES

- [1] “Malaysia: car ownership among consumers 2024 | Statista.” Accessed: Jun. 06, 2024. [Online]. Available: <https://www.statista.com/statistics/1029277/malaysia-car-ownership-among-consumers/>
- [2] J. C. Viegas, “The use of impulse ventilation for smoke control in underground car parks,” *Tunnelling and Underground Space Technology*, vol. 25, no. 1, pp. 42–53, Jan. 2010, doi: 10.1016/j.tust.2009.08.003.
- [3] S. Kerber and W. D. Walton, “Characterizing Positive Pressure Ventilation using Computational Fluid Dynamics.”
- [4] S. Lu, Y. H. Wang, R. F. Zhang, and H. P. Zhang, “Numerical study on impulse ventilation for smoke control in an underground car park,” in *Procedia Engineering*, Elsevier Ltd, 2011, pp. 369–378. doi: 10.1016/j.proeng.2011.04.671.
- [5] “Motor Vehicle Fires | Fairfield, OH.” Accessed: Jun. 06, 2024. [Online]. Available: <https://www.fairfield-city.org/341/Motor-Vehicle-Fires>
- [6] B. Truchot, F. Fouillen, and S. Collet, “An experimental evaluation of toxic gas emissions from vehicle fires,” *Fire Saf J*, vol. 97, pp. 111–118, Apr. 2018, doi: 10.1016/j.firesaf.2017.12.002.
- [7] B. Truchot, F. Fouillen, S. Collet, and S. Collet, “An experimental evaluation of the toxic gas emission in case of vehicle fires,” 2016. [Online]. Available: <https://ineris.hal.science/ineris-01863930>

Numerical Simulation of Heat Dispersion around Engineering Tower due to Condenser Installation

Mohammad Iqbal Haqim bin Mohamad Robi^a and Nik Nazri bin Nik Ghazali^{b*}

Department of Mechanical Engineering,
Faculty of Engineering, Universiti Malaya,
50603, Kuala Lumpur, Malaysia

Email: ^a iqball1haqim@gmail.com, ^b nik_nazri@um.edu.my

*Corresponding author

ABSTRACT

The effects of condensers of the split-unit air-conditioners that serve in the Engineering Tower, University of Malaya were studied numerically. Heat energy released by the condensing units induces a high temperature air plume which has its temperature rise upward to the top of the building. When the plume reaches the upper floor, its elevated temperature reduces the condenser efficiency and may even spoil the air-conditioners operation because of the high temperature cut. In this study, air flow simulation/computational tool are being used to predict the airflow of the heat dissipated by the condenser and the on-coil temperature. The model of the Engineering Tower was designed using SolidWorks and the placement of the condensers is used with maximum number of condensers that can be installed. The simulation was done by Ansys Student 2024 R2, the velocity of the wind and the outflow from the condenser are 1.0 m/s and 1.5 m/s respectively. The heat dispersion from the condensers is observed. External louvers installed at certain distances which are 0.3 meters and 0.6 meters to study the effect of louvers installation on the heat buoyancy. Two types of louvers are installed which are single louvers and double louvers. The louvers installed channel the heat downward and reduce the stack effect of the heat dispersion.

Keywords: Airflow; Condensers; Heat Dispersion; Louvers; Simulation

1. INTRODUCTION

Air conditioning is spreading worldwide because it's becoming crucial in dealing with climate change issues [4]. More people are staying indoors for longer periods of time, which has increased the need for apartments to have indoor environments that are comfortable, productive, and healthy [3]. Installing an air-conditioning system helps to prevent discomfort and health problems.

The energy consumption in air-conditioning lies in its efficiency. The coefficient of the performance (COP) of the air-conditioners will drop by around 3% if the on-coil temperature of the condenser units increases by 1 °C, and the air-conditioners will trip if the temperature remains above 45 °C for an extended period [2] because of the excessive condenser working pressure.

2. METHODOLOGY

The study focuses on the heat dispersion from split-unit air conditioner condensers installed at the back of the Engineering Tower at the University of Malaya because it has most of the condensers and has confined spaces that complicate heat dissipation. The computational domain for the analysis extends 30 x 35 x 35 meters around the building. The condensers are 0.5 x 0.7 x .03 meters in size. The hot air from the condensers exits at 1.5 m/s, while the wind speed around the building is approximately 1.0 m/s. The temperatures of the air from the condensers and the wind are about 45°C and 30°C, respectively. The study examines the heat dispersion of the maximum number of air-conditioning systems and the effect of louver installation.

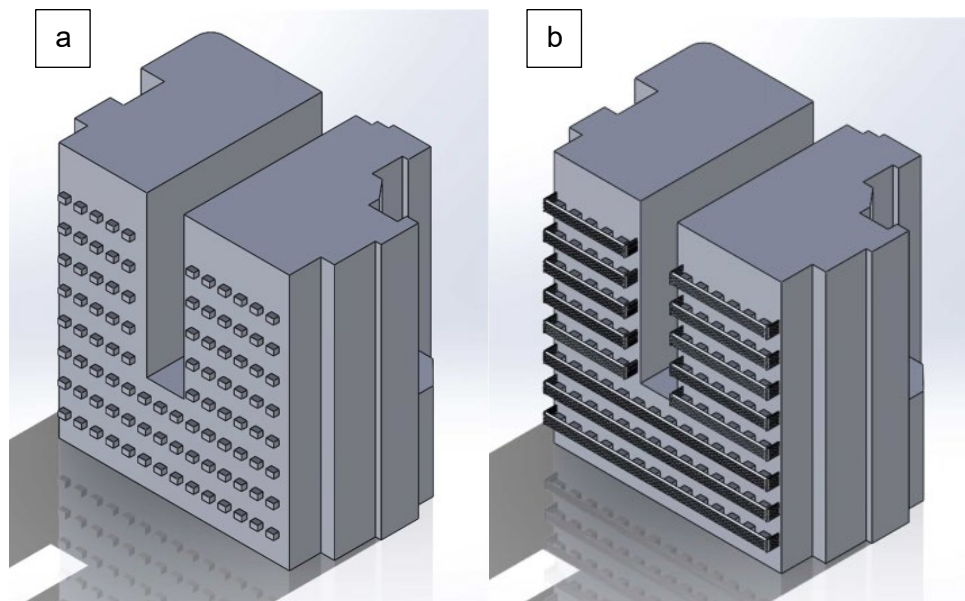


Figure 1. Engineering tower with condenser (a) without louver (b) with louver

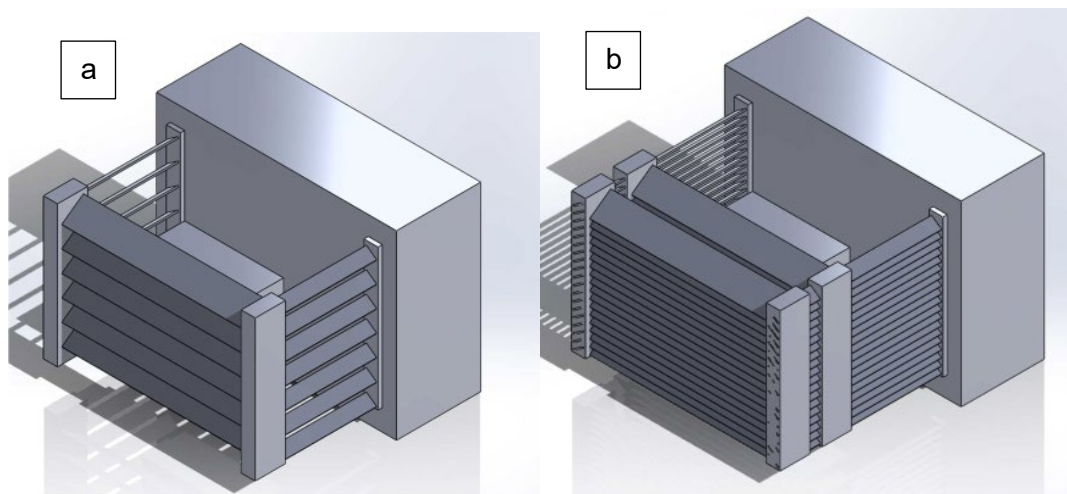


Figure 2. Condenser with louver (a) single louver (b) double louver

The maximum number of condensers (Fig. 1-a) is used to see the effect of heat dispersion at the desired location. Figure 1-b shows when the louvers were installed at the back of the engineering tower to reduce the effect of heat buoyancy that can cause temperature build-up.

Ansys Student 2024 R1 was used to run the simulation. This software can only run simulations with meshing numbers not exceeding 1000000. The maximum condenser with louvers cannot be run because it produces 5000000 mesh numbers. Thus, the simulation runs with only one condenser shown in figure 2. In this study, two types of louvers are used, which are single louver and double louvers.

Table 1. Louver’s condition

| Louver condition | Distance between louvers and condenser (m) | Louver Spacing (m) |
|------------------|--|--------------------|
| Single Louvers | 0.3 | 0.05 |
| | | 0.10 |
| | | 0.15 |
| | 0.6 | 0.05 |
| | | 0.10 |
| | | 0.15 |
| Double Louvers | 0.3 and 0.6 | 0.05 |
| | | 0.15 |

3. RESULTS AND DISCUSSION

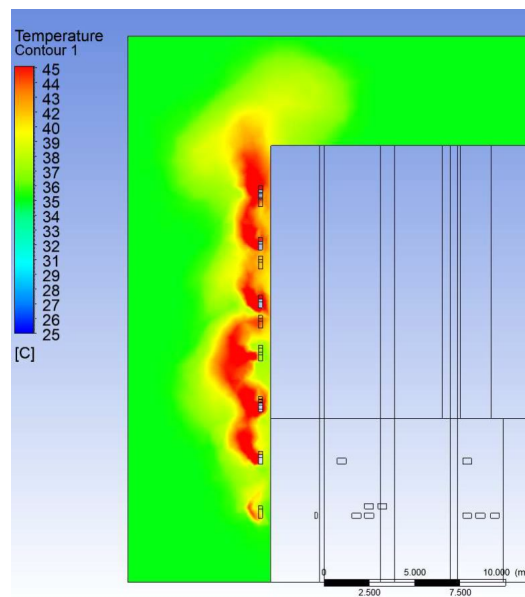
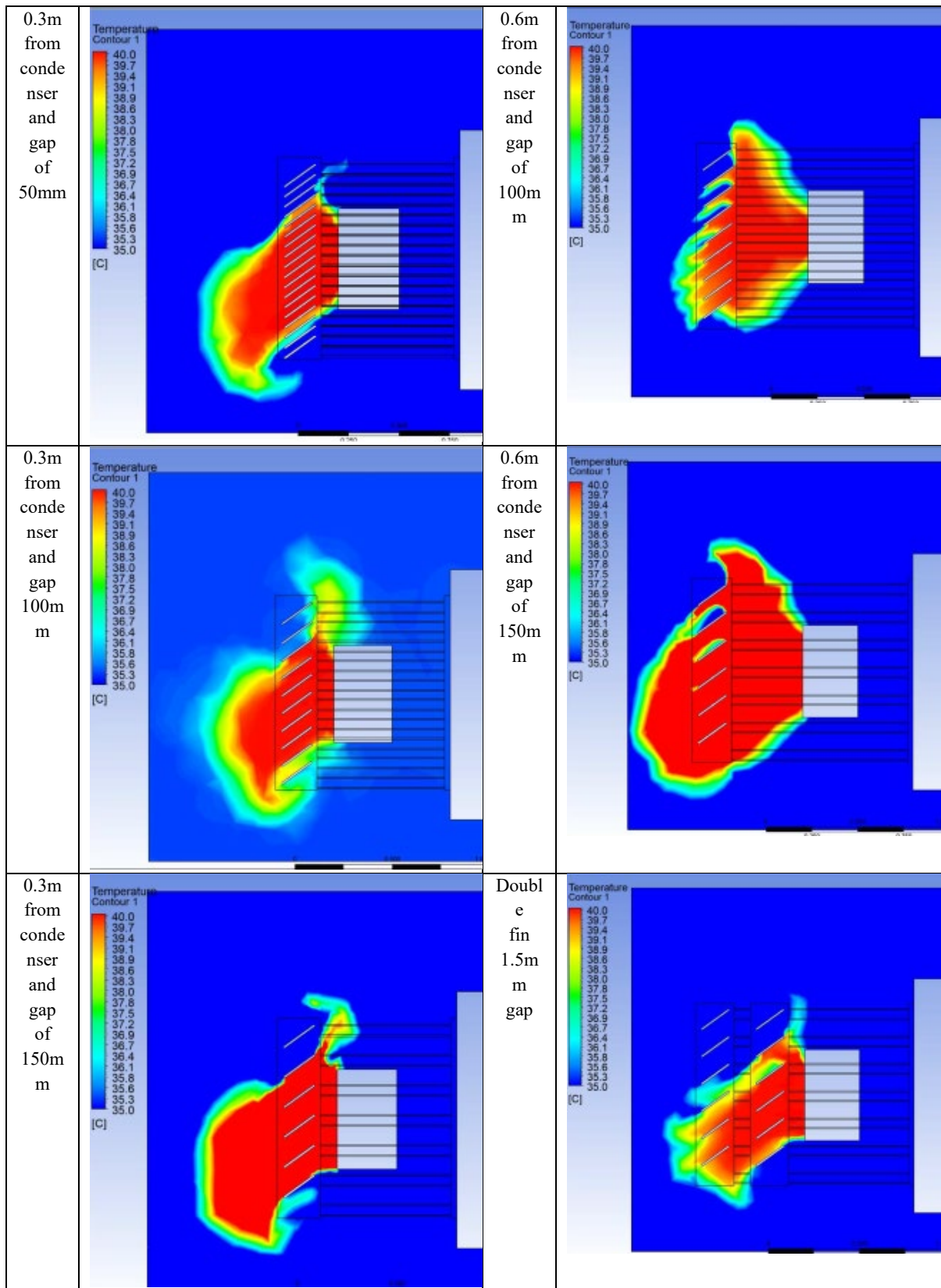
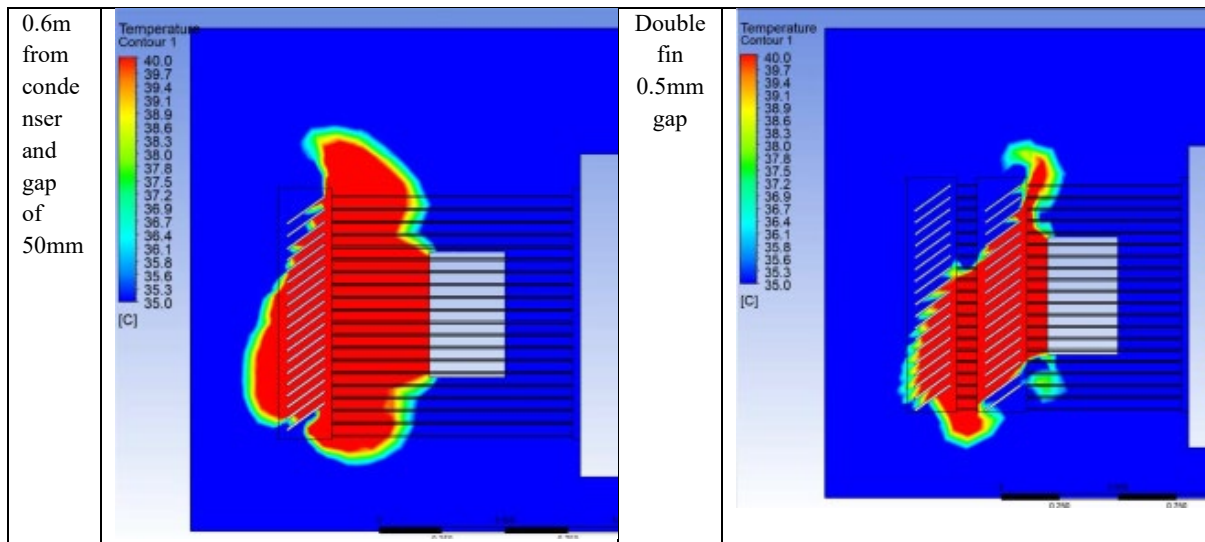


Figure 3. Temperature buildup at the engineering tower

The front face of the condenser is designed to release hot air generated during the heat exchange process. However, heat dissipated from the condenser will tend to move upward due to the principle of heat buoyancy, where warmer air rises because it is less dense than cooler air. The average temperature taken at 0.3 meters above the condenser is 37.92°C.

Table 2. The effect of Louvers' installation





The installation of louvers has a significant impact on the dispersion patterns. The louvers installed at distances of 0.3 meters from the condenser effectively channel the heat flow compared to the louvers installed at distances of 0.6 meters. Due to buoyancy effect, the heat flow for the louvers at 0.6 meters goes upward before being directed downward by the louvers. This heat flow will stack when more condensers are installed at vertical positions.

Table 3: The temperature taken at 0.3 m above condenser

| Louver condition | Distance between louvers and condenser (m) | Louver Spacing (m) | Average Temperature before louvers installation (°C) | Temperature (°C) | Temperature Difference (%) |
|------------------|--|--------------------|--|------------------|----------------------------|
| Single Louvers | 0.3 | 0.05 | 37.92 | 30.971 | 18% |
| | | 0.10 | | 35.390 | 7% |
| | | 0.15 | | 31.287 | 17% |
| | 0.6 | 0.05 | | 32.853 | 13% |
| | | 0.10 | | 31.358 | 17% |
| | | 0.15 | | 31.367 | 17% |
| Double Louvers | 0.3 and 0.6 | 0.05 | | 30.748 | 19% |
| | | 0.15 | | 31.476 | 17% |

Table 3 shows that the installation of louvers results in a more effective heat dispersion, indicated by lower average and maximum temperatures and a reduced temperature gradient. This improved heat management contributes to a higher coefficient of performance for the air conditioning system, demonstrating the beneficial impact of controlling heat buoyancy with louvers.

By analyzing the table, it was evident that double louvers significantly improved the distribution of dissipated heat, thereby enhancing the overall efficiency of the air conditioning system. This is because, by installing the external louvers, the temperature at 0.3 meters from the condenser can be reduced from 37.92°C to 30.971°C for single louvers and 30.476°C for double louvers.

The percentage difference between before installing the louvers and after is from 7% to 19%. The highest percentage difference is by the double louvers with a 0.05 meters gap between the louvers. And

the lowest one is by the single louvers distance between the louvers and the condenser is 0.3 meters and the gap between louvers is 0.1 meters.

4. CONCLUSION

In conclusion, the heat dispersed by the condenser is important to make sure the air-conditioning system can work effectively. Installing the condenser in a vertical position will cause heat to stack due to heat buoyancy. Reducing heat buoyancy means reducing the temperature build-up. Thus, the efficiency of air-conditioning systems can be increased. Chow et al., 2002 stated that the coefficient of performance (COP) of the air-conditioners will drop by around 3% if the on-coil temperature of the condenser units increases by 1 °C [2].

Installing the louvers can improve the heat buoyancy. Heat dispersed by the condensers is directed downward by the louvers. The effect of heat stacking can be reduced by installing the louvers. The average temperature without louvers installation is 37.92°C and can be reduced to 30.971°C for single louvers and 30.748°C for double louvers installation, which are 18% and 19%, respectively. This difference in temperature is considered large and can greatly impact the air-conditioning efficiency.

REFERENCES

- [1] Chow, T. T., & Lin, Z. (1998). Prediction of on-coil temperature of condensers installed at tall building re-entrant. *Applied Thermal Engineering*, 19(2), 117–132. [https://doi.org/10.1016/S1359-4311\(98\)00042-8](https://doi.org/10.1016/S1359-4311(98)00042-8)
- [2] Chow, T.T. & Lin, Z. & Yang, X.Y. (2002). Placement of condensing units of split-type air-conditioners at low-rise residences. *Applied Thermal Engineering*, 22. 1431-1444. 10.1016/S1359-4311(02)00068-6.
- [3] Kwag, B. C., Kim, G. T., & Im, D. (2023). Evaluation of the impact of installation environment for a condensing unit of a split-type air conditioner in a plant room of Korean apartment dwellings. *International Journal of Refrigeration*, 156, 207–218. <https://doi.org/10.1016/j.ijrefrig.2023.10.002>
- [4] Randazzo, T., Filippo Pavanello, & Enrica De Cian. (2023). Adaptation to climate change: Air-conditioning and the role of remittances. *Journal of Environmental Economics and Management*, 120, 102818–102818. <https://doi.org/10.1016/j.jeem.2023.102818>

Computational Study of Two-phase Flow (Mixture of Water-air) in Venturi Nozzle Structure

Adli Al-Wafi bin Mohd. Normarzuki ^a and Poo Balan Ganesan ^{b*}

Department of Mechanical Engineering,
Faculty of Engineering, Universiti Malaya,
50603, Kuala Lumpur, Malaysia

Email: ^a adlinormarzuki@gmail.com, ^b poo_ganesan@um.edu.my

*Corresponding author

ABSTRACT

Water quality is a critical factor in numerous industries, and maintaining a high oxygen content is vital. Various mechanisms such as venturi tubes, nozzles, and orifice tubes are employed to mix air and water effectively. This research utilizes Computational Fluid Dynamics (CFD) to examine the effects of input velocity on flow and mixing within a 3D Venturi Nozzle. The study also compares different turbulence models to simulate the nozzle's behaviour and assesses multiphase flow by aligning simulation results with experimental data. Addressing a gap in fluid flow dynamics within 3D Venturi nozzles, this research holds significance for fluid mechanics, industrial processes, and environmental engineering. The methodology includes designing the 3D geometry of the Venturi nozzle, simulating various cases with CFD, testing different inlet velocities, and evaluating turbulence models. Findings indicate that the RNG turbulence model provides consistent results with minimal errors, revealing patterns of vortices and asymmetry. These insights contribute to enhancing aeration efficiency and energy conservation in industrial applications.

Keywords: Water quality; Venturi nozzle; CFD; Turbulence models; Multiphase flow

1. INTRODUCTION

The study delves into multiphase flow dynamics within venturi nozzles, employing Computational Fluid Dynamics (CFD) to model interactions between water and air. Venturi nozzles, crucial for enhancing water aeration in fields like agriculture and wastewater treatment, are investigated to optimize air entrainment and mixing processes, aiming to improve oxygen efficiency and energy conservation. Using ANSYS Fluent, the research addresses challenges in cost-effective multiphase mixing methods and limited design exploration for venturi nozzle aerators.

Objectives include assessing water inlet velocity effects on flow characteristics, comparing swirling and non-swirling nozzle geometries, and evaluating turbulence models. ANSYS Fluent with the Eulerian model and k-epsilon turbulence model is utilized to compare different water inlet velocities and turbulence models, aiding in understanding and optimizing gas-liquid interactions within venturi nozzles for enhanced efficiency and performance.

2. METHODOLOGY

The study focuses on designing venturi nozzles using ANSYS DesignModeler, with particular emphasis on nozzle 1 and nozzle 2 for fluid domain simulations. Nozzle 1 features a water inlet of 48.20 mm, twelve 1.5 mm air inlets, and a 26.80 mm outlet, with variants incorporating axial swirl elements (S1, S2, S3) with aspect ratios of 2.0, 2.5, and 3.0, respectively. Nozzle 2 includes a 48.20 mm water inlet, a 1.5 mm ring-shaped air inlet, and a 26.80 mm outlet.

Mesh quality is critical for accurate CFD simulations, particularly orthogonality and skewness. ANSYS Meshing generates six meshes for nozzle 1 and nozzle 2, with mesh independence analysis indicating mesh 4 as optimal. Mesh enhancements, including inflation layers and adaptive sizing, are applied to improve accuracy and refine the mesh.

Table 1. Mesh 4 Qualities

| Mesh Metric | Average Value for Nozzle 1 | Average Value for Nozzle 2 |
|------------------------|----------------------------|----------------------------|
| Max Aspect Ratio | 5.374 | 8.360 |
| Min Element Quality | 0.016 | 0.241 |
| Min Orthogonal Quality | 0.043 | 0.201 |
| Max Skewness | 0.957 | 0.799 |

Simulations in ANSYS Fluent utilized the Eulerian model and k-epsilon turbulence model, investigating the influence of water inlet velocity and nozzle geometry on passive air suction capability. Six cases with varying flow rates were analysed, comparing results using different turbulence models to validate against experimental data from the Journal of Applied Fluid Mechanics [1], ensuring the reliability of the venturi nozzle designs.

3. RESULTS AND DISCUSSION

The research investigates the impact of water inlet velocities on venturi nozzle dynamics, utilizing the RNG k-epsilon turbulence model for simulations. These findings are pivotal, showcasing the substantial influence of water inlet velocity on simulated air inlet velocity, crucial for optimizing nozzle performance.

In Nozzle 1, simulations at various water inlet velocities (169.15 LPM, 140.89 LPM, and 114.44 LPM) reveal fluctuations in the RNG k-epsilon model's accuracy with changing water flow rates. The model is most precise at 169.15 LPM, with only a 6.84% error, suggesting its optimal performance under the tested conditions. Similarly, Nozzle 2 is evaluated at different velocities (169.29 LPM, 141.08 LPM, and 115.29 LPM), with the model demonstrating the lowest error at 141.08 LPM, with a 14.00% deviation from experimental values. This suggests each nozzle has a distinct optimal operating velocity for air suction efficiency.

The study also compares three turbulence models—Standard k-epsilon, RNG, and Realizable—using consistent water inlet velocity to determine their predictive accuracy. The RNG model outperforms others for Nozzle 1, with the lowest error percentage, indicating its suitability for complex flow conditions. Conversely, for Nozzle 2, the Standard k-epsilon model surprisingly exhibits better accuracy, suggesting it may be better suited for certain geometries or steadier flows.

These insights are vital for computational fluid dynamics, emphasizing the importance of selecting the right turbulence model based on specific flow conditions and nozzle geometries. Accurate CFD simulations are crucial for designing efficient fluid systems and predicting their behaviour under operational conditions.

4. CONCLUSION

This study delves into the impact of water inlet velocity on venturi nozzle dynamics through computational fluid dynamics (CFD). Optimal velocities for different nozzles are identified, with the RNG k-epsilon turbulence model emerging as the most accurate for simulations, adept at capturing complex flow patterns within nozzles. The research emphasizes the significance of selecting suitable velocities and turbulence models to improve mixing efficiency and energy utilization in nozzle aerators. Despite computational constraints, the study provides valuable insights into nozzle aerator optimization, offering a reliable predictive tool for engineering applications and contributing substantially to the field.

REFERENCES

- [1] Goo, W. H., Ganesan, P. B., Yong, K. W., Ahmad, M. Y., Yau, Y. H., & Hamad, F. (2023). Air Bubble Size and Its Transition in a Horizontal Tube Produced by Venturi-Nozzle

THEME: MANUFACTURING

Investigating Sustainable Behaviour of UM Community Towards Sustainable Development Goals (SDGs)

Nur Aimi Shazliana binti Md Samil ^a and Salwa Hanim binti Abdul Rashid ^{b*}

Department of Mechanical Engineering,
Faculty of Engineering, Universiti Malaya,
50603, Kuala Lumpur, Malaysia

Email: ^a aimishazliana@gmail.com, ^b salwa_hanim@um.edu.my

*Corresponding author

ABSTRACT

This study examines sustainable awareness among the Universiti Malaya (UM) community regarding sustainable initiatives on campus. The main initiatives include UM Living Labs Initiatives, UM Living Labs Circular Economy Initiatives, UM Smart Campus Initiatives, and UM Community Engagement Centre's (UMCares) Initiatives. Findings reveal that the UM Smart Campus Initiative is the most popular, while UM Community Engagement Centre's (UMCares) Initiative receives less attention. The UM community shows high levels of pro- ecological behaviour, self-efficacy in reducing energy consumption, and support for equitable treatment and social equity. Respondents highlight the need for more events, activities, and educational campaigns to boost community participation. These findings emphasize the importance of sustainable initiatives and community engagement in promoting environmental stewardship and social equity at the university.

Keywords: Awareness; Community Engagement; Energy Conservation; Sustainability; UM Initiatives

1. INTRODUCTION

Sustainability is increasingly critical for institutions worldwide, addressing environmental challenges and promoting sustainable development. Universities significantly contribute to carbon footprints and play a pivotal role in shaping future leaders who will implement the Sustainable Development Goals (SDGs) [3]. Universiti Malaya has launched various initiatives to promote sustainability within its community [2]. Understanding the effectiveness of these initiatives and the factors influencing sustainable behaviours among UM community members is essential for achieving long-term sustainability goals [1]. This project explores the sustainable behaviours of the UM community in relation to the SDGs, providing valuable insights and recommendations to enhance UM's sustainability efforts.

2. METHODOLOGY

This study at Universiti Malaya uses a mixed methods approach to investigate the sustainable behaviour of its community regarding the Sustainable Development Goals (SDGs). The quantitative phase includes structured surveys with closed- ended questions distributed to a representative sample of students and staff, collecting numerical data on relevant variables. The qualitative component uses

open-ended questions to gather in-depth insights and suggestions for improving sustainable initiatives. Content analysis identifies themes from the qualitative responses, complementing the quantitative data. The questionnaire comprises five sections: demographics, SDG knowledge, awareness of UM's sustainable initiatives, evaluation of sustainable behaviours, and suggestions for improvement.

3. RESULTS AND DISCUSSION

Table 1 shows that the most popular initiative is the UM Smart Campus Initiative, while the least popular is the UM Community Engagement Centre's (UMCares) Initiative.

Table 1. Awareness level and participation of UM community towards UM sustainable initiatives.

| Perceptions from each respondent toward the initiatives | UM Living Labs Initiatives | UM Living Labs Circular Economy Initiatives | UM Smart Campus Initiatives | UM Community Engagement Centre's (UMCares) Initiatives |
|---|----------------------------|---|-----------------------------|--|
| Heard AND joined most (%) | 27.8 | 17.1 | 39.2 | 17.7 |
| Heard AND joined some (%) | 31.0 | 30.4 | 51.9 | 10.8 |
| Heard some BUT never joined (%) | 29.1 | 21.5 | 5.7 | 27.8 |
| Never heard AND never joined (%) | 12.0 | 31.0 | 3.2 | 43.7 |

Based on the Table 2, UM community demonstrated high levels of pro-ecological behaviour, self-efficacy in reducing energy consumption, equitable treatment irrespective of physical or gender bias, and support for equal treatment of minorities and individuals across all socioeconomic conditions.

Table 2. Top 5 sustainable practices and behaviours of UM community

| Rank | Behaviours | Factor | Mean | S. D. |
|------|--|--------------------------|------|-------|
| 1 | I turn off tap when not in use. | Pro-ecological behaviour | 4.73 | 0.720 |
| 2 | I turn off lights because I believe it can reduce the energy consumption. | Self-efficacy | 4.53 | 0.787 |
| 3 | I treat people equally without physical bias | Equitable behaviour | 4.46 | 0.811 |
| 4 | I support treating minorities and people of all socioeconomic condition equally. | | 4.41 | 0.875 |
| 5 | I treat people equally without gender bias. | | 4.37 | 0.948 |

4. CONCLUSION

In conclusion, Universiti Malaya organizes four main sustainable initiatives, including UM Living Labs Initiatives, UM Living Labs Circular Economy Initiatives, UM Smart Campus Initiatives, and UM Community Engagement Centre's (UMCares) Initiatives, with UM Smart Campus Initiative emerging as the most popular among the community. Despite variations in community demonstrates commendable levels of pro-ecological behaviour, self- efficacy in energy conservation, equitable treatment, and support for minorities and individuals across socioeconomic conditions. However, to further enhance community engagement, respondents recommend increasing event, activity, awareness, and educational campaigns. These findings underscore UM's commitment to sustainability and highlight opportunities for continued improvement through targeted initiatives and outreach efforts.

REFERENCES

- [1] Nor Kalsum Mohd Isa. (2016). Sustainable campus and academic staffs awareness and behaviour in Malaysia's institutions of higher learning: A case study of UPSI. *Geografia: Malaysian Journal of Society and Space*. 12. 89-99.
- [2] Universiti Malaya Sustainability and Development Centre (UMSDC) (2023) UM SDG Report 2022.
- [3] Žalėnienė, I., & Pereira, P. (2021). Higher education for sustainability: A global perspective. *Geography and Sustainability*, 2(2), 99–106. <https://doi.org/10.1016/j.geosus.2021.05.001>

Process Parameter Optimization of Selective Laser Melting Ti-6Al-4V Using Density Control and Defect Criterion by Analytical Approach

Muhammad Lutfi bin Mohd Salleh^a and Mohd Sayuti Ab Karim^{b*}

Department of Mechanical Engineering,
Faculty of Engineering, Universiti Malaya,
50603, Kuala Lumpur, Malaysia

Email: ^a lutfisallehasan@gmail.com, ^b mdsayuti@um.edu.my

*Corresponding author

ABSTRACT

Selective Laser Melting (SLM) is used in Additive Manufacturing to create complex metal alloy parts, such as Ti-6Al-4V, for aerospace, aircraft, and automotive industries requiring high reliability. However, unoptimized parameters like laser power and scan speed can cause defects and low-density parts, deteriorating mechanical properties. An improved parameter map was developed using an analytical approach combining Defect Prevention and High Density Criteria, employing the Heat Moving Equation in MATLAB to predict melt pool dimensions. Validation with empirical and analytical data showed an 84.67% similarity and a 2.43% error. The study found that to avoid defects, scan speed and laser power must be above the new lack of fusion line and below the keyholing line, with balling likely at high speeds above 1.5 m/s. The optimized region was validated with accuracies of 91.7%, 76.7%, and 73.7% for lack of fusion, optimized, and keyholing, respectively.

Keywords: Additive Manufacturing; Defect Prevention; Optimization; Selective Laser Melting; Ti-6Al-4V

1. INTRODUCTION

Defects and low-density parts in the SLM process are caused by unoptimized parameters such as laser power, scan speed, hatch distance, and layer thickness. High-density control and defect prevention are commonly used criteria for optimization. However, Promopattum et al. reported that small pores still appear in printed parts even when parameters are within the defect-free space [2]. Therefore, improving the existing optimized parameter space is necessary to ensure high-quality parts. By combining high-density and defect prevention criteria, a more accurate optimized operating space can be created, as it requires satisfying multiple conditions to ensure the production of defect-free parts.

2. METHODOLOGY

The model employs a mathematical equation to determine the melt pool dimensions. The MATLAB code begins by defining material properties such as thermal conductivity, melting temperature, heat capacity, and absorption. Next, the output domain and the number of points in it are defined. A for loop calculates the dimensionless temperature at each point. The melt pool dimensions are then plotted in

the xy-plane or xz-plane based on this temperature. Figure 1 shows the programming flowchart for the analytical model in MATLAB.

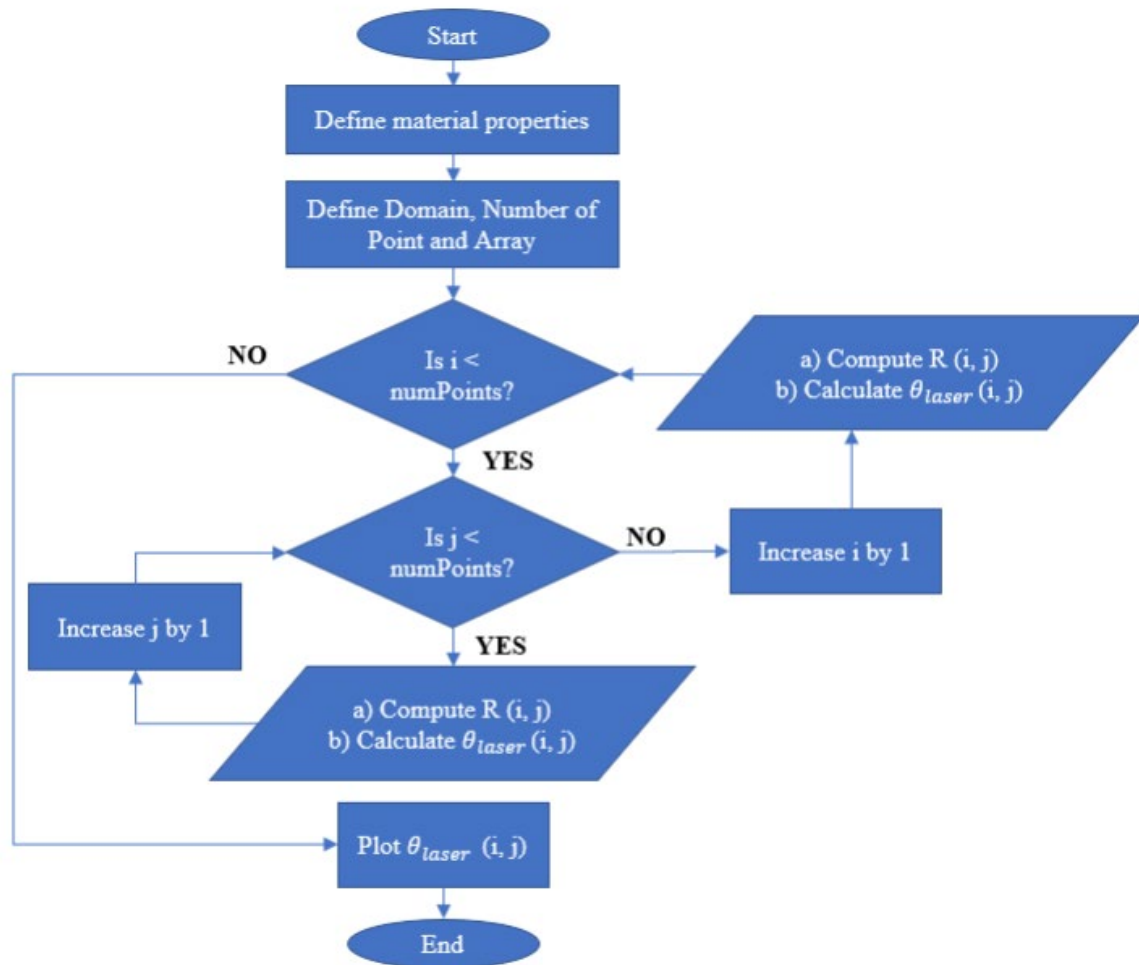


Figure 1. Programming Flowchart of Analytical Model in MATLAB

The melt pool dimension is computed using the Heat Moving Solution model for each combination of scan speed and laser power same as the optimized map from literature. Then, the computed melt pool dimension is evaluated based on High Density and Defect Prevention Criteria where there are three requirements for each criterion. The melt pool is considered good when all requirements are satisfied. The requirements are listed in Table 1.

Table 1. Requirement for both High Density & Defect Prevention

| High Density Criteria | Defect Prevention Criteria | | |
|---|--|-------------------------|--|
| | Lack of Fusion | Balling | Keyholing |
| Based on available empirical data for Ti-6Al-4V | $\left(\frac{H}{W}\right)^2 + \left(\frac{L}{d}\right)^2 \leq 1$ | $\frac{\pi w}{l} > 0.2$ | $\frac{\Delta H}{h_s} > \frac{\pi T_b}{T_m}$ |

Defect-prevention separation lines for lack of fusion, keyholing and balling are generated by satisfying defect prevention criteria while for high-density separation lines, the optimized melt pool metrics range must be determined first using available data from literature.

3. RESULTS AND DISCUSSION

The model is validated with empirical results reported by Kusuma and is validated with analytical results reported by Ning et al. The model is validated with a similarity of 84.67% empirically and an average percentage error of 2.43% analytically. The generated lack of fusion separation line able to classify small pores printed part as lack of fusion that is otherwise categorized as good printed part [2]. Therefore, it can be concluded the new separation line defines a lack of fusion constraint better than the existing separation line as shown in Figure 2.

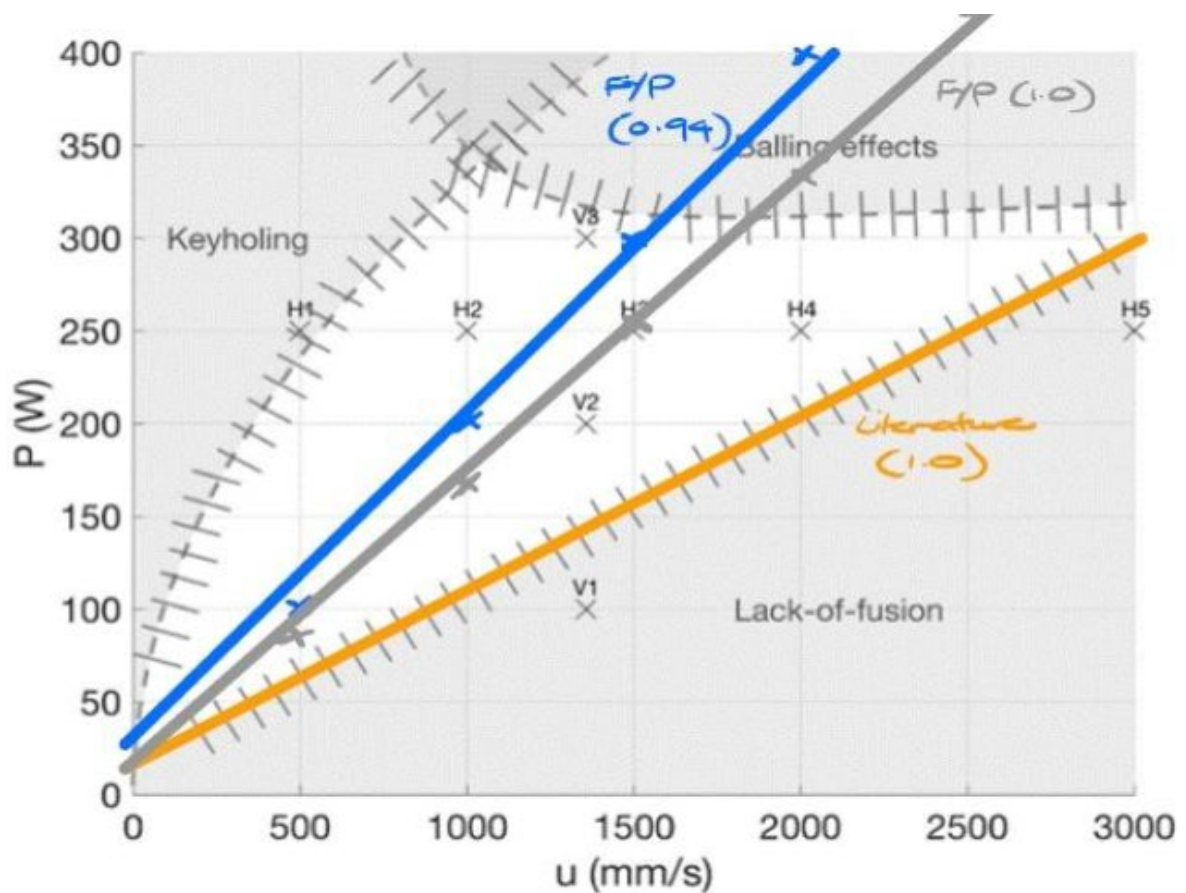


Figure 2. Comparison New Separation Line and Existing Separation Line (Lack of Fusion)

All separation lines from defect criteria are combined with high-density criteria separation lines to produce a new and novel optimized parameter map to ensure the absence of defect and low-density print. Each area of defect and the low-density area is highlighted in the map while the white region lies the combination of parameters that can produce a high-quality print as shown in Figure 3.

Finalized Optimized Parameter Map (Defect & Density Criteria)

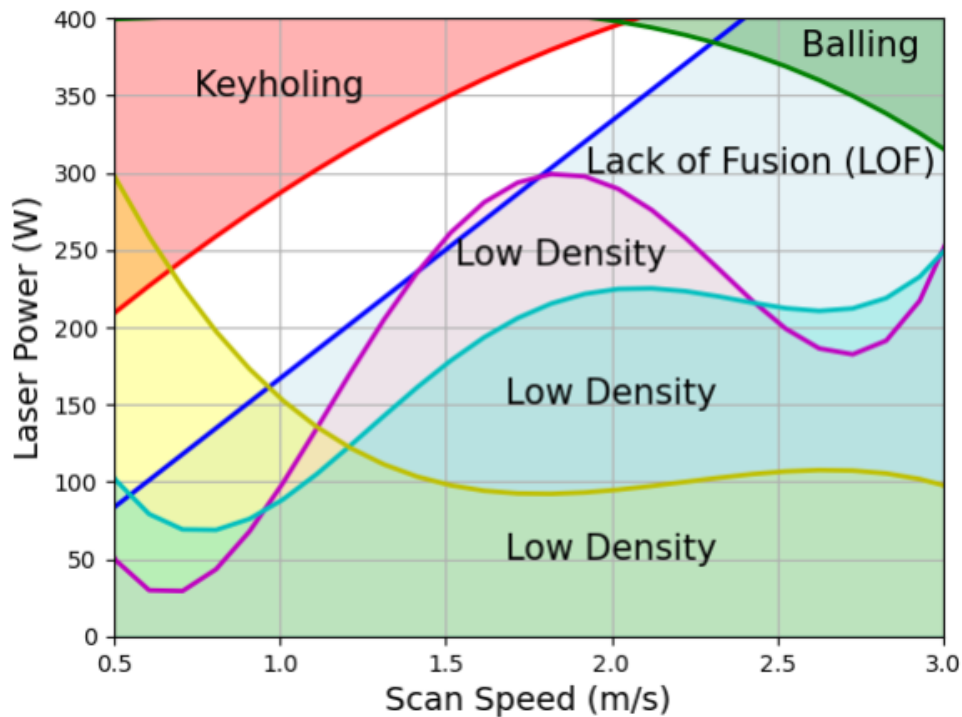


Figure 3. Finalized Optimized Parameter Map using Defect & High-Density Criteria

4. CONCLUSION

In conclusion, the Moving Heat Analytical Model in MATLAB was successfully developed to predict melt pool dimensions. The model showed 84.67% similarity with empirical results and 2.43% error with analytical results from the literature. The optimized parameter region was validated with empirical data, the model achieved accuracies of 91.7%, 76.7%, and 73.7% for lack of fusion, optimized, and keyholing, respectively.

REFERENCES

- [1] Ning, J., Sievers, D. E., Hamid Garmestani, & Liang, S. Y. (2019). Analytical Thermal Modeling of Metal Additive Manufacturing by Heat Sink Solution. *Materials*, 12(16), 2568–2568. <https://doi.org/10.3390/ma12162568>
- [2] Patcharapit Promoppatum, & Yao, S.-C. (2019). Analytical evaluation of defect generation for selective laser melting of metals. *the International Journal of Advanced Manufacturing Technology/International Journal, Advanced Manufacturing Technology*, 103(1-4), 1185–1198. <https://doi.org/10.1007/s00170-019-03500-z>

Grading of Wooden Products based on Defect Detection and Classification using You Only Look Once (YOLO) Method

Athirah binti Ridzuan ^a and Azuddin bin Mamat ^{b*}

Department of Mechanical Engineering,
Faculty of Engineering, Universiti Malaya,
50603, Kuala Lumpur, Malaysia

Email: ^a athirahridz07@gmail.com, ^b azuddin@um.edu.my

*Corresponding author

ABSTRACT

Wood, valued for its aesthetic, durability, and toughness, is essential in industries like interior design and furniture. However, surface defects can lower demand and damage reputations. Manual defect detection is labour-intensive and inconsistent, highlighting the need for automated grading systems. This study aims to develop a machine learning model using the YOLOv8 algorithm to detect wood defects, including cracks, dead knots, holes, live knots, and knots with cracks with a detection performance mAP of more than 70%. The model should be able to classify defects in real-time during quality inspections, grading wood into A, B, or C categories. The images were captured, annotated, and augmented to create a dataset of 3168 images. The model, trained on Google Colab for 100 epochs, achieved an overall mAP50 of 72.4%, with specific defect mAP50 scores of 72.4% for cracks, 88.9% for dead knots, 43.3% for holes, 75% for live knots, and 82.1% for knots with cracks. It was also able to grade the wooden items according to the presence of defects on the wood. This demonstrates effective performance in wood defect detection, except for holes due to their subtle appearance.

Keywords: Wood Defect Detection; YOLOv8 Algorithm; Machine Learning; Quality Inspection; Real-time Classification

1. INTRODUCTION

Modern timber production companies require quick, efficient methods to identify wood defects to enhance revenue and customer satisfaction. Technologies like air-coupled ultrasonic (Wang et al., 2007), stress wave (Du et al., 2018), 3D laser (Peng et al., 2016), and computer vision are used for defect detection. Air-coupled ultrasonic detects defects through density differences but is unstable (Fang et al., 2017). Stress wave technology requires fixed sensor placement, limiting flexibility (Li et al., 2020). 3D laser technology struggles with small defect detection (Jiang et al., 2019). Computer vision techniques, including colorimetric methods (Boardman et al., 1992) and HIS colour models (Momin et al., 2017), offer promising solutions but have limitations in defect diversity and sensitivity to input data (Dawood et al., 2017). Thus, efficient defect detection technology is crucial for quality control in the timber industry.

Object detection models such as Faster RCNN, SSD, and YOLO are used for identifying wood defects. Faster R-CNN provides high accuracy but is slow due to its two-stage process (Ren et al., 2016). SSD

is faster but less accurate (Tsang, 2018). YOLO combines speed and precision, making it ideal for real-time applications (Redmon et al., 2016). YOLOv8, the latest version, improves detection speed and accuracy, processing images quickly while maintaining high precision and recall, crucial for effective defect detection in the timber industry (Redmon & Farhadi, 2018; Kundu, 2023).

Despite advancements, current models struggle with small defect detection and real-time processing, critical for industrial applications. Many methods lack flexibility to identify diverse defect types within a single model (Dawood et al., 2017). YOLOv8 addresses these gaps by offering a versatile, cost-effective, automated solution that integrates seamlessly into existing workflows, enhancing defect detection and classification in the timber industry (Momin et al., 2017).

2. METHODOLOGY

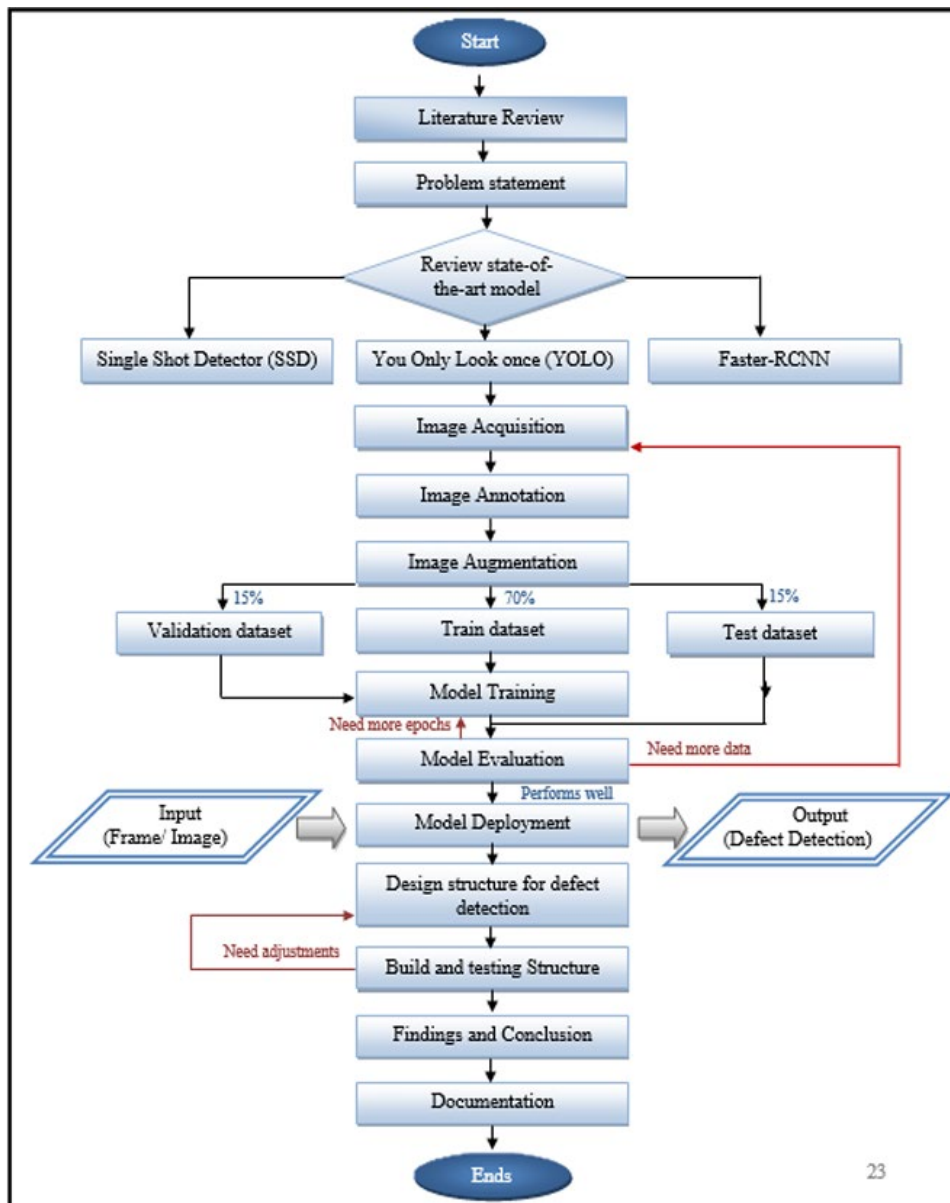


Figure 1. Flow of overall project procedure

The development of the wood defect detection and classification system involved a comprehensive methodology. By using iPhone 11, 1320 high-resolution images of various wood defects was acquired.

The images were then annotated using Roboflow, classifying defects to cracks, dead knots, holes, live knots, and knots with cracks. The dataset was then divided into training (70%), validation (15%), and testing (15%) sets. The annotated images were then augmented to 3168 images using techniques like rotation, hue adjustment, brightness alteration, exposure tweaks, and blurring, ensuring a robust training set. After that, the model was imported to Google Colab Pro to be trained using YOLOv8 for 100 epochs, leveraging GPU capabilities for efficient processing. Evaluation metrics such as precision, recall, and mean Average Precision (mAP) were used to assess the model's performance, with a target mAP of over 70%.

For real-time implementation, the trained model was integrated into a system that processed video frames captured by the Creative Live! Cam Sync 4K webcam. The system identified and classified defects, displaying bounding boxes around detected defects and providing real-time grading of the wooden products into grades A, B, and C based on the number and type of defects. A physical prototype was constructed using PVC laminated block board and pine wood to provide a stable and precise setup for the Webcam.



Figure 2. Setup for defect detection

3. RESULTS AND DISCUSSION

After training the model, the performance of the system was evaluated. Based on Table 1, it is found that the model achieved an overall mAP50 of 72.4%. The highest mAP is for the class dead knot and knot with cracks (88.9% and 82.1% respectively) A moderately good mAP was shown by live knot(75%) and crack (72.4%). Holes demonstrated the lowest mAP at 43.3%. This may happen due to the small size and variant shape of holes, which makes it harder for the system to generalize to new, unseen data.

The system accuracy for detection and grading was validated through three case study where the wood undergone real-time defect detection using webcam. It was found that dead knot, live knot and knot with cracks shows high confidence score when being detected (more than 0.7).

Table 1. Class wise Result for Wood Defect Detection

| Classes | Input Annotations | | | Output | | |
|-----------------|-------------------|------------|------|---------------|------------|----------|
| | Train | Validation | Test | Precision (%) | Recall (%) | MAP (50) |
| Crack | 346 | 65 | 61 | 51.90 | 69.1 | 72.4 |
| Dead knot | 456 | 105 | 92 | 83.1 | 78.5 | 88.9 |
| Holes | 440 | 69 | 105 | 58.8 | 24.6 | 43.3 |
| Live knot | 342 | 67 | 54 | 74.5 | 71.6 | 75.0 |
| Knot with crack | 303 | 68 | 75 | 87.2 | 79.4 | 82.1 |
| All | 1887 | 374 | 387 | 72.5 | 69.1 | 72.4 |

However, the system shows the crack performance can be further improve since variation of crack size and shapes could make it challenging for the system to adapt to new data. mAP of holes score (less than 0.5) when being detected possibly due to it's small and subtle feature that makes it more difficult for webcam to detect it.

The model's ability to classify wooden products into the correct grade (to grade A, grade B and grade C) based on the number and type of defects was demonstrated in this case study as shown in Figure 3.

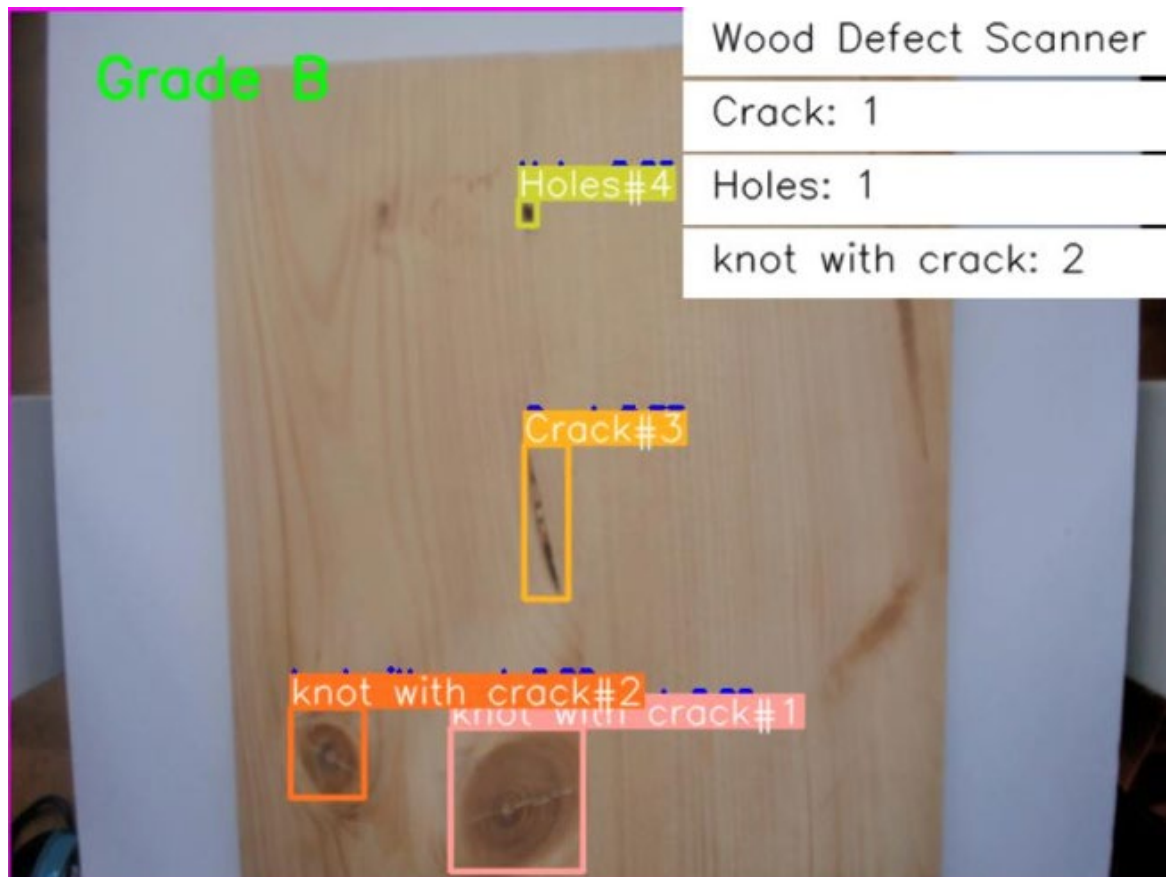


Figure 3. Frame capture defect detection on wood item 1 using live webcam

4. CONCLUSION

In this project, the wood defect detection model developed using the YOLOv8 algorithm demonstrated robust performance in detecting and classifying various wood defects, including cracks, dead knots, holes, live knots, and knots with cracks. The model achieved high mean Average Precision (mAP) values for dead knots (88.9%) and knots with cracks (82.1%), indicating strong detection capabilities. However, the detection of holes proved challenging, with a recall of 24.6% and an mAP of 43.3%, due to the subtle features and small size of the defects. Cracks and live knots performed well with mAP scores of 72.4% and 75%, respectively. Overall, the model achieved an average precision of 72.5% and a recall of 69.1%, meeting the target mAP of over 70%, ensuring accurate defect identification and classification. Additionally, the system successfully graded wooden items into categories A, B, and C based on the number of detected defects.

Future work should focus on improving training data quality and model tuning to enhance performance, especially for subtle defects like holes. Utilizing advanced, high-resolution cameras and high-speed computers will improve real-time processing accuracy and efficiency. These enhancements will significantly benefit the timber industry by making defect detection and grading more efficient and profitable.

REFERENCES

- [1] Xu, Y., Zhang, K., & Wang, L. (2021). Metal Surface Defect Detection Using Modified YOLO Algorithms, 14(9), 257. doi:<https://doi.org/10.3390/a14090257>
- [2] Peng, Z., Yue, L., & Xiao, N. (2016, December 19). Simultaneous Wood Defect and Specie. Detection with 3D Laser. International Journal of Optics, 2016. doi:<https://doi.org/10.1155/2016/7049523>
- [3] Fang, Y., Lin, L., Feng, H., Lu, Z., & Emms, G. W. (2017, May). Review of the Use of Air-coupled Ultrasonic Technologies for Nondestructive Testing of Wood and Wood Products. Computers and Electronics in Agriculture, 79-87. doi:<https://doi.org/10.1016/j.compag.2017.03.015>
- [4] Li, X., Qian, W., Cheng, L., & Chang, L. (2020). A Coupling Model Based on Grey Relational Analysis and Stepwise Discriminant Analysis for Wood Defect Area Identification by Stress Wave. BioResources, 15(1), 1171-1186.
- [5] Jiang, S., Zhou, Z., & Wang, K. (2019). Literature Review and Comparison of Wood Testing Methods and Research on Application Technology of Computer 3D Scanning Detection. AICS 2019: Proceedings of the 2019 International Conference on Artificial Intelligence and Computer Science (pp. 418-422). Wuhan, Hubei, China: Association for Computing Machinery. doi:<https://doi.org/10.1145/3349341.3349443>
- [6] Boardman, B. E., Senft, J. F., McCabe, G. P., & Ladisch, C. M. (1992, January). Colorimetric Analysis in Grading Black Walnut Veneer. Wood and Fiber Science, 24(1), 99-107. Retrieved from <https://wfs.swst.org/index.php/wfs/article/view/1858>
- [7] Momin, M. A., Yamamoto, K., & Miyamoto, M. (2017). Machine Vision based Soybean Quality Evaluation. Computers and Electronics in Agriculture, 452-460. doi:<https://doi.org/10.1016/j.compag.2017.06.023>.

- [8] Dawood, T., Zhu, Z., & Zayed, T. (2017, September). Machine Vision-based Model for Spalling Detection and Quantification in Subway Networks. *Automation in Construction*, 81, 149-160. doi:<https://doi.org/10.1016/j.autcon.2017.06.008>
- [9] Ren, S., He, K., Girshick, R., & Sun, J. (2016, January 6). Faster R-CNN: Towards Real-Time Object Retrieval. Retrieved from <https://arxiv.org/abs/1506.01497>
- [10] Tsang, S.-H. (2018, November 3). Review: SSD- Single Shot Detector (Object Detection). Retrieved from Medium: <https://towardsdatascience.com/review-ssd-single-shot-detector-object-detection-851a94607d11>
- [11] Kundu, R. (2023, January 17). YOLO: Algorithm for Object Detection Explained. Retrieved from <https://www.v7labs.com/blog/yolo-object-detection>

An Exploratory Research of Electrospinning Multiplane Configuration: Effects of Jets Working Parameter on Nanofiber Production Rate

Muhammad Shafiz Danial bin Ismadi^a and Edzrol Niza bin Mohamad^{b*}

Department of Mechanical Engineering,
Faculty of Engineering, Universiti Malaya,
50603, Kuala Lumpur, Malaysia

Email: ^a shafizdaniel@gmail.com, ^b edzrol@um.edu.my

*Corresponding author

ABSTRACT

The method of electrospinning, known for its versatility, offers a straightforward way to create nanofibers. However, traditional single-nozzle setups limit large-scale applications due to restricted fiber production. This research explores the impact of using multiple nozzles to increase fiber yield and improve fiber quality. Specifically, the study examines how adjusting the distance between planes of nozzles affects the electric field and, consequently, the strength and morphology of nanofibers produced from a polyethylene oxide (PEO) polymer solution. The distance between nozzle planes was varied to observe its effect on the electric field strength. Experiments measured the resulting nanofibers' morphology, while simulations analyzed the electric field around the nozzles. Results indicate that a stronger and more uniform electric field, achieved with a 2-2 cm interplane distance, produces more orderly and aligned fibers. These findings highlight the electric field's crucial role in determining the mechanical properties of electrospun nanofibers, offering potential for advanced material development.

Keywords: Electrospinning; Electric field; Multiplane configuration; Nanofibers; Nozzles

1. INTRODUCTION

Electrospun fibers are typically produced using the electrospinning method. Electrospinning is a fabrication process that produces nanometer-sized fibers from a polymer solution, driven by high voltage and characterized by electrohydrodynamic phenomena. Multi-nozzle and multiplane configuration in electrospinning setup are investigated for this paper because it is widely utilized for higher production rate of nanofiber even though the free-surface electrospinning is introduced to mitigate problems related to multiple nozzles. It is because multi-nozzle electrospinning setup is simpler and more versatile allowing it to enhance control over fiber distribution [1].

2. METHODOLOGY

The equipment and materials involved in this project include ANSYS Maxwell software, polyethylene oxides (PEO), an electronic balance, a magnetic stirrer, a power supply, syringes, a syringe pump, a

22G nozzle needle, a nozzle holder, plastic tubes, an aluminium foil collector, a high-speed camera, power supply and Digimizer software. Fig. 1 below shows the flowchart of methodology of this project.

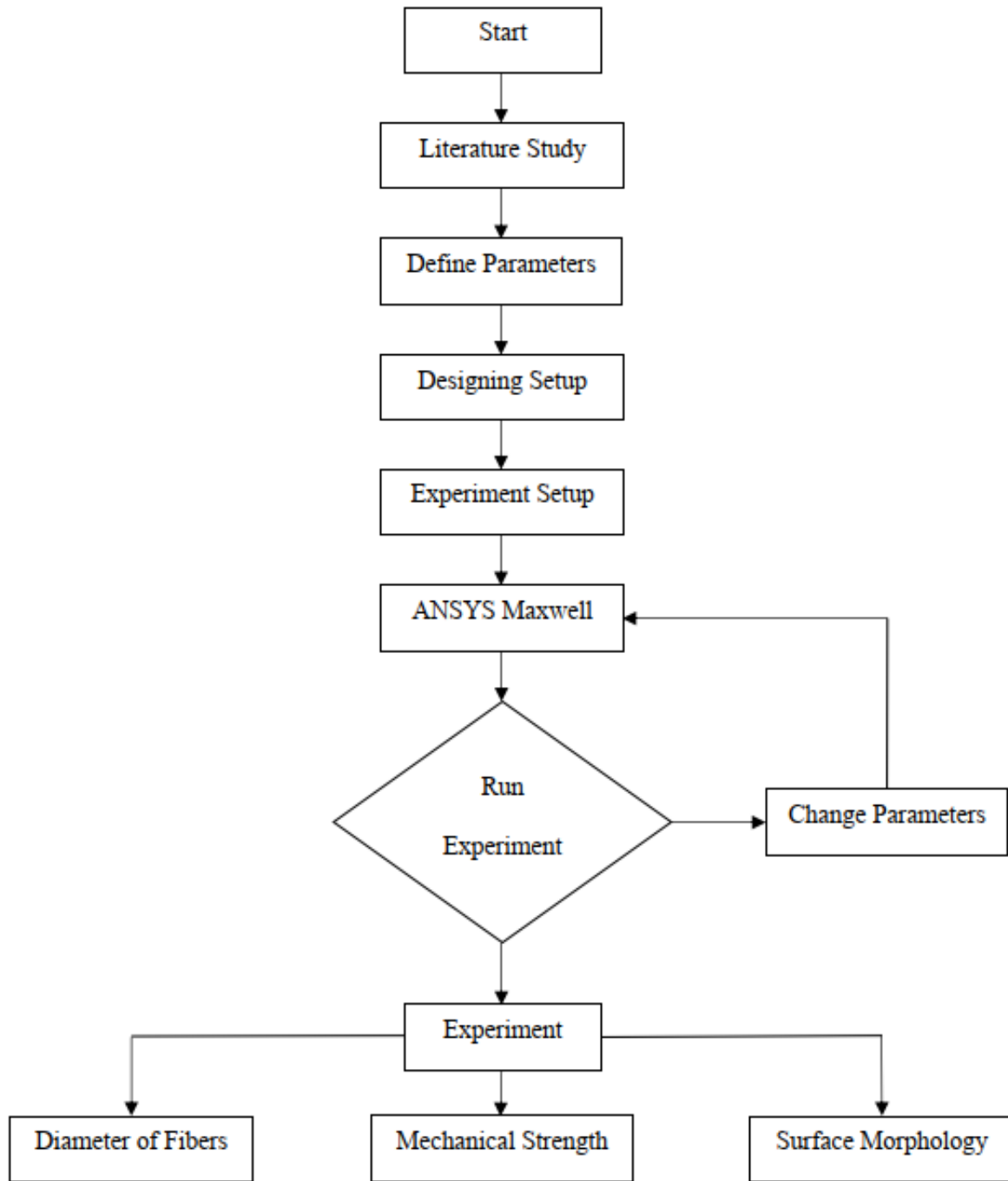


Figure 1. Flowchart of methodology

2.1 Simulation using ANSYS Maxwell

Each nozzle in the simulation was assigned a voltage of 20kV, connected to the positive terminal, while the collector was assigned a voltage of 0kV, connected to the ground terminal. Fig. 2 below shows the 3D modeling of the electrospinning setup with the electrostatic solution type.

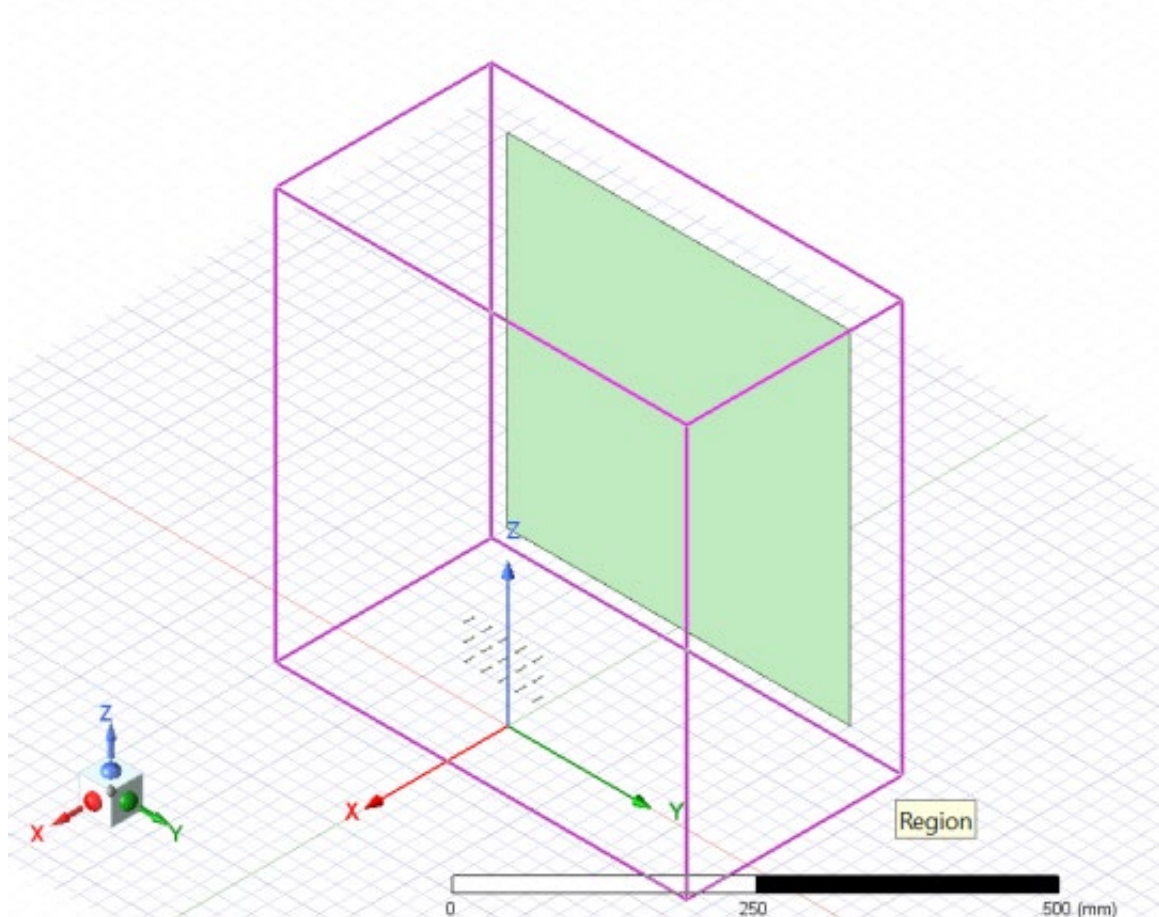


Figure 2. Electrospinning setup with electrostatic solution type

In this case, the equation involved to find the electrical field is as the equation (1) stated below:

$$E = \frac{V}{D} \quad (1)$$

Where; E is electric field strength, V is potential difference and D is distance between nozzles and collector.

2.2 Experimental Approach

The methodology of the experimental approach includes preparing polymer solution by using polyethylene oxide (PEO), setup for electrospinning, observation of fiber jets and characterization of fibers by using FESEM analysis. The main components of the electrospinning setup include syringe needle, polyethylene oxide (PEO) and power supply. The setup of electrospinning for multiplane nozzles is as depicted in the Fig. 3 below:

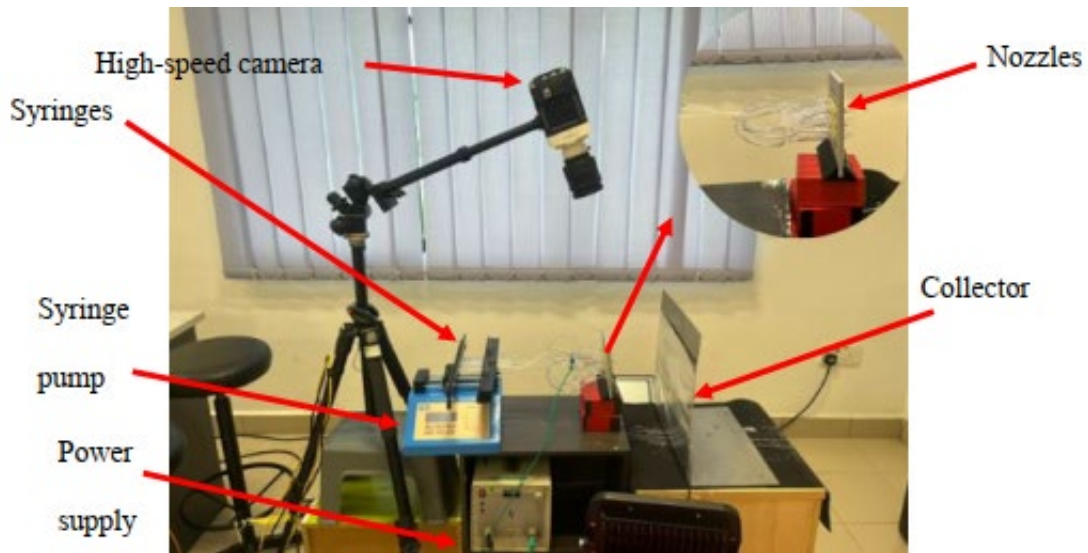


Figure 3. Setup of electrospinning for multiplane nozzles

3. RESULTS AND DISCUSSION

This section is divided into two parts: simulation results and discussion, and experiment results and discussion.

3.1 Simulation using ANSYS Maxwell

Fig. 4 depicts the bar graph of mean max value of electrical field plot against types of configurations were plotted for better visualization. It shows a significant difference in terms of electric field magnitude as additional planes are introduced, there is a decrease in the electric field values when compared to the control experiment. Calculating the average electric field values, the control experiment has an average of $1.2875E+07$ V/m. Among the configurations employed in the multi-nozzle setup with three planes, the '2-2 cm interplane distance' configuration has the highest average electric field value which is $8.8145E+06$ V/m. Conversely, the '4-2 cm interplane distance' configuration has the lowest average electric field value at $6.4400E+06$ V/m, suggesting that unequal spacing between planes leads to decreased electric field values. The highest value of the electric field can influence jet formation into nanosized fibers by enhancing the stretching and thinning effects.

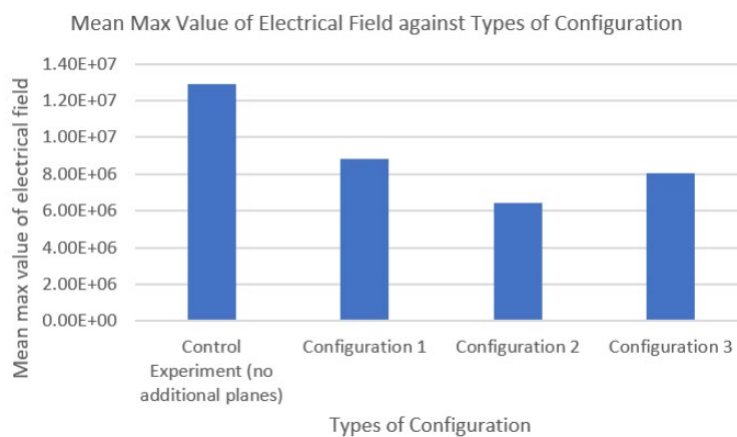


Figure 4. Bar graph of Mean Max Value of Electrical Field plot against Types of Configurations

Among the configurations employed in the multi-nozzle setup with three planes, the '2-2 cm interplane distance' configuration has the highest average electric field value. It is because there is higher coulomb repulsion force when the planes are closer to each [3]. Conversely, the '4-2 cm interplane distance' configuration has the lowest average electric field value, suggesting that unequal spacing between planes leads to decreased electric field values because there is less coulomb repulsion force.

3.2 Experimental Approach

For jet deflection analysis, a bar graph of angle of jet deflection against interplane distance was plotted as in the Fig. 5 below.

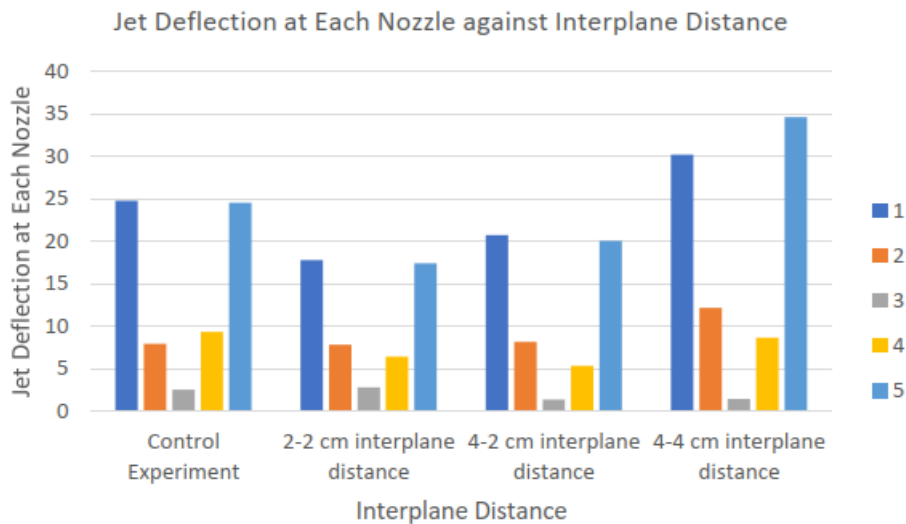


Figure 5. Bar Graph of Angle of Jet Deflection against Interplane Distance

It was identified that the outermost nozzles for each run, produce the highest jet deflection. This corresponds with the facts that the outermost nozzles of the setup will experience greater jet deflection due to having a one-sided external electrical field from another nozzle. Meanwhile, the innermost nozzle for each run had the smallest jet deflection. This is because it is constrained by the electrical fields of the adjacent nozzles.

For nanofiber diameter analysis, Fig. 6 shows the bar graph of mean diameter of nanofiber on each spot (micrometre) against distance between plane. It is observed that the nanofibers obtained from each configuration are generally smooth with fewer beads along the strands. 2-2 cm interplane distance produces the most uniform nanofibers, with the smallest difference between the highest and lowest mean diameters, which is 0.3062 μm . This is because the symmetrical setup results in a symmetrical electrical field distribution, uniformly controlling the field at each nozzle resulting in whipping effect of polymer jet [2].

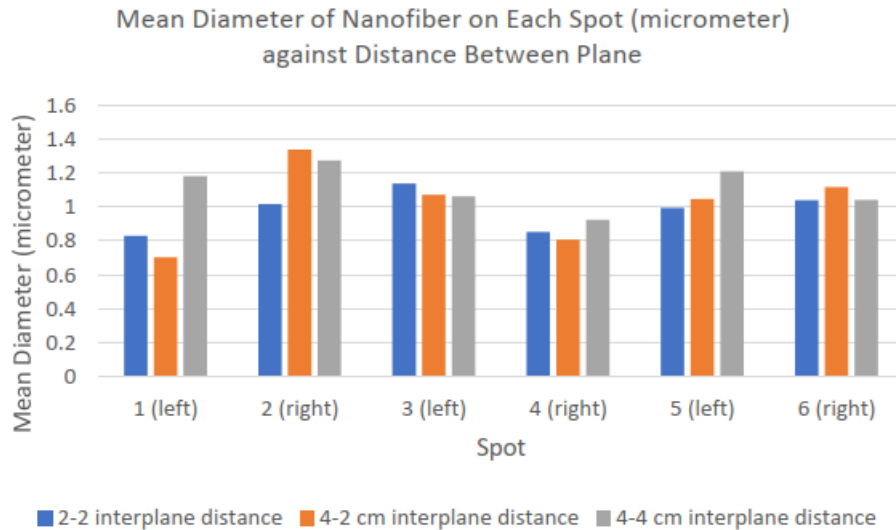


Figure 6. Bar graph of Mean Diameter of Nanofiber on Each Spot (micrometre) against Distance Between Planes

4. CONCLUSION

It can be concluded that the arrangement of the nozzles in multi-plane with multi-nozzle configuration affects the electric field in the process, behaviour of jets and fiber properties. In this study, the equally-spaced interplanes (2-2 cm) setup is found to be resulting in a more uniform electric field in the vicinity of the nozzles.

REFERENCES

- [1] Hanna Sofia Salehuddin, W. N. L. M., Edzrol Niza Mohamad. (2017). Multiple-jet electrospinning methods for nanofiber processing: A review. *Materials and Manufacturing Processes*, 33(5), 479-498. doi:10.1080/10426914.2017.1388523
- [2] Hanna Sofia Salehuddin, W. N. L. M., Edzrol Niza Mohamad. (2021). Simulation and experimental study of parameters in multiple-nozzle electrospinning: Effects of nozzle arrangement on jet paths and fiber formation. *Journal of Manufacturing Processes*, 62, 440-449. doi:10.1016/j.jmapro.2020.12.024
- Yu-Ke Wu, Z.-J. L., Jie Fan¹, Liang Wang, Peng-Fei Zhang, Jian Liu, and Yong Liu. (2019). Improved Fiber Uniformity and Jet Number in Multi-spinneret Electrospinning via Auxiliary Electrode. *Fibers and Polymers*, 20, 1172-1179. doi:10.1007/s12221-019-8859-2

Development Of Last-Mile Vaccine Delivery System for Government Health Clinics in Selangor – A Vehicle Routing Study

Muhammad Syazani bin Muhammad Nizam^a and Siti Nurmaya binti Musa^{b*}

Department of Mechanical Engineering,
Faculty of Engineering, Universiti Malaya,
50603, Kuala Lumpur, Malaysia

Email: ^a 17207384@siswa.um.edu.my, ^b nurmaya@um.edu.my

*Corresponding author

ABSTRACT

This study explores the development of a last-mile vaccine delivery system targeting government health clinics in Selangor, Malaysia, emphasizing the resolution of logistical challenges to enhance vaccine distribution efficiency. The investigation was catalyzed by the critical necessity for efficient vaccine distribution highlighted during the COVID-19 pandemic. The research incorporated a problem analysis of existing systems, followed by the evaluation of current methods and the simulation of optimized routes using algorithmic strategies, specifically the Nearest Neighbor Approach and Large Neighborhood Search. The findings reveal a significant enhancement in distribution efficiency, evidenced by a reduction in average travel distance by 27.98 km, representing a 13.88% decrease. This optimization translates into lower operational costs and improved vaccine accessibility, crucial in health emergency.

Keywords: Algorithm; Delivery; Optimization; Routing; Vaccine

1. INTRODUCTION

This research aims to develop an optimized last-mile vaccine delivery system for government health clinics in Selangor using innovative vehicle routing algorithm by addressing logistical challenges to improve efficiency and ensure timely access to vaccines.

1.1 Problem Statement

Current last-mile vaccine delivery in Selangor struggles with route optimization and logistical challenges, particularly in remote areas [2]. These inefficiencies lead to delays and increased vaccine wastage, especially during health crises like the COVID-19 pandemic. Urgent implementation of Vehicle Routing Problem (VRP) strategies is necessary to enhance route efficiency and optimize resource utilization for critical healthcare needs [1].

1.2 Objectives

1. To investigate the challenges and issues related to last-mile vaccine delivery.
2. To identify the various distribution methods for delivery system.
3. To propose a last-mile vaccine delivery system for government health clinics in Selangor.

2. METHODOLOGY

Fig. 1 shows the flowchart of the whole system starting with data preparation, algorithm implementation and verification.

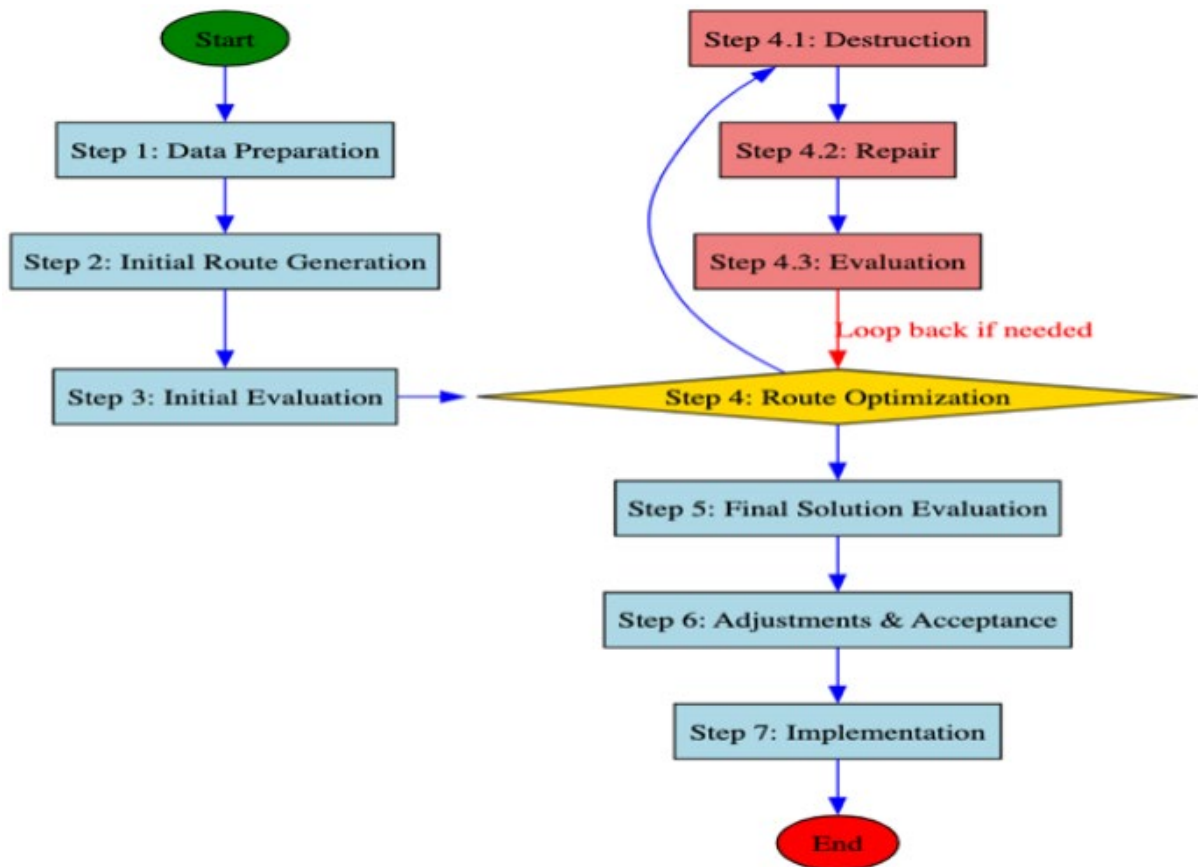


Figure 1. Algorithm Implementation and Verification Flowchart

Fig. 2 illustrates the fundamental visualisation of the TSP and LNS algorithm which was used in the optimization.

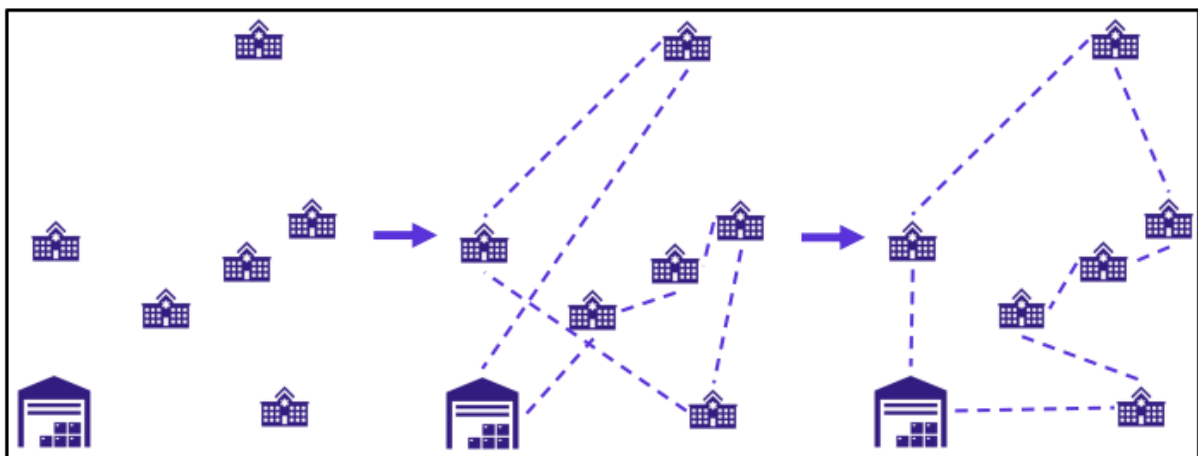


Figure 2 TSP and LNS.

Traveling Salesman Problem (TSP): Used to generate initial feasible routes, considering each vehicle's route as a separate TSP.

Large Neighborhood Search (LNS): Improved initial routes by exploring large segments of the solution space through a cycle of destruction and repair. [3]

3. RESULTS AND DISCUSSION

Fig. 3 displays the overall optimized travel distances across depots, showing significant reductions achieved through the Large Neighborhood Search (LNS) algorithm.

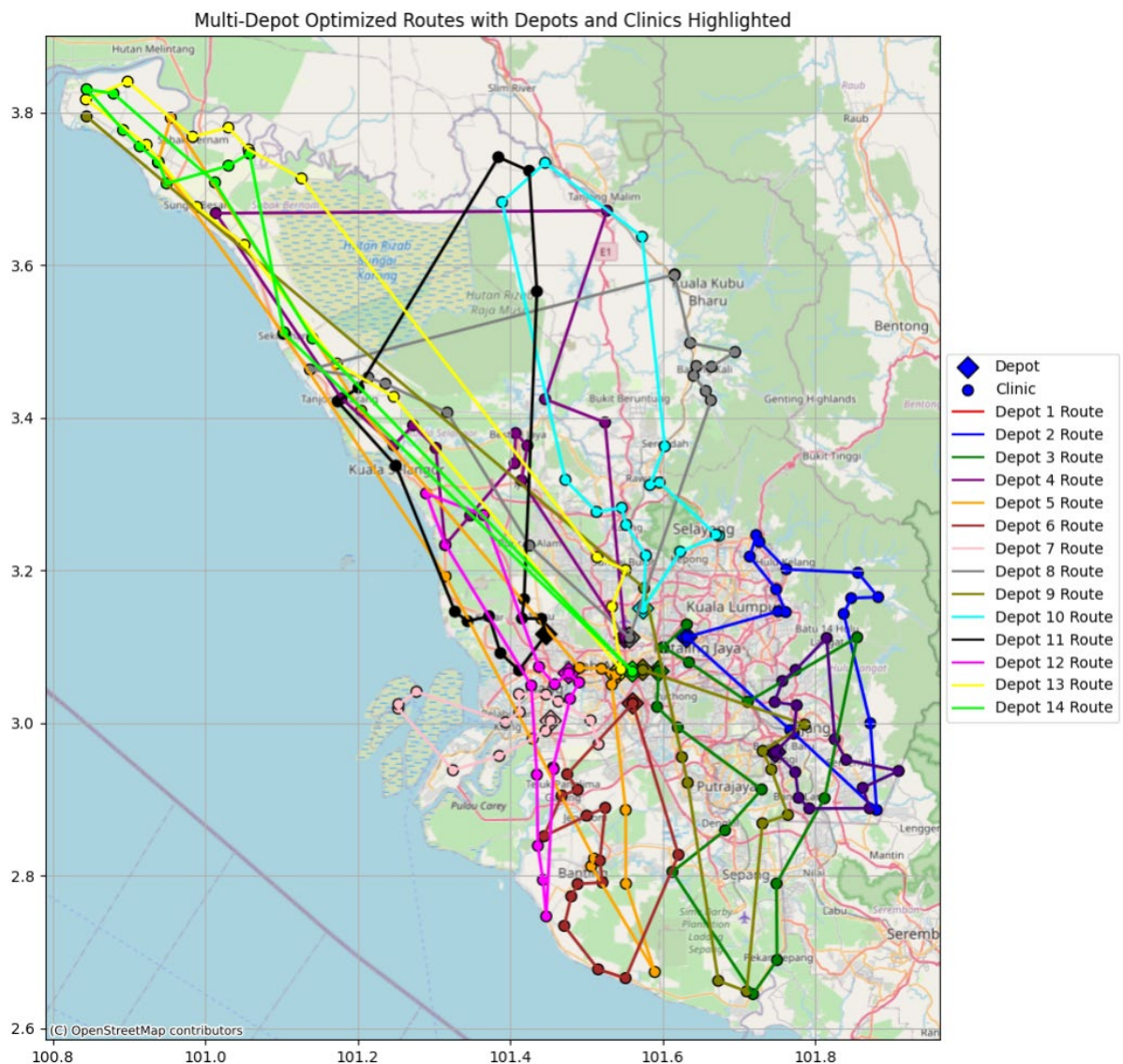


Figure 3. Optimized routes

From Fig. 4, the largest reduction can be seen on routes serviced by depot 8, reduced from 400.11 to 239.71km which is a 40.09% reduction. The average travel distance was able to be reduced by 13.88% Crucial for cost-saving and efficiency.

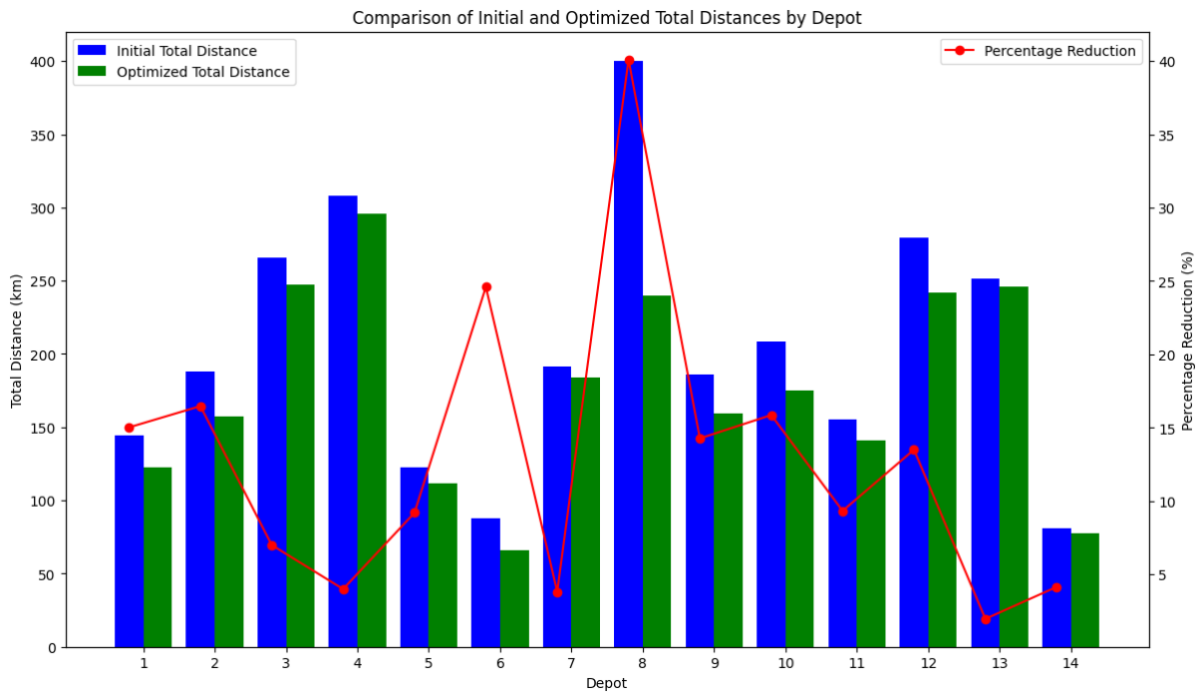


Figure 4. Comparison of Initial and Optimized Routes

3.1 Impact of Increased Fleet Capacity

Table 1 shows that increasing truck capacity boosts vaccine supply. It can optimize vehicle allocation, crucial during pandemics where demand factor can spike up to 20 to 40 times.

Table 1. Various Fleet Capacity and Demand

| Truck Capacity (doses) | Last Demand Factor | Total Demand |
|------------------------|--------------------|--------------|
| 115200 | 8 | 752,877 |
| 234240 | 17 | 1,505,754 |
| 353280 | 26 | 2,258,631 |
| 472320 | 34 | 2,927,855 |
| 591360 | 43 | 3,680,732 |

3.2 Impact of Changing Depot Locations

Fig. 4 shows the suggested the new depot locations determined using the center of gravity methods in each district.



Figure 4. New Depot Locations Optimized Routes

As a result, the total travel distance was reduced by 53.49% and average travel times were reduced by 27.66%.

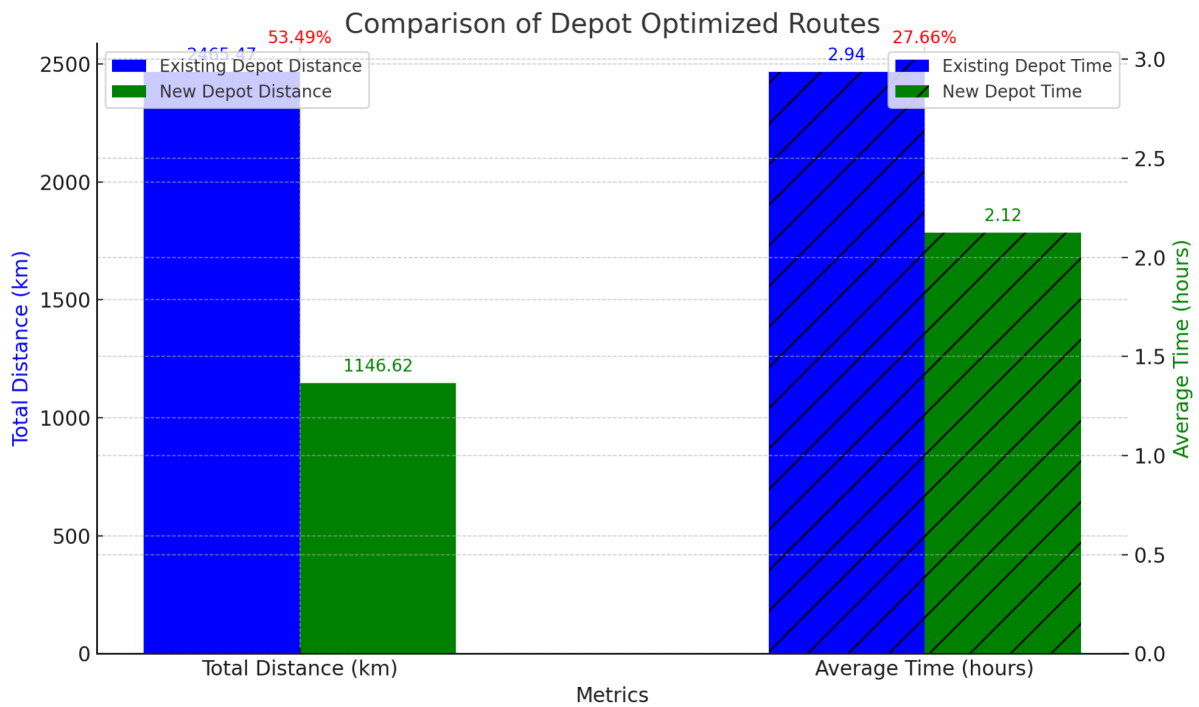


Figure 5. Comparison between Old and New Depot Locations.

4. CONCLUSION

The study identified key challenges in last-mile vaccine delivery in Selangor, notably access disparities in rural areas and varying demands. Through a detailed analysis of vehicle routing parameters, areas needing improvement were highlighted. A new delivery system using the TSP and LNS algorithms was developed, reducing delivery distances by an average of 13.88% across Selangor, significantly enhancing efficiency. Further analysis found moving the depot closer to the rural areas reduced travel distance by more than half.

REFERENCES

- [1] Fahrni, M. L., Ismail, I. A.-N., Refi, D. M., Almeman, A., Yaakob, N. C., Saman, K. M., Mansor, N. F., Noordin, N., & Babar, Z.-U.-D. (2022). Management of COVID-19 vaccines cold chain logistics: a scoping review. *Journal of Pharmaceutical Policy and Practice*, 15(1). <https://doi.org/10.1186/s40545-022-00411-5>
- [2] S.S, R. S., Omar, M., Moin, N. H., & Smith, D. K. (2010). Locational analysis of public health facilities: a case study of Telok Panglima Garang, Selangor, Malaysia. *Malaysian Journal of Science*, 29(2), 98–118. <https://doi.org/10.22452/mjs.vol29no2.2>
- [3] Yuan, R. (2022). An Optimization of COVID-19 Vaccine Distribution in Canada Based on the VRP Model. *Journal of Physics: Conference Series*, 2381(1), 012114. <https://doi.org/10.1088/1742-6596/2381/1/012114>

Lightweight Design and Fabrication of Water Bottle Replenishing Tool

Naim bin Nasri ^a and Tan Chin Joo^{b*}

Department of Mechanical Engineering,
Faculty of Engineering, Universiti Malaya,
50603, Kuala Lumpur, Malaysia

Email: ^a naimnasri05@gmail.com, ^b tancj@um.edu.my

*Corresponding author

ABSTRACT

This study focuses on the design, fabrication, and user evaluation of a novel water bottle replenishing tool intended to assist in lifting and replacing heavy 5-gallon water bottles on top-loading water dispensers. Motivated by the need to alleviate physical strain associated with handling large water bottles, particularly for women, the elderly, and those with physical limitations, the primary objective was to create a cost-effective, easy-to-use, and ergonomically beneficial tool that could be easily stored when not in use. The project included conceptual design, material selection, prototyping, and user testing. Results from laboratory and field tests indicated a significant reduction in physical effort and positive user feedback, highlighting the tool's potential to enhance safety and usability.

Keywords: Compactness; Ergonomics; Safety; Usability; Water Dispensers

1. INTRODUCTION

The prevalent use of large, cumbersome water bottles necessitates innovative solutions to prevent injuries and improve usability in water dispensing practices. The conventional method of manually lifting and inverting water bottles poses risks of back injuries and strains, particularly affecting women, the elderly, and those with physical limitations [1]. These ergonomic challenges are compounded by the significant weight of a full 5-gallon water bottle, which can weigh approximately 18.9 kilograms. This research stems from the need to address these ergonomic and safety challenges through a tailored design that simplifies the bottle handling process.

Existing devices and patents, such as MY 184822-A, focus on mechanisms to lift, invert, and secure a 5-gallon water bottle into top-loading type water dispensers [3]. However, these devices are often unsuitable for a residential setup due to their cost, size, and complexity in terms of storage. Hence, a new approach was required to develop a solution that is not only effective in function but also cost effective, compact, and user-friendly. This led to the creation of a water bottle replenishing tool that utilizes the typically unused space behind a water dispenser, optimizing storage and accessibility while addressing the challenges of lifting and inverting large water bottles.

The design of the tool was influenced by a thorough review of existing patents, including MY-184822-A, which provides a foundational framework for lifting mechanisms but falls short in terms of cost efficiency and space utilization for residential users. Studies have shown that ergonomic interventions can significantly reduce the physical strain associated with lifting activities, particularly for women and the elderly who are more susceptible to musculoskeletal disorders due to their physical nature [2].

To overcome these limitations, the proposed design incorporates two primary innovations: a compact wall-mounted structure that enhances space efficiency and an ergonomic mechanism that significantly reduces the physical effort required to lift and invert the bottle.

2. METHODOLOGY

The development of the water bottle replenishing tool was underpinned by a systematic design process aimed at meeting key criteria such as affordability, compactness, ease of operation, and user friendliness. The goal was to cater to a diverse user base, including those with lower household incomes, by creating a tool that simplifies the task of lifting and inverting a 5-gallon water bottle—traditionally a significant ergonomic challenge.

Initially, two designs were conceptualized with a focus on leveraging underutilized wall space in domestic settings, a strategy that enhances spatial efficiency and ensures the tool's accessibility. Each design incorporated innovative mechanisms to minimize the physical effort required by the user, essential for enhancing the ergonomic handling of heavy water bottles. Of the two proposed designs, the second was selected due to its simplicity, fewer component requirements, and lower cost implications. This chosen design was further refined using SOLIDWORKS, which facilitated precise adjustments and optimizations before moving into the prototyping phase.

To ensure the structural integrity and functionality of the design under operational conditions, Finite Element Analysis was conducted. This simulation was crucial in identifying and addressing potential stress points and strain distributions across the tool, particularly during the lifting and inverting processes. The analysis informed decisions on material selection and design modifications, with 4080 Aluminum Extrusion being selected for its optimal balance of strength, cost, and weight. The tool's fabrication employed standard metalworking techniques—cutting, drilling, and threading—that were chosen for their feasibility in low-cost production settings. The processes were tailored to be straightforward, ensuring that the final assembly could be easily managed by end-users with minimal technical skills.

3. RESULTS AND DISCUSSION

The prototype of the water bottle replenishing tool was extensively tested to evaluate its functionality in terms of lifting and inverting a 5-gallon water bottle. These tests confirmed the prototype's ability to handle the weight and dimensions of standard water bottles without any structural failures or safety issues. The tool successfully lifted and inverted the water bottle into the dispenser, demonstrating robustness and stability during operation.

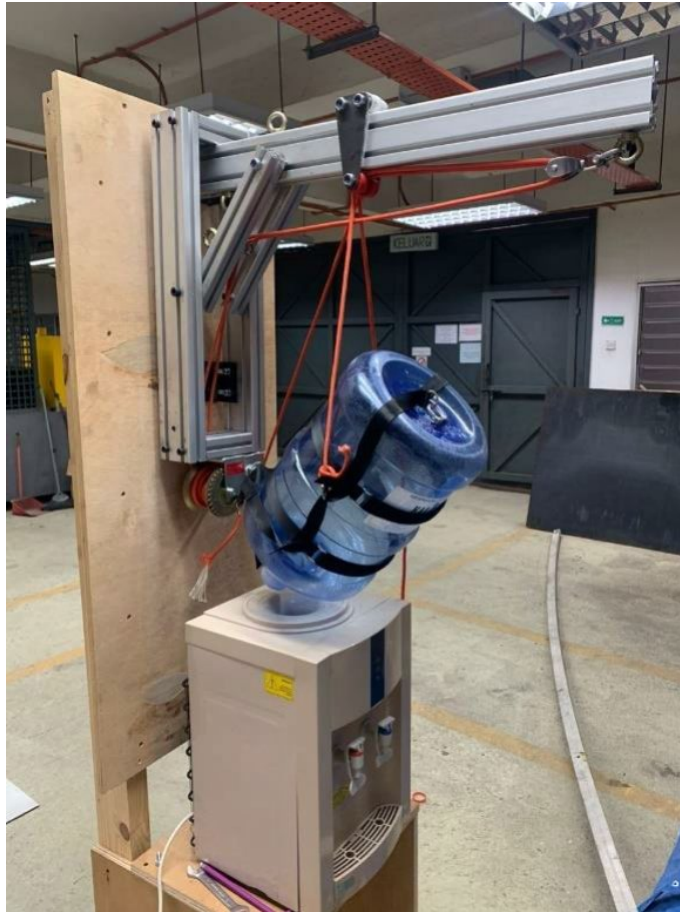


Figure 1. Fabricated Bottled Water Lifting Tool



Figure 2. Fabricated Tool in Folding Position

A user experience survey was conducted to gather feedback from potential end-users, focusing on ease of use, safety, and overall satisfaction. While the tool was generally well-received, with users appreciating the reduced effort required for bottle handling, several areas for improvement were highlighted:

- 1) Some users reported that the force required to operate the tool, particularly the hand winch, was still a bit high, indicating that further enhancements are needed to reduce physical exertion.
- 2) Feedback suggested that while the tool was stable, the folding mechanism could be improved to ensure safer operation and storage.

The evaluation of the design objectives indicates the design of the water bottle replenishing tool successfully achieved cost-effectiveness. By utilizing materials such as 4080 Aluminum Extrusion and employing manufacturing processes that are both economical and scalable, the project adhered to budget constraints and align with the project's aim to provide a financially accessible solution for users. The wall-mounted design of the tool effectively capitalized on underutilized space, thus meeting the objective of compactness. While the tool performed well in terms of space-saving when installed, user feedback suggested the need for further improvements in the tool's storage and folding mechanism to enhance usability and safety when the tool is not in active use.

Finally, the tool generally meets basic safety standards, confirming its structural integrity and stability during operation. However, the results from user testing indicated a requirement for enhancements in the ergonomic design and the safety features of the tool. Specifically, improvements are needed to reduce the operational effort and to refine the folding mechanism, ensuring it is secure and user-friendly.

4. CONCLUSION

This research confirms that the developed water bottle replenishing tool substantially mitigates the risks and physical efforts traditionally associated with handling large water bottles. Through continuous improvement based on user feedback, the tool has been refined to meet the needs of its intended user base effectively. The ergonomic innovations introduced have the potential to significantly enhance quality of life and reduce injury risks, promoting broader adoption and improving safety in water bottle handling practices across various settings.

REFERENCES

- [1] Ahlgren, C., Malmgren Olsson, E. B., & Brulin, C. (2012). Gender analysis of musculoskeletal disorders and emotional exhaustion: interactive effects from physical and psychosocial work exposures and engagement in domestic work. *Ergonomics*, 55(2), 212-228. doi:10.1080/00140139.2011.646319
- [2] Saat, N. Z. M., Hanawi, S. A., Farah, N. M. F., Hanafiah, H., & Zuha, A. A. (2022). Relationship between physical activity and musculoskeletal disorders among low income housewives in Kuala Lumpur: A cross sectional study. In *PloS one* (Vol. 17, pp. e0274305). United States: Public Library of Science. doi:10.1371/journal.pone.0274305
- [3] Tan, C. J. & Jian, F. L. (2021). A bottle replenishing tool for top loading type water dispenser (Malaysian Patent No. MY-184822-A). Intellectual Property Corporation of Malaysia. <https://patents.google.com/patent/MY184822A/en?q=MY-184822-A>

Design & Development of Laboratory Scale Hydraulic Press for Recycling Metal Chips

Muhammad Haziq Iqbal bin Adnan^a and Tuan Zaharinie binti Tuan Zahari^{b*}

Department of Mechanical Engineering,
Faculty of Engineering, Universiti Malaya,
50603, Kuala Lumpur, Malaysia

Email: ^a hzqbal.lr@gmail.com, ^b tzaharinie@um.edu.my

*Corresponding author

ABSTRACT

Recycling metal chips (MCs) yielded from machining activities such as turning is feasible via pelleting. A machine was developed at a laboratory scale to recycle the MCs. The machine consisted of a hybrid metal die and hydraulic press machine structure. The development processes were market analysis, designing, modeling, simulating, fabricating, and testing. The structure and metal die were made of refurbished metals. Two different collar sizes were originally crafted yet found enough for a single piece. Varied load from the hydraulic press was applied to compact MC powder in various collar configurations. Two more components need to be added for the pellet extraction. Besides, some parts failed for a few reasons that were analysed via Root Cause Analysis (RCA). Instant modification was performed to prove the functional concept with some justified compromises.

Keywords: Circular Economy; Hydraulic Press; Metal Chips; Recycling; Simulation

1. INTRODUCTION

Metal chips (MCs) are a significant byproduct of machining processes such as turning, grinding, and milling. At Universiti Malaya, these MCs are frequently generated during teaching and research activities. Proper recycling of these MCs not only ensures a safer workshop environment but also supports the university's commitment to a circular economy. This research aimed to design and develop a laboratory-scale hydraulic press machine to compact MCs into briquettes, reducing dependency on new metal pellets and optimizing recycling activities. Besides, a concept of a hybrid metal die was introduced here, where two different pellet sizes can be produced in a single die. This study consumed available refurbished metals in Universiti Malaya. Functional testing of the metal die was executed to prove the hybrid concept.

2. METHODOLOGY

Initial design ideas were sketched based on market analysis of existing specifications. The chosen design was then modeled using SOLIDWORKS. Refurbished metals available at Universiti Malaya were used. Due to the absence of specific metal properties, assumptions were made for 3D modeling and simulation, which showed that AISI 1020 (mild steel) performed better in yield strength. Then, the hydraulic press machine and metal die were fabricated using available workshop machines and other

procured materials. Functional testing was conducted to verify the hybrid concept. Two different metal chips were collected from reciprocal saw and surface grinder machines, respectively. They were compressed and ejected in the fabricated metal die at 5, 10, and 15 tonnes. Root Cause Analysis (RCA) via Fault Tree Analysis (FTA) were performed to address component failures during testing, leading to modifications that improved the system's performance.

3. RESULTS AND DISCUSSION

Idea 3 as shown in Figure 1 provides a simple connection without requiring such modifications. This idea not only facilitates the implementation process but also reduces associated risks. This machine would compress the same way a man compresses an object with both hands. Thus, it needs a top-tapered shaft. The market analysis shows that the top-tapered shaft is the most effective way to adjust the shaft's depth to provide downward force from the top to compress the MCs and extract the pellet out. This feature overcomes the drawback of a permanent shaft which is developed in other ideas.

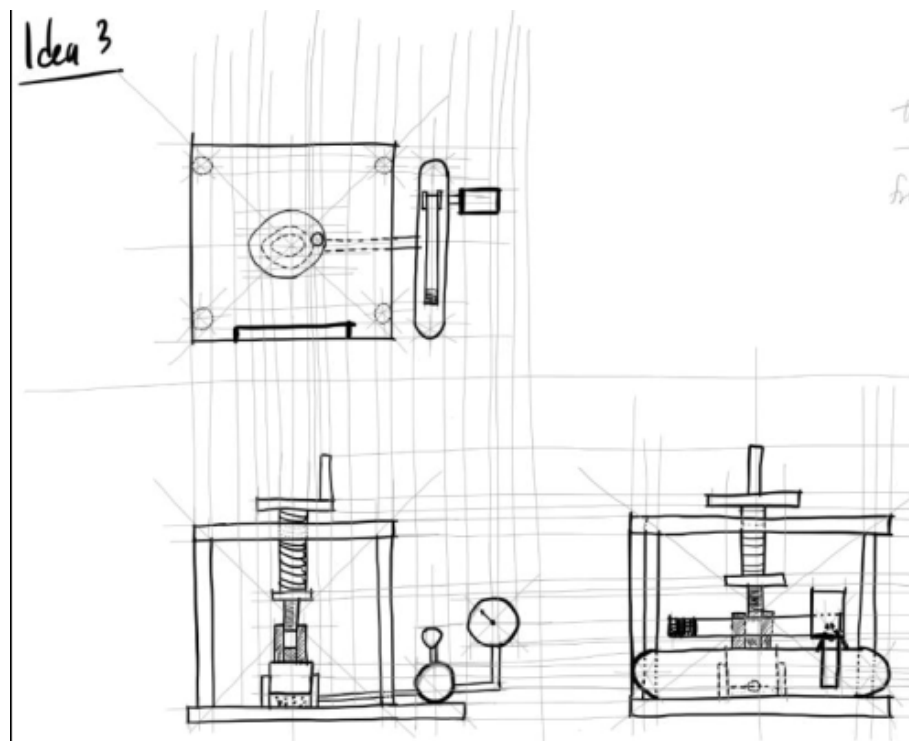


Figure 1. The selected idea & concept for the structure of press machine

Figure 2 is the model of the laboratory hydraulic press machine consists of 11 parts while 6 parts are required for the model of metal die. The overall height is almost like a 6-liter portable dispenser water bottle, and it has been developed to meet the scale of existing models in the market.

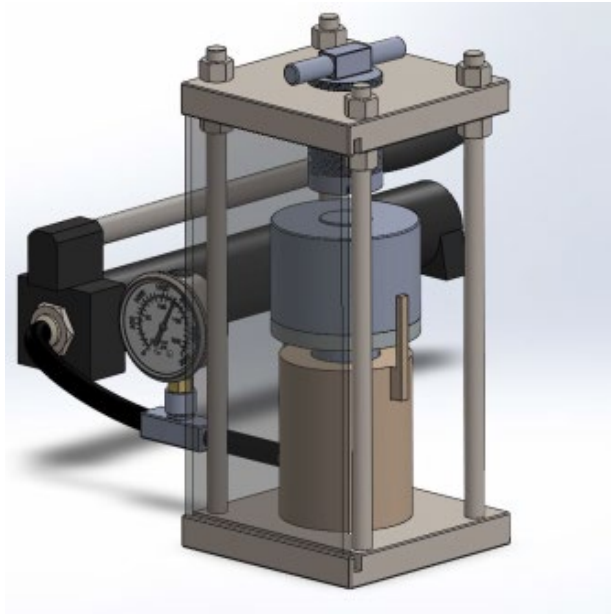


Figure 2. The hydraulic press machine

Most laboratory hydraulic press manufacturers use metal dies, requiring different sizes for different pallets [2]. A hybrid metal die with 10 mm (left) and 30 mm (right) as pictured in Figure 3 in section view was developed with two types of collars to fit the same die size. A clearance fit design ensures small clearance and easy assembly under high external loads [3].

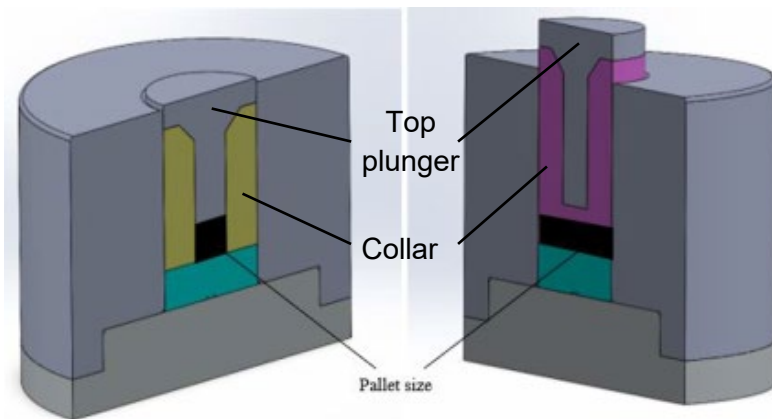


Figure 3. Metal die with hybrid concept

SS 316 and AISI 1020 are the assumed refurbished materials. Each material bears almost uniform maximum stress at each designated external load but do not over their respective yield strength. Thus, the structure would be safe with this load capacity as presented in Figure 4.

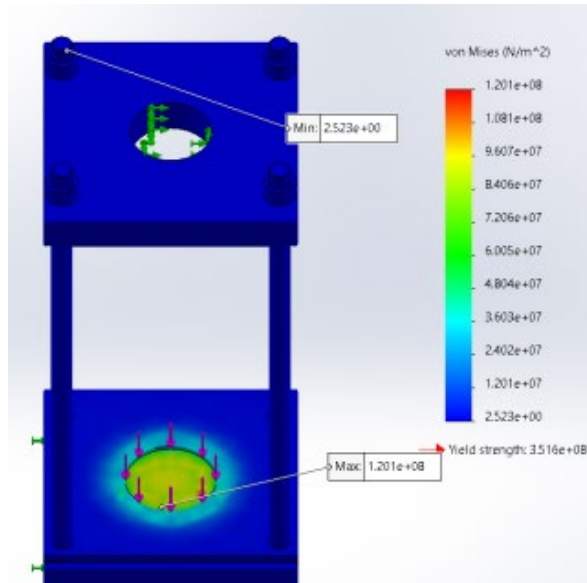


Figure 4. Simulation for machine's structure

Quality analysis and simulations of both metal dies revealed critical deformation of the top plunger and collar, surpassing the yield strength of AISI 1020 under a 30-ton hydraulic force (see Figure 5).

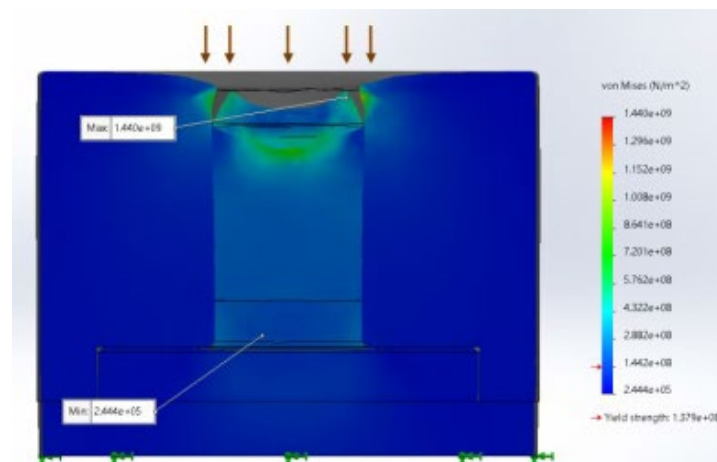


Figure 5. Simulation for metal die

Most metal die parts were made from refurbished mild steel, cutting prototype costs by 70%. Manufactured on a three-jaw lathe using various tools and feed rates for desired finishing, they followed JIS B 0401 for clearance fit. Some parts had showed corrosion because no coating applied (refer Figure 6).

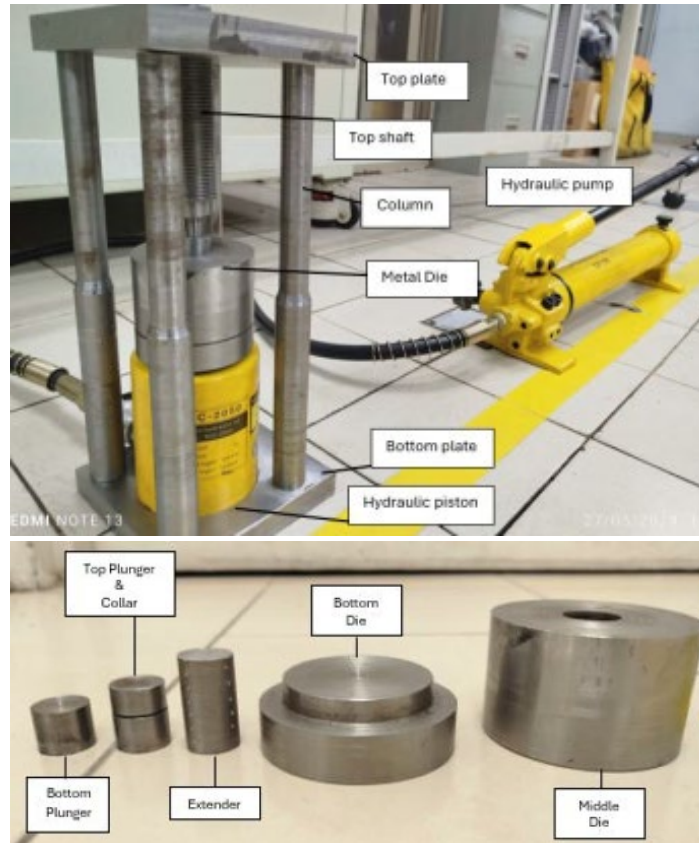


Figure 6. Hydraulic press machine with metal die

Figure 7 shows some samples that were compressed under load, with 10 mm pellets requiring 5 tons to form a solid pellet. Higher loads of 10 and 15 tons were used for 20 mm pellets. Having the smallest surface area will result to the highest stress and significant strain hardening, resulting in greater density. Strain hardening impacts pellet properties, enhancing density and strength [1].



Figure 7. Different pellet sizes were produced

Extractor collars were essential for pellets ejection. Components as depicted Figure 8 were chosen accordingly: scrap C-collar metal for 20 mm die and an abandoned ball bearing for 10 mm die, proving successfully the concept of pellet extraction at different sizes.



Figure 8. Extractor collars at different sizes

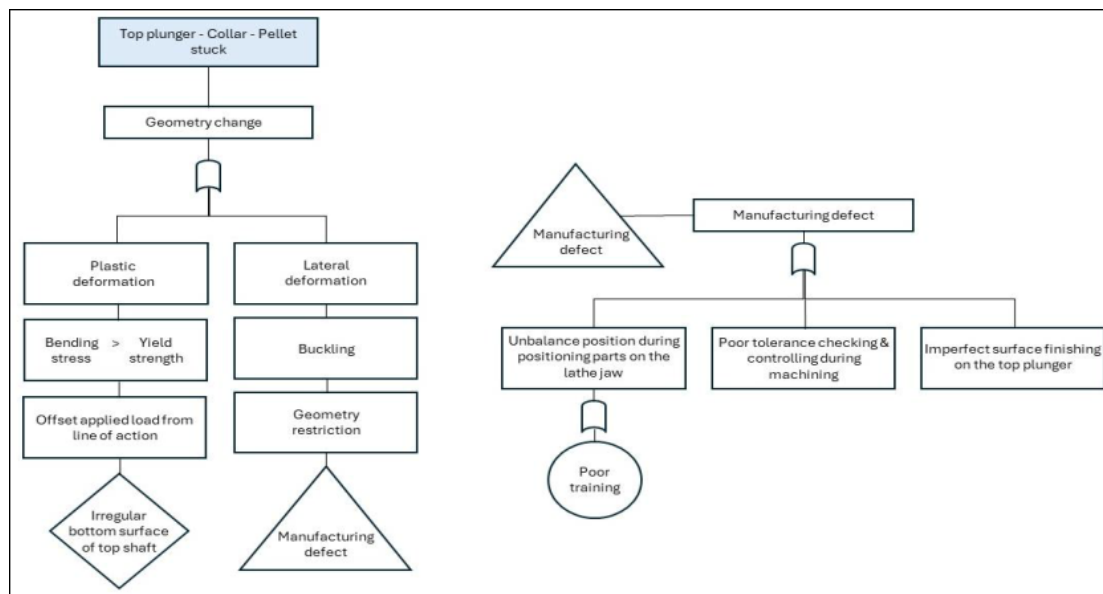


Figure 9. RCA for failed components

As depicted in Figure 9, The top event in the FTA was the stuck top plunger, collar, and pellet. Manufacturing defects led to lateral deformation, with lack of training identified as the root cause. Plastic deformation due to irregular bottom surface of the top shaft was noted, requiring an instant modification on the failed components. 10 mm die had used a slightly undersized collar and using an M10 bolt with a mild steel plate for even pressure distribution while 20 mm die deployed an extender

(see Figure 6) with same diameter. Hence, a lower quality in pellet finishing, such as crater-like edge on the pellet was the compromised element which leads to a finding that tolerance played significant roles in producing them.

4. CONCLUSION

Machining advances produce waste, addressed through recycling, with briquetting as a convenient method. Market analysis suggests developing a laboratory hydraulic press from refurbished mild steel. SOLIDWORKS modelling and static simulations were conducted, revealing plastic deformation due to high tonnage. The prototype utilized over 70% refurbished materials and cost with potential enhancements. Testing revealed pellet quality issues and identified root causes of component failures. The developed metal die proved functional for various pellet sizes.

REFERENCES

- [1] Ju, X., Zhang, K., Chen, Z., & Zhou, J. (2020). A Method of Adding Binder by High-Pressure Spraying to Improve the Biomass Densification. *Polymers*, 12(10), 2374. <https://doi.org/10.3390/polym12102374>
- [2] Specac. (n.d.). Evacuable pellet dies. <https://specac.com/wp-content/uploads/2023/11/Evac-dies-datasheet-RevB-23-10-25.pdf>
- [3] Velling, A. (2020, August 14). *Limits & Fits | Types of Fits Explained & Tolerance Charts. Fractory*. <https://fractory.com/limits-and-fits/>

SolidWorks Training Module for Technicians

Ahmad Faris Afham bin Sahari ^a and Aznijar bin Ahmad Yazid ^{b*}

Department of Mechanical Engineering,
Faculty of Engineering, Universiti Malaya,
50603, Kuala Lumpur, Malaysia

Email: ^a afas2001@gmail.com, ^b aznijar@um.edu.my

*Corresponding author

ABSTRACT

The SolidWorks Training Module for Technicians is a comprehensive and practical module aimed at improving the proficiency and understanding of technicians in utilizing SolidWorks, a prominent computer-aided design (CAD) software. The purpose of this training module is to cater to the special requirements of technicians by offering focused instruction and hands-on practice of SolidWorks functionalities. The content development process commences by gathering and analyzing data from the current training module and the accessible online course. The curriculum is strategically structured to sequentially address essential subjects, striking a harmonious equilibrium between academic comprehension and practical implementation via interactive exercises and projects. The SolidWorks Training Module for Technicians is the complete training module created for the project. It consists of all the chapters that have been determined in the module. The chapters serve as an introductory section to SolidWorks. The SolidWorks Training Module for Technicians has been specifically developed to equip technicians with the necessary expertise and understanding to effectively employ SolidWorks in their daily responsibilities. The training module empowers technicians to enhance design quality, minimize errors, and optimize productivity.

Keywords: SolidWorks; CAD software; Training module; Technicians; Design productivity

1. INTRODUCTION

This research project aims to create a comprehensive SolidWorks training module specifically designed for technicians with no prior computer-aided design (CAD) experience. The objective is to equip technicians with essential skills to proficiently utilize SolidWorks for designing and modeling mechanical components and systems. In the competitive industrial landscape, efficient CAD tool usage is crucial for optimizing design processes and enhancing productivity. However, technicians often lack proficiency in SolidWorks, hindering their ability to effectively contribute to the design and production process.

By developing a technician-focused training module, this project seeks to bridge the gap in technicians' SolidWorks expertise. The module will provide step-by-step instructions, interactive tutorials, and practical examples to enable technicians to generate, modify, and evaluate designs autonomously.

2. METHODOLOGY

2.1 Data Collection and Analyzation

Data collecting helps identify target audience learning needs. The SolidWorks training module can be tailored to readers' skill levels by incorporating content from other modules and online courses. This ensures relevant, engaging, and learning-focused content.

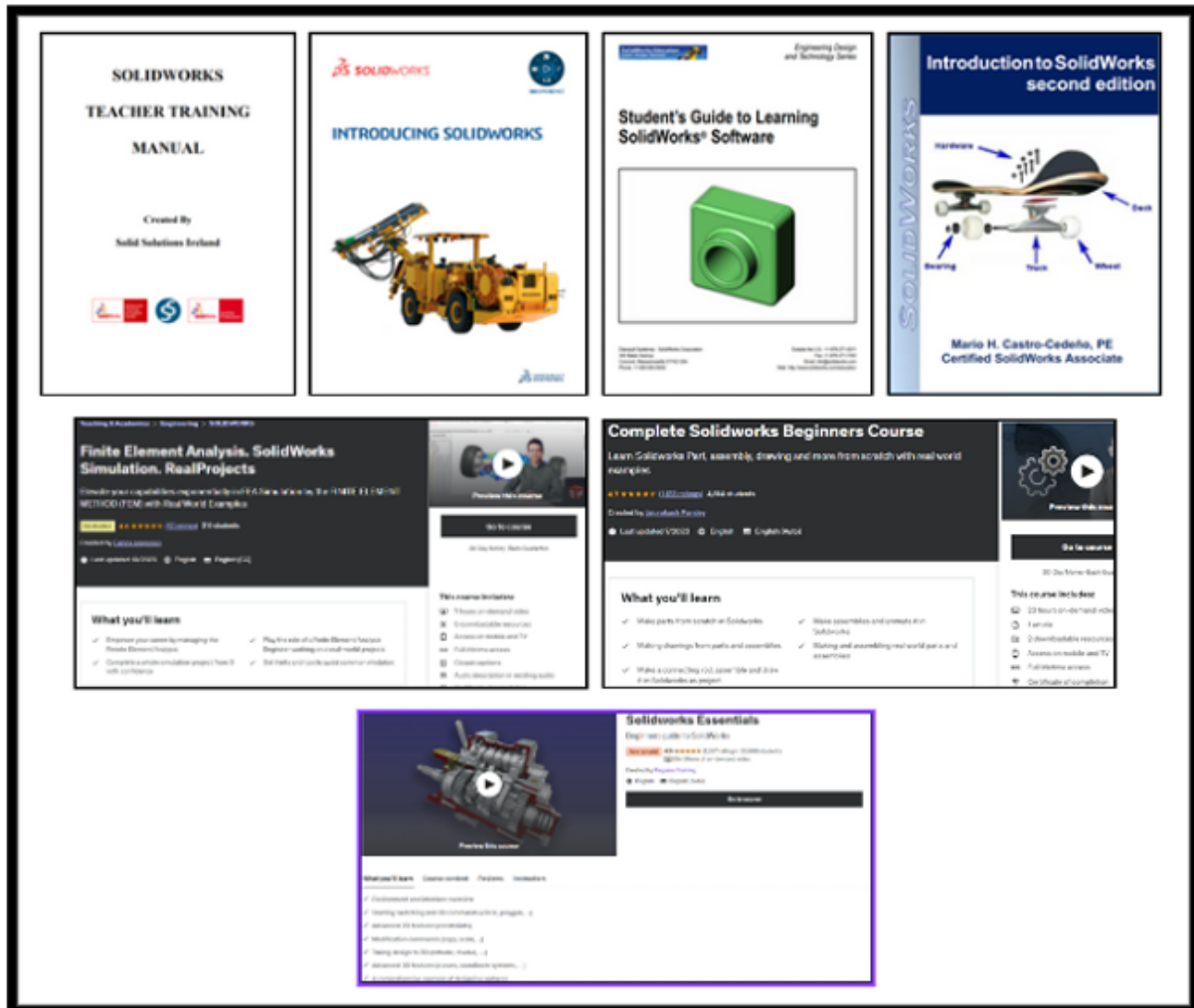


Figure 1. Example of available training module and online course of SolidWorks Training

2.2 Define Learning Objectives

Upon thorough analysis of all the reference modules and completion of the online course, several learning objectives were identified and evaluated. The primary goal is to generate three-dimensional models using SolidWorks. The next objective is to construct or put together various components or parts. The third objective entails the production of intricate and comprehensive drawings, and the last objective entails the identification and resolution of issues through troubleshooting.

2.3 Curriculum Design

Once all the learning objectives have been determined and finalized, the topic for the training module may be prepared to facilitate content production and the creation of hands-on exercises for the module. The chapter that are included in the module are introduction to SolidWorks, sketching, 3D modelling, assemblies, drawing and documentation, and design validation and analysis

2.4 Content Development

The module's content can be prepared with the assistance of the curriculum design. The generated content must meet all the specified learning objectives to make sure that the objective of the project is achievable. Continuous modification guarantees that the training module stays up-to-date and influential, empowering technicians to improve their productivity, efficiency, and proficiency in SolidWorks.

2.5 Hands-on Exercise

Once the module's content is completed, hands-on exercise can be created. The hands-on practice must be pragmatic, providing explicit instructions to ensure that all readers can easily follow along without encountering any difficulties.

3. RESULTS AND DISCUSSION

3.1 SolidWorks Training Module for Technicians

The SolidWorks Training Module for Technicians is the finished training module developed for the project. It consists of 6 total chapters that have been decided in the module. The 6 chapters are an Introduction of SolidWorks, Sketching, 3D Modelling, Assemblies, Drawing and Documentation, and Design Validation and Analysis. Each chapter will have their respective exercise for the user to follow along. An extra chapter is added to compile all the useful tips given throughout the module. The full module can be downloaded from:

https://drive.google.com/file/d/1AVdghXmaKW_8aS-103GEofRS2D6dUt0P/view?usp=drive_link

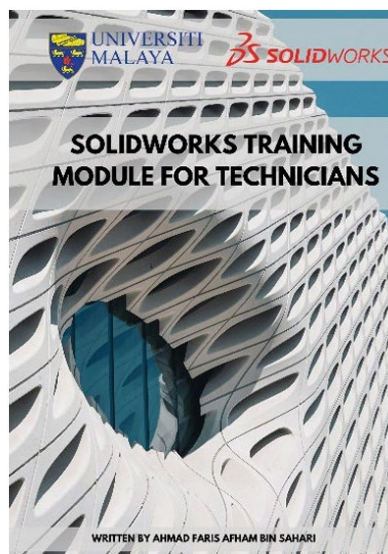


Figure 2. Cover page for the SolidWorks Training Module for Technician

3.2 Website for SolidWorks Training Module for Technicians

The website for the SolidWorks Training Module for Technicians has been created as a substitute for the written training module. This website may be accessed via both computers and phones, enhancing the accessibility of the training programme.

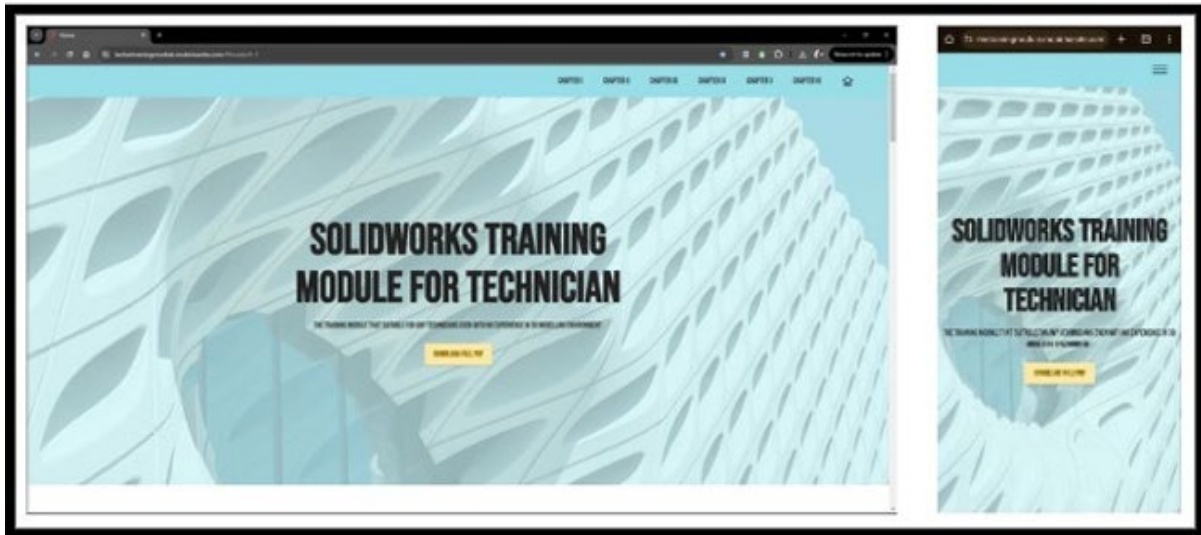


Figure 3. Web and mobile view of the website

The PDF version of the module can also be downloaded from the website. This will make sure that user can always reach the training module if the internet is available. The link to the website is <https://techietrainingmodule.mobirisesite.com>

3.3 Difference between the training module that have been developed with the existing training module

The primary distinction lies in the fact that the newly designed training module will possess a significantly more straightforward design compared to the preexisting module. The application of the Pareto principle is the reason behind the development of the training module. The Pareto principle, sometimes known as the 80/20 rule, asserts that a significant majority (about 80%) of the effects or outcomes can be attributed to a small minority (around 20%) of the causes or factors.

3.4 Discussion

Developing a SolidWorks Training Module for Technicians offers several advantages, but also poses some limitations. The main advantage is that it enables technicians to fully leverage SolidWorks in their daily work. Thorough training helps technicians create accurate 3D models, assemble components effectively, conduct analyses, and generate comprehensive technical drawings.

However, creating an effective training module requires tailoring it to the specific needs and skill levels of the target technicians. Striking the right balance between theory and practical application is crucial for ensuring technicians can apply their knowledge in real-world scenarios. Another limitation is keeping the training module up to date with the latest SolidWorks versions and features. Failure to do so can render the training module outdated and less valuable over time.

By addressing both the advantages and limitations, organizations can develop a comprehensive SolidWorks Training Module that effectively equips technicians with the necessary skills and knowledge to optimize their use of the software, ultimately enhancing the overall design and engineering processes.

4. CONCLUSION

The SolidWorks Training Module for Technicians is a thorough training that provides technicians with the essential skills and knowledge to efficiently utilize SolidWorks in their engineering and design processes. Through the successful completion of this training, technicians will acquire an enhanced comprehension of 3D modelling, assembly development, design analysis, and technical drawing generation. These are all essential skills for contemporary engineering professionals.

REFERENCES

- [1] Castro-Cedeno, M. (2022). Introduction to SolidWorks, second edition. Retrieved from Academia.edu
website:https://www.academia.edu/9910518/Introduction_to_SolidWorks_second_edition
- [2] FUNDAMENTALS OF 3D DESIGN AND SIMULATION. (n.d.). Retrieved From <https://www.solidworks.com/sites/default/files/2020-05/Fundamentals3DDesign-SIM-ENG-SV.pdf>
- [3] INTRODUCING SOLIDWORKS. (n.d.). Retrieved from <https://files.solidworks.com/pdf/introsr.pdf>
- [4] SOLIDWORKS TEACHER TRAINING MANUAL Created By Solid Solutions Ireland. (n.d.). Retrieved from <https://t4.ie/pdf/teacher%20manual%20r3.pdf>

Universiti Malaya Student Residence Audit: Student Satisfaction Towards Facilities Management

Muhammad Amir Arif bin Mohamed Maliki^a and Aznijar bin Ahmad Yazid^{b*}

Department of Mechanical Engineering,
Faculty of Engineering, Universiti Malaya,
50603, Kuala Lumpur, Malaysia

Email: ^a amirxrif@gmail.com, ^b aznijar@um.edu.my

*Corresponding author

ABSTRACT

This study investigates student satisfaction towards facilities management at Universiti Malaya's 12th Residential College (KK12) in light of a large number of complaints reported in UM Helpdesk between October 2023 and March 2024. The research addresses the pressing need to rectify discrepancies in resident satisfaction by identifying critical indicators that requiring immediate attention and proposing strategies for improvement. This research employed an adopted and adapted questionnaire employing a 5-point Likert scale across 16 indicators. The findings indicate that KK12 residence are moderately satisfied with overall facilities; nonetheless, they highlight significant concerns about WIFI or internet connection, laundry services, and bathroom and toilet quality, with mean ratings of 2.87, 2.81, and 2.69, respectively. These discrepancies are not merely inconveniences but are intricately intertwined with students' well-being and academic pursuits, potentially impeding their holistic development. The study emphasizes the importance and significance of resolving these issues in order to create an atmosphere advantageous to student success.

Keywords: Facilities Management; Internet Connectivity; Laundry Services; Student Satisfaction; Universiti Malaya.

1. INTRODUCTION

From October 2023 to March 2024, Universiti Malaya's 12th Residential College (KK12) had the highest number of helpdesk reports (2,015), indicating unique issues impacting residents' quality of life. These complaints may signal structural flaws in infrastructure, administration, or service delivery, affecting resident satisfaction and trust in the college's supportiveness. Addressing these issues is crucial to prevent further dissatisfaction and enhance residential life. This research aims to comprehensively assess KK12's challenges and propose tailored solutions based on empirical data, benefiting both KK12 residents and other residential colleges in Universiti Malaya.

2. METHODOLOGY

This study utilizes a cross-sectional research design to assess residential satisfaction at Universiti Malaya's 12th Residential College (KK12). A questionnaire survey comprising 28 questions, validated through a content validity test with an 80 percent relevancy score, was employed. A pilot survey with 40 respondents ensured the questionnaire's practical execution. Simple random sampling was adopted, targeting a minimum sample size of 249 respondents. These questions were adapted from previous studies and aim to measure KK12 residents' satisfaction towards all the facilities.

The questionnaire has 9 questions on the respondents' demographic characteristics, 3 questions on overall residential satisfaction (ORS) index and 16 questions on maintenance management. A 5-point Likert scale was used to assess the satisfaction.

3. RESULTS AND DISCUSSION

The ORS index, gauging overall residential satisfaction, revealed that the largest portion of respondents (30.6%) felt neutral about their current residence, while satisfied and very satisfied respondents together accounted for 30.6%. Dissatisfied and very dissatisfied respondents made up 38.9% of the total. Table below presents descriptive statistics for the 16 indicators.

Table 1: Descriptive statistic of the indicators

| Indicator | Mean | Std. Deviation | Satisfaction Level |
|----------------------|------|----------------|--------------------|
| Electricity | 3.53 | 1.023 | Satisfied |
| Internet | 2.87 | 1.44 | Dissatisfied |
| Water supply | 3.23 | 1.44 | Satisfied |
| Bathroom | 2.69 | 1.46 | Dissatisfied |
| Laundry machine | 2.81 | 1.39 | Dissatisfied |
| Lift/stairs | 3.16 | 1.41 | Satisfied |
| Lighting | 3.32 | 1.47 | Satisfied |
| Fan | 3.39 | 1.42 | Satisfied |
| Ventilation | 3.45 | 1.36 | Satisfied |
| Bedroom furniture | 3.19 | 1.45 | Satisfied |
| Bedroom arrangement | 3.27 | 1.49 | Satisfied |
| Security and privacy | 3.60 | 1.44 | Satisfied |
| Activity center | 3.12 | 1.41 | Satisfied |
| Sport area | 3.28 | 1.48 | Satisfied |
| Food court | 3.95 | 1.24 | Very satisfied |
| Ironing tools | 3.37 | 1.48 | Satisfied |

Note: Very satisfied (mean ≥ 4), satisfied (mean ≥ 3), dissatisfied (mean < 3), very dissatisfied (mean < 2)

3.1 Bathroom and Toilet Assessment

An assessment was done for all block in KK12. Block A stands out with superior conditions, with 59% of toilets and 64% of bathrooms rated A, indicating well-maintained and comfortable facilities. Block B presents the most critical situation, with only 10% of toilets and 13% of bathrooms rated A, and a

substantial 48% of toilets and 49% of bathrooms rated C (unusable). Block C and D show balanced results but more to B-rated. The analysis shows that while combining A and B ratings indicates compliance with DOSH 1:7 bathroom-to-person ratio standards [1] in most blocks, the reliance on B-rated (uncomfortable but usable) facilities highlights potential issues.

3.2 UM Helpdesk Report Assessment

An assessment on bathroom and toilet issues in KK12 was done to study the maintenance process through helpdesk. It revealed significant inefficiencies in the maintenance process. Despite a high volume of complaints, response and resolution times were notably inadequate. Simple issues, like changing a showerhead or fixing a flush handle, exceeded the stipulated resolution time of 10 working days set by JPPHB. This highlights concerns about the maintenance culture within residential colleges, particularly in KK12.

3.3 Laundry Machine Demand Analysis

A demand study on washing machines in KK12's male and female blocks revealed distinct usage patterns and resident satisfaction issues. Female block washers experienced longer wait times, with wait periods up to 60 minutes, while male block wait times rarely exceeded 40 minutes. Female blocks reported more frequent maintenance and payment issues, including money being trapped and machines not accepting payments. Residents recommended QR code payments and better maintenance routines. Overall, dissatisfaction with laundry facilities was higher in female blocks.

4. CONCLUSION

This study has successfully measured student satisfaction with facilities management at KK12, highlighting areas needing improvement. The management should put more concerns regarding internet connectivity, laundry services, and bathroom quality. Findings emphasized the need for substantial improvements, especially in these critical areas. Improved facilities are crucial for enhancing student well-being and academic performance. The study recommends focused upgrades in bathroom facilities, continuous monitoring of WIFI connectivity, and adding laundry machines in the female block. By addressing these concerns, the university can significantly enhance student satisfaction and academic achievement.

REFERENCES

Idris, N. F. B. (n.d.). Official website Department of Occupational Safety and Health - Welfare Facilities. <https://www.dosh.gov.my/index.php/construction-safety-v/welfare-facilities>

Design and Fabrication of a Prototype Floating Structure for Integrated Solar, Wind, and Wave Energy Harvesting

Fauzan Ariff bin Shahrizal ^a and Norhafizan bin Ahmad ^{b*}

Department of Mechanical Engineering,
Faculty of Engineering, Universiti Malaya,
50603, Kuala Lumpur, Malaysia

Email: ^a fauzan.shahrizal@gmail.com, ^b norhafizan@um.edu.my

*Corresponding author

ABSTRACT

This paper presents the design and fabrication of a prototype offshore energy harvester that integrates wind, solar, and wave energy collection into a single structure. The research aims to provide insights into the stability and feasibility of a floating structure capable of supporting this energy harvesting system in offshore environments, characterized by extreme waves and unpredictable conditions. The project involves designing and fabricating a floating structure that meets the necessary specifications to withstand offshore conditions, utilizing a combination of physical fabrication methods and computer-aided design (CAD) to ensure precision and reliability. The research process includes defining the problem, designing and fabricating the prototype, assembling the floating structure, and integrating the energy harvesting components. This approach demonstrates the practical application of CAD and precision machinery in manufacturing, contributing to technical knowledge and skills in the field. The resulting prototype offers ease of assembly and robust connections, making it a practical and efficient solution for offshore energy harvesting. The design and fabrication successfully meet the intended specifications, validating the effectiveness of the integrated wind, solar, and wave energy harvester.

Keywords: Offshore Energy Harvester; Wind-Solar-Wave Integration; Floating Structure Design; Computer-Aided Design; Prototype Fabrication

1. INTRODUCTION

The integration of these technologies into a single platform offers promising potential for enhanced energy generation efficiency in marine environments. Marine environments present vast renewable energy resources, and floating structures serve as effective platforms for harnessing wind, solar radiation, and wave energy. Leveraging technological advancements, particularly in CAD software, allow for precise design and optimization, reflecting a modern approach to developing such prototypes.

The increasing demand for sustainable energy sources has driven research into renewable technologies, especially offshore wind energy. Floating offshore wind harvesters offer advantages over traditional fixed structures, addressing spatial constraints of onshore turbines and climate concerns (Breton et al., 2009). Offshore wind energy is emerging as a viable alternative, with studies highlighting its potential in Europe, North America, and Malaysia, where techno-economic feasibility and optimal locations for wind farms are assessed (Mekhilef et al., 2011). The Malaysian Fit-in Tariff (FiT) further enhances the prospects (Ahmad et al., 2011). Additionally, the combined utilization of wind and wave energy in

offshore waters has become a research hotspot. This study explores a novel integrated wind-wave power generation platform, focusing on the size optimization of the point absorber wave energy converter (WEC) combined with a semi-submersible floating wind turbine foundation (Zhang et al., 2022).

2. METHODOLOGY

Utilizing Computer-Aided Design (CAD) software, 3D models of the various components of the floating structure are created. This step involves designing the structural elements, energy harvesting systems (wind turbines, wave energy converters, solar panels), and the overall layout of the integrated energy harvesting platform.

To evaluate the model, we calculate the buoyancy needed by the structure to stay afloat in the offshore environment. For buoyancy, the buoyant force is computed by subtracting the weight of the pontoon from the weight of the water it displaces, ensuring accurate assessment of the structure's ability to stay afloat. Equation 1 explained the way to determine the buoyant force of the prototype.

$$F_{\text{buoyant}} = \rho g V_{\text{fluid}} \quad (1)$$

The Factor of Safety of the prototype needs to be calculated as it provides understanding on the structure failure and safety. A safety factor exceeding 1 denotes a secure design capable of withstanding loads beyond its anticipated capacity. Equation 2 explained the way to determine the Factor of safety in the prototype.

$$FOS = \frac{\text{Total Downward Forces (TDF)}}{\text{Buoyant Force (Fb)}} \quad (2)$$

If the $TDF > Fb$ = structure will remain in the static position

If the $TDF < Fb$ = structure will shift upward.

A detailed fabrication plan is developed based on the CAD models and virtual assembly results. This plan outlines the materials required, fabrication techniques, assembly procedures, and quality control measures to ensure the successful construction of the prototype floating structure. The hydrostatic analysis is done to assess the feasibility of the project.

The research paper's measurement analysis underscores the importance of precise measurements, tools, and data evaluation in assessing the fabrication quality and alignment of the prototype floating structure.

3. RESULTS AND DISCUSSION

The model depicted in Figure 1 showcases all the connections and components, meticulously highlighted for clarity and reference.

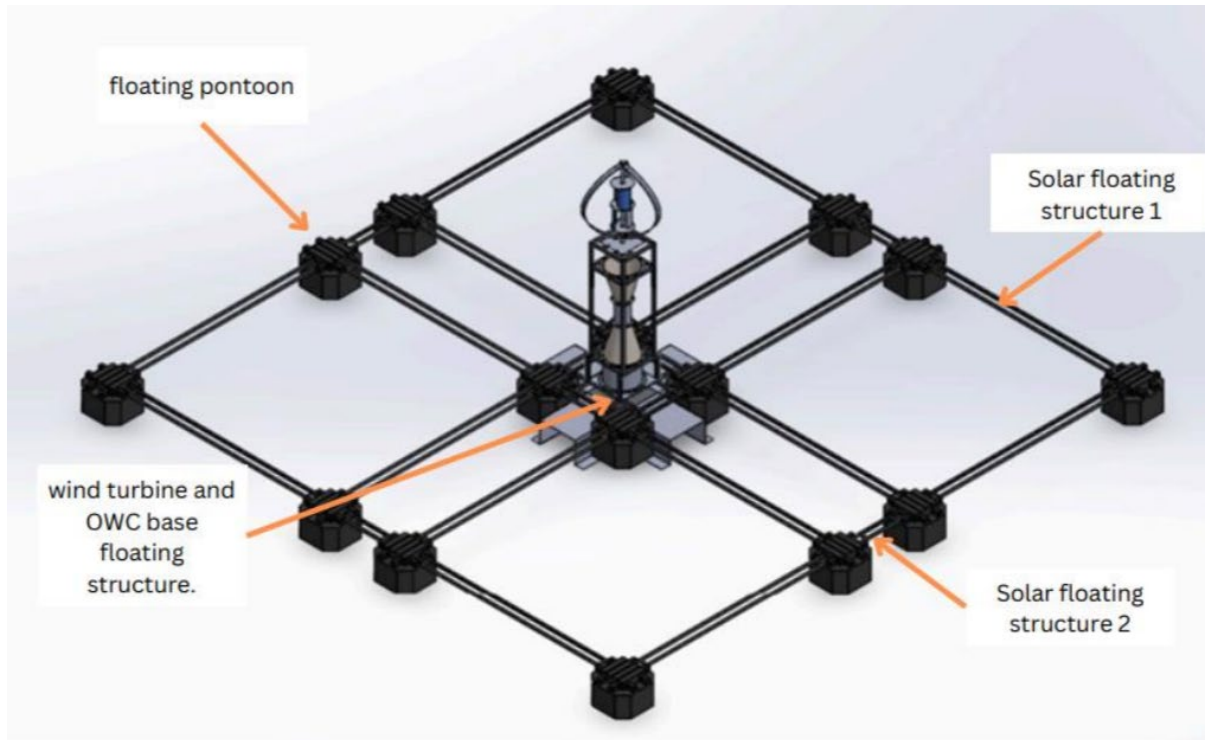


Figure 1. The complete modelling of the solar wind wave energy harvester.

The measurement analysis

The research paper's measurement error analysis emphasizes pinpointing and quantifying discrepancies between actual measurements of fabricated components and dimensions outlined in computer aided design (CAD) models. Tables 1 and 2 comprehensively outline all deviations observed between CAD and actual components, detailing challenges encountered and discussed.

Table 1: The deviations of the Actual and CAD components

| Components | Actual Dimension (mm) | CAD dimension (mm) | Deviation (mm) | Percentage Error (%) |
|--|-----------------------|--------------------|----------------|----------------------|
| Wind turbine and OWC base structure | | | | |
| Overall Length | 2291 | 2160 | 131 | 6.06 |
| Overall Width | 2293 | 2160 | 133 | 6.15 |
| Overall Height | 50 | 50 | 0 | 0.00 |
| Solar panel structure 1 | | | | |
| Average Length | 4380 | 4390 | 10 | 0.23 |
| Average Width | 2430 | 2450 | 2 | 0.82 |
| Average Height | 50 | 50 | 0 | 0.00 |

| Solar panel structure 2 | | | | |
|-------------------------------------|---------|---------|-----|------|
| Average Length | 1326 | 1330 | 4 | 0.30 |
| Average Width | 250 | 245 | 5 | 2.04 |
| Average Height | 50 | 50 | 0 | 0.00 |
| Full configuration of the structure | | | | |
| Overall Length | 12965.0 | 12890.0 | 75 | 0.58 |
| Overall Width | 13017 | 12890.0 | 127 | 0.99 |
| Overall Height | 560 | 540 | 0 | 3.57 |

Table 2: The deviations of gap of the components

| Component | CAD model measurement (mm) | Fabrication Design measurement (mm) | Difference (mm) | Percentage of derivations (%) |
|-------------------------------------|----------------------------|-------------------------------------|-----------------|-------------------------------|
| Solar floating structure 1 | | | | |
| A1 | 145 | 145 | 0 | 0 |
| A2 | 145 | 143 | 2 | 1.38 |
| A3 | 145 | 145 | 0 | 0 |
| A4 | 145 | 142 | 3 | 2.07 |
| A5 | 145 | 145 | 0 | 0 |
| A6 | 145 | 144 | 1 | 0.69 |
| A7 | 145 | 145 | 0 | 0 |
| A8 | 145 | 143 | 2 | 1.38 |
| A9 | 145 | 145 | 0 | 0 |
| A10 | 145 | 142 | 3 | 2.07 |
| A11 | 145 | 145 | 0 | 0 |
| A12 | 145 | 143 | 2 | 1.38 |
| A13 | 145 | 142 | 3 | 2.07 |
| A14 | 145 | 142 | 3 | 2.07 |
| A15 | 145 | 145 | 0 | 0 |
| A16 | 145 | 144 | 1 | 0.69 |
| Solar floating structure 2 | | | | |
| B1 | 145 | 142 | 3 | 2.07 |
| B2 | 145 | 142 | 3 | 2.07 |
| B3 | 145 | 141 | 4 | 2.76 |
| B4 | 145 | 142 | 3 | 2.07 |
| Wind turbine and OWC base structure | | | | |
| C1 | 145 | 143 | 2 | 1.38 |
| C2 | 145 | 143 | 2 | 1.38 |
| C3 | 145 | 141 | 5 | 2.76 |
| C4 | 145 | 140 | 5 | 3.45 |

All the challenges have been highlighted in order to achieve the accurate designs in this prototype. Fabricating prototypes from CAD designs poses challenges in achieving precision due to machine tolerance, human error, and measurement inaccuracies.

Table 3: The results of calculations.

| Parameter | Result |
|---------------------------------------|---------|
| Factor of Safety | 13.80 |
| Total Buoyancy Force From The Pontoon | 84800 N |
| Center of Gravity (COG) | 2.85 m |
| Metacentric Height (GM) | 32.02 m |

The factor of safety is exceeded 1 noted that the structure can support the structure weight. The derived metacentric height (GM) signifies a positive margin between center of gravity and metacenter, ensuring resilience against external forces and minimizing tilting.

4.0 CONCLUSION

The study achieved its objectives of designing and fabricating a prototype floating structure integrating wind turbines, oscillating water columns, and solar panels for renewable energy harvesting, demonstrating the feasibility of combining multiple renewable energy systems.

REFERENCES

- [1] Buoyancy White Paper. Go to National Precast Concrete Association. (n.d). <https://precast.org/2022/08/npcarevises-and-updates-its-buoyancywhite-paper/>
- [2] Breton, S., & Moe, G. (2009). Status plans and technologies for offshore wind turbines in Europe and North America. *Renewable Energy*, 34, 646-654.
- [3] Mekhilef, S., & Chandrasegaran, D. (2011). Assessment of off-shore wind farms in Malaysia. *TENCON 2011 - 2011 IEEE Region 10 Conference*, 1351-1355.

Design and Development of a Gamified Augmented Reality-based Teaching and Learning System for Industrial Robot

Lucy Sii Leh Ting ^a and Yap Hwa Jen ^{b*}

Department of Mechanical Engineering,
Faculty of Engineering, Universiti Malaya,
50603, Kuala Lumpur, Malaysia

Email: ^a lucyting0816@gmail.com, ^b hjyap737@um.edu.my

*Corresponding author

ABSTRACT

Robotic kinematics presents challenges in understanding complex relationships between robotic joints and spatial configurations, especially in educational settings with limited access to real industrial robots. This project introduces a gamified augmented reality (AR) application for robotic kinematics education, integrating gamification elements such as Goals, Access, Feedback, Collaboration, and Challenges (GAFCC). The application provides interactive and practical learning experiences through teaching, tutorial, and game modes, allowing students to explore and manipulate robotic joints and end-effector positions. Validation of the forward kinematics module was conducted using RobotDK, demonstrating percentage errors of less than 14% for the x and y axes. The z-axis showed a higher percentage errors, which were mitigated through adjustments in Unity 3D. Surveys with 40 participants indicated high engagement and motivation, with over 80% preferring the gamified AR approach over traditional methods. This research successfully demonstrates the effectiveness of gamified AR in enhancing the teaching and learning of robotic kinematics.

Keywords: Robotic Kinematics; Augmented Reality; Gamification; Education; Forward Kinematics

1. INTRODUCTION

The augmented reality (AR) market in education is set to grow from USD 10.37 billion in 2022 to USD 68.71 billion by 2026, driven by the challenges of traditional teaching methods during the COVID-19 pandemic and the high costs and logistical constraints of using real industrial robots for educational purposes. To address these issues, this project has developed a gamified AR application utilizing the Mixed Reality Toolkit (MRTK), Unity 3D, and HoloLens. The application, which integrates gamification principles, GAFCC based on flow theory and goal-setting theory, allows students to interact with virtual industrial robots, thereby enhancing engagement and making complex robotic kinematics more accessible and engaging.

2. METHODOLOGY

2.1 Software Setup

The AR application was developed using Unity 3D, with C# programmed in Visual Studio. MRTK was integrated to facilitate AR features, and the ROS enabled communication between the robot and the Unity simulation. RobotDK was utilized to assist in the validation process.

2.2 User Interface Development

The user interface was designed to be intuitive and engaging. The first scene is welcoming homepage with clickable buttons, animations, and background music. While the second scene is teaching mode developed using presentation slides to convey basic robotics concepts. Next the third scene is tutorial mode include forward and inverse kinematics where students can manipulate joint angles and observe the end-effector positions. Forward kinematic module was validated with RobotDK.

2.3 Game Level Development

Two game levels were created to enhance learning through interaction and challenges. The game level 1 included pick and place task integrated with GAFCC elements. While the game level 2 similar as level 1 but increased complexity of tasks.

2.4 Deployment

The application was deployed on HoloLens 2, providing an immersive AR experience for students.

2.5 Survey Research

A survey was conducted to evaluate the effectiveness of the gamified AR application. 40 participants were involved, comparing their engagement, motivation, and knowledge acquisition with traditional learning methods. The survey results were compared with systematic literature review. [1]

3. RESULTS AND DISCUSSION

3.1 Validation of Kinematics Module

To ensure accuracy, the end-effector positions calculated by Unity 3D were compared with result of RobotDK. The validation showed percentage errors of less than 14% for the x and y axes, while the z axis had higher percentage errors, 65% to 83%. These discrepancies in the z-axis can be mitigated through adjustments in Unity 3D, ensuring the overall accuracy of the kinematics model.

3.2 User Interface

The user interface was designed to be intuitive and engaging.

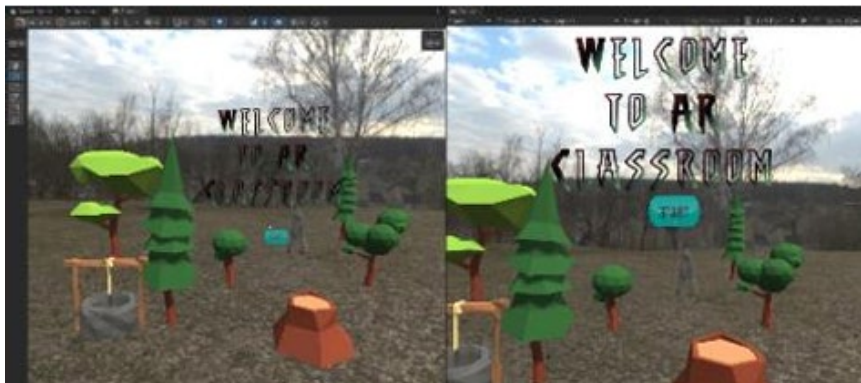


Figure 1. Scene 1

3.3 Game Levels and Gamification

Two game levels were created to promote interactive learning through gamification.

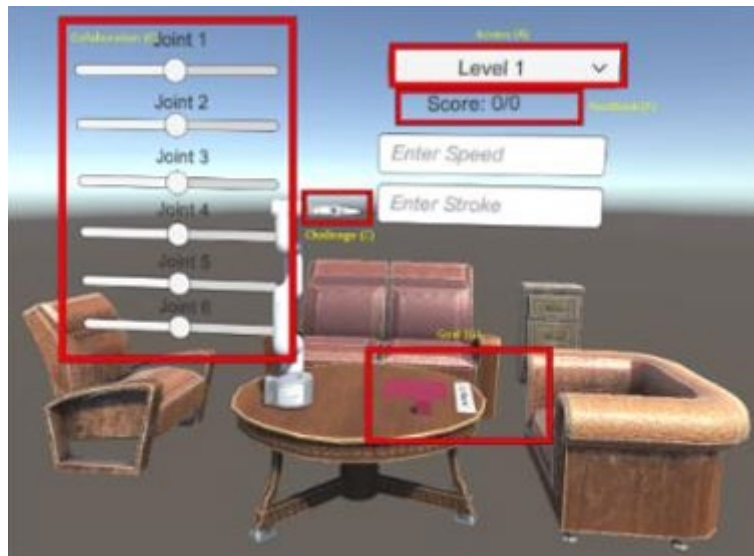


Figure 5. Game level 1

Place object in plane



Completed



Figure 6. Pick and place task

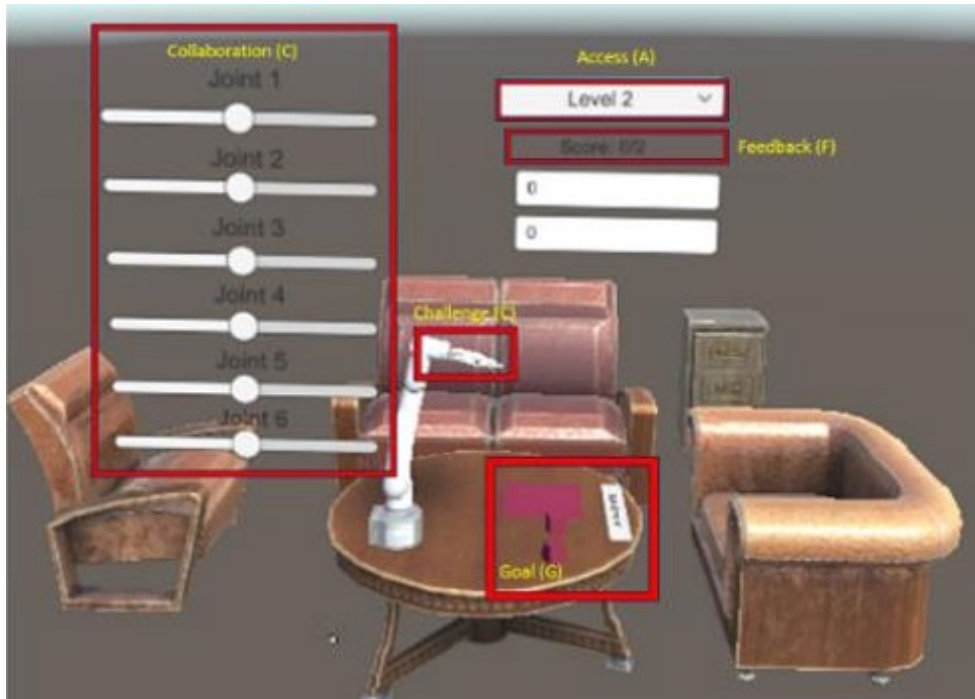


Figure 7. Game level 2

3.4 Survey Results

A survey was conducted with 40 participants to evaluate the effectiveness of the gamified AR. The survey compared the participants' engagement, motivation, and knowledge acquisition with traditional learning methods. The results indicated high levels of student engagement and a preference for the gamified AR approach, with over 80% of participants favouring this method. This is further validated by systematic literature review. [1]

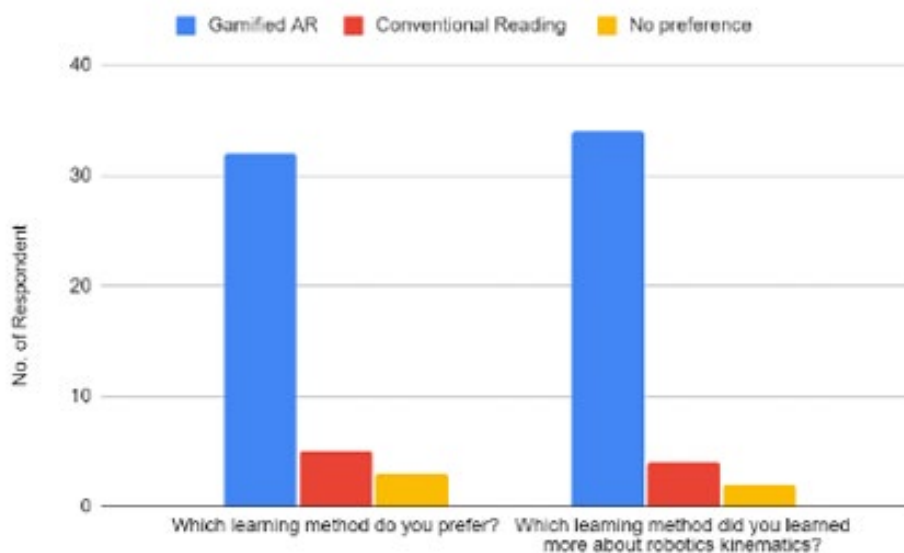


Figure 8. Preference learning method of participants

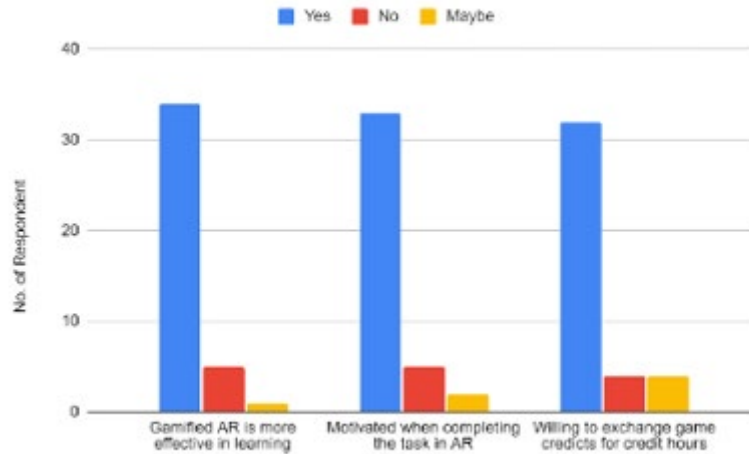


Figure 9. Motivation and effectiveness survey on gamified AR.

3.5 Discussion

The results demonstrate that the gamified AR application significantly enhances student engagement and motivation compared to traditional learning methods. The integration of gamification elements such as goals, access, feedback, collaboration, and challenges contributed to this increase in engagement. The user friendly interface and immersive experience provided by HoloLens 2 further supported effective learning.

While the validation of the forward kinematics module showed minor discrepancies in the z-axis, these can effectively mitigated through adjustments in Unity 3D. The overall accuracy of the kinematics model was maintained, ensuring a reliable educational tool.

4. CONCLUSION

This research developed a gamified augmented reality (AR) application for industrial robotics education, utilizing Unity 3D, HoloLens 2, and the ROS. Incorporating gamification elements GAFCC, the application proved engaging and interactive. Validation of the forward kinematics module with RobotDK confirmed accuracy, with less than 14% error for the x and y axes while higher z axis errors can be mitigated through Unity adjustments. Survey results from 40 participants showed enhanced engagement, motivation, and knowledge acquisition, with over 80% favouring this method over traditional approaches, indicating the application's potential to revolutionize industrial robotics education. Future enhancements could include additional game levels and expanded kinematics modules to further improve learning outcomes.

REFERENCES

- [1] Lampropoulos, G., Keramopoulos, E., Diamantaras, K., & Evangelidis, G. (2022). Augmented Reality and Gamification in Education: A Systematic Literature Review of Research, Applications, and Empirical Studies. *Applied Sciences*, 12(13), 6809. <https://www.mdpi.com/20763417/12/13/6809>

Development of Image Guided Positioner for Robot Drilling in the Aerospace Manufacturing Industries

Wong Pui Teng^a and Yap Hwa Jen^{b*}

Department of Mechanical Engineering,
Faculty of Engineering, Universiti Malaya,
50603, Kuala Lumpur, Malaysia

Email: ^a wongpuiteng26@gmail.com, ^b hjyap737@um.edu.my

*Corresponding author

ABSTRACT

In the aerospace manufacturing industry, hole quality is crucial for structural integrity and user safety, as aircraft often face extreme weather conditions. Inspection of pilot holes is a routine safety protocol to ensure the highest standard of operational safety. Manual inspection of the large number of pilot holes is inaccurate, time-consuming, and delays the manufacturing process. This research proposes the development of an economical and reliable automated hole inspection and localization system using image processing techniques. Several offset detection models are built and tested, and the best-performing model is then used to build the automated offset correction system by integrating image processing code with a low-cost camera and KUKA industrial robot. The chosen model is performing the best with average RMSE of 0.042018mm and average processing time of 0.016282s for 1 image. The system is then tested under different lighting conditions and is concluded to work best in brighter conditions at 1035 Lux. The accuracy of the system, validated with a trained YOLOv8 deep learning algorithm, achieved a high precision with an RMSE value of 0.0848601mm.

Keywords: Robotic Kinematics; Augmented Reality; Gamification; Education; Forward Kinematics

1. INTRODUCTION

Inspection of pilot holes is important for structural integrity and user safety of aircraft. However, due to the large number of holes, manual hole inspection presents various problems that are labour intensive, time consuming and inaccurate. To address this problem, researchers have been developing various non-destructive inspection techniques such as ultrasonic scanning and interferometry, but they are too costly [1]. Later, the vision-based inspection system, which is a system of digital cameras and computer with image processing software for feature extraction, was introduced [2].

The image processing market is a promising field and is growing with a CAGR of 21.8% [3]. Many research on the utilization of image processing in the aerospace industry has been conducted such as for the inspection of possible icing on aircraft surface and for aircraft type identification [4,5]. Image processing is also widely used in hole detection application, especially for diameter detection, offset detection and correction. For example, the diameter of holes drilled in baffle plates used in power plants are detected and inspected using image processing [6].

2. METHODOLOGY

In this research, the image processing algorithms steps are image enhancement, filter, image segmentation and centroid detection. The first part of the research is to determine the best offset detection model. First, the images and offset values corresponding to each image are obtained from the COGNEX industrial camera. Using Python language, 6 image processing models using different algorithms are created and the offset values from these algorithms are benchmarked with the offset values from COGNEX to get the average RMSE. By training YOLOv8 model, 2 additional models are created where one model accepts raw images for prediction whereas the other model accepts images preprocessed using image processing for prediction. As this application requires fast and accurate computations, the allowable processing time and RMSE are 0.5seconds and 0.1mm respectively. By comparing these 2 metrics for the 8 models created, the best model is chosen for building the offset correction algorithm.

Table 1. Algorithms for all offset detection models

| | Image Enhancement | Filter | Image Segmentation | Centroid Detection |
|---|-------------------|------------------|---------------------|--------------------|
| A | Grayscale | Gaussian | Truncated Threshold | CHT |
| B | Grayscale | Median | Truncated Threshold | CHT |
| C | Grayscale | Truncated Median | Truncated Threshold | CHT |
| D | Grayscale | Gaussian | Binary Threshold | CCM |
| E | Grayscale | Median | Binary Threshold | CCM |
| F | Grayscale | Truncated Median | Binary Threshold | CCM |
| G | - | - | - | YOLOv8 |
| H | Grayscale | Gaussian | Truncated Threshold | YOLOv8 |

**Note: Circular Hough Transform (CHT), Centroid Compensation Method (CCM)*

To utilize the image processing algorithm for real time offset correction, the robot vision setup is done by mounting the Logitech C920 Pro HD webcam and ring-shaped external lamp to the aluminium profile support. The webcam is mounted at 6cm directly above the rectangular plate whereas the lamp is placed around the webcam. Next, the holes position on the plate is setup using the KUKA smartPAD.

The second part of the research is to create automated offset correction algorithm that can switch on the webcam continuously, perform real-time offset detection and send offset values obtained to KUKA robot for offset correction. For the Python code to receive and send signals to KUKA robot, TCP/IP protocol is used for the two-way communication channel. After successfully setting up the automated offset correction system, the system is tested at different lighting conditions to determine the best working condition for this system. Lastly, the offset values obtained from system testing are validated by running the real-time images captured using the trained YOLOv8 algorithm.

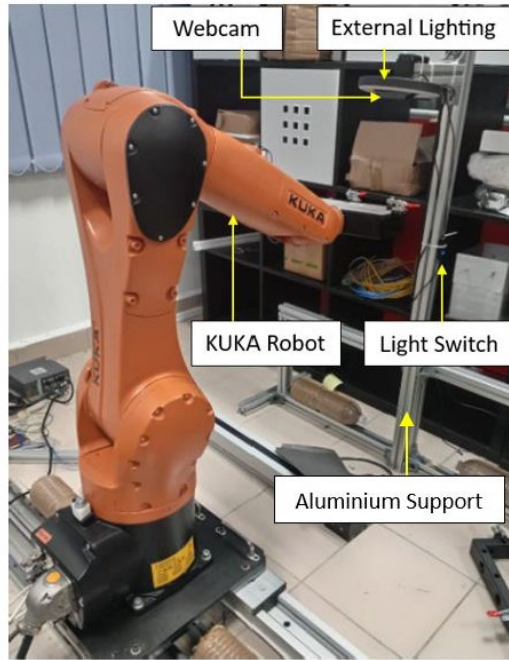


Figure 1. Robot Vision Setup



Figure 2. Holes position on rectangular plate

3. RESULTS AND DISCUSSIONS

From the first part of the project, the average RMSE and image processing time are obtained for each model and the best model chosen is Model A as it has high accuracy and best time efficiency.

Table 2. Results for all offset detection models

| Model | Average RMSE (mm) | Time for 200 images (s) | Time for 1 image (s) |
|-------|-------------------|-------------------------|----------------------|
| A | 0.042018 | 3.2563 | 0.016282 |
| B | 0.044813 | 9.9295 | 0.049648 |
| C | 0.046957 | 1204.6771 | 6.023386 |
| D | 0.040626 | 470.9601 | 2.354801 |
| E | 0.041740 | 153.3940 | 0.766970 |
| F | 0.040626 | 990.3018 | 4.951509 |
| G | 0.064176 | 603.7259 | 3.018630 |
| H | 0.052346 | 640.016 | 3.200080 |

For the second part of the research, the automated offset correction system has been successfully created and tested with the robot vision setup. For each hole, 3 images are captured which represent before offset correction, after 1st attempt offset correction and 2nd offset correction. The system is tested at 3 different lighting conditions which are dimmer, ambient and brighter condition with lighting intensity of 8 Lux, 135 Lux and 1035 Lux respectively. For dimmer condition, offset correction could not be done at all due to insufficient illumination that impacts the camera's ability to differentiate details in

the image. At ambient condition, the average offset values after 1st and 2nd offset correction are around 0.05mm and 0.007mm whereas the average time to process 1 image is 0.01555s. As for brighter condition, the average offset values after 1st and 2nd offset correction are around 0.008mm and 0.005mm, whereas average time to process 1 image is 0.01576s.

For ambient condition, the offset values after 1st attempt can be further reduced, justifying the need of 2nd attempt offset correction. For brighter condition, since the offset values after 1st attempt is already sufficiently low, a single attempt offset correction is sufficient for high accuracy and with the short time needed to process 1 image, the overall time needed for the system can be greatly reduced.

Lastly, validation is done by comparing the offset values obtained from the system with offset values from YOLOv8. The average RMSE obtained from ambient condition is 0.142649mm, which is slightly higher than allowable RMSE and hence, unacceptable. As for brighter condition, average RMSE is 0.084860mm which meets the required tolerances of lower than 0.1mm.

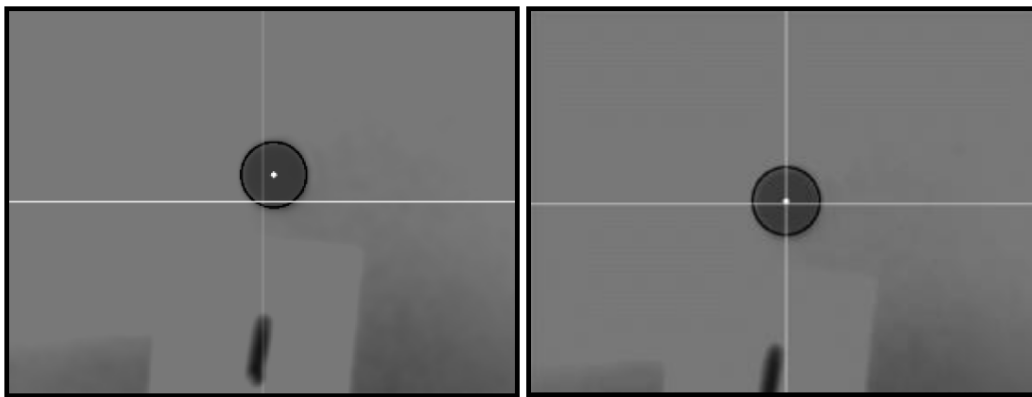


Figure 3. Image captured before (left) and after (right) running the offset correction system

4. CONCLUSION

In conclusion, different image processing models has been developed for offset detection and the best performing model chosen is Model A with average RMSE of 0.042018mm and image processing time of 0.016282s for 1 image. Next, this model is integrated with the robot vision setup which consists of a low-cost camera and KUKA industrial robot, to create an automated offset correction system. This system works best at brighter condition where the processing time taken is 0.01576s and average offset values after offset correction is near zero which is about 0.005mm. Validation using YOLOv8 is also done and the average RMSE obtained is 0.084860mm which meets the required tolerances in aerospace industry.

REFERENCES

Hernandez, A., Maghami, A., & Khoshdarregi, M. (2020, 20-23 April 2020). A Machine Vision Framework for Autonomous Inspection of Drilled Holes in CFRP Panels. 2020 6th International Conference on Control, Automation and Robotics (ICCAR).

Wei, D., Li, D., Tang, D., Wang, H., & Peng, Y. (2022). Deep learning approach for defective spot welds classification using small and class-imbalanced datasets. *Neurocomputing*, 477. <https://doi.org/10.1016/j.neucom.2022.01.004>

Data Bridge Market Research. (2022). *Global Image Processing Systems Market – Industry Trends and Forecast to 2029*. Retrieved Nov 20 from <https://www.databridgemarketresearch.com/reports/global-image-processing-systems-market>

Oleshko, T., Kvashuk, D., & Heiets, I. (2019). Image recognition in unmanned aviation using modern programming languages. *SN Applied Sciences*, 1(12), 1686. <https://doi.org/10.1007/s42452-019-1739-y>

Karacor, A., Abay, R., & Torun, E. (2011). Aircraft classification using image processing techniques and artificial neural networks. *Pattern Recognition and Artificial Intelligence*, 25, 1321.

Sachan, D., & Aravalli, S. C. (2018). Image Processing Technique for Drilled Holes Inspection in Large Rectangular Plate. 21-27. <https://doi.org/10.9790/9622-0803012127>

THEME: MATERIALS

Fabrication and Testing of Nanofiber Reinforced Composite

Lim Jia Chen ^a and Amalina binti Muhammad Afifi ^{b*}

Department of Mechanical Engineering,
Faculty of Engineering, Universiti Malaya,
50603, Kuala Lumpur, Malaysia

Email: ^a jc.lim.011106@gmail.com, ^b amalina@um.edu.my

*Corresponding author

ABSTRACT

This study focuses on enhancing composite materials by incorporating Polyvinylidene fluoride (PVDF) nanofibers into epoxy matrices. The primary objectives are to demonstrate the superior mechanical performance of these nanofiber-reinforced composites, improve adhesion techniques for practical applications, and assess their structural integrity. The research involves the fabrication and characterization of PVDF nanofiber-reinforced epoxy composites. To achieve this, optimal electrospinning parameters were established to produce uniform PVDF nanofiber mats, and sonication was used to enhance adhesion between the nanofibers and the epoxy resin. Scanning Electron Microscopy (SEM) was employed to observe the formation and distribution of the nanofiber mats within the matrix, ensuring proper integration. Compressive testing was performed on 1 cm cubed specimens to evaluate their mechanical properties. While the initial focus was on automotive applications, the study's findings are relevant to advancing composite technology for various industrial uses, paving the way for the development of high-performance, durable materials.

Keywords: Polyvinylidene Fluoride; Nanofiber-Reinforced Composites; Mechanical Performance; Adhesion Techniques; Scanning Electron Microscopy

1. INTRODUCTION

Composite materials, created by combining two or more distinct components, are essential in various industrial applications due to their unique ability to merge the advantages of different materials. This research focuses on developing composites that offer enhanced mechanical properties while maintaining lightweight characteristics. Polyvinylidene fluoride (PVDF) nanofibers are integrated into epoxy matrices to develop composites with superior mechanical performance. The study explores the challenges associated with nanofiber adhesion and distribution within the epoxy matrix, aiming to optimize fabrication techniques for applications. By addressing practical these challenges, the research aims to advance composite technology and improve the performance and reliability of nanofiber reinforced materials in diverse industrial settings.

2. METHODOLOGY

The methodology includes the fabrication and characterization of PVDF nanofiber reinforced epoxy composites. Key steps involve:

1) Electrospinning Parameters: Establishing optimal conditions for electrospinning to produce uniform PVDF nanofiber mats.



Figure 1. The electrospinning process setup.

2) Sonication Process: Enhancing adhesion between PVDF nanofibers and epoxy resin through sonication.

3) Scanning Electron Microscopy (SEM): Utilizing SEM to observe the nanofiber mats' formation and distribution.

4) Compressive Testing: Conducting compressive tests on 1 cm cubed composite specimens to evaluate their mechanical properties.

The combination of these techniques ensures the production of high-quality nanofiber-reinforced composites with improved performance characteristics.

3. RESULTS AND DISCUSSION

SEM analysis confirmed the proper formation and distribution of nanofibers. From the observations, the best parameters of the electrospinning are determined at 25 wt% PVDF concentration, 7:3 DMF: Acetone solvent ratio, and a 9.0 mL/hour feed rate, with an applied voltage of 22.0 kV. Besides that, tip-to-collector distance is kept at 10cm and the mixing of the DMF, Acetone and PVDF powder is done at 40°C at 550 rpm using the stirrer.

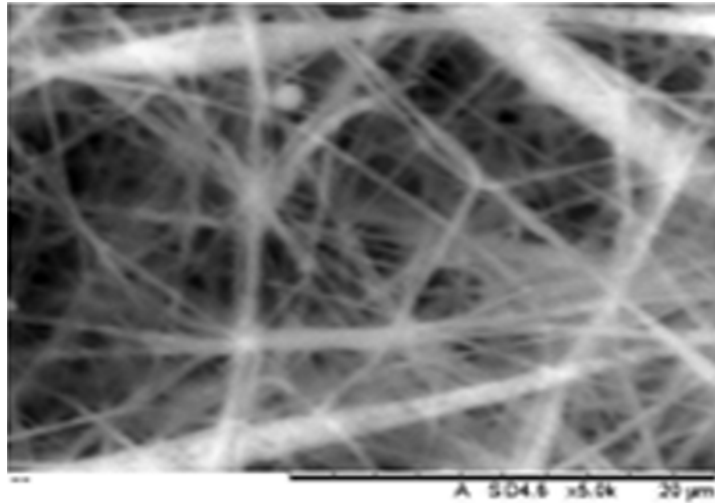


Figure 2. The SEM micrograph for the best parameters set.

The results demonstrate the successful incorporation of PVDF nanofibers into the epoxy matrix, with improved mechanical properties observed in the composites.

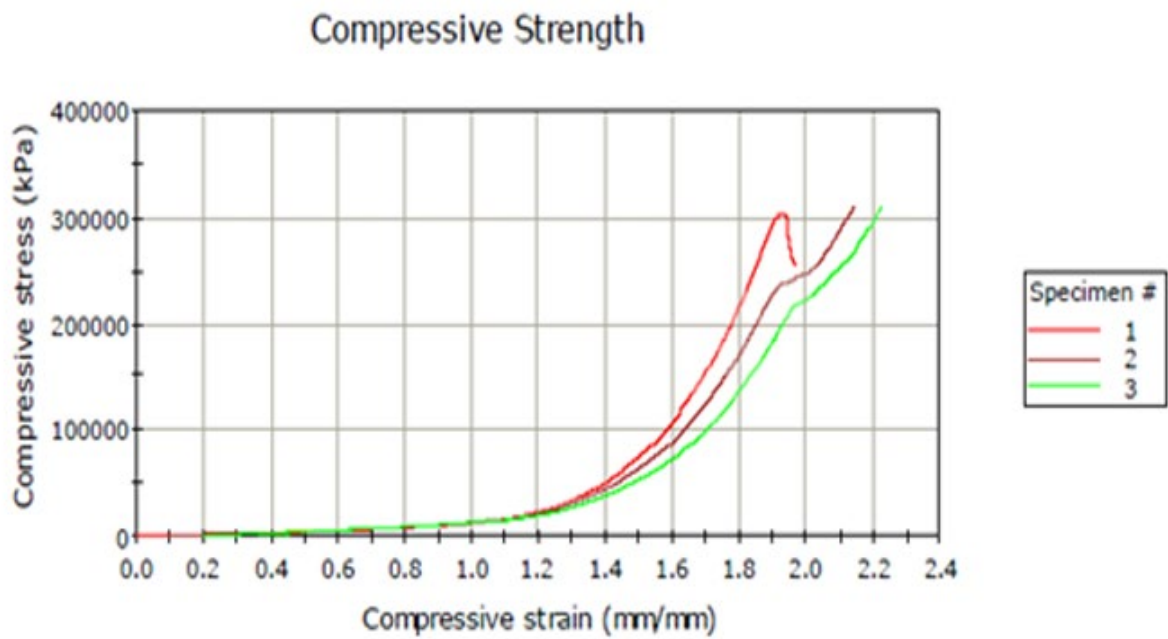


Figure 3. The Stress-Strain Curve for the Compression Test.

Table 1: The Compression Test Results

| Specimen # | Compressive Stress at Maximum Load (MPa) | Maximum Compressive Load (kN) |
|--------------------------------------|--|-------------------------------|
| S1 (Pure epoxy) | 304.312 | 51.42879 |
| S2 (Composite without sonication) | 310.651 | 52.50005 |
| S3 (Composite with sonication) | 310.653 | 52.50041 |

The results indicate that the incorporation of PVDF nanofibers improves the compressive strength of the epoxy matrix, with sonicated specimens (S3) showing marginally better performance compared to non-sonicated ones (S2). However, due to the Universal Testing Machine's load limit, the full compressive strength potential of the composites could not be assessed. This issue may be due to the small specimen size which is not a standard.

The systematic approach to parameter optimization and SEM analysis provided valuable insights into the influence of PVDF nanofiber morphology on composite performance. The findings are significant for developing advanced composite materials with superior performance for various industrial applications. The slight improvement in mechanical properties with sonication suggests that further refinement in fabrication techniques could enhance composite performance. Despite the limitations in mechanical testing, the study demonstrates the feasibility of fabricating PVDF nanofibers reinforced epoxy composites with improved mechanical properties.

4. CONCLUSION

This research concludes that incorporating PVDF nanofibers into epoxy matrices enhances the mechanical performance of the resulting composites. The optimized electrospinning and sonication processes ensure effective adhesion and uniform distribution of nanofibers, contributing to the composites' overall structural integrity. Despite challenges with non-standard specimen sizes affecting mechanical testing, the detailed SEM analysis provides critical insights for future development and application of nanofiber-reinforced composites.

REFERENCES

- [1] Karbhari, V. M. (2007). 2 - Fabrication, quality and service-life issues for composites in civil engineering. In V. M. Karbhari (Ed.), *Durability of Composites for Civil Structural Applications* (pp. 13-30): Woodhead Publishing.
- [2] Háková, M., Havlíková, L. C., Chvojka, J., Erben, J., Solich, P., Švec, F., & Šatínský, D. (2018). A comparison study of nanofiber, microfiber, and new composite nano/microfiber polymers used as sorbents for on-line solid phase extraction in chromatography system. *Analytica Chimica Acta*, 1023, 44-52. doi:<https://doi.org/10.1016/j.aca.2018.04.023>

Microstructural Characterisation of Labu Sayong and Implications on Cooling Action

Muhammad Nur Asyraf bin Norwan Chik^a and Hendrik Simon Cornelis Metselaar^{b*}

Department of Mechanical Engineering,
Faculty of Engineering, Universiti Malaya,
50603, Kuala Lumpur, Malaysia

Email: ^a asyrafnorwan@gmail.com, ^b h.metselaar@um.edu.my

*Corresponding author

ABSTRACT

Labu Sayong, a traditional Malaysian pottery from Perak, acclaimed for its distinctive cooling properties via evaporative cooling. This study, conducted as a two-semester Final Year Project (FYP), examined the micro-scale cooling performance, compositions, and microstructural influence of Labu Sayong. Samples of two compositions, one without volcanic ash and one with volcanic ash, underwent forming processes which includes clay mixing, slip forming, drying, and firing. Analytical techniques like Munsell Color Test, XRD, FTIR, XRF and SEM were employed for visual, compositional and structural study. Density and porosity were measured using Archimedes' Principle, while cooling actions were experimentally assessed. Result relates microstructure and porosity with cooling efficiency. Labu Sayong, rich in SiO₂ and aluminosilicates, shows a porous matrix, contributing to cooling and evaporation rates. Addition of volcanic ash results in loosely, fragmented and smaller grains, leading to increased pores' distribution area and less dense matrix, increasing surface area for heat dissipation and cooling efficiency.

Keywords: Clay; Cooling; Labu Sayong; Microstructure; Porosity

1. INTRODUCTION

Labu Sayong, a traditional water storage vessel from Perak, Malaysia, employs a cooling mechanism based on capillary transport and evaporative cooling. Facilitating the porous structure of clay, which enables water movement through capillary action. The clay's small pores draw water to the surface of the vessel, where it undergoes evaporation. This process absorbs heat from the water, thereby lowering its temperature [1]. The efficiency of this cooling mechanism is linked to the microstructure of the clay, including porosity and pore size distribution, which influences the rate of capillary transport and evaporation [3].

Studies on Malaysian clay used for pottery reveals that North Peninsular Malaysia's clay primarily contains of Silicon (Si), Aluminum (Al), Iron (Fe), Titanium (Ti), and Calcium (Ca), of varying concentrations. Sayong clay specifically, renowned for its high-quality pottery, consists of 27.7% Si, 12.6% Al, 0.57% Fe, 0.08% Ti, and 2.32% K, highlighting its unique composition [2]. X-ray fluorescence and diffraction are typically employed to analyze these elements. The predominance of iron in certain pottery and ceramic explains the brownish coloration, while a high K/Ti ratio in others is consistent with the presence of illite. Such analyses underscore the regional differences in clay composition and the impact on pottery quality.

2. METHODOLOGY

The research entails the comprehensive preparation of sintered Labu Sayong samples, emphasizing the analysis of compositional percentages, the mixing process, clay forming techniques, drying procedures, and the firing process. The study incorporates multiple tests and analyses to elucidate the microstructural and porosity effects. Tests which include X-Ray Diffraction (XRD), Fourier-Transform Infrared Spectroscopy (FTIR), X-Ray Fluorescence (XRF), and Energy Dispersive X-ray Spectroscopy (EDS) are carried out to conduct compositional analysis. Scanning Electron Microscopy (SEM) is conducted for microstructural analyzation of Labu Sayong. The test will be carried out on samples such as raw Sayong clay, raw volcanic ash, fired Labu Sayong, and fired Labu Sayong (50g volcanic ash mix).

Density and porosity measurements of Labu Sayong will be conducted using Archimedes' Principle. For visual analysis, the Munsell Color Chart will be employed. Moreover, water cooling experiments, without fan and with fan (forced convection) will be designed and conducted on the Labu Sayong to comprehend parameters such as cooling and evaporation rate. The cooling Labu Sayong samples will also undergo SEM analysis to investigate their microstructure. Results from the cooling experiments will be correlated with microstructural and porosity analyses to enhance understanding of the samples. Determining and comprehending the relation between microstructure and composition, with the cooling action of Labu Sayong.

3. RESULTS AND DISCUSSION

Analyses of Labu Sayong samples, with and without volcanic ash, through XRD, XRF, FTIR, and EDS, reveal significant similarities in mineral and chemical compositions that contribute to their robustness. XRD and XRF highlight a substantial SiO₂ content (50.24%), primarily as quartz, which enhances thermal stability and hardness. Aluminium compounds, detected as microcline and muscovite (19.65% Al₂O₃), improve hardness and electrical insulation. Potassium (8.16% K₂O), titanium dioxide (1.86% TiO₂ as rutile), and calcium (1.04% CaO as laumontite) further contribute to the material's structural integrity and resistance properties. FTIR analysis shows consistent absorption bands indicating kaolinite, montmorillonite, smectite, and quartz, with additional peaks suggesting organic compounds and hydrated phases. EDS results confirm high concentrations of oxygen, silicon, and aluminium, essential for structural integrity and thermal stability. These findings collectively underscore Labu Sayong's durability, thermal resistance, and multifunctionality, making it suitable for various applications.

| No. | Component | Result | Unit | Det. limit | EL. line | Intensity |
|-----|--------------------------------|---------|-------|------------|----------|-----------|
| 1 | Al ₂ O ₃ | 24.8832 | mass% | 0.02722 | Al-KA | 4.8646 |
| 2 | SiO ₂ | 52.4327 | mass% | 0.03938 | Si-KA | 7.8321 |
| 3 | P ₂ O ₅ | 1.6950 | mass% | 0.01952 | P -KA | 0.2487 |
| 4 | K ₂ O | 8.0197 | mass% | 0.03019 | K -KA | 0.9915 |
| 5 | CaO | 0.9102 | mass% | 0.01212 | Ca-KA | 0.5474 |
| 6 | TiO ₂ | 1.2773 | mass% | 0.03316 | Ti-KA | 0.1540 |
| 7 | MnO | 0.1107 | mass% | 0.00706 | Mn-KA | 0.0634 |
| 8 | Fe ₂ O ₃ | 9.8951 | mass% | 0.01209 | Fe-KA | 8.0302 |
| 9 | ZnO | 0.0846 | mass% | 0.00574 | Zn-KA | 0.2099 |
| 10 | As ₂ O ₃ | 0.0000 | mass% | 0.02777 | As-KA | 0.2495 |
| 11 | Rb ₂ O | 0.3269 | mass% | 0.00387 | Rb-KA | 2.8448 |
| 12 | Y ₂ O ₃ | 0.0000 | mass% | 0.02537 | Y -KA | 1.8501 |
| 13 | ZrO ₂ | 0.1865 | mass% | 0.00413 | Zr-KA | 1.9336 |
| 14 | Nb ₂ O ₅ | 0.0693 | mass% | 0.00450 | Nb-KA | 0.7256 |
| 15 | PbO | 0.1063 | mass% | 0.01161 | Pb-LB1 | 0.2992 |

Figure 1. XRF result for raw Sayong Clay (0g ash).

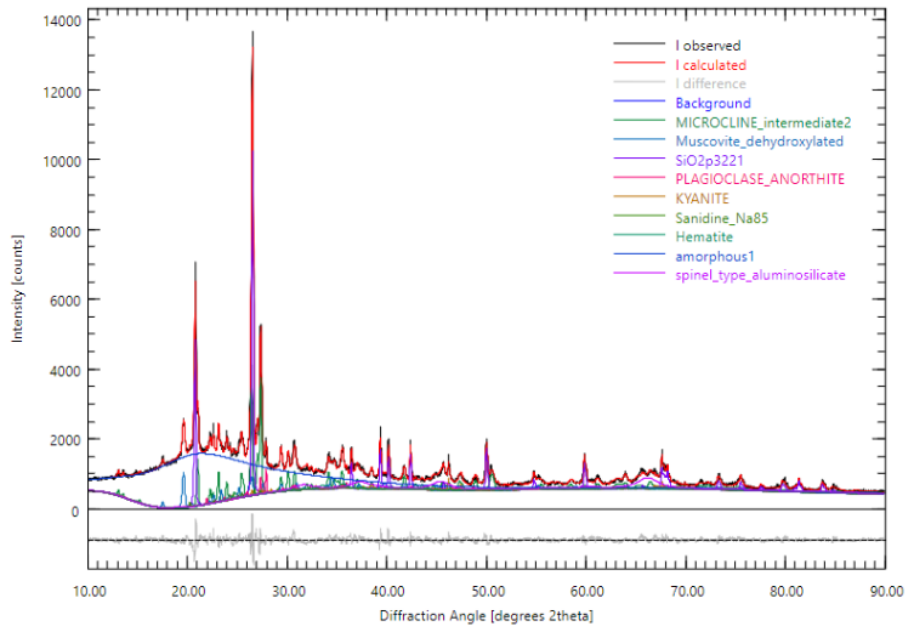


Figure 2. XRD pattern of Sayong (50g Ash).

The microstructure analysis of Labu Sayong clay, with and without volcanic ash, reveals significant differences in porosity and grain arrangement. Freshly fired Labu Sayong without ash displays a dense matrix with fine, plate-like clay particles and larger, irregular grains, showing noticeable porosity that impacts density and mechanical properties. In contrast, adding volcanic ash results in smaller, fragmented grains within a more porous matrix. SEM images show that both samples have irregularly shaped grains and significant porosity, beneficial for cooling due to enhanced heat dissipation. However, the water-cooled samples exhibit a more homogeneous and compact microstructure with reduced porosity, potentially improving mechanical properties but diminishing cooling efficiency over time due to decreased evaporation rates [4][5].

The water-cooling experiment on Labu Sayong highlights volcanic ash's role in temperature regulation. In setups without forced convection (no fan), water in Labu Sayong (50g ash) rapidly drops from 27°C to 16°C within 4 hours and maintains 17°C for 48 hours, whereas water in ash-free sayong drops from 26°C and stabilizes at 17-18°C. Sayong with ash recorded slightly higher water-cooling rate. Stable cooling evaporation rates are recorded in both. With forced convection (with fan), Labu Sayong (50g ash) shows enhanced water-cooling, maintaining lower temperatures longer. Despite slightly lower porosity in ash-containing Sayong (30%) than ash-free Sayong (31%), SEM analysis however indicates that the higher water-cooling and evaporation rates may be due to increased porosity distribution, facilitating heat dissipation through evaporation.

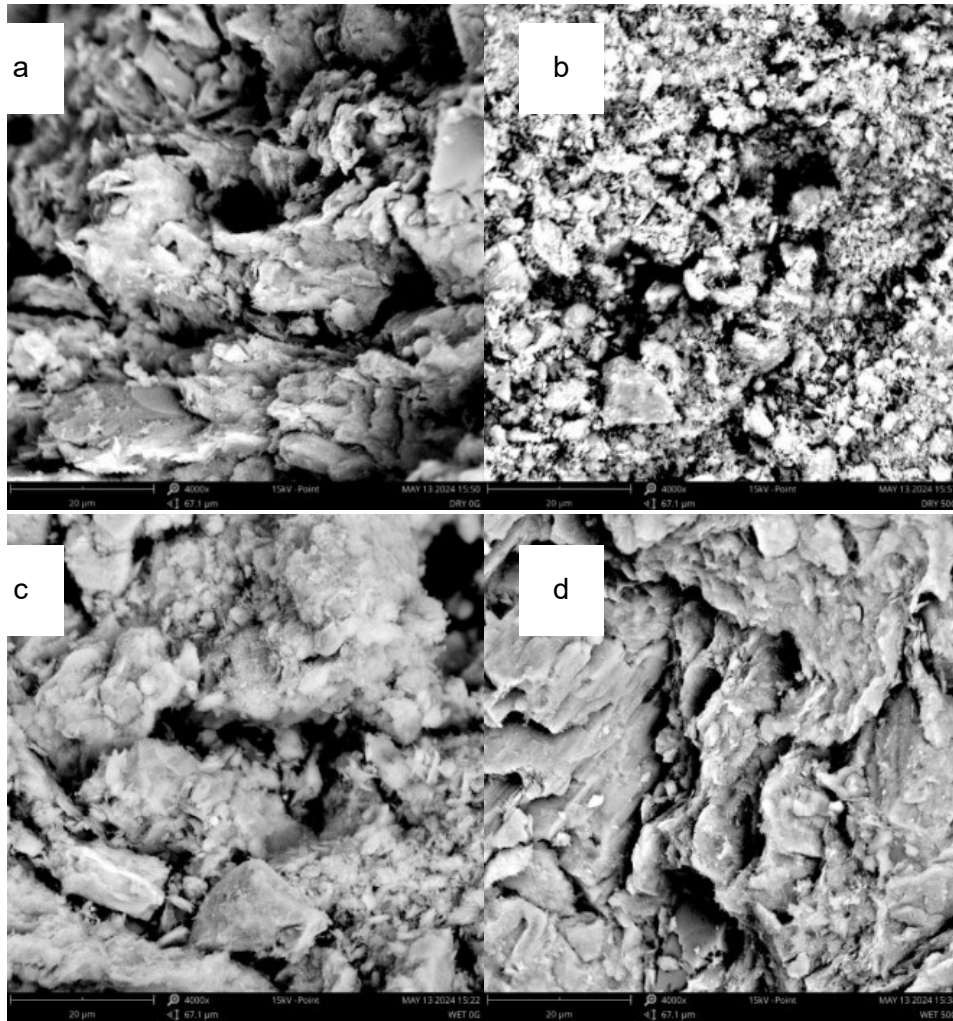


Figure 3. SEM Micrograph of Sayong (a) Dry 0g ash (b) Dry 50g ash (c) Cooling 0g ash (d) Cooling 50g ash

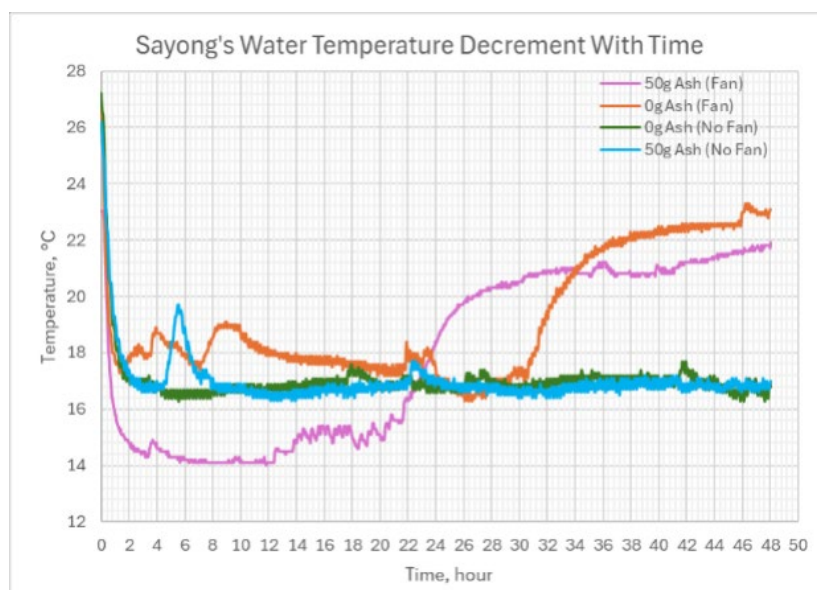


Figure 4. Sayong's water temperature decrement.

4. CONCLUSION

Labu Sayong, with and without volcanic ash, boasts a rich composition including silicon dioxide (SiO₂) and aluminium compounds. Additionally, elements like potassium, titanium dioxide (TiO₂), and trace elements are present. The aluminosilicate-rich ceramic matrix ensures structural integrity and thermal stability. Microstructural features like grain size and porosity impacts water cooling and evaporation rates. Labu Sayong with volcanic ash exhibits increased porosity distribution area, though both 0g and 50gash sayong shows similar porosity percentage (around 30%), facilitating rapid water cooling through evaporation, due to enhanced water absorption and larger surface area for heat dissipation. However, continued water exposure may reduce porosity over time, leading to grain compaction, diminishing the cooling effectiveness.

REFERENCES

- [1] Abdul Halim, M. A. (2019). Traditional Malay Pottery and its Cooling Mechanisms. *Asian Cultural Heritage Review*, 12, 88-95.
- [2] Ahmad, N., Abu Bakar, N., Abdul Wahab, M. F., & Mokhtar, M. (2009). Characterization of clay from several areas in Malaysia for pottery production. *Journal of Asian Earth Sciences*, 34(1), 59-65.
- [3] Meenakshi, S. P. (2020). Porous Ceramics: Capillary Action and its Applications. *Journal of Ceramic Science*, 34(2), 45-58.
- [4] Sarkar, R., & Dan, A. (2018). Influence of water cooling on the microstructure and mechanical properties of ceramics. *Ceramics International*, 44(1), 1205-1214.
- [5] Smith, J., Jones, M., & Williams, T. (2020). Microstructural evolution and performance of traditional water-cooled ceramics. *Journal of Material Science*, 55(12), 889-901.

Silicon Nitride for Carbon Capture

Liang Ai Lin ^a and Hendrik Simon Cornelis Metselaar ^{b*}

Department of Mechanical Engineering,
Faculty of Engineering, Universiti Malaya,
50603, Kuala Lumpur, Malaysia

Email: ^a ailin_liang@hotmail.com, ^b h.metselaar@um.edu.my

*Corresponding author

ABSTRACT

Porous silicon nitride is a promising material for CO₂ adsorption due to its high chemical and thermal stability, large specific surface area, and tunable pore diameter, making it suitable for carbon capture. Traditional CO₂ extraction methods using aqueous amines are energy-intensive and environmentally challenging. This study explores the synthesis of mesoporous silicon nitride via diimide decomposition, using silicon tetrachloride and pentane solution as starting materials. The research investigates how varying precipitation temperatures (from room temperature to 40°C) affect the CO₂ adsorption capabilities of the synthesized silicon nitride. Characterization techniques such as XRD, FESEM, FTIR, and TGA are employed to evaluate the structural and adsorption properties. The goal is to determine the potential of silicon nitride as a more sustainable and efficient carbon capture material compared to existing methods, addressing global warming by mitigating CO₂ emissions. However, the end product synthesized is silicon dioxide instead of silicon nitride due to its susceptibility to oxidation, hence the results will focus on the porosity of silicon dioxide.

Keywords: Porous Silicon Nitride; CO₂ Adsorption; Mesoporous Materials; Diimide Decomposition; Carbon Capture

1. INTRODUCTION

This research aims to synthesize mesoporous silicon nitride for carbon capture. This will be done by carrying out diimide decomposition using silicon tetrachloride and pentane solution as the starting materials using argon-filled glove box. The CO₂ adsorption capability of the prepared mesoporous silicon nitride sample will then be measured, and multiple characterization techniques will be conducted. Several samples of silicon nitride will be prepared under different precipitation temperature where the most optimum temperature that produce sample with the highest CO₂ adsorption capability will be determined. The existing method for extracting CO₂ from flue gas relies on the absorption of CO₂ by aqueous amines. However, this approach is characterized by its high energy consumption and is environmentally impractical due to challenges associated with water and solvent recycling [1], [2]. Besides, the corrosive interaction between oxygen and the acidic components of combustion gas with amines further contributes to its drawbacks. This highlights the need to develop thermally stable solid materials with high adsorption values to facilitate efficient CO₂ capture via physisorption. The 3 main objectives of this research project is to firstly, synthesis mesoporous silicon nitride sample. Secondly, verify its CO₂ adsorption capability. Thirdly, to investigate the parameters that affect the CO₂ adsorption capability.

2. METHODOLOGY

In this project, mesoporous silicon nitride will be synthesized using diimide decomposition method based on method of Kaskel et al [3]. CO₂ adsorption capability of the prepared mesoporous silicon nitride will then be verified where the precipitation temperature is varied to observe the effect on the CO₂ adsorption capability. The mixture will be reacted with gaseous ammonia to obtain a fine white powder consist of silicon diimide and ammonium halide which will undergo dehalogenation to yield silicon nitride. The main materials are silicon tetrachloride, pentane and ammonia while the main equipment used are argon-filled glove box, oven and horizontal tube furnace. Several characterization techniques such as XRD, FTIR, FESEM and TGA are employed to investigate the pore structure of prepared mesoporous silicon nitride sample along with its carbon capture capability. A total of 6 samples are synthesized at different precipitation temperatures: room temperature, 30°C, 35°C and 40°C using diimide decomposition investigate the method relationship to between precipitation temperature and carbon adsorption capability.

3. RESULTS AND DISCUSSION

XRD results confirmed the amorphous nature of the prepared samples. The presence of broad peak at around 22° further supports the amorphous structure of these samples. The XRD characterization is very similar for all 6 samples. The precipitation temperature and ammonia forms used do not seem to cause any changes in the XRD results. By comparing with XRD pattern of silicon dioxide by Mohamed [4], we conclude that the sample synthesized is an amorphous silicon dioxide instead of silicon nitride.

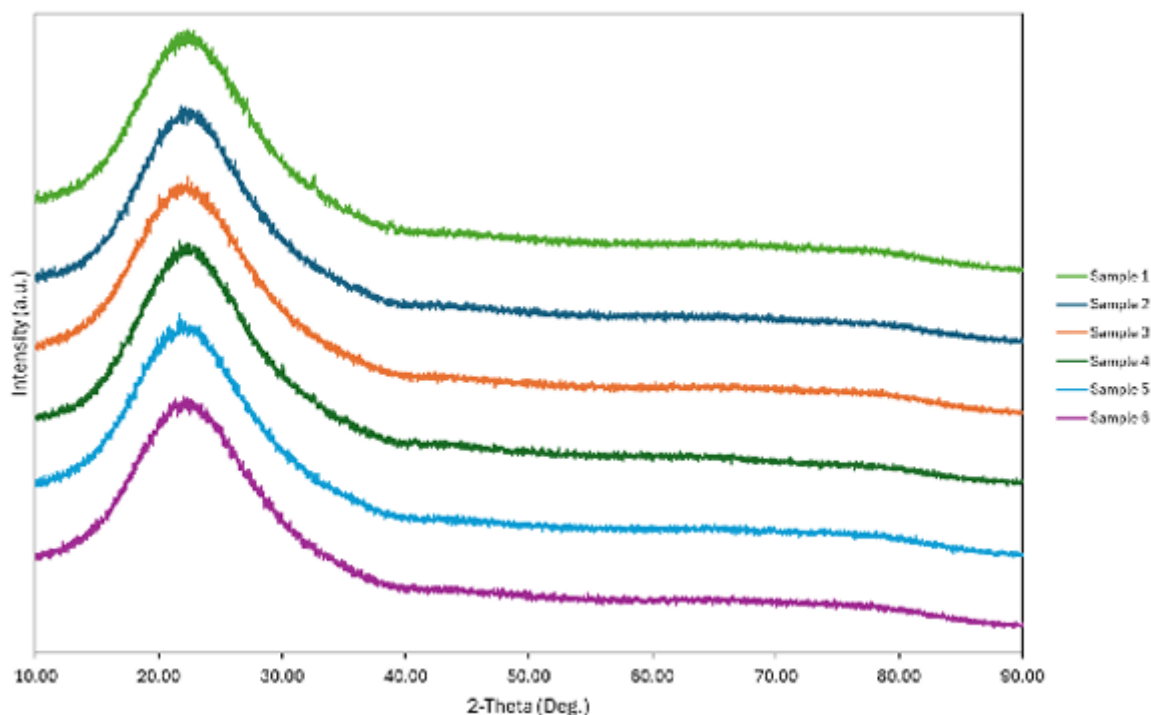


Figure 1. XRD Results

The synthesized samples were also analyzed for identification and characterization of functional groups on silica particles using FTIR spectroscopy in the spectral range of 500-4000 cm⁻¹. The samples displayed typical absorption bands similar of silica at 797.97 cm⁻¹ and 1053.78 cm⁻¹. These bands are attributed to the siloxane bond (797.97 cm⁻¹) and Si-O-Si bending (1053.78 cm⁻¹). [5][6]

Fig.2 shows the FTIR results obtained for Sample 2 to Sample 6. From the chart, we can observe that Sample 2, 3, and 4 have similar spikes while Sample 5 and 6 have similar patterns. The difference could be induced by the heating of ammonia in different forms during the dehalogenation process in horizontal tube furnace.

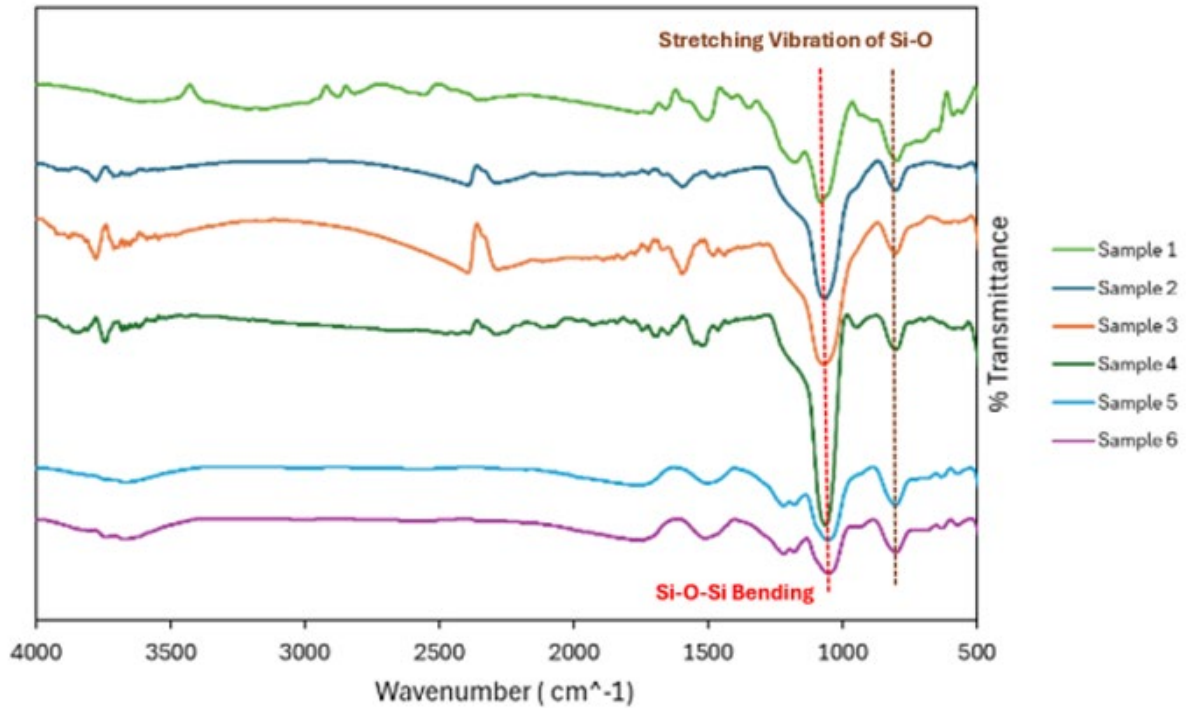


Figure 2. FTIR Results

Table 1. Pore Size of Samples

| Sample | Observation | Average Pore Size (nm) |
|--------|--|------------------------|
| 1 | Visible pores, relatively large, more spherical particles observed | 1761.47 |
| 2 | Very large pores, Certain parts difficult to see silicon structure (spherical), pores inside covered with more precipitate | 6267 |
| 3 | Very large pores, more compact compared to Sample 2 | 6333.67 |
| 4 | Very tiny pores, particles clump together, high dense | 149.17 |
| 5 | Compact, small pores | 572.77 |
| 6 | Large pores | 4103.67 |

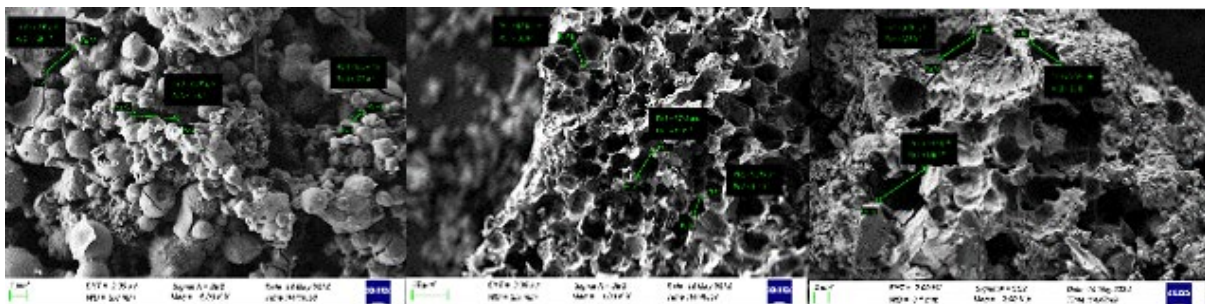


Figure 3. Sample 1, Sample 2 and Sample 3 (left to right)

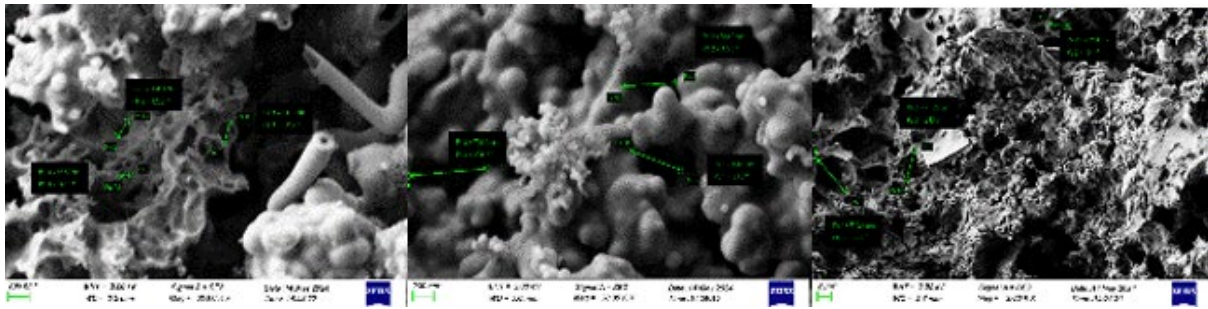


Figure 4. Sample 4, Sample 5 and Sample 6 (left to right)

By comparing the pore size of Sample 2 vs Sample 3, and Sample 5 vs Sample 5, we can identify the trend of pore size in relation to the precipitation temperature. Both comparisons show that the pore size increases with the increase of precipitation temperature.

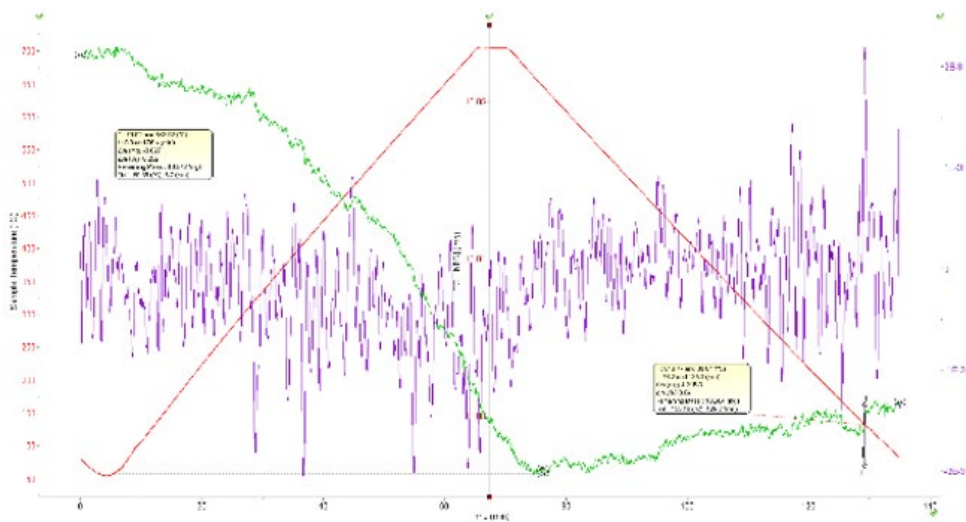


Figure 5. TGA Results for Sample 1

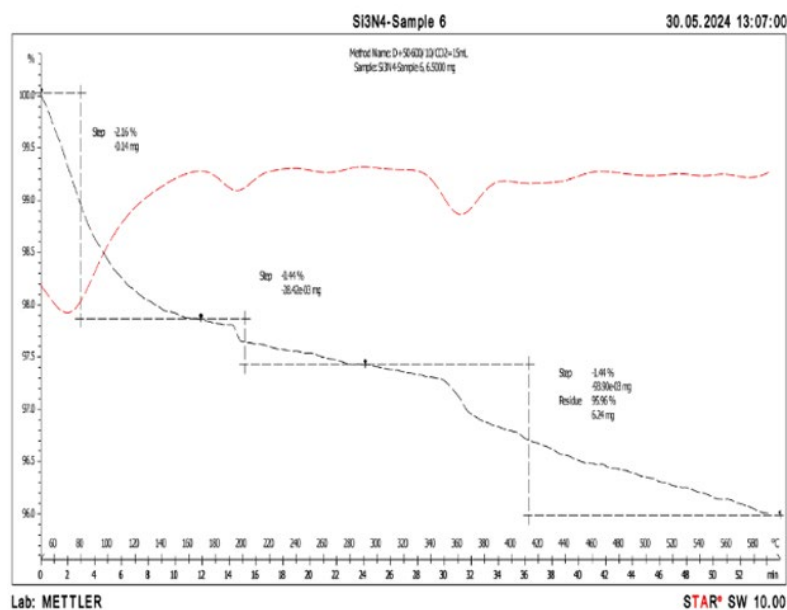


Figure 6. TGA Results for Sample 6

For Sample 1 which is synthesized at room temperature, it demonstrates slight gas adsorption with mass increase from 10.573mg to 10.604mg. Meanwhile for Sample 6 synthesized at 40°C, the mass of sample increase from 6.5mg to 6.24mg, which shows no sign of gas adsorption. Based on the results obtained, we observed that the gas adsorption capability decreases when the precipitation temperature increases.

4. CONCLUSION

For first objective, this study has utilized diimide decomposition method to synthesis silicon nitride. However, due to the easily oxidized nature of sample, silicon dioxide is synthesized instead. And the analysis later on will revolve around the gaseous adsorption capability of silicon dioxide. For second objective, the CO₂ adsorption capability of the prepared sample is verified. For third objective, the precipitation temperature is the parameter that has been investigated to identify its effect on the CO₂ adsorption capability of the sample. Based on the 2 samples sent for TGA, it is observed that the gas adsorption capability decreases as the precipitation temperature increases.

REFERENCES

- [1] Z. Liang, M. Marshall, and A.L. Chaffee: CO₂ adsorption-based separation by metal organic framework (Cu-BTC) versus zeolite (13X). *Energy Fuels* 23(5), 2785 (2009)
- [2] A. Sayari and Y. Belmabkhout: Stabilization of amine-containing CO₂ adsorbents: Dramatic effect of water vapor. *J. Am. Chem.Soc.* 132(18), 6312 (2010)
- [3] Kaskel, S., Schlichte, K. & Zibrowius, B. (2002). Pore size engineering of mesoporous silicon nitride materials. *Phys. Chem. Chem. Phys.*, 2002, 4, 1675–1681.
- [4] Mohamed Abdul Ghani, Nik Noor & Saeed, M. & Hazwani Hashim, Izyan. (2017). Thermoluminescence (TL) response of silica nanoparticles subjected to 50 Gy gamma irradiation.. *Malaysian Journal of Fundamental and Applied Sciences.* 13. 10.11113/mjfas.v13n3.593.
- [5] Wardhani, Gladys & Nurlela, Nurlela & Azizah, Mia. (2017). Silica Content and Structure from Corn Cob Ash with Various Acid Treatment (HCl, HBr, and Citric Acid). *Molekul.* 12. 174. 10.20884/1.jm.2017.12.2.382.
- [6] Mehmood, Yasir & Ullah Khan, Ikram & Shahzad, Yasser & Khalid, Syed & Asghar, Sajid & Irfan, Muhammad & Asif, Muhammad & Khalid, Ikrima & Yousaf, Abid & Hussain, Talib. (2019). Facile synthesis of mesoporous silica nanoparticles using modified sol-gel method: Optimization and in vitro cytotoxicity studies. *Pakistan Journal of Pharmaceutical Sciences.* 32. 1805-1812.

Microwave Carbonization of Oil Palm Kernel Shell (OPKS) using Activated Carbon as Absorber

Muhammad Ariffuddin bin Mohd Sabari^a and Shaifulazuar bin Rozali^{b*}

Department of Mechanical Engineering,
Faculty of Engineering, Universiti Malaya,
50603, Kuala Lumpur, Malaysia

Email: ^a muhdariffuddin1201@gmail.com, ^b azuar@um.edu.my

*Corresponding author

ABSTRACT

This study investigates the conversion of oil palm kernel shells (OPKS) into biochar via microwave pyrolysis, utilizing Activated Carbon as a microwave absorber. Operating at 2.45 GHz with a peak power output of 800 watts, microwave pyrolysis parameters ranged from 180W to 600W for durations of 10, 20, and 30 minutes, with nitrogen gas purging before each experiment to eliminate oxygen. Temperature profiles highlighted the efficiency of 450W, reaching stability early, suggesting it as a practical power level for effective pyrolysis. Biochar analysis revealed deepening coloration with prolonged pyrolysis, indicating enhanced carbonization. SEM analysis depicted varied pore sizes, suggesting potential structural alterations. EDS analysis demonstrated a consistent trend of increasing carbon content and decreasing oxygen content with longer heating times, peaking at 59.87% atomic concentration for the 600W, 30-minute sample. Bomb calorimeter analysis affirmed the energy potential of biochar, with the highest Gross Calorific Value (GCV) observed at 600W for 30 minutes. These findings offer insights for optimizing microwave pyrolysis parameters, providing a sustainable solution for waste management in the palm oil industry.

Keywords: Activated carbon; Biochar production; Gross calorific value; Microwave pyrolysis; Oil palm kernel shell.

1. INTRODUCTION

The African oil palm (*Elaeis guineensis* Jacq.) has been a crucial source of oil for centuries, and in recent decades, it has become a major global commodity. Predominantly cultivated in Southeast Asia, particularly in Indonesia and Malaysia, oil palm trees produce palm oil and palm kernel oil, vital for both food and non-food applications. The most commonly grown variety in Malaysia is Tenera, a hybrid known for its high yield of oil. Despite its economic benefits, the palm oil industry generates significant waste, including oil palm kernel shell (OPKS), which constitutes around 64% of the bunch mass. Traditionally, OPKS is either burned for energy or left to decompose, leading to environmental concerns. With the increasing demand for sustainable waste management, utilizing OPKS for biochar production through pyrolysis presents a promising solution.

This study focuses on the microwave pyrolysis of OPKS using activated carbon as a microwave absorber. By varying the power levels and exposure times, the research aims to optimize the production of biochar, characterized by its high gross calorific value and substantial porosity. The findings are

expected to contribute to efficient and sustainable waste management practices in the palm oil industry, offering valuable insights for future biomass utilization and applications.

2. METHODOLOGY

The oil palm kernel shells (OPKS) used in this study were obtained from Palong Cocoa Palm Oil Mills and prepared by sun-drying to reduce moisture content, followed by grinding into particles between 1.18 mm and 1.7 mm. For each of the 12 samples prepared, a 70:30 ratio of OPKS to activated carbon (AC) was used, with each sample containing 70 grams of OPKS and 30 grams of AC. The AC was ground to a size smaller than 1.18 mm. The mixture was placed in a conical flask to facilitate the absorption of microwaves by the AC, enabling rapid heating during pyrolysis.

The experimental setup utilized a modified home microwave oven operating at 2.45 GHz with a peak power output of 800 watts. A 500ml conical flask with an airtight rubber stopper and ports for nitrogen flushing, a thermocouple, and bio-gas outlet was used. The flask was purged with nitrogen gas at a flow rate of 4 L/min for 2 minutes before each run to ensure safety by eliminating oxygen. The microwave pyrolysis parameters were set at power levels of 180W, 300W, 450W, and 600W for durations of 10, 20, and 30 minutes. After pyrolysis, the produced biochar was collected and weighed.

Characterization of the biochar involved multiple analyses: temperature monitoring during pyrolysis using a thermocouple connected to a computer, calorific value determination with an IKA C200 Bomb Calorimeter, and surface morphology examination through Scanning Electron Microscopy (SEM) and Energy Dispersive X-ray Spectroscopy (EDS). These tests provided detailed insights into the chemical, structural, and energy-related properties of the biochar, supporting its potential applications in various fields.

3. RESULTS AND DISCUSSION

3.1 Biochar Yield and Properties

The pyrolysis of oil palm kernel shell (OPKS) results in biochar production, characterized by three stages of thermal degradation: drying, devolatilization, and carbonization. Longer pyrolysis durations deepen the color of the biochar, indicating enhanced carbonization and potential for various applications such as soil amendment and carbon sequestration (Qin et al., 2022). For example, biochar produced at 600W for 30 minutes exhibited a deep color and higher carbon content of 62%, suggesting its suitability for carbon sequestration purposes.

3.2 Scanning Electron Microscopy (SEM) Analysis

SEM analysis reveals changes in pore size and structure of biochar produced from OPKS at different power levels and durations. Higher power levels and longer heating times initially result in larger pore sizes, followed by potential structural collapse or densification [5]. For instance, biochar produced at 600W for 30 minutes exhibited a pore size of 8.116 micrometers, indicating extensive volatilization and expansion. The presence of both large and tiny pores suggests versatile applications for biochar, leveraging its diverse pore sizes in areas such as soil amendment and water purification. Fig. 1 depicts biochar produced by the pyrolysis of OPKS at 600W after 30 minutes.

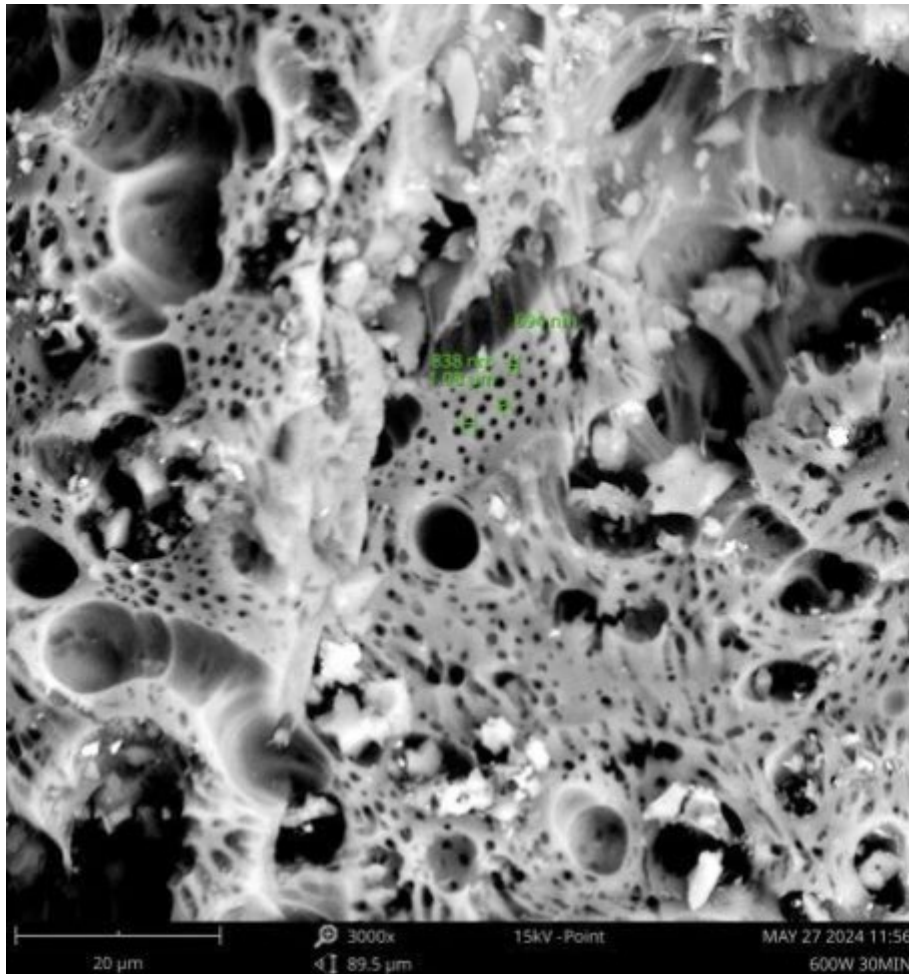


Figure 1. SEM Image for 600W 10 minutes OPKS Biochar

3.3 Energy-dispersive X-ray Spectroscopy (EDS) Analysis

EDS analysis shows increasing carbon content and decreasing oxygen content with prolonged heating at all power levels (180W, 300W, 450W, and 600W), indicating enhanced carbonization and volatile expulsion during pyrolysis [1]. For example, Fig. 2 shows the EDS spectrum for biochar produced at 450W for 30 minutes, exhibited the highest carbon content of 60.59% and an oxygen content of 0.33%. Boron content remains relatively stable, suggesting minimal influence by pyrolysis conditions. These results highlight the potential of microwave pyrolysis to produce biochar with high carbon content suitable for energy applications.

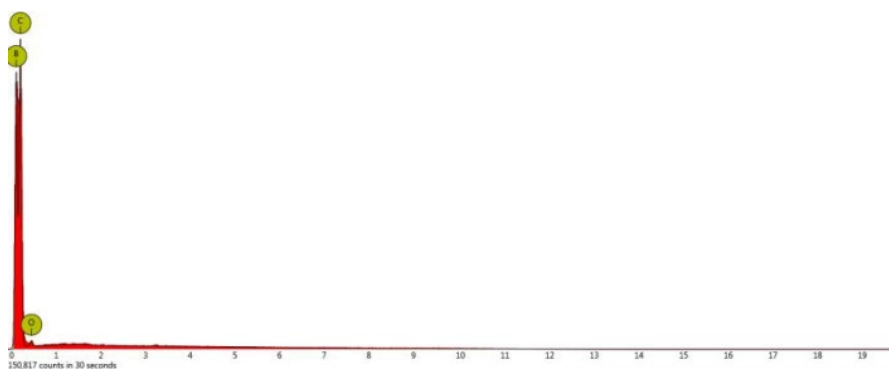


Figure 2. EDS Spectrum for 450 W 30 min

3.4 Temperature Reading Analysis

The temperature profiles during microwave pyrolysis of oil palm kernel shells (OPKS) demonstrate rapid initial temperature rises followed by plateaus, indicative of a two-stage process. Higher power levels (600W and 450W) lead to faster initial temperature increases compared to lower power levels (300W and 180W), aligning with microwave heating principles [3]. Figure 3 shows the Temperature Profile of Microwave Pyrolysis at 180W, 300W, 450W, and 600W for 30 Minutes.

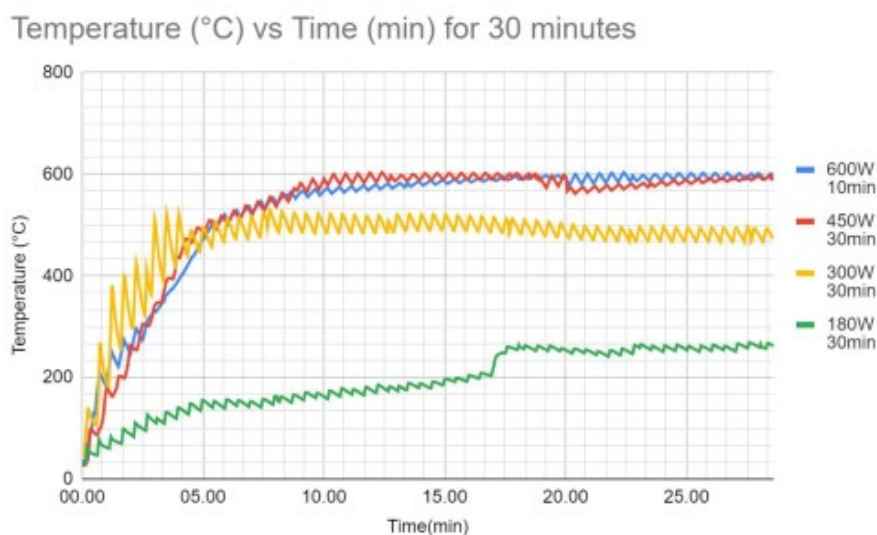


Figure 3. Temperature Profile of Microwave Pyrolysis at 180W, 300W, 450W, and 600W for 30 Minutes

Notably, activated carbon (AC) acts as a microwave absorber, facilitating rapid and efficient energy transfer to the sample. This is evident in the swift temperature rise observed in the 600W and 450W samples, which reach similar maximum temperatures despite the difference in power levels. The high surface area of AC enables effective interaction with microwave radiation, converting it into heat. Consequently, AC enhances the heating rate and overall efficiency of the pyrolysis process, contributing to thorough thermal decomposition of OPKS and the production of high-quality biochar. Further optimization studies should consider the role of AC in maximizing energy transfer and biochar yield during microwave pyrolysis.

3.5 Bomb Calorimeter Analysis

Bomb calorimeter analysis demonstrates a positive correlation between microwave power levels and processing durations with biochar energy content (Gross Calorific Value, GCV) [2]. Higher power levels and longer durations result in higher GCVs, indicating a promising potential for microwave pyrolysis to produce biochar with significant energy potential from OPKS. For example, biochar produced at 600W for 30 minutes exhibited a GCV of 28213 J/g, highlighting its potential as a renewable energy source. Further optimization is required to fine-tune duration and power levels for maximum energy yield.

4. CONCLUSION

The study successfully achieved its objectives by evaluating the microwave absorption properties of activated carbon, establishing its suitability for pyrolysis. Variation in microwave power levels and exposure times significantly impacted the efficiency and yield of biochar from oil palm kernel shells (OPKS), highlighting the importance of optimization. Characterization of OPKS-derived biochar revealed substantial porosity, indicating its potential for soil enhancement and pollutant adsorption. Overall, the research underscores the effectiveness of microwave pyrolysis in producing biochar with diverse applications, advancing sustainable solutions in energy, agriculture, and environmental management.

REFERENCES

- [1] Boona, S. R. (2021). Quantitative SEM-EDS Analysis of Semi-Transparent Samples. *Microscopy Today*, 29(1), 42–48. doi:10.1017/S1551929520001790
- [2] Bridgwater, A. V., & Grassi, G. (Eds.). (2012). *Biomass pyrolysis liquids upgrading and utilization*. Springer Science & Business Media.
- [3] Li, H., Xu, J., Nyambura, S. M., Wang, J., Li, C., Zhu, X., ... & Wang, Y. (2022). Food waste pyrolysis by traditional heating and microwave heating: A review. *Fuel*, 324, 124574. <https://doi.org/10.1016/j.fuel.2022.124574>
- [4] Qin, F., Zhang, C., Zeng, G., Huang, D., Tan, X., & Duan, A. (2022). Lignocellulosic biomass carbonization for biochar production and characterization of biochar reactivity. *Renewable and Sustainable Energy Reviews*, 157, 112056. <https://doi.org/10.1016/j.rser.2021.112056>
- [5] Yashim, M. M., Razali, N., Saadon, N., & Rahman, N. A. (2016). Effect of activation temperature on properties of activated carbon prepared from oil palm kernel shell (OPKS). *ARP Journal of Engineering and Applied Sciences*, 11(10), 6389-6392.

Effect of Catalyst on Carbonization of Oil Palm Empty Fruit Bunch (EFB)

Amsyar bin Khairom ^a and Shaifulazuar Rozali ^{b*}

Department of Mechanical Engineering,
Faculty of Engineering, Universiti Malaya,
50603, Kuala Lumpur, Malaysia

Email: ^a amsyarkhairomp@gmail.com, ^b azuar@um.edu.my

*Corresponding author

ABSTRACT

This study addresses the waste disposal issues associated with Malaysia's empty fruit bunch (EFB) from oil palm by examining the production and characterization of biochar through slow pyrolysis. Utilizing catalysts Zinc Oxide (ZnO), Magnesium Oxide (MgO), and Potassium Hydroxide (KOH), investigation of the effects of heating time and temperature on biochar quality. Experiments were conducted at temperatures of 250°C, 350°C, and 450°C, with heating times of 30 and 60 minutes, resulting in 18 distinct samples. The biochar produced was analyzed using a bomb calorimeter for heating value, Scanning Electron Microscopy (SEM) for structural characterization, and Energy-dispersive X-ray Spectroscopy (EDS) for chemical composition. Findings indicate that catalyst type, temperature, and heating duration significantly influence biochar properties, providing insights for optimizing EFB waste conversion into valuable solid fuel.

Keywords: biochar production; empty fruit bunch; slow pyrolysis; catalyst effects; structural characterization

1. INTRODUCTION

Malaysia, along with Indonesia, is a leading palm oil producer. Despite its benefits, the industry has significant environmental impacts. Palm oil mills consume large amounts of water and energy and generate substantial solid waste, by-products, wastewater, and air pollution. Significant byproducts include palm kernel shell (PKS) and empty fruit bunch (EFB), comprising 4.5% and 22% of the weight per ton of fresh fruit bunches (FFB), respectively. Empty fruit bunch (EFB), a major byproduct of palm oil processing, is often discarded, leading to environmental issues due to greenhouse gas emissions during decomposition. Annually, palm oil mills generate about 22 to 23 million tons of EFB. To maximize biochar production from oil palm waste like Empty Fruit Bunch (EFB), slow pyrolysis is ideal. This process, conducted in batches at 300°C to 700°C with a slow heating rate over an extended period, efficiently produces both biochar and bio-oil.

Catalysts enhance the production of desired products like biochar by promoting specific reaction to the pathways later and aiding deoxygenation during pyrolysis. They lower the activation energy needed, reducing the temperature required for organic decomposition and improving energy efficiency. This study analysed biochar produced by slow pyrolysis in a tube furnace, using a catalyst to maximize biochar yield and improve both its quality and quantity.

Slow pyrolysis typically produces three main products: char, bio-oil, and biogas. All these products are usually collected for analysis. However, the primary goal of this tube furnace slow pyrolysis is to collect biochar, so collecting syngas and bio-oil is not required. At the end of the experiment, the biochar is gathered from the tube furnace, weighed, labelled, and stored for further analysis.

2. METHODOLOGY

2.1 Preparation of Empty Fruit Bunch (EFB) to get biochar

The Empty Fruit Bunch (EFB) is divided into small pieces, weighing 2 grams, and mixing with 1 gram of catalyst before placing it in an alumina boat for the tube furnace. During slow pyrolysis, the sample is inserted into the tube furnace, and oxygen is removed using nitrogen gas, initiating the heating process. The study tests three types of catalysts which are Magnesium Oxide (MgO), Potassium Hydroxide (KOH), and Zinc Oxide (ZnO), at temperatures of 250°C, 350°C, and 450°C for 30 and 60 minutes each. There will be 18 samples for slow pyrolysis.

2.2 Material characterization

The biochar surface structure and composition will be analyzed using Scanning Electron Microscopy (SEM), Energy-Dispersive X-ray Spectroscopy (EDS), and a Bomb Calorimeter. SEM will be employed to examine the biochar surface, revealing features such as globules, pores and smooth areas, which help assess the performance of the pyrolysis process. EDS will provide detailed compositional analysis. The Bomb Calorimeter machine will measure the heating value of each biochar sample from the experiment, providing essential data on its energy content.

3. RESULTS AND DISCUSSION

3.1 Scanning Electron Microscopy (SEM) for biochar collected.

Below is an example of ZnO biochar with 60 minutes heating time pores. For ZnO with a 60-minute heating time, pore diameters decrease as temperature rises. At 250°C, the pore diameter is 7.06 μm , which slightly decreases to 7.03 μm at 350°C and further reduces to 6.70 μm at 450°C, indicating a significant temperature dependent reduction.

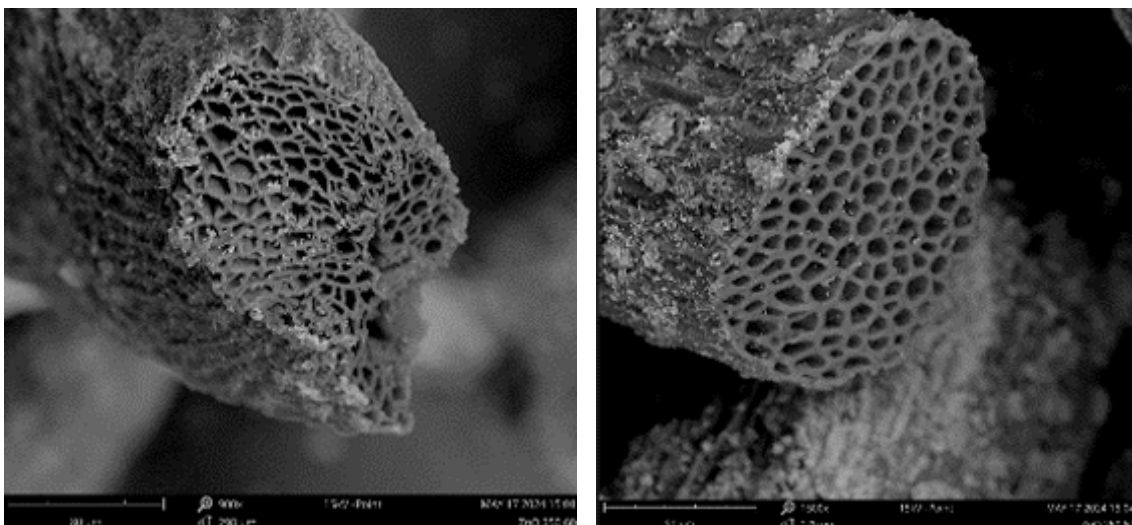


Figure 1 and Figure 2. SEM images of ZnO carbon taken at 250 °C for 60 minutes

During the slow pyrolysis of empty fruit bunches, pores form as the organic material decomposes and volatile compounds are released, creating a porous structure. The process concludes when smoke emission stops. Conditions like temperature, heating rate, and residence time significantly influence pore size, distribution, and quantity, with lower temperatures resulting in larger pores.

Table 1. Average pores diameter of ZnO for 60 minutes heating time

| Types of catalyst | Temperatures (°C) | Heating Time (mins) | Average Pores diameter (µm) |
|-------------------|-------------------|---------------------|-----------------------------|
| ZnO | 250 | 60 | 7.06 |
| ZnO | 350 | 60 | 7.03 |
| ZnO | 450 | 60 | 6.70 |

3.2 Energy-Dispersive X-ray Spectroscopy (EDS)

All the biochar samples predominantly consist of carbon, indicating that the pyrolysis process effectively transformed the organic material into a stable, carbon-rich product. The high carbon content demonstrates that the Empty Fruit Bunch (EFB) material was almost entirely converted into biochar, except for the sample treated with ZnO at 450°C for 60 minutes. This sample showed lower carbon content because the temperature and heating duration were no longer optimal. This suboptimal condition led to a significant release of volatile compounds, reducing the volatile matter in the resulting carbon. Additionally, the data suggests that non-flaking ash formed around the carbon during carbonization was burned off, contributing to a decrease in the weight of the carbonized sample.

3.3 Bomb Calorimeter

The heating value of ZnO pyrolysis consistently exceeds 20 MJ/kg, making it the most effective catalyst among those tested. Its significant heating value indicates superior performance, underscoring ZnO potential as the best catalyst for enhancing energy output in the pyrolysis of EFB.

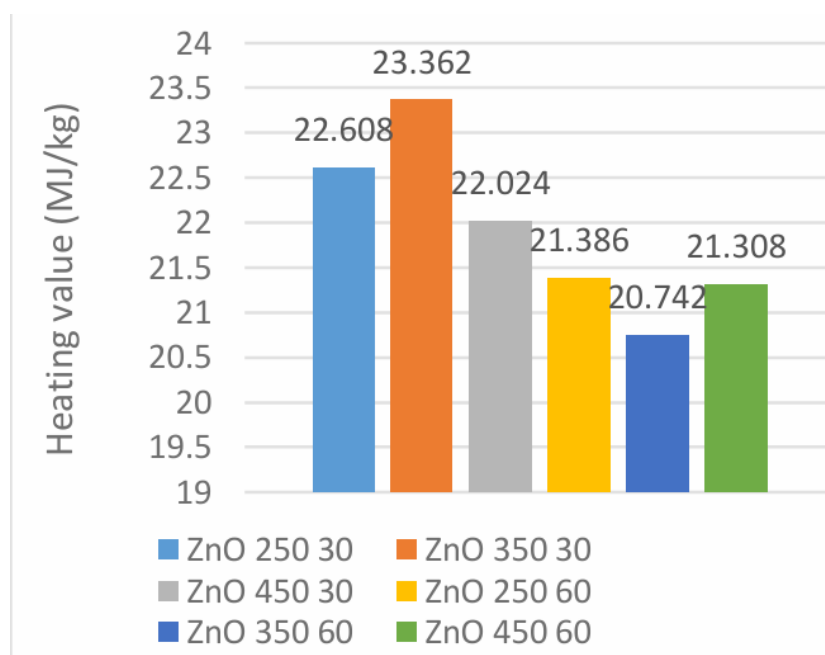


Figure 3. Heating value for ZnO catalyst for 30 minutes and 60 minutes

4. CONCLUSION

The slow pyrolysis of Empty Fruit Bunch (EFB) using ZnO catalyst shows high heating values above 20 MJ/kg, with the highest at 23.362 MJ/kg at 350°C for 30 minutes. Pore diameters are varied with temperature, diameters decreasing at 350°C but increasing at 450°C. Carbon content analysis indicated lower values at higher temperatures, yet heating values remained significant, highlighting ZnO effectiveness as a catalyst for Empty Fruit Bunch (EFB) during pyrolysis.

REFERENCES

- [1] Gholizadeh, M., Meca, S., Zhang, S., Clarens, F., & Hu, X. (2024). Understanding the dependence of biochar properties on different types of biomasses. *Waste Management*, 182, 142–163. <https://doi.org/10.1016/j.wasman.2024.04.011>
- [2] Li, Y., Gupta, R., Zhang, Q., & You, S. (2023). Review of biochar production via crop residue pyrolysis: Development and perspectives. *Bioresource Technology*, 369, 128423. <https://doi.org/10.1016/j.biortech.2022.128423>
- [3] Lee, X. J., Lee, L. Y., Gan, S., Thangalazhy-Gopakumar, S., & Ng, H. K. (2017). Biochar potential evaluation of palm oil wastes through slow pyrolysis: Thermochemical pyrolysis characterization and pyrolytic kinetic studies. *Bioresource Technology*, 236, 155–163. <https://doi.org/10.1016/j.biortech.2017.03.105>

Simulation and Analysis of IMC Behaviour in SAC305/Nano-Fe Solder under Mechanical Loading and Temperature Variations

Ben Lee How Yin ^a and Goh Yingxin ^{b*}

Department of Mechanical Engineering,
Faculty of Engineering, Universiti Malaya,
50603, Kuala Lumpur, Malaysia

Email: ^a benlee1218@outlook.com, ^b gohyingxin@um.edu.my

*Corresponding author

ABSTRACT

This research investigates the behaviour of intermetallic compounds (IMCs) in SAC305 solder reinforced with nano-Fe under mechanical loading and temperature variations. The study aims to address the brittleness and reliability issues associated with thick IMCs in SAC305 solder. By incorporating nano-Fe using a flux doping technique, the research explores the impact on IMC behaviour, microstructure, and mechanical properties of the solder joints. The study employs FESEM, EDX, and nanoindentation tests to characterize the solder and IMCs. The findings reveal that nano-Fe and sub-zero temperature aging alter IMC morphology, hinder IMC growth, and with 2.0 wt.% nano-Fe being optimal for suppressing IMC growth (50.1% reduction), while 1 wt.% maximizes the IMC Young's modulus from 147.57 GPa to 154.58 GPa and hardness from 2.30 GPa to 2.37 GPa. The nanoindentation simulation model constructed using ABAQUS CAE accurately captures IMC mechanical behaviour.

Keywords: Intermetallic Compound Behavior; SAC305 Solder; Nano-Fe Reinforcement; Mechanical Properties; IMC Growth Suppression

1. INTRODUCTION

The rapid development of microelectronics has led to the need for smaller, faster, and more efficient electronic devices. Traditionally, Pb-based solders were used, but due to their toxicity, lead-free solders, particularly Sn-Ag-Cu (SAC) alloys, have become popular alternatives. However, SAC solders have their own challenges, such as the formation of brittle intermetallic compounds (IMCs), limited compliance, and high cost [9].

To overcome these challenges, researchers have been exploring the incorporation of nanoparticles into Pb-free solder pastes as they could refine the microstructures, inhibiting IMC growth [8], and improving mechanical properties. Among the various nanoparticles, nano-Fe has shown promise in enhancing the mechanical properties, thermal characteristics, and reliability of solder joints [10]. Previous research has investigated the effects of thermal aging on IMC growth [4], but there are still gaps in understanding the impact of sub-zero temperatures on solder joints with and without nano-Fe. Additionally, there is a need for further exploration into the optimal concentration of nano-Fe for maximizing mechanical properties. The existing research using the Vickers microhardness test [12] and shear test [2] also lacks comprehensive studies on the nanoscale mechanical properties of nano-Fe/SAC 305 solder joints using

advanced techniques like nanoindentation testing. Furthermore, research is scarce on simulating the IMC behaviour within nano-Fe/SAC 305 solder joints.

2. METHODOLOGY

2.1 Sample Preparation

Different weight percentages (1.0 wt.% and 2.0 wt.%) of nano-Fe flux were prepared by manually mixing commercial Fe nanoparticles with commercial TACFlux 089HF solder flux. Copper substrates were cut into 10mm x 10mm x 1mm dimensions using CNC Wire Cut Electrical Discharge Machining (EDM). 0.01g of nano-Fe doped flux was applied evenly on each substrate, followed by thin SAC305 solder pieces (8mm x 8mm x 0.1mm). The samples were reflowed at 260°C for 5 minutes in a preheated tube furnace, then left to cool for 30 minutes before cooling at room temperature. Reflowed samples were aged at -20°C for 14, and 28 days.

2.2 IMC Behavior Studies

The ZIESS Gemini Auriga Crossbeam Field Emission Scanning Electron Microscopy (FESEM) was used to investigate the microstructure and morphology of IMCs. The samples were magnified at 500x and 2000x, with a 15 kV accelerating voltage and Backscattered Electron Detection (BSD). Energy Dispersive X-ray (EDX) analysis was conducted to examine the composition of the IMCs formed. The thickness of IMC layers was calculated using ImageJ software by dividing the area (A) and length (L) of IMCs.

2.3 Nanoindentation Test

Nanoindentation testing was performed using a Hysitron UBI 750 Nanoindenter with a Berkovich diamond indenter tip ($\phi = 70.3^\circ$). The test parameters included a peak load of 1000 μN and a total duration of 100 seconds (20s loading, 60s hold, 20s unloading). The test was repeated multiple times on each sample to ensure statistical validity. Eq. 1 – 5 enables the calculation of contact depth h_c , hardness (H), reduced Young's modulus, (E_r), Young's modulus and stiffness (S) [6] with the assumptions: $E_1 = 1141 \text{ GPa}$, $\nu_1 = 0.07$ [5], $\nu = 0.3$ [1].

$$h_c = h_{max} - \epsilon \frac{P_{max}}{S} \quad (1)$$

$$H = \frac{P_{max}}{A} \quad (2)$$

$$S = \left(\frac{dP}{dh}\right)h_{max} \quad (3)$$

$$E_r = \frac{\sqrt{\pi}}{2\beta} \left(\frac{S}{\sqrt{A}}\right) \quad (4)$$

$$\frac{1}{E_r} = \left(\frac{1 - \nu^2}{E}\right) + \left(\frac{1 - \nu_1^2}{E_1}\right) \quad (5)$$

2.4 Simulation of Nanoindentation Test

A 2D axisymmetric model of the IMC layer and Berkovich indenter tip was created in ABAQUS CAE (Figure 1). The IMC layer was modelled as a flat, homogeneous, isotropic, elastic-plastic material. The Berkovich indenter tip considered a rigid body, is modelled as homogeneous and isotropic. Material

properties for the IMC layer and indenter tip were defined based on experimental data and literature [3, 11]. The simulation involved a static, general analysis step with a total time of 10.01 seconds, mirroring the experimental test time. Boundary conditions were applied to maintain symmetry and simulate a rigid substrate. A peak force of 998 μN was applied to the indenter tip, following the same loading-hold-unloading profile as the experiment.

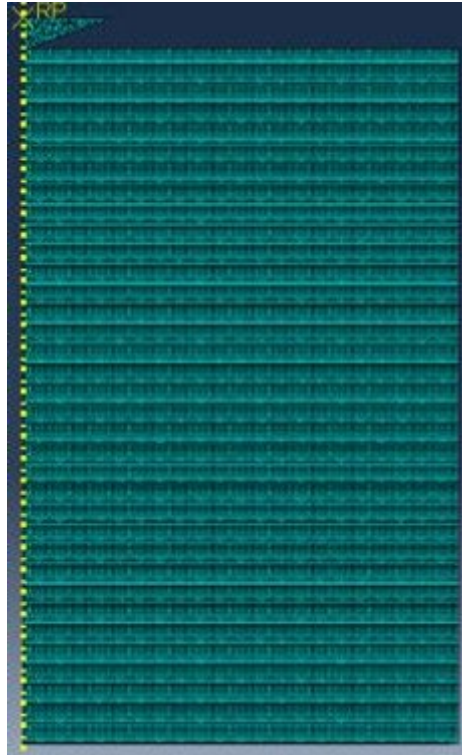


Figure 1. Simulation model

3. RESULTS AND DISCUSSION

3.1 Morphology and Interfacial Studies

FESEM analysis revealed that the morphology of the IMC layer transitioned from scallop-type to planar and needle-like with the addition of nano-Fe (0, 1.0, and 2.0 wt. %). This change is attributed to nano-Fe acting as a diffusion barrier [10], hindering the growth of Cu_6Sn_5 and Cu_3Sn IMCs. EDX analysis confirmed the presence of nano-Fe particles in both the solder and Cu substrate, although the detected amount was lower than the initial addition, possibly due to rejection during flux doping or oxidation.

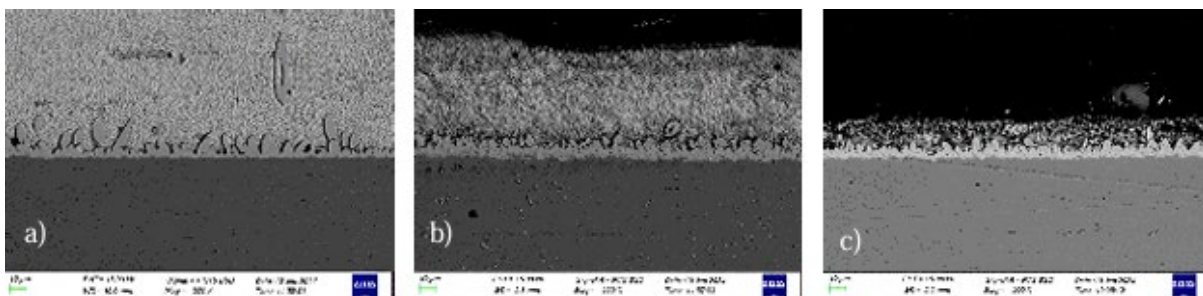


Figure 2. FESEM images of SAC305-xnano-Fe (a) x=0 (b) x = 1.0 wt %. (c) 2.0 wt %. at 500 magnifications.

3.2 IMC Growth Studies

The study observed a decrease in the growth of Cu₆Sn₅ and Cu₃Sn IMCs with increasing nano-Fe concentration in as-reflowed samples. This suggests that nano-Fe hinders the formation and growth of these IMCs during reflow.

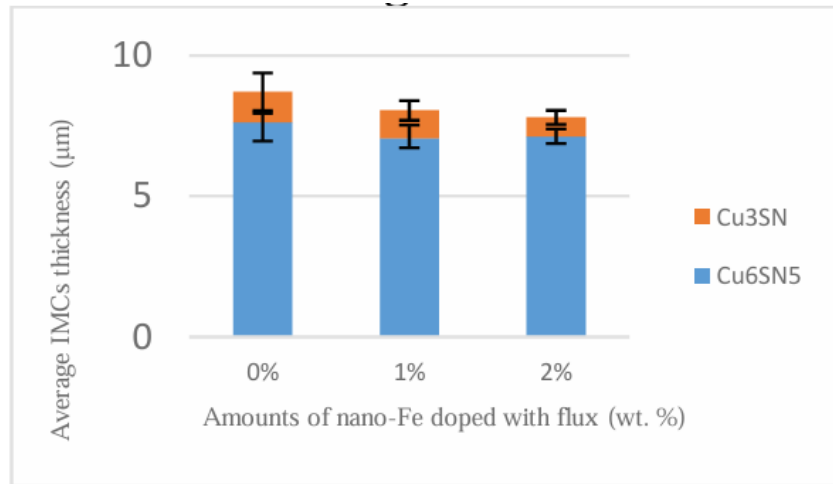


Figure 3. Effects of amount of nano-Fe additions on the average IMCs thickness

3.3 Sub-zero Temperature Aging and IMC Growth Studies

Sub-zero temperature aging (-20°C for 14 and 28 days) led to a morphological transition of the IMC layer from scallop-like (0 wt.% nano-Fe) to flattened in SAC305 solder joints with 1.0 and 2.0 wt.% nano-Fe. The average total IMC thickness varied with nano-Fe concentration and aging duration. The solder joint with 2.0 wt.% nano-Fe showed a consistent decrease in IMC thickness over time, indicating that this concentration is optimal for suppressing IMC growth.

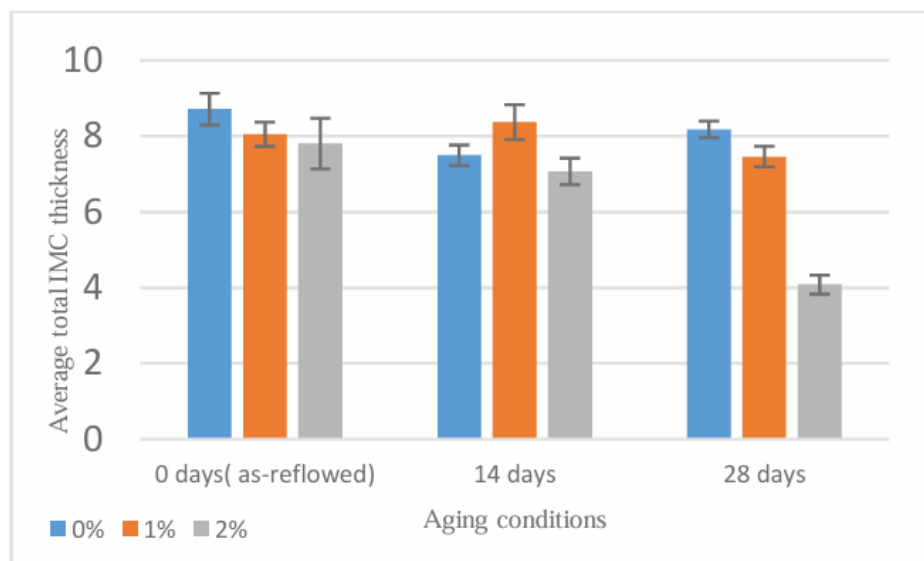


Figure 4. Average total IMC thickness of SAC305-xnano Fe (x = 0, 1.0, 2.0 wt %) after aged at -20°C for 0(as reflowed), 14, 28 days.

3.4 Experimental Nanoindentation Studies

Nanoindentation tests results showed that the addition of 1.0 wt.% nano-Fe increased the Young's modulus and hardness of the IMC, likely due to the inhibition of dislocation movement and grain boundary sliding [7]. However, further increasing the nano-Fe concentration to 2.0 wt.% led to a decrease in Young's modulus, while the hardness remained almost constant.

Table 1. Average values of nanoindentation results

| Nano-Fe (wt %) | h_c (nm) | E_r (GPa) | E (GPa) | S ($\mu\text{N}/\text{nm}$) | H (GPa) |
|----------------|------------|-------------|-----------|---------------------------------|-----------|
| 0 | 79.07 | 142.19 | 147.57 | 103.77 | 2.63 |
| 1 | 81.19 | 148.07 | 154.58 | 111.14 | 2.37 |
| 2 | 95.18 | 118.99 | 120.82 | 97.39 | 2.36 |

3.5 Nanoindentation Simulation Studies

The nanoindentation simulation model successfully captured the mechanical behaviour of the IMC layer, aligning with experimental results. The model revealed stress and strain distributions consistent with expected behaviour under localized indentation. The correlation between high-stress regions and high plastic strain areas confirmed the material's response to loading beyond the elastic limit Figure 5.

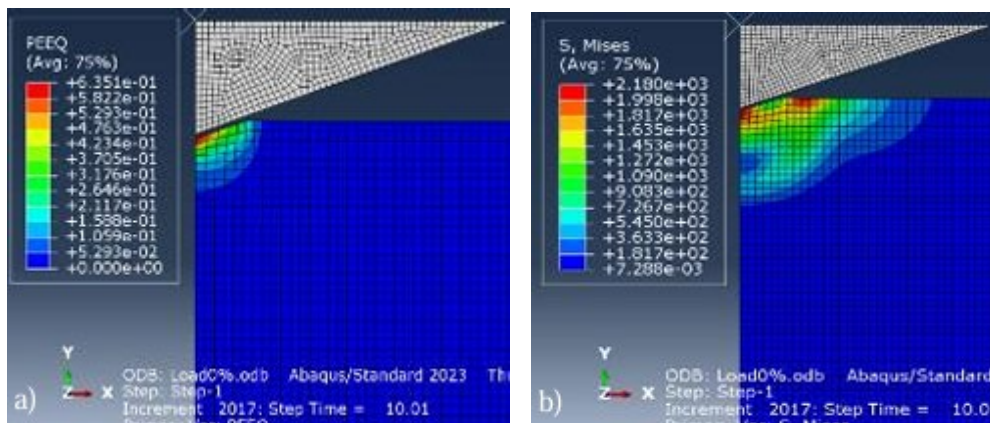


Figure 5. (a) Equivalent plastic strain (b) Mises stress contours (0 wt% nano-Fe)

4. CONCLUSION

The incorporation of nano-Fe into SAC305 solder joints effectively mitigates IMC layer growth and enhances mechanical properties. The optimal nano-Fe concentration of 2 wt.% suppresses IMC growth during reflow and sub-zero temperature aging, while 1 wt.% maximizes Young's modulus and hardness. The nanoindentation simulation model constructed using ABAQUS CAE accurately captures IMC mechanical behaviour, offering a valuable tool for future research.

REFERENCES

- [1] Bachok, Z., Saad, A., Abas, M., Ali, M., & Fakpan, K. (2022). STRUCTURAL ANALYSIS ON NANOCOMPOSITES LEAD FREE SOLDER USING NANOINDENTATION. *Journal of Advanced Manufacturing Technology (JAMT)*, 16(2).

- [2] Bui, Q. V., & Jung, S. B. (2014). Evaluation of mechanical properties of low-Ag ball grid array solder joints using a high-speed ball shear test. *Journal of Alloys and Compounds*, 589, 590-595. <https://doi.org/https://doi.org/10.1016/j.jallcom.2013.11.199>
- [3] Choudhury, S. F., & Ladani, L. (2016). Local shear stress-strain response of Sn-3.5Ag/Cu solder joint with high fraction of intermetallic compounds: Experimental analysis. *Journal of Alloys and Compounds*, 680, 665-676. <https://doi.org/https://doi.org/10.1016/j.jallcom.2016.04.184>
- [4] Hu, X., Xu, T., Jiang, X., & Li, Y. (2016). Interfacial reaction and IMCs growth behavior of Sn3Ag0.5Cu/Ni solder bump during aging at various temperatures. *Journal of Materials Science: Materials in Electronics*, 27(5), 4245-4252. <https://doi.org/10.1007/s10854-016-4288-9>
- [5] Liu, C. Z., & Chen, J. (2007). Nanoindentation of lead-free solders in microelectronic packaging. *Materials Science and Engineering: A*, 448(1), 340-344. <https://doi.org/https://doi.org/10.1016/j.msea.2006.10.056>
- [6] Oliver, W. C., & Pharr, G. M. (2004). Measurement of hardness and elastic modulus by instrumented indentation: Advances in understanding and refinements to methodology. *Journal of Materials Research*, 19(1), 3-20. <https://doi.org/10.1557/jmr.2004.19.1.3>
- [7] Shnawah, D. A.-A., Said, S. B. M., Sabri, M. F. M., Badruddin, I. A., & Che, F. X. (2012). Microstructure, mechanical, and thermal properties of the Sn-1Ag-0.5Cu solder alloy bearing Fe for electronics applications. *Materials Science and Engineering: A*, 551, 160-168. <https://doi.org/https://doi.org/10.1016/j.msea.2012.04.115>
- [8] Tan, A. T., Tan, A. W., & Yusof, F. (2015). Influence of nanoparticle addition on the formation and growth of intermetallic compounds (IMCs) in Cu/Sn-Ag-Cu/Cu solder joint during different thermal conditions. *Science and technology of advanced materials*.
- [9] Tang, Y., Luo, S. M., Li, G. Y., Yang, Z., & Hou, C. J. (2018). Ripening Growth Kinetics of Cu₆Sn₅ Grains in Sn-3.0Ag-0.5Cu-xTiO₂/Cu Solder Joints During the Reflow Process. *Journal of Electronic Packaging*, 140(1). <https://doi.org/10.1115/1.4038861>
- [10] Wodak, I., Yakymovych, A., & Khatibi, G. (2023, 10-14 May 2023). Hybrid Solder Joints: Morphology and Mechanical Properties of lead-free Sn-based Solders with nano-sized Fe doped Flux. 2023 46th International Spring Seminar on Electronics Technology (ISSE),
- [11] Wu, J.-Y., Kao, C. R., & Yang, J.-M. (2019). Mechanical reliability assessment of Cu₆Sn₅ intermetallic compound and multilayer structures in Cu/Sn interconnects for 3D IC applications. 2019 IEEE 69th Electronic Components and Technology Conference (ECTC),
- [12] Xu, S., Chan, Y. C., Zhang, K., & Yung, K. C. (2014). Interfacial intermetallic growth and mechanical properties of carbon nanotubes reinforced Sn3.5Ag0.5Cu solder joint under current stressing. *Journal of Alloys and Compounds*, 595, 92-102. <https://doi.org/https://doi.org/10.1016/j.jallcom.2014.01.083>

Assessment of Creep Resistant Materials and Low-Quality Steam Impact on Steam Turbine Blade

Noor Amnan bin Hijattulah^a and Mohd Zamri bin Zainon^{b*}

Department of Mechanical Engineering,
Faculty of Engineering, Universiti Malaya,
50603, Kuala Lumpur, Malaysia

Email: ^a nooramnan5@gmail.com, ^b zzainon@um.edu.my

*Corresponding author

ABSTRACT

The essential components of steam turbines are the turbine blades. They are the primary energy-driven parts of the steam turbine at every level, where power is produced by pressurising steam. Carbon fibre, molybdenum TMZ and waspaloy are high creep resistant material and have excellence potential to be used as steam turbine blade material. Additionally, the steam quality in a turbine is not 100% dry and effects the overall efficiency of the turbine. This study investigates the structural and thermal performance of three high creep resistant materials to be used to manufacture steam turbine blades. This study also investigates the effects of low-steam quality on the turbine blades. Two types of blades design were modelled by using SolidWorks. The structural and thermal analysis is conducted using ANSYS® Static Structural and ANSYS® Steady State Thermal respectively. The simulation of low-quality steam acting on the turbine blade is conducted using ANSYS® Fluent. Based on the analysis, waspaloy outperformed all other materials in terms of structural and thermal performance. Additionally, the low-quality steam effect the blades by producing the highest erosion rates in the central region of the blade and there are formation of eddies occurring at the trailing edge of the reaction blade.

Keywords: Creep Resistance; Erosion; Simulation; Steam Turbine; Thermal Analysis

1. INTRODUCTION

In the pursuit of enhancing the efficiency of steam turbines, there is a critical need for materials that can withstand elevated temperatures and resist the detrimental effects of creep. Stainless steel, although possessing favourable properties, it can be vulnerable to the effects of creep. Another crucial factor to consider is the quality of the steam. Achieving 100% steam quality is not possible due to various factors [2]. The steam quality in a turbine may as well drop which will impact the longevity and efficiency of the turbine. Therefore, understanding the behaviour of low-quality steam on the blades is crucial to optimise the design and enhance the overall efficiency in power generation.

2. METHODOLOGY

Two types of turbine blades are used in this study which are the impulse and reaction blade. The 3D model of the blade was designed and developed using SolidWorks. The model was then imported to ANSYS® Static Structural for the structural analysis. The properties of the materials were defined, and mesh was generated on the geometry with element size of 0.2m and a refined factor of 2. The centrifugal

stress was modelled by applying rotational velocity at the centre of rotation of the turbine and the load exerted by the steam was modelled by applying distributed load on the blade's surface.

For the thermal analysis, the blade models were imported to ANSYS® Steady State Thermal. The properties of the materials were defined, and the same mesh properties were used. Convection boundary is applied to the blade. The film coefficient and the ambient temperature are taken as $0.0025 \text{ W/mm}^2\text{°C}$ and 22°C respectively [1]. For the low-quality steam simulation, the blade models were imported to ANSYS® Fluent. Enclosure is created to develop the flow path of the steam. All the surfaces and bodies are provided with names to define the boundary conditions. The mesh is generated with tetrahedrons method, element size of 0.1m and edge sizing with 200 divisions. On the setup modules, the analysis type is set to steady state. Wet steam model was selected for the fluid with 0.1 water volume fraction. The inlet velocity was defined, and the outlet pressure is set to atmospheric pressure. The simulation was run with minimum iterations of 1 and maximum of 1000.

3. RESULTS AND DISCUSSION

For the structural analysis, the results show that waspaloy has the best performance than other materials in handling structural stresses, exhibiting lower stress values and minimal deformation under simulated operating conditions. Carbon fiber, although showing the least stress, underwent significant deformation, indicating its unsuitability for the high- stress environment of steam turbines. Molybdenum TMZ displayed poor performance, with high stress and deformation levels, further confirming its inadequacy for turbine blade manufacturing.

For the thermal analysis, the results show that waspaloy demonstrated superior thermal properties, maintaining the lowest temperature gradients and highest total heat flux, suggesting effective heat dissipation capabilities suitable for steam turbine application. Meanwhile, carbon fiber showed the highest temperature gradients and lowest heat flux, highlighting its limitations in turbine applications.

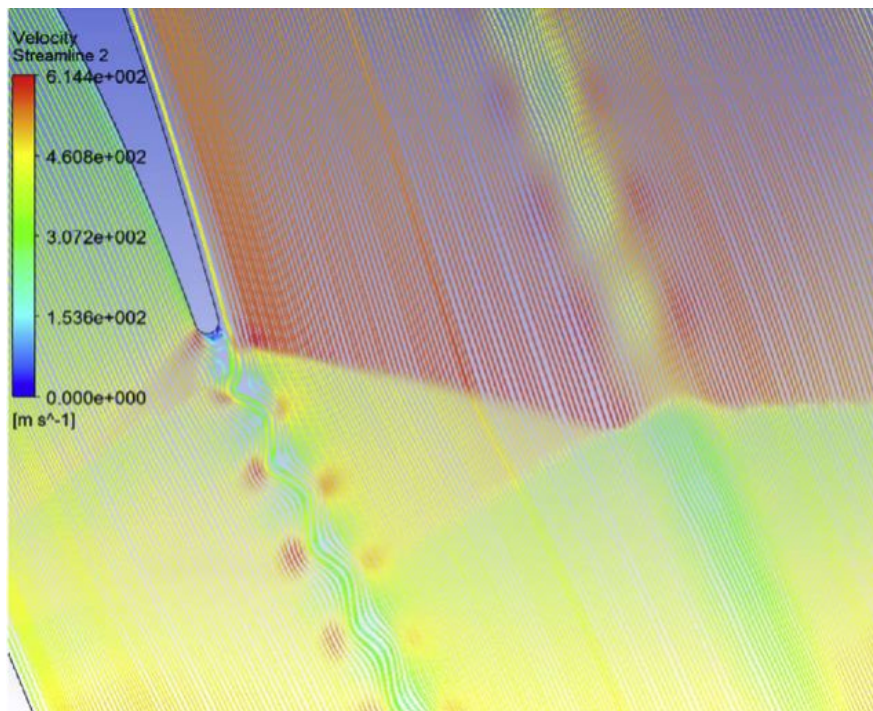


Figure 1. Velocity streamlines on the reaction blade

From the low-quality steam simulation, it was found that there is a noticeable formation of eddies on trailing edge of the reaction blade. However, for the impulse blade, the presence of water droplet does not appear to significantly alter the fundamental flow behaviour. Additionally, the low-quality steam will cause water droplets to be deposited at the blade's surface. For impulse blade, water droplets deposition is concentrated in the central region, whereas for reaction blades, it is highest at the leading edge and decreases towards the trailing edge. Water droplets deposited can cause corrosion of the blade surface over time, leading to blade damage and reduced lifespan. Moreover, the simulation reveals the erosion pattern on the blade and shows that the highest erosion rates concentrated in the central region of both types of blades.

4. CONCLUSION

The study shows that waspaloy has the best performance in terms of structural and thermal analysis which indicates its suitability to be used for steam turbine blade applications. Besides that, the simulation of low-quality steam reveals that there is formation of eddies at the trailing edge of the blade, the water deposition pattern and the erosion pattern on the blade. This study provides a framework for engineers to optimize blade design or explores coating technologies that can enhance the durability and efficiency of the blades.

REFERENCES

- [1] Durgesh E., Charan, B. D. B. S., Bharadwaj, Y. M. S. V., Suraj, S. S., Sai, K. D. S. N., & Pavan, P. E. (2023). Analysis of Steam Turbine Blade. *Journal of Emerging Technologies and Innovative Research*, 10(4).
- [2] Risko, J. R. (2020, May 1). *Steam Quality Considerations*. Chemical Engineering. <https://www.chemengonline.com/steam-quality-considerations/>.

Giving a Second Life to Campus Waste Paper

Amar Fikry Bin Mohd Aznan ^a and Muhammad Khairi Faiz bin Ahmad Hairuddin^{b*}

Department of Mechanical Engineering,
Faculty of Engineering, Universiti Malaya,
50603, Kuala Lumpur, Malaysia

Email: ^a amarfikry@gmail.com, ^b mkhairifaiz@um.edu.my

*Corresponding author

ABSTRACT

In a world facing mountains of waste and environmental degradation, sustainability of materials is crucial. This Final Year Project (FYP) tackles wastepaper disposal and sustainable toilet paper production on campus. Universities generate significant paper waste, second only to food waste, leading to environmental degradation and increased deforestation due to high demand for virgin wood pulp. This project aims to recycle campus wastepaper into eco-friendly toilet paper and enhance its properties for campus use. The methodology includes experimenting with production methods, adding additives to improve toilet paper properties, and testing these improvements. Results demonstrated the success of the production method and the enhanced properties of the toilet paper with the selected additives compared to campus toilet paper.

Keywords: Sustainability; Wastepaper recycling; Toilet paper production; Additives; Environmental impact

1. INTRODUCTION

Conventional Toilet Paper Production

Tissue paper is produced in factories with large machines operating at speeds of 100 to 120 km/h, producing 2 million rolls daily. This process consumes significant resources: 1 million liters of water, 300,000 kWh of electricity, and 200,000 kg of steam. Production begins with stock fibers, either virgin or recycled. Virgin fibers typically come from wood, but alternatives like straw or sugar cane are used. During pulping, lignin is removed to free fibers and eliminate impurities. The stock, mostly water with less than 1% fiber, is sprayed onto a paper machine where water is gradually removed. The felt carries the paper web to a suction press roll and a Yankee drying cylinder, which removes water and dries the paper.

Deinking Processes

Flotation deinking removes ink from waste paper pulp using surfactants and air, causing ink particles to float and mix with foam, which is then removed. This method is commonly used for graphic papers like newsprint. Bleaching removes colorants and brightens pulp using agents like hydrogen peroxide and sodium dithionite. Enzymatic deinking employs enzymes to help separate ink from fibers, reducing the need for alkali and detergent. Wash deinking involves washing waste paper pulp over a wire screen to remove ink and other elements, though it's less effective for heavily printed papers.

Properties of Toilet Paper

Toilet paper quality depends on strength, softness, absorbency, whiteness, and visual appeal. It should be strong yet comfortable, absorb moisture effectively, and appear clean. Dry strength measures tensile stress resistance in dry conditions, while wet strength assesses durability when wet.

Strengthening Toilet Paper

Through-air drying (TAD) is a major drying system for tissue paper that, although it increases energy costs, offers significant advantages such as increased bulk, softness, absorbency, and crossdirectional strength. The higher bulk is particularly beneficial as it leads to fiber savings, making the process cost-effective in the long run.

Creping, essential for the feel and softness of tissue paper, involves using a blade to direct the paper web away from the drying surface. In TAD drying, the Yankee cylinder is used for further drying and creping, though alternatives exist. The TAD dryer can achieve creping by running the dryer and former at different speeds, pushing the paper web to create the creped structure.

The chemical process for strengthening toilet paper involves enhancing both dry and wet strength. For improving dry strength, long fibers and additives like cationic starch, polyacrylamides (PAM), and carboxymethyl cellulose (CMC) are utilized. Long fibers enhance bonding, while cationic starch improves strength, water drainage, and paper quality. PAMs, available in various forms, efficiently enhance paper strength without significantly altering its properties. CMC boosts tensile strength, tear resistance, and internal bonding, also contributing to softness and absorbency.

Wet strength is enhanced using additives like melamine-formaldehyde, polyamideepichlorohydrin (PAE), and glyoxylated polyacrylamide (GPAM). These additives create cross-links with cellulose fibers, improving moisture resistance and ensuring the paper retains strength when wet. Melamine-formaldehyde and PAE resins are particularly effective, with PAE also offering innovations in resin dosage efficiency. GPAM enhances both dry and wet strength, optimizing manufacturing efficiency and paper quality.

To improve solubility and water absorption, quaternary ammonium compounds and reduced amounts of strength additives are used. Quaternary ammonium compounds, or debonders, enhance softness by obstructing fiber bonding, while strategic reduction of dry and wet strength additives increases paper solubility. Additionally, polyvinyl alcohol (PVA) is employed to enhance water absorption, increasing porosity and bulk without compromising strength. These approaches ensure a balance between strength, solubility, and absorbency in toilet paper production.

2. METHODOLOGY

Handsheets preparation

The first step in making toilet paper from recycled paper is to weigh the amount of recycled paper to ensure consistent thickness and reliable results for strength testing. The shredded paper is then blended with water to create a pulp, and during this pulping process, additives are introduced in varying concentrations (10%, 20%, 30%) to determine the optimal amount.

Next the solution is deinked. The pulp mixture is then poured into a large container for moulding, where it is evenly distributed using a mould and deckle before draining the water. The drying process follows, which can be done using the sun, a fan, or a hair dryer. Finally, the dried toilet paper is peeled off the mould and inspected for defects

Testing of Toilet Paper

The dry strength, water absorption, and solubility of toilet paper were tested using specific experiments. For dry strength, ISO 1265-4:2022 guidelines were followed, utilizing a Universal Tensile Test Machine to measure tensile strength, tear resistance, and internal bonding by pulling samples until breakage. Water absorption was tested by dropping water onto samples and measuring the absorbed droplet's diameter. Solubility was assessed by dissolving a toilet paper sample in water using a spinning machine, filtering the solution, drying the pulp, and weighing it to determine the extent of dissolution. Each test was repeated multiple times to obtain average values. The fibre composition is then observed using an optical microscope

3. RESULTS AND DISCUSSION

The results show that the sample with Guar Gum as the additive obtained the highest tensile index while Polyacrylamide obtained the best water absorption and finally Carboxymethyl Cellulose obtained the best solubility. Past studies show that the length of fibers in toilet paper significantly influences its strength due to increased interfiber bonds. Results from the tensile test indicate that Guar Gum at 20% concentration achieved the highest tensile index, attributed to its densely packed structure with extensive interfiber bonds. In contrast, Modified Starch, with fewer interfiber bonds, showed the lowest tensile index. For water absorption, Polyacrylamide exhibited the highest absorption due to its porous structure, while Guar Gum had the lowest due to its nonporous nature. The solubility of toilet paper largely depends on the type of bonding agent used. CMC, which dissolves well in water, proved to be the best additive overall, balancing strength, absorption, and solubility, making it the preferred choice for campus use.



Figure 1. Fibre Composition of Guar Gum at 20% wt%

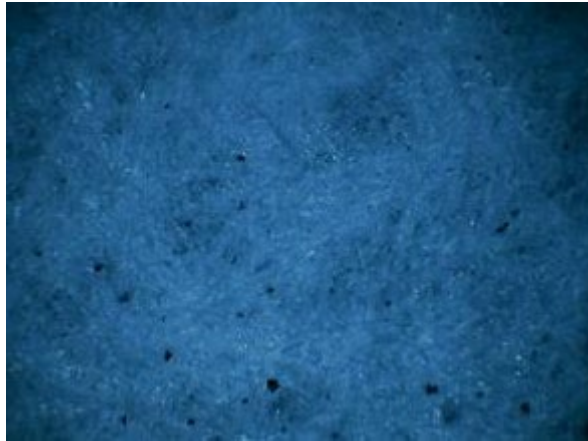


Figure 2. Fibre Composition of PAM at 10% wt%



Figure 3. Fibre Composition of CMC at 30% wt%

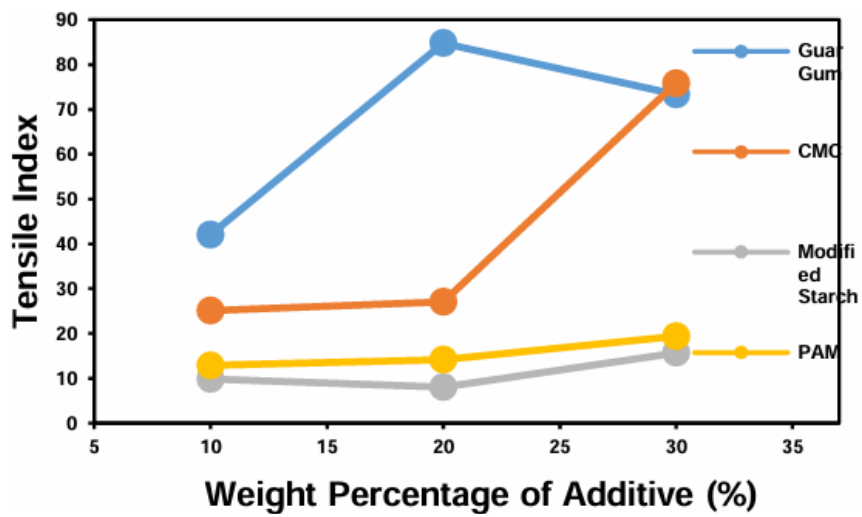


Figure 4. Graph of Tensile Index

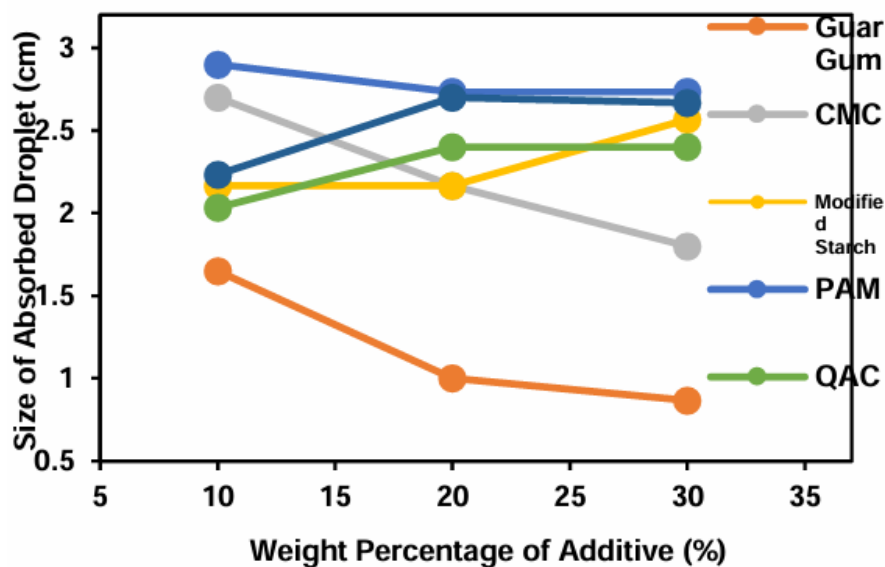


Figure 5. Graph of Water Absorbency

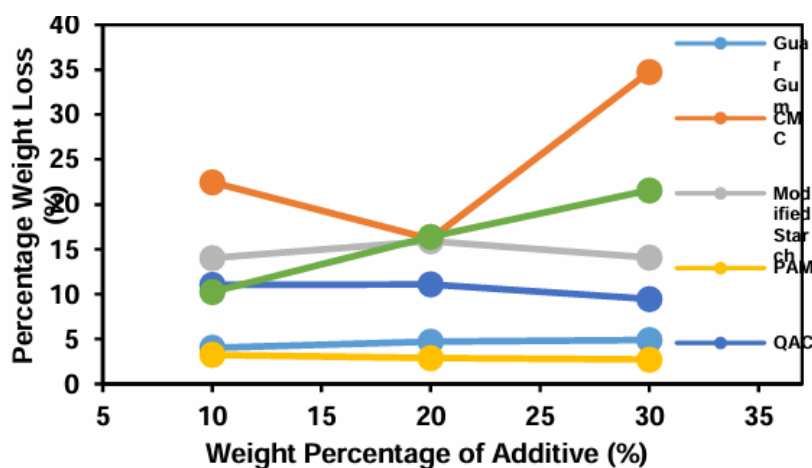


Figure 6. Graph of Solubility

4. CONCLUSION

The project aimed to convert campus waste paper into soluble toilet paper and improve its properties for campus use. The first objective was achieved by developing a simple, energy-efficient method using pulping, deinking, moulding, and drying, which any university can replicate to reduce paper waste. The second objective was met by testing various additives to enhance the toilet paper's properties. Guar gum improved tensile strength, PAM increased water absorption, and CMC enhanced solubility. CMC at 30% concentration was the best additive, making the toilet paper a suitable replacement for store-bought options.

REFERENCES

- [1] Elmas, G., & Bekiroglu, S. (2019). Effect of toilet tissue Paper on residential sewerage-line clogging. *BioResources*, 14, 7068-7079. <https://doi.org/10.15376/biores.14.3.7068-7079>
- [2] Ferreira, A. C. S., Aguado, R., Bértolo, R., Carta, A. M. M. S., Murinho, D., & Valente, A. J. M. (2022). Enhanced water absorption of tissue paper by cross-linking cellulose with poly(vinyl alcohol). *Chemical Papers*, 76(7), 4497-4507. <https://doi.org/10.1007/s11696-022-02188-y>

Characterising Shear State Mechanical Properties and Thermomechanical Finite Element Analysis of SAC305 Solder

Chan Wei Juan^a and Muhammad Khairi Faiz bin Ahmad Hairuddin^{b*}

Department of Mechanical Engineering,
Faculty of Engineering, Universiti Malaya,
50603, Kuala Lumpur, Malaysia

Email: ^a wjchan@live.com, ^b mkhairifaizum.edu.my

*Corresponding author

ABSTRACT

96.5Sn-3.0Ag-0.5Cu (SAC305) solder alloy is one of the most popular lead-free solders used in power electronic modules. Solder failure, usually via thermomechanical fatigue, is of serious concern. As solders experience predominantly shear stresses, the material model used in finite element modelling should accurately simulate the shear behaviour. In this research, a shear-based material constitutive model for SAC305 solder alloy was constructed using bilinear kinematic hardening and Norton's creep law. Finite element modelling was used to simulate a single lap shear using ANSYS to describe the temperature and strain rate dependent shear properties of SAC305. The model produced shear stress-strain curves in reasonable agreement with experimental data. The model is conservative as it overpredicted plastic strains under monotonic shear loading. Although simpler than the Anand model, the model produced comparable results under monotonic and cyclic shear loading. For thermal cycling, the accumulated plastic work/volume was overestimated and stress relaxation at low temperature dwell was ignored.

Keywords: SAC305 Solder Alloy; Thermomechanical Fatigue; Shear-Based Model; Finite Element Modelling; Creep Law

1. INTRODUCTION

SAC305 is the leading alternative of leadbased solder alloys used in power electronic modules. Solder failure, often by thermomechanical fatigue, is of major concern because the reliability of power electronic modules depends on the reliability of the solder joints. The reliability and thermomechanical behaviour of the solder joints depend on the inherent mechanical properties of the solder. Therefore, this calls for further research on the mechanical properties of SAC305 solder alloys to ensure their reliability. Many studies have focused on the tensile properties of solder alloys. However, solder alloys experience predominantly shear stresses when in operation. Limited studies have been conducted to characterise the shear properties of SAC305 solder alloys numerically.

2. METHODOLOGY

A shear-based material constitutive model for SAC305 alloy was constructed, initially using bilinear isotropic hardening [1] and Norton's creep law [2] based on literature. To characterise the shear state mechanical properties, finite element simulation of a single lap shear was performed in ANSYS at temperatures of 25 °C and 125 °C and strain rates of 0.01 s⁻¹ and 0.0001 s⁻¹ using displacement-controlled loading (Figure 1). Shear stress-strain curves were calculated for monotonic and cyclic shear loading. Based on cyclic loading results, the model was refined to use bilinear kinematic hardening. Finally, the thermomechanical behavior of SAC305 solder in power electronic modules under thermal cycling was evaluated. Thermal cycling from -40 °C to 125 °C was performed and the variation of plastic work/volume and von Mises stress in the solder was calculated.

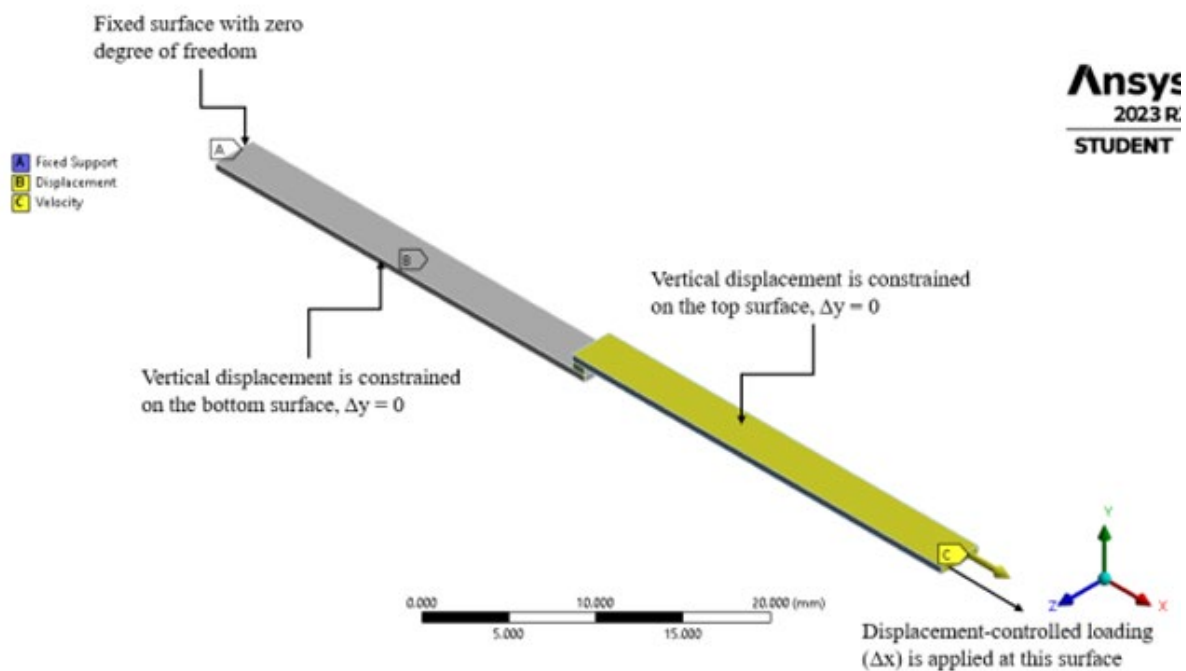


Figure 1. Finite element model of lap shear specimen with boundary conditions

3. RESULTS AND DISCUSSION

The proposed model predicted shear stress-strain curves with reasonable agreement ($\leq 11.61\%$ error within plastic region) compared to experiment under monotonic shear (Figure 2). It is conservative as it overestimated plastic strains. The model made excellent agreement with the Anand model in predicting plastic work/volume (Figure 3). The plastic work/volume is greater at 25 °C than at 125 °C. For cyclic shear, the model predicted similar maximum shear stress and strains with the Anand model (Figure 4). Larger shear stress range and smaller shear strain range were predicted at 25 °C than at 125 °C.

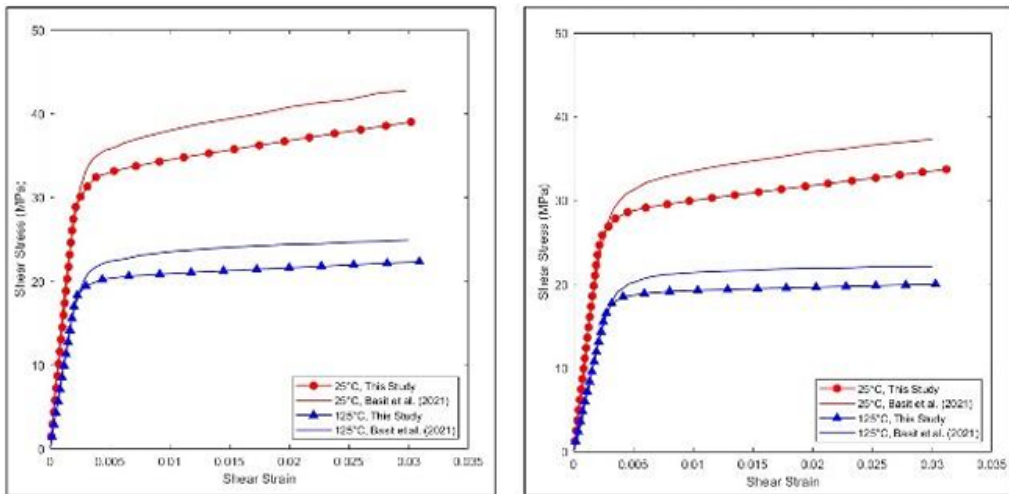


Figure 2. Shear-stress strain curves from experiment and finite element model under monotonic shear

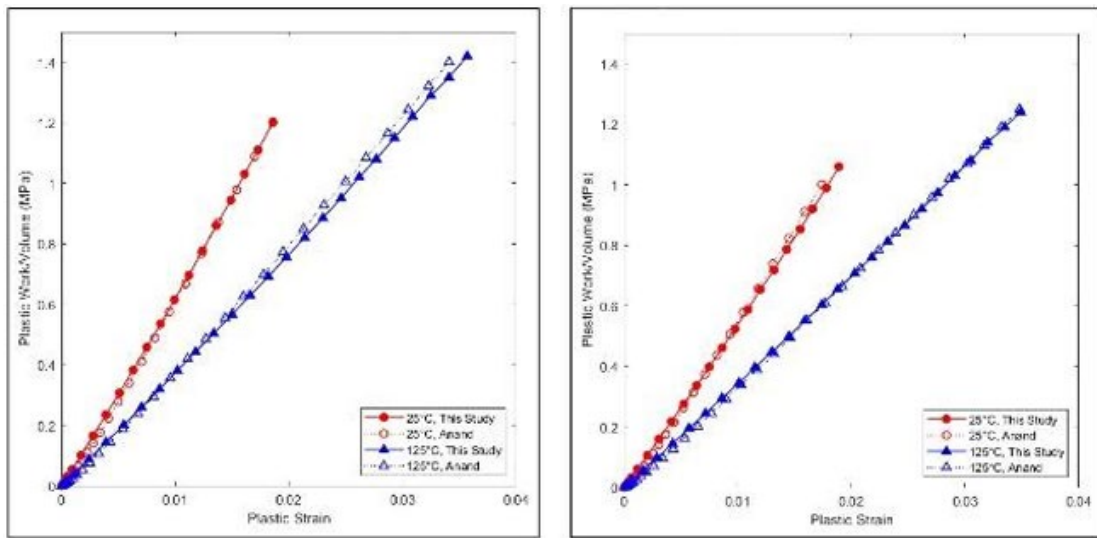


Figure 3. Plastic work/volume-plastic strain plots from Anand model and finite element model

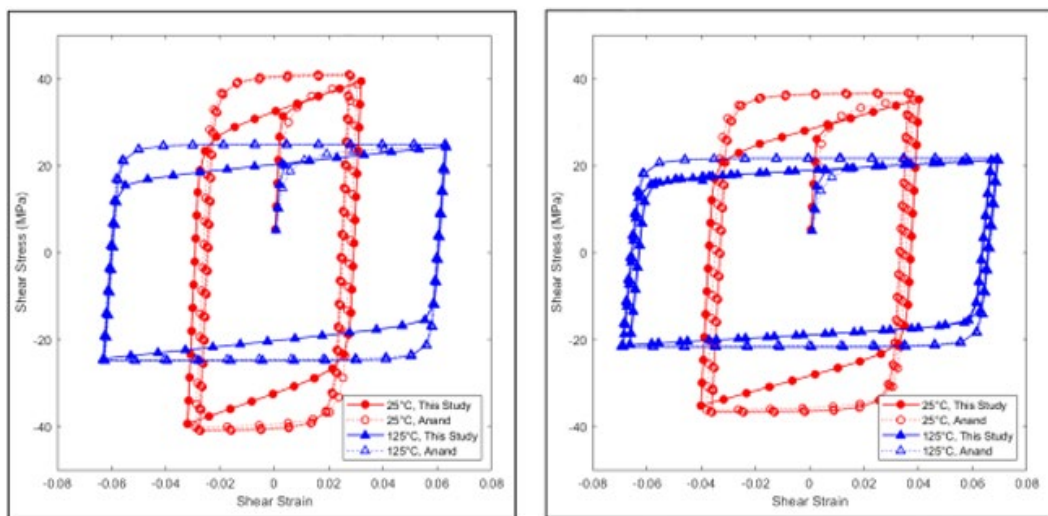


Figure 4. Shear stress-strain curves from Anand model and finite element model under cyclic shear

For thermal cycling, the model overestimated the accumulated plastic work/volume than the Anand model. It also underpredicted stress and ignored stress relaxation at low temperature dwell.

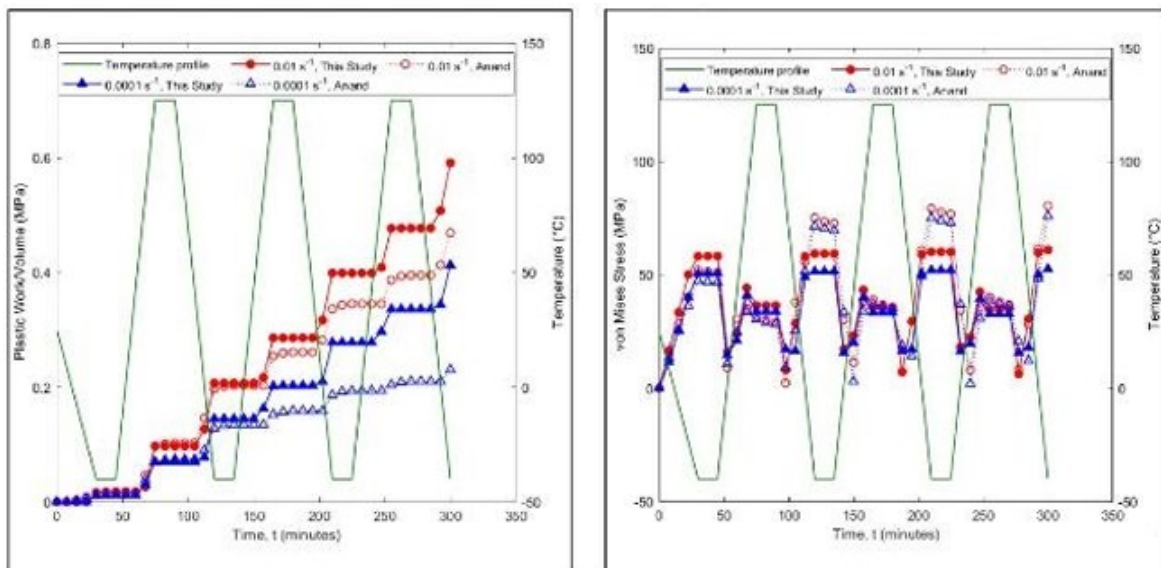


Figure 5. Plastic work/volume and von Mises stress at solder joint from Anand model and finite element model under thermal cycling

4. CONCLUSION

Solder joints in service mainly experience fatigue shear stresses. This study is significant as it investigated the temperature and strain rate dependent shear properties of SAC305 solder and provided a comprehensive insight of their actual response in the real world. In this study, a shear-based material constitutive model for SAC305 was constructed using bilinear kinematic hardening and Norton's creep law. From finite element simulation of a single lap shear, the proposed model is conservative as it overpredicted plastic strains during monotonic shear loading compared to experimental data. Although simpler than the Anand model, the model closely predicted the response of SAC305 solder under monotonic and cyclic shear loading. Thermal cycling simulation showed stress relaxation at high temperature dwell but ignored it at low temperature dwell.

REFERENCES

- [1] Basit, M. M., Burdick, D., & Aglan, H. (2021). Analysis of the viscoplastic behavior of Pb-free solder using lap shear joints. *Microelectronics Reliability*, 119, 114091. doi:<https://doi.org/10.1016/j.microrel.2021.114091>
- [2] Hsu, C.-M., Lin, A.-D., & Kuang, J.-H. (2013). The Creep Parameters of SAC305 Unleaded Solders. *Advances in Materials Science and Engineering*, 2013, 838075. doi:10.1155/2013/838075

Corrosion Inhibition for Carbon Steel in Alkaline Environment by Addition of *Andrographis Paniculata* Extract

Asrul Faiq bin Fazli ^a and Nazatul Liana binti Sukiman ^{b*}

Department of Mechanical Engineering,
Faculty of Engineering, Universiti Malaya,
50603, Kuala Lumpur, Malaysia

Email: ^a faiqfazli27@gmail.com, ^b nazatul@um.edu.my

*Corresponding author

ABSTRACT

In the oil and gas sector, corrosion is a serious problem that can have an impact on different stages of the production, refining, and transportation processes. Metal deterioration brought on by a chemical reaction with the environment is known as corrosion, and it can result in equipment failure, safety risks, and financial losses. Corrosion in the oil and gas industry requires a comprehensive approach that is proactive, like the use of corrosion inhibitors. The analysis of the behaviour of oil and gas structures, particularly carbon steel, in corrosive environments such as salinity and alkaline environments, is the main goal of this research. The study also looks at the various concentrations at which Kalmegh Leaves can function as a corrosion inhibitor. The metal sample of ASTM 516 Grade 70, carbon steel, will be immersed for fourteen days at neutral (pH 7), and alkaline (pH 10, pH 12) in 0 wt.%, 10 wt.%, 20 wt.% and 30 wt.% of Kalmegh solution. The outcome from the immersion test, the corrosion rate was also tested using the cyclic potentiodynamic polarisation method. Following the completion of the immersion test for each sample, the surface morphology of the corrosion product was captured and analysed using an optical microscope (OM) and scanning electron microscopy. The most caustic pH environment and the effectiveness of andrographolide in Kalmegh Leaves as a corrosion inhibitor are determined by comparing all the results.

Keywords: corrosion inhibition; oil and gas industry; carbon steel; Kalmegh leaves; alkaline environments

1. INTRODUCTION

Corrosion is a key difficulty in preserving material integrity and durability, especially in the oil and gas industry, where pipelines are subjected to a variety of corrosive conditions like alkaline. Carbon steel, like A516, is often used in pipelines due to its strength and longevity. However, it is prone to corrosion, which can result in operational problems, and safety risks. Traditional corrosion inhibitors frequently contain chemicals that are potentially hazardous to the environment, forcing the search for more sustainable alternatives.

Kalmegh Leaves (*Andrographis Paniculata*) have been identified as a potential organic corrosion inhibitor. These leaves are known for their therapeutic benefits, and they contain Andrographolide, a chemical that inhibits rusting. The usage of organic inhibitors is consistent with the growing need for ecologically friendly industrial solutions.

2. METHODOLOGY

The base material, A516 Carbon Steel cut into square pieces with dimensions of 12.7 mm X 12.7 mm. The samples were ground with 180#, 400#, 600#, 800# and 1200# sandpaper washed with acetone and ultrasonic cleaner. The corrosion samples were then exposed under alkaline condition with the addition of corrosion inhibitor, Kalmegh Leaves (*Andrographis Paniculata*) in various concentration.

2.1 pH solution preparation

Using the concept of molarity, concentration, and volume to obtain the pH solution like in Table 1:

Table 1: Parameter for pH solution

| pH | Volume (ml) | Mass of NaCl (g) | Mass of NaOH (g) |
|----|-------------|------------------|------------------|
| 7 | 1000 | 58.44 | - |
| 10 | 1000 | 58.44 | 0.004 |
| 12 | 1000 | 58.44 | 0.4 |

Check the pH value using pH meter and adjust it by adding weak acid or base.

2.2 Kalmegh Solution Preparation

Kalmegh Leaves powder was weighed and soaked with 80% of ethanol using ratio of 1:10. The mixture was shook using magnetic stirrer with 200 rpm speed for 24 hours. The mixture was then filtered using filter paper. After filtration, the stock solution was stored in the chiller for further used. Mix Kalmegh Leave Extract (KLE) based on the three different concentrations (10 wt.%, 20 wt.%, 30 wt.%) in the 100 ml pH solution to produce Kalmegh solution (KS). This solution will act as corrosion inhibitor for the experiment

2.3 Weight Loss Method (WL)

The tests were carried out for 14 days under room temperature and will be immersed in the different setting of pH and KS concentration. After 14 days, weight loss and the corrosion rate was calculated using this formula:

Corrosion Rate

$$\text{Corrosion Rate, } CR \left(\frac{mm}{y} \right) = \frac{87.6 w}{Atd} \quad (1)$$

where w is corrosion weight loss of mild steel (mg), A is the area of the coupon (cm²), t is the exposure time (h), and D is the density of mild steel (gcm⁻³).

2.4 Cyclic Polarisation Potentiodynamic Polarisation (CPP)

Three electrodes, Working Electrode, Reference Electrode and Counter Electrode were connected to metal sample, Saturated Calomel Electrode (SCE) and positive terminal of potentiationstat respectively. In EC Lab software, set the scan rate to 10-mV/s and 1 minute rest period.

Tafel was extrapolated to obtain the value of E_{corr} and I_{corr}. The corrosion rate was calculated using Faraday's Law:

$$\text{Corrosion Rate, } CR \left(\frac{mm}{y} \right) = \frac{0.00327 I_{corr} (EW)}{D} \quad (2)$$

where I_{corr} is corrosion current density ($\mu\text{A}/\text{cm}^2$), EW is the equivalent weight of the corroding metal (g/eq) and D is the density of the corroding metal (g/cm^3).

2.5 Surface Characterisation

The samples morphology was observed using Optical Microscope (OM) with magnification of 20x and Field Emission Scanning Electron Microscope (FESEM) with 500x and 1000x magnification and 15 kV of accelerated voltage. The elemental characterisation also conducted using Energy Dispersive X-Ray (EDX) that performed along with FESEM.

3. RESULTS AND DISCUSSION

3.1 Corrosion rate (WL and CPP)

Figure 1 shows the corrosion rate against concentration of KS for 3 samples in each pH using WL. Corrosion rate decreases with higher concentration of KS for all three pHs especially in alkaline (pH 10, pH 12). However, the effectiveness of KS is the lowest at pH 7 as the corrosion rate fluctuate at certain concentrations.

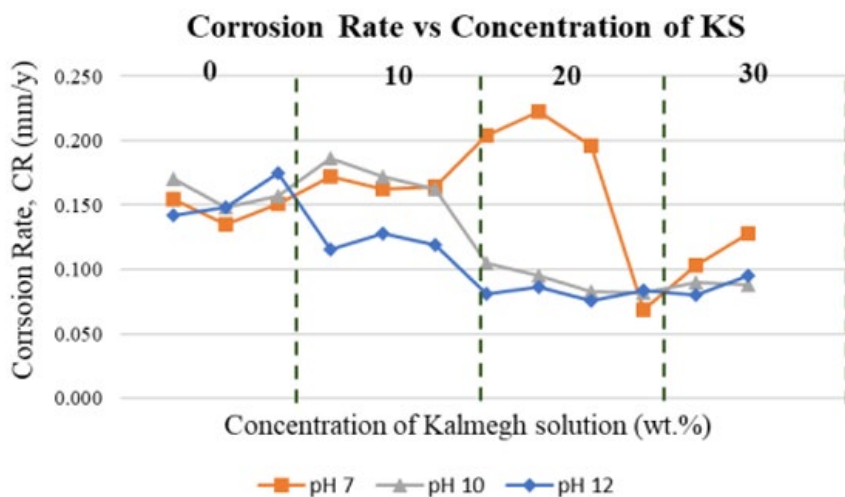


Figure 1. Weight Loss (WL)

Whereas Figure 2 exhibit corrosion rate from CPP with more significant decreasing trend especially between 0 wt.% and 10 wt.% KS for all 3 pHs.

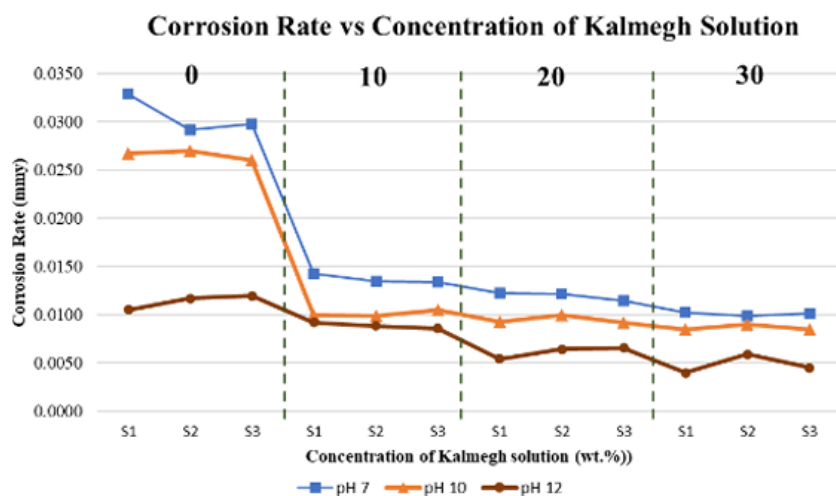


Figure 2. Cyclic Potentiodynamic Polarisation (CPP)

3.2 Tafel Extrapolation

Figure 3 shows as pH rises, E_{corr} become more electropositive in 0 wt.% KS.

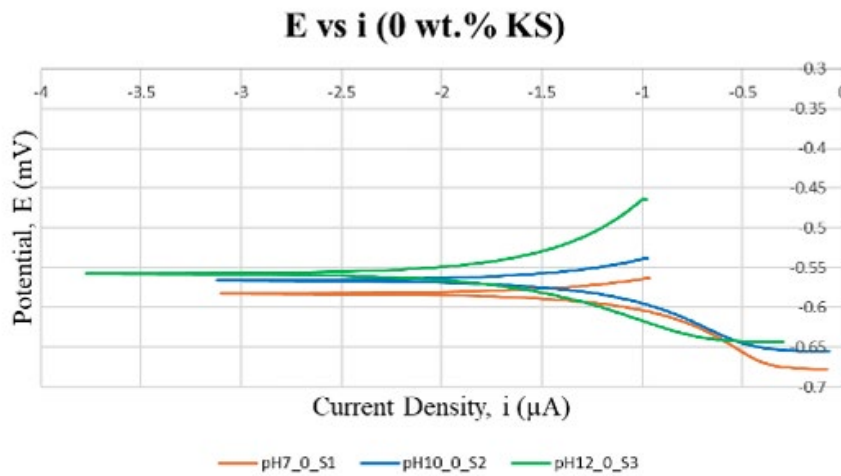


Figure 3. Polarisation curves for all pH without KS

Like Figure 4, with the addition of KS does not change the inversely proportional between pH and E_{corr} value.

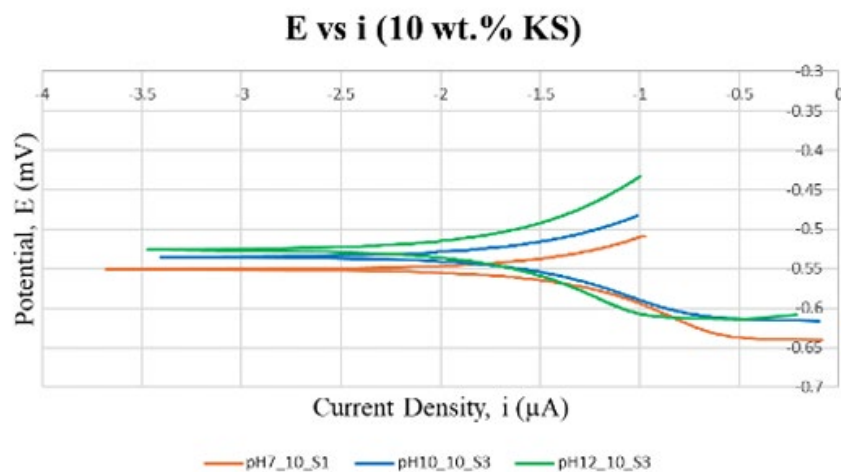


Figure 4. Polarisation curves for all pH with KS

Table 2 shows I_{corr} decreases with large value for each pH, indicates the effect of KS to slow down the corrosion rate even at 10 wt.% KS.

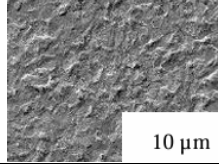
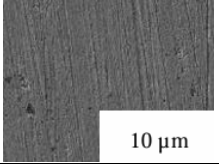
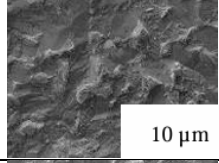
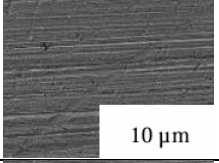
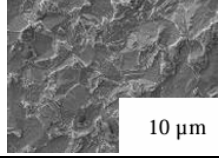
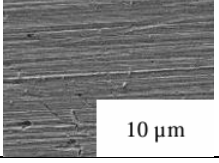
Table 2: Tafel Extrapolation with and w/o KS

| Concentration (wt.%) | pH | Average Corrosion Current Density, I _{corr} , avg | Average Corrosion Electrode Potential, E _{corr} , avg |
|----------------------|----|--|--|
| 0 | 7 | 10.122 | -568.068 |
| | 10 | 8.784 | -580.949 |
| | 12 | 3.772 | -569.627 |
| 10 | 7 | 4.536 | -550.257 |
| | 10 | 3.348 | -522.537 |
| | 12 | 2.937 | -523.335 |

3.3 Surface Morphology using FESEM/EDX

Table 3 shows that all images in all pH become smoother and even after the addition of KS at 10 wt.%. This is supported when Fe content at pH 10 and pH 12 are higher signs that oxidation of Fe is lower unlike in pH 7.

Table 3. Surface morphology and elemental analysis

| pH | 0 wt.% (Without KS) | | 10 wt.% (With KS) | |
|----|--|---------------------------------------|---|--------------------------------------|
| 7 |  | Wt.% Fe:91.20 C:4.64 O:2.78 |  | Wt.% Fe:87.73 C:6.63 O:4.39 |
| 10 |  | Wt.% Fe:91.76 C: 4.87 O:1.99 |  | Wt.% Fe:93.37 C:3.12 O:2.38 |
| 12 |  | Wt.% Fe:89.35 C:6.39 O:2.64 |  | Wt.% Fe:92.63 C:3.54 O:1.92 |

4. CONCLUSION

In conclusion, Kalmegh Leaves (*Andrographis Paniculata*) effectively inhibit corrosion in A516 Carbon Steel under alkaline conditions. Increasing concentrations of KS significantly reduced corrosion rates, especially at pH 10 and pH 12, as shown by WL and CPP method. Tafel extrapolation indicated lower I_{corr} and more E_{corr} with the presence of KS. Surface analysis via FESEM/EDX revealed smoother surfaces and reduced oxidation in KLE-treated samples. These findings highlight Kalmegh Leaves as a promising, environmentally friendly corrosion inhibitor for steel in alkaline environments.

REFERENCES

- [1] Li, W., & Li, D. Y. (2006). Influence of surface morphology on corrosion and electronic behavior. *Acta Materialia*, 54(2), 445–452. <https://doi.org/10.1016/J.ACTAMAT.2005.09.017>
- [2] Nwoye, C. I., & Nwigwe, U. S. (2025). Novel Green Corrosion Inhibitor for Mild Steel Protection in an Alkaline Environment. *Portugaliae Electrochimica Acta*, 43(1), 11–22. <https://doi.org/10.4152/pea.2025430102>
- [3] Perez, T. E. (2013). Corrosion in the oil and gas industry: An increasing challenge for materials. *JOM*, 65(8), 1033–1042. <https://doi.org/10.1007/S11837-013-0675-3/TABLES/2>
- [4] Tang, D. Z., Du, Y. X., Lu, M. X., Liang, Y., Jiang, Z. T., & Dong, L. (2015). Effect of pH value on corrosion of carbon steel under an applied alternating current. *Materials and Corrosion*, 66(12), 1467–1479. <https://doi.org/10.1002/MACO.201508365>
- [5] Tuttle, R. N. (1987). Corrosion in Oil and Gas Production. *Journal of Petroleum Technology*, 39(07), 756–762. <https://doi.org/10.2118/17004-PA>

Andrographis Paniculata Leaves Extract as a Sustainable Additive in Epoxy Coating for Anti-Corrosion Protection of Carbon Steel

Mohammad Iffat Zakwan bin Noorulkhairi^a and Nazatul Liana binti Sukiman^{b*}

Department of Mechanical Engineering,
Faculty of Engineering, Universiti Malaya,
50603, Kuala Lumpur, Malaysia

Email: ^a17203166@siswa.um.edu.my, ^b nazatul@um.edu.my

*Corresponding author

ABSTRACT

Corrosion poses a significant challenge in the oil and gas industry, leading to structural degradation and substantial economic losses. This Final Year Project investigates the potential of *Andrographis paniculata* (Kalmegh) leaves extract as a sustainable additive in epoxy coatings for the corrosion protection of A516 Grade 70 carbon steel. The project involves preparing Kalmegh leaves extract (KLE) using ethanol, confirmed via Fourier Transform Infrared (FTIR) Spectroscopy for the presence of andrographolide. KLE is incorporated into epoxy coatings at 10 wt.%, 20 wt.%, and 30 wt.% concentrations and applied to mild steel surfaces. Cyclic potentiodynamic polarization (CPP) testing evaluates the corrosion behavior of the coated samples. Tafel plot analysis shows that the 30 wt.% KLE/epoxy coating demonstrates the highest effectiveness in reducing corrosion. This study aims to develop eco-friendly and effective corrosion protection solutions for the oil and gas industry.

Keywords: corrosion inhibition; oil and gas industry; carbon steel; Kalmegh leaves; alkaline environments

1. INTRODUCTION

Carbon steel, particularly ASTM A516 Grade 70, is extensively used in the oil and gas industry for its excellent mechanical properties, weldability, and cost-effectiveness. This steel has the necessary properties for pressure vessels and boilers, including easy welding and resistance to cracking under stress [1]. Although carbon steels are easy to handle and have good mechanical properties, they tend to corrode easily [2], especially in harsh and corrosive environments, which can significantly reduce its lifespan and compromise structural integrity.

In recent years, there has been a growing interest in sustainable and eco-friendly corrosion inhibitors derived from natural sources. *Andrographis Paniculata* (Kalmegh) leaves extract (KLE) is a promising natural additive known for its medicinal properties, including anti-inflammatory and antibacterial effects, which may also offer corrosion inhibition capabilities. The active compound andrographolide, found in Kalmegh, exhibits strong anti-inflammatory, antibacterial, and antioxidant activities. These properties suggest that Kalmegh extract could serve as an effective, natural corrosion inhibitor when added to protective coatings, providing an environmentally friendly alternative to traditional chemical additives.

2. METHODOLOGY

Sample Preparation

The research involved the use of ASTM A516 Grade 70 carbon steel as the substrate material. The carbon steel samples were cut into 25mmx25mm dimensions suitable for coating and corrosion testing procedures.

Kalmegh Leaves Extract (KLE) Preparation

The Kalmegh leaves extract (KLE) was prepared by soaking Kalmegh powder in 80% ethanol with a ratio of 1:10. Then, it was stirred with magnetic stirrer at 200rpm for 24 hours. The mixture was filtered using filter paper. Once filtered, the mixture was evaporated using rotary evaporator in 40°C water bath at 5rpm.

Fourier Transform Infrared Spectroscopy (FTIR)

Fourier transform infrared spectroscopy (FTIR) was performed on the KLE to identify and confirm the presence of andrographolide, the bioactive compound responsible for potential corrosion inhibition.

KLE/Epoxy Coating Formulation and Fabrication

The KLE was incorporated into the epoxy resin to create the KLE/epoxy coatings. The formulation process involved mixing the epoxy resin with the KLE and a polyamine hardener in a ratio of 6.5:1 (epoxy:polyamine).

Corrosion Characterization

The corrosion resistance of the coated samples was evaluated using cyclic potentiodynamic polarization (CPP) testing. The electrolyte used was a 1M NaCl solution.

Surface Characterization

Surface characterization was performed using an optical microscope (OM) to examine the surface morphology of the coated samples after immersion for 35 days in 1M NaCl solution.

3. RESULTS AND DISCUSSION

Fourier Transform Infrared Spectroscopy (FTIR)

The FTIR spectra of the KLE showed characteristic absorption bands corresponding to the functional groups present in andrographolide. Key peaks were observed at specific wavenumbers, indicating the presence of hydroxyl, carbonyl, and aromatic groups, which are consistent with the molecular structure of andrographolide.

KLE/Epoxy Fabrication

Dry film thickness (DFT) of each sample were measured by using DFT gauge after the second layer was cured. All samples satisfied the recommended DFT based on the manufacturer's datasheet.

Tafel Polarization

The results from the cyclic potentiodynamic polarization tests clearly indicate that the incorporation of Kalmegh leaves extract (KLE) into epoxy coatings significantly improves the corrosion resistance of A516 carbon steel. Among the tested concentrations, the 30% KLE/epoxy coating provided the most effective corrosion protection, as evidenced by the lowest icorr values, which correspond to the slowest corrosion rates. Despite the negative Ecorr values across all samples, the critical factor is the icorr value, which shows that the 30% KLE/epoxy coating is the most suitable for mitigating corrosion in harsh

environments, such as those found in the oil and gas industry. The increase in the concentration of andrographolide in KLE increases the protection of carbon steel from corrosion. This highlights the potential of Kalmegh leaves extract (KLE) as a sustainable and highly effective additive for corrosion inhibition.

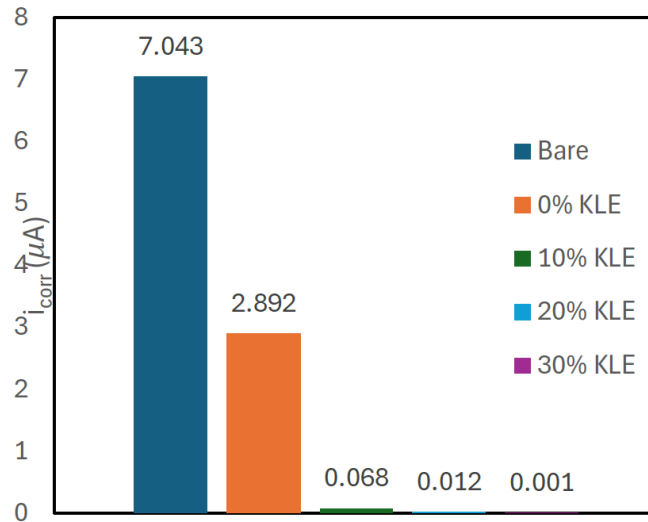


Figure 1. Influence of KLE towards corrosion current density, i_{corr} .

Surface Morphology

The high concentration of KLE in the epoxy matrix significantly enhanced the coating's corrosion inhibition properties, providing the most effective protection against the corrosive environment. The 30% KLE/epoxy coating maintained its integrity throughout the immersion period, resulting in minimal material loss and an almost pristine surface. This superior performance highlights the 30% KLE/epoxy coating as the most effective formulation for corrosion protection.

4. CONCLUSION

In conclusion, this research has demonstrated that incorporating *Andrographis paniculata* (Kalmegh) leaves extract (KLE) into epoxy coatings significantly enhances the corrosion resistance of A516 Grade 70 carbon steel, particularly in marine environments. The plant extract has shown promise as a sustainable and eco-friendly additive, offering a viable alternative to traditional, more harmful corrosion inhibitors. Specifically, the 30% KLE/epoxy coating exhibited the best performance, with the lowest corrosion current density and a significant shift in corrosion potential towards the positive region, indicating improved corrosion resistance. This study fills a critical research gap by exploring the application of plant extracts in corrosion prevention, thus paving the way for further investigations into natural, sustainable solutions in the oil and gas industry. The success of KLE as a corrosion inhibitor highlights the potential for broader application of bio-based additives in various industrial coatings.

REFERENCES

- 1] Peasura, P. (2015). Application of response surface Methodology for modeling of postweld heat treatment process in a pressure vessel Steel ASTM A516 Grade 70. *The Scientific World Journal*, 2015, 1–8. <https://doi.org/10.1155/2015/318475>
- 2] Haghshenas, N., Nejat, A., & Chini, S. F. (2022). A superhydrophobic anticorrosion silicone coating for covering cell body, joints and seawater storage in hydrogen production plants. *International Journal of Hydrogen Energy*, 47(62), 26589–26599. <https://doi.org/10.1016/j.ijhydene.2022.01.009>

Polymer added with MgO for Remineralize and Removal of Heavy Metals in Contaminated Water

Dhaneish Kumar ^a and Nor Ishida binti Zainal Abidin ^{b*}

Department of Mechanical Engineering,
Faculty of Engineering, Universiti Malaya,
50603, Kuala Lumpur, Malaysia

Email: ^a dhaneish25@gmail.com, ^b ishida@um.edu.my

*Corresponding author

ABSTRACT

The study aimed to address the global issue of water contamination by developing and evaluating PVDF enhanced MgO membranes for the removal of heavy metals Cu and Pb and the remineralization of Mg ions. The study developed PVDF enhanced MgO membranes to address water contamination by removing heavy metals (Cu and Pb) and remineralizing Mg ions. Using phase inversion casting, membranes with varying MgO ratios (0%, 10%, 20%, 30%) were fabricated. FESEM analysis showed that the membranes' porous structure became more compact after filtration, indicating successful heavy metal adsorption. FTIR results revealed changes in chemical composition, suggesting functional group transformations. XRD confirmed the presence of PVDF and MgO crystalline phases, with MgO enhancing structural properties. ICP-OES demonstrated increased removal and remineralization efficiencies with higher MgO content, with the 30% PVDF-MgO membrane achieving the highest removal efficiencies for Cu (45.96%) and Pb (35.08%) and remineralizing Mg ions up to 5.521 mg/L. Reusability tests showed that the 30% PVDF-MgO membrane maintained high performance over multiple cycles, indicating its potential for sustainable water treatment.

Keywords: Water Contamination; PVDF-MgO Membranes; Heavy Metal Removal; Membrane Reusability; Sustainable Water Treatment

1. INTRODUCTION

The global demand for freshwater is rapidly increasing, projected to outstrip supply by 40% by 2030, exacerbated by water pollution and climate change. Contaminated water, laden with heavy metals like lead (Pb) and copper (Cu), poses severe health risks, including kidney damage, cancer, and various acute illnesses, contributing to millions of deaths annually. Current water treatment methods, while effective, have limitations, necessitating innovative solutions. This research focuses on developing a novel filtration membrane using polymer-enhanced magnesium oxide (MgO) blended with polyvinylidene fluoride (PVDF) to address dual challenges: removing heavy metals and remineralizing water with magnesium (Mg). Advanced analytical techniques such as FESEM, FTIR, XRD, and ICP-OES will be employed to evaluate the membrane's effectiveness. This study aims to provide sustainable water treatment solutions, addressing both global heavy metal pollution and the need for remineralized water, thereby contributing to public health and environmental sustainability.

2. METHODOLOGY

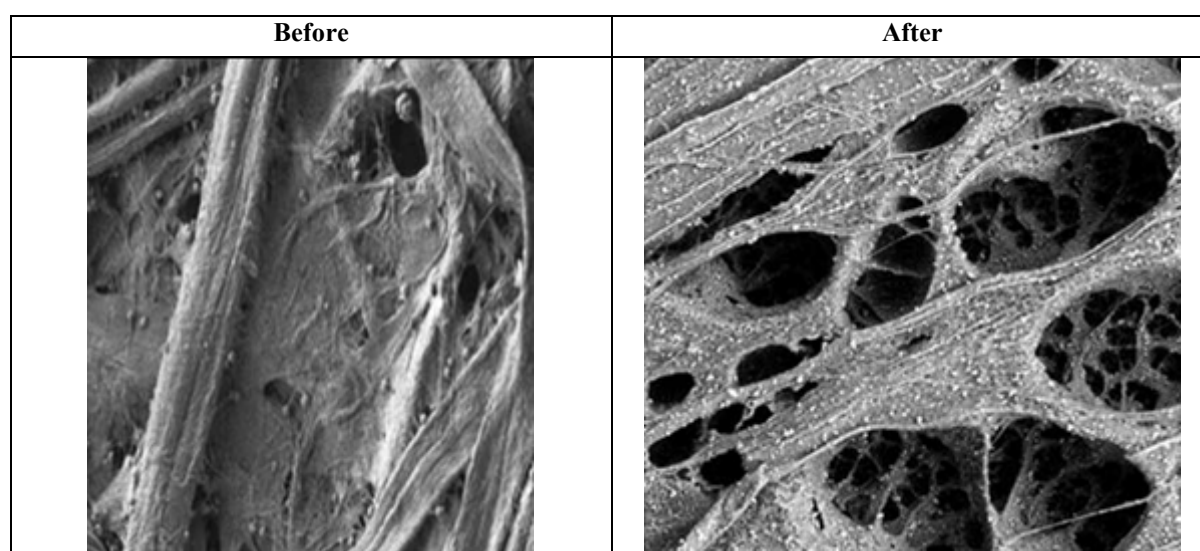
The methodology for this research involved a comprehensive review and analysis of existing water filtration methods to address the problem of heavy metals and mineral deficiencies in consumable water. Materials used included PVDF powder, MgO powder, and DMF solvent, sourced from reputable suppliers. The PVDF and MgO were blended in varying ratios (0%, 10%, 20%, 30%) and dissolved in DMF, followed by stirring, degassing, and casting to form membranes. These membranes were tested for heavy metal removal using a stock solution of copper and lead ions. The filtration performance was evaluated over 20 cycles, and the most efficient membrane was further tested for reusability using 40 and 60 cycles. Characterization techniques such as FESEM, FTIR, XRD, and ICP-OES were employed to assess the structural, chemical, and morphological properties of the membranes before and after filtration. This methodology ensured a thorough evaluation of the PVDF-MgO membranes' effectiveness in water purification applications

3. RESULTS AND DISCUSSION

3.1 FESEM Results

The FESEM analysis of PVDF-MgO membranes with varying MgO ratios (0%, 10%, 20%, and 30%) reveals significant morphological changes pre- and post-filtration. Initially, all membranes exhibit a highly porous structure, ideal for heavy metal adsorption. Post-filtration, the membranes become more compact and uniform, indicating successful Cu and Pb ion adsorption. The 0% MgO membrane shows a marked reduction in pores, while the 10% and 20% membranes display better MgO particle distribution, enhancing mechanical stability. The 30% MgO membrane maintains a well-blended structure with minimal agglomeration and significant pore reduction. These findings highlight the membranes' effectiveness in heavy metal removal and the importance of MgO content in optimizing performance, though regeneration is needed to restore filtration capacity.

Table 1. FESEM Images of PVDF-MgO Membrane (30%) ratio Before and After Filtration

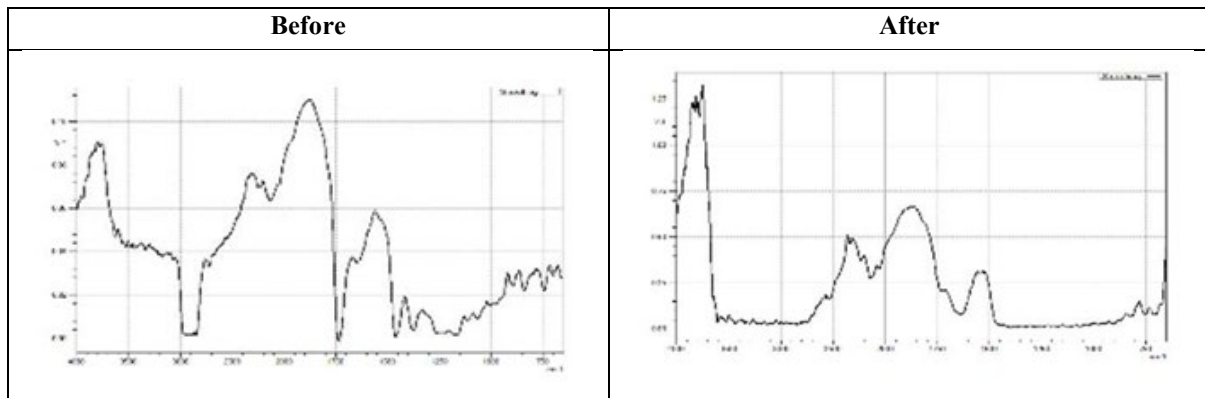


3.2 FTIR results

The FTIR analysis of PVDF-MgO membranes before and after filtration reveals significant changes in their chemical composition and structure. Before filtration, the PVDF-MgO (0%) membrane shows prominent peaks around 3400 cm^{-1} (O-H stretching) and 2900 cm^{-1} (C-H stretching), indicating a

complex chemical structure. Post-filtration, these peaks are less pronounced, suggesting a more homogeneous material due to the removal or transformation of certain components. For the PVDF-MgO (30%) membrane, the pre-filtration spectrum shows characteristic peaks of PVDF and MgO interactions. After filtration, increased intensity of the O-H peak and changes in C-H, C=C, and CF vibrations indicate altered chemical interactions and potential changes in the membrane's surface properties and hydrophilicity.

Table 2. FTIR Spectrum of PVDF-MgO (0%) Ratio Membrane Before and After Filtration



3.3 XRD Results

The XRD analysis of the PVDF-MgO (30%) ratio membrane before and after filtration reveals the presence of both α and β phases of PVDF, with a prominent β -phase peak at $2\theta = 20^\circ$, indicating enhanced piezoelectric properties. The presence of MgO is confirmed by peaks at higher angles (e.g., $2\theta = 38^\circ, 45^\circ, 65^\circ$). Post-filtration, the XRD pattern shows that the crystalline structure of PVDF and MgO remains intact, suggesting structural stability and integrity of the membrane even after exposure to heavy metal ions Cu and Pb during filtration.

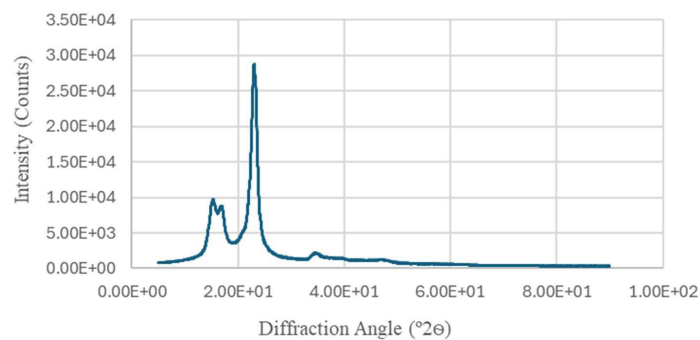


Figure 1. X-ray Diffraction (XRD) Pattern of PVDF-MgO (30%) Ratio Membrane After Filtration

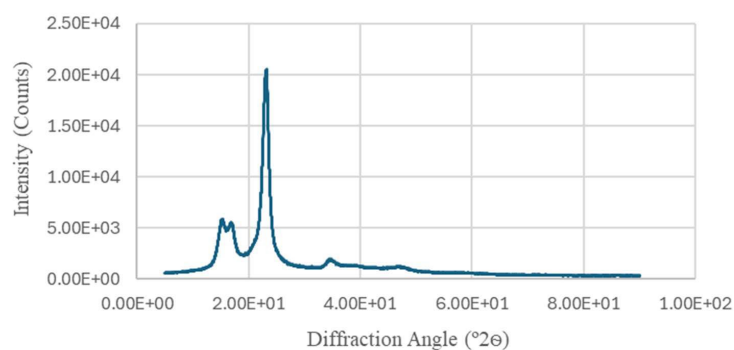


Figure 2. X-ray Diffraction (XRD) Pattern of PVDF-MgO (30%) Ratio Membrane After Filtration

3.4 ICP-OES Results

The ICP-OES analysis reveals that the 30% PVDF-MgO membrane is the most efficient in removing heavy metal ions, achieving removal efficiencies of 45.96% for Cu and 35.08% for Pb, significantly higher than membranes with lower MgO content. This enhanced performance is attributed to the increased adsorption sites provided by MgO particles. Additionally, the 30% PVDF-MgO membrane demonstrates effective remineralization, with Mg ion concentrations reaching 5.521 mg/L after filtration. Reusability testing over 20, 40, and 60 cycles shows sustained high removal efficiencies, with Cu removal efficiency increasing from 45.96% to 53.83% and Pb from 35.08% to 49.87%. The membrane also consistently releases Mg ions, with concentrations rising from 5.521 mg/L to 6.247 mg/L, indicating its durability and effectiveness in both heavy metal removal and remineralization over extended use. These results underscore the potential of the 30% PVDF-MgO membrane for industrial wastewater treatment applications.

Table 3. Concentration of Mg, Cu and Pb ions (mg/L) before and after filtration using different ratios of PVDF-MgO membrane

| PVDF – MgO Ratio (%) | Concentration of Mg (mg/L) | | Concentration of Cu (mg/L) | | Concentration of Pb (mg/L) | |
|----------------------|----------------------------|------------------|----------------------------|------------------|----------------------------|------------------|
| | Before Filtration | After Filtration | Before Filtration | After Filtration | Before Filtration | After Filtration |
| 0 | 0 | 0 | 1000.0 | 942.5 | 1000.0 | 952.4 |
| 10 | 0 | 2.438 | 1000.0 | 821.3 | 1000.0 | 852.3 |
| 20 | 0 | 4.456 | 1000.0 | 683.6 | 1000.0 | 744.6 |
| 30 | 0 | 5.521 | 1000.0 | 540.4 | 1000.0 | 649.2 |

4. CONCLUSION

The study successfully fabricated and characterized PVDF-MgO membranes with varying MgO ratios (0%, 10%, 20%, and 30%) using the phase inversion casting technique. The incorporation of MgO significantly enhanced the membranes' performance in removing heavy metals Cu and Pb and in remineralizing Mg ions into the water. FESEM analysis showed a transition from a highly porous to a more compact structure post-filtration, indicating effective heavy metal adsorption. FTIR and XRD analyses confirmed chemical and structural changes, respectively, with the 30% PVDF-MgO membrane achieving the highest removal efficiencies for Cu (45.96%) and Pb (35.08%), and effective Mg remineralization (5.521 mg/L). Reusability tests demonstrated the membrane's stability and efficiency, highlighting its potential for sustainable water treatment.

REFERENCES

- [1] Agasti, N. (2021). Decontamination of heavy metal ions from water by composites prepared from waste. *Current Research in Green and Sustainable Chemistry*, 4, 100088. <https://doi.org/10.1016/j.crgsc.2021.100088>
- [2] Chan, K., Li, C., Wang, D., & Lai, J. (2023). Formation of Porous Structures and Crystalline Phases in Poly(vinylidene fluoride) Membranes Prepared with Nonsolvent-Induced Phase Separation—Roles of Solvent Polarity. *Polymers*, 15(5), 1314. <https://doi.org/10.3390/polym15051314>
- [3] Saxena, P., & Shukla, P. (2021). A comprehensive review on fundamental properties and applications of poly(vinylidene fluoride) (PVDF). *Advanced Composites and Hybrid Materials*, 4(1), 8–26. <https://doi.org/10.1007/s42114-021-00217-0>

UV-Curable Urethane Acrylate from Palm Oil for Waterproof Coating

Shaatish Rao A/L Jeeva^a and Nor Ishida binti Zainal Abidin^{b*}

Department of Mechanical Engineering,
Faculty of Engineering, Universiti Malaya,
50603, Kuala Lumpur, Malaysia

Email: ^a shaatishraojeeva@gmail.com, ^b ishida@um.edu.my

*Corresponding author

ABSTRACT

This study explores the development of a UV-curable urethane acrylate coating derived from palm oil, aimed at providing a sustainable alternative for waterproof coatings. The primary objectives were to synthesize the coating, optimize its formulation, and evaluate its mechanical performance compared to petroleum-based alternatives. The methodology involved the preparation of epoxidized palm oil, its conversion to epoxidized palm oil liquid acrylate (EPOLA), and subsequent synthesis of palm oil-based urethane acrylate (POBUA). Various concentrations of photoinitiator were tested to determine the optimal formulation. Results indicated that a 5% photoinitiator concentration provided the best balance of curing efficiency, hardness, and adhesion. The coating demonstrated excellent adhesion and moderate hydrophilicity, with a contact angle of 52 degrees. The study concludes that UV-curable POBUA coatings offer a viable, eco-friendly alternative to traditional coatings, with potential applications in various industries.

Keywords: Epoxidized Palm Oil; Hydrophilicity; Photoinitiator; UV-Curable Coating; Waterproofing

1. INTRODUCTION

This research aims to develop UV-curable urethane acrylate (PUA) from palm oil for waterproof coatings, focusing on the role of photoinitiator concentration. Initially, the study will analyze the chemical and physical properties of PUA, including molecular structure, viscosity, and UV-curing behavior. Waterproofing capabilities will be tested via water contact angle measurements and hardness.[3] The research will then optimize the PUA formulation by varying photoinitiator concentrations to enhance waterproofing and evaluate environmental impacts.[1]

Mechanical performance, including hardness and hydrophobicity, will be compared to petroleum-based alternatives. Durability tests under various conditions will ensure long-term effectiveness.[2] Characterization techniques like FTIR spectroscopy and rheological analysis will be employed. This project aims to create an efficient, eco-friendly, UV-curable urethane acrylate coating from palm oil.

2. METHODOLOGY

2.1 Synthesis of Epoxidized Palm Oil

A 250 mL three-neck round-bottom flask with a reflux condenser, thermometer, and mechanical stirrer is used to heat and stir a mixture of formic acid and palm oil at 900 rpm. Hydrogen peroxide is gradually added. After completion, the mixture is neutralized with distilled water, sodium chloride, and sodium hydrogen carbonate solution. Anhydrous sodium sulphate is added overnight to remove water, and the product is filtered.

2.2 Synthesis of Epoxidized Palm Oil Acrylate (EPOLA)

Epoxidized palm oil (EPOP), triethylamine, and 4-methoxyphenol are stirred at 40°C for one hour. Acrylic acid is added in a 1:1 mole ratio with EPOP, and the mixture is heated to 110°C until the acid value drops below 15 mg KOH/g. The EPOLA is purified by washing with distilled water.

2.3 Synthesis of Palm Oil Based Urethane Acrylate

EPOLA, TDI, and HEA react in a 1:1:1 ratio in a 2L flask with a condenser, mechanical stirrer, and thermometer. EPOLA and 4-mp are stirred at 50°C, TDI is added at 70°C, and HEA is added after three hours at 80°C. The PUA polymer is monitored using FTIR and stored in a temperature-controlled cabinet.

2.4 Preparation of UV-Curable POBUA Coating

A POBUA formulation with 5%, 10%, and 15% Irgacure 184 photoinitiator is developed. The resins are applied to 4 cm x 4 cm ceiling boards. Tests for gel content, pencil hardness, surface roughness, cross hatch adhesion, contact angle measurement, and SEM analysis are conducted on the coated samples.

3. RESULTS AND DISCUSSION

3.1 FTIR Analysis

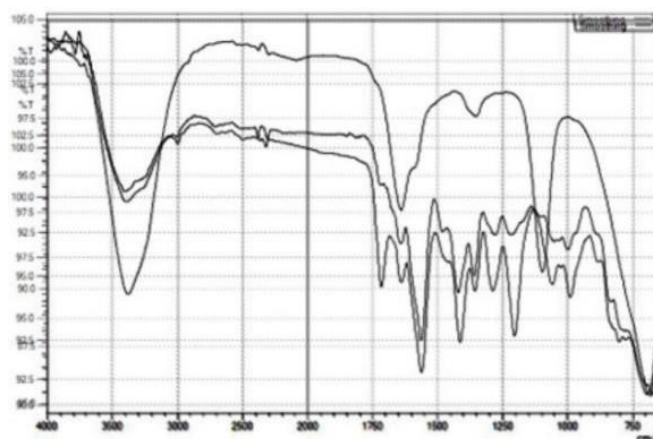


Figure 1. FTIR Spectrum for EPOP, EPOLA and POBUA

EPOP shows epoxy group introduction (1250 cm^{-1} , 1160 cm^{-1}), retention of ester carbonyl (1740 cm^{-1}), and aliphatic C-H (2920 cm^{-1} , 2850 cm^{-1}). EPOLA shows hydroxyl groups (3400 cm^{-1}), carbonyl (1730 cm^{-1}), aromatic rings ($1500\text{-}1000\text{ cm}^{-1}$), and complex structures (below 1000 cm^{-1}). POBUA shows

hydroxyl groups (3400 cm^{-1}), carbonyl (1700 cm^{-1}), C=C stretching (1600 cm^{-1}), aromatic rings ($1500\text{--}1000\text{ cm}^{-1}$), and complex structures (below 1000 cm^{-1}).

3.2 Surface Roughness Measurement

Table 1. Surface Hardness Measurement

| Sample | Hardness Value ($\mu\text{ in}$) | | |
|----------------|------------------------------------|-------|-------|
| | Ra | Rq | Rz |
| 5% | 12.81 | 15.87 | 45.20 |
| 10% | 12.81 | 15.87 | 45.20 |
| 15% | 12.81 | 15.87 | 45.20 |
| Average | 12.81 | 15.87 | 45.20 |

The average Ra ($12.81\mu\text{ in}$), Rq ($15.87\mu\text{ in}$), and Rz ($45.20\mu\text{ in}$) values indicate a moderately rough surface with significant peak-to-valley variations, which may hinder waterproof coating performance. Smoother surfaces with lower roughness values are preferred for better adhesion and sealing.

3.3 Gel Content

The gel content of palm oil-based urethane acrylate (POBUA) increases with higher photo-initiator concentrations, peaking at 98.637% for 10% concentration, indicating enhanced UV curing and polymerization. Consistent results across samples suggest a reproducible curing process.

Table 2. Gel Content of Sample with Different Photoinitiator Concentration

| Sample | Mass before Curing | Mass after Curing | Mass Difference | Percentage of Gel Content |
|--------|--------------------|-------------------|-----------------|---------------------------|
| 5% | 30.3 | 28.3 | 2.0 | 93.399 |
| 10% | 39.6 | 36.2 | 3.4 | 91.414 |
| 15% | 35.2 | 32.6 | 2.6 | 92.614 |

3.4 Crosshatch Adhesion Test

The Cross Hatch Adhesion Test shows that palm oil-based urethane acrylate coatings exhibit excellent adhesion with 0.00% coating removal across 5%, 10%, and 15% photo-initiator concentrations. However, the 10% and 15% samples were tacky and not fully cured, indicating the need for improved curing to ensure optimal performance.

Table 3. Crosshatch Adhesion Test of Sample with Different Photoinitiator Concentration

| Sample | Total number of coating grid | Number of coating grid removed | Percentage of coating removed (%) |
|--------|------------------------------|--------------------------------|-----------------------------------|
| 5% | 9 | 0 | 0.00 |
| 10% | 9 | 0 | 0.00 |
| 15% | 9 | 0 | 0.00 |

3.5 Contact Angle Measurement

The contact angle measurements show increasing hydrophilicity with higher photo-initiator concentrations: 52° (5%), 46° (10%), and 38° (15%). This suggests that the palm oil-based urethane acrylate contains polar functional groups, enhancing surface wettability due to hydrogen bonding and surface energy changes from the curing process.

Table 4. Contact Angle of Sample with Different Photoinitiator Concentration

| Specimen/Sample | Contact Angle |
|-----------------|---------------|
| 5% | 52° |
| 10% | 46° |
| 15% | 38° |

3.6 Pencil Hardness Test

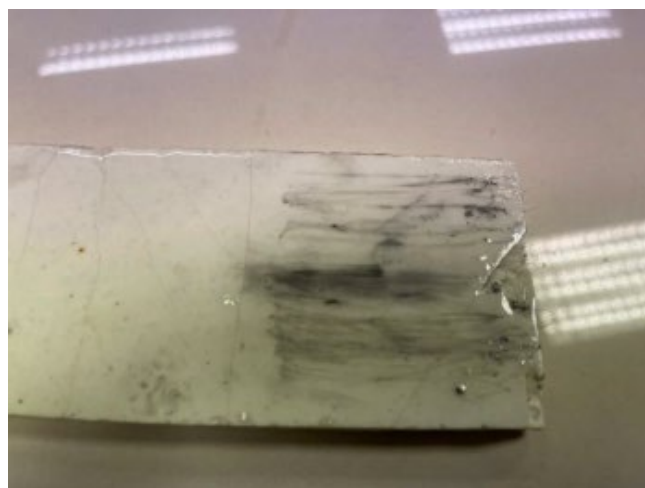


Figure 2. Pencil hardness test sample of 5% photoinitiator

The scratch resistance of UV-curable palm oil-based urethane acrylate coatings was evaluated using varying photoinitiator concentrations. The 5% photoinitiator sample showed the best scratch resistance up to 6H hardness, while higher concentrations (10% and 15%) diminished scratch resistance at lower hardness levels. Excessive photoinitiator (15%) likely led to over-curing and a brittle structure prone to scratches, highlighting the importance of optimizing photoinitiator concentration and curing parameters.

3.7 Scanning Electron Microscope

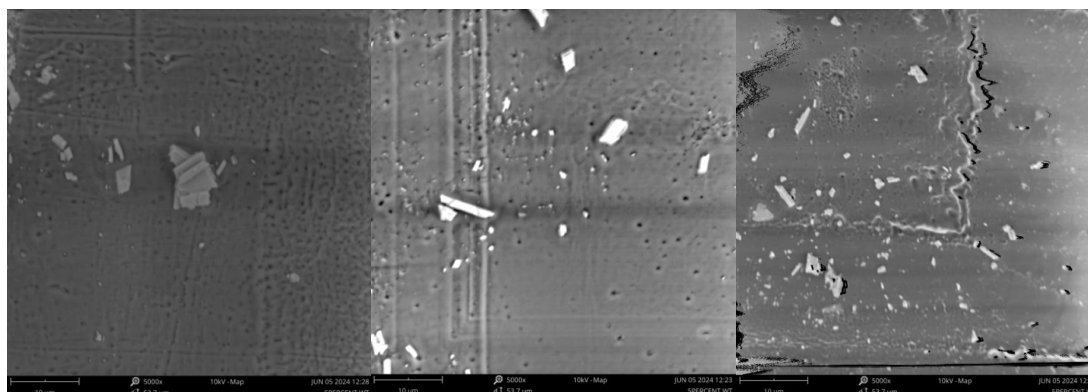


Figure 3. SEM Imaging of Sample with Different Photoinitiator Concentration

SEM images show that increasing photoinitiator concentrations in UV- curable palm oil-based urethane acrylate led to more heterogeneous surfaces with larger and more numerous particles. Higher concentrations result in faster curing times but may cause uneven curing, affecting mechanical properties, adhesion, and waterproof effectiveness.

4. CONCLUSION

This research successfully developed UV- curable palm oil-based urethane acrylate coatings, confirmed by FTIR analysis. The synthesis of EPOP, EPOLA, and POBUA was achieved. Mechanical tests, surface analysis, and SEM imaging evaluated the coatings' performance, wettability, and microstructure. These coatings exhibit promising waterproof properties and eco- friendly potential as a sustainable alternative to traditional coatings.

REFERENCES

- Karabulut, N. (2019). UV-curable urethane acrylate resin from palm fatty acid distillate. *Journal of Radiation Research and Applied Sciences*, 12(1), 1-10. <https://doi.org/10.1016/j.jrras.2018.12.001>
- Ismail, N. B., Jamaluddin, A. N., Norizham, N. A., Nor, N. H. M., Othman, N., Alias, M. S., Abdul Halim, K. A., Mohamed, M., & Harun, M. H. (2021). Characterization of hydrophobic UV-curable acrylated coating from palm oil-based urethane acrylate (POBUA) for wood coating application. *Journal of Radiation Research and Applied Sciences*, 14(2), 1-15.
- Salleh, M. Z., Badri, K. H., Mahmood, M. H., & Ahmad, S. H. (2021). Synthesis of UV-curable hyperbranched urethane acrylate from palm oil oleic acid. *Journal of Radiation Research and Applied Sciences*, 14(3), 1-12.

Development of Bioplastic from Food Waste

Jeslin Yew Wei Chen ^a and Suriani Binti Ibrahim ^{b*}

Department of Mechanical Engineering,
Faculty of Engineering, Universiti Malaya,
50603, Kuala Lumpur, Malaysia

Email: ^a u2003998@siswa.um.edu.my, ^b sue_83@um.edu.my

*Corresponding author

ABSTRACT

This research focuses on utilizing prawn shells to extract chitosan and produce bioplastic films. Methodologically, prawn shells undergo pre-treatment, demineralization, deproteination, and deacetylation processes, followed by material identification using FTIR to calculate the degree of deacetylation. Chitosan-starch composite films are fabricated and characterized using FTIR, DSC, FESEM, and EDX techniques. Soil biodegradation is assessed using ASTM D5988 standards. Results show successful fabrication of chitosan-starch composite film from the extracted chitosan with a 76.16% deacetylation rate. The films exhibit varying thermal properties influenced by glycerol content, with higher glycerol levels accelerating soil biodegradation. This study highlights the potential of utilizing prawn shell waste for sustainable bioplastic production, contributing to waste reduction and environmental sustainability initiatives.

Keywords: Chitosan Extraction; Prawn Shell Waste; Bioplastic Film; Soil Biodegradation; Environmental Sustainability

1. INTRODUCTION

Plastic pollution is a critical global issue, prompting the search for sustainable alternatives to petroleum-based plastics. Bioplastics, made from renewable sources like plant starches and animal proteins, offer a promising solution. Chitosan-based materials, derived from crustacean exoskeletons such as prawns, stand out due to their biodegradability, biocompatibility, and versatility. Adding glycerol to chitosan-starch bioplastic films has been found to enhance biodegradation rates, emphasizing the importance of glycerol in developing sustainable materials to combat plastic pollution.

2. METHODOLOGY

Prawn shells were pre-treated by washing, drying at 160°C, and grinding. The shells were then demineralized with 1M HCl at room temperature for 1 hour, washed until neutral, and dried at 60°C for 18 hours. Deproteination was done using 10% NaOH at 80°C for 2 hours, followed by neutralization and drying overnight at 80°C. Deacetylation involved treating with 50% NaOH at 100°C for 2.5 hours, washing thoroughly, and drying overnight at 80°C. For the chitosan-starch composite films, chitosan was dissolved in acetic acid, mixed with starch, water, and glycerol at ratios of 2:1, 1:1, and 0.5:1 (glycerol to chitosan), and stirred at 600rpm, 75°C for 1 hour. The mixture was then cast and dried at 70°C for 48 hours to form the composite film.

3. RESULTS AND DISCUSSION

3.1 FTIR Spectroscopy

The interactions between chitosan, starch and glycerol were investigated. The spectrum of the chitosan-starch composite film is illustrated in Fig. 1.

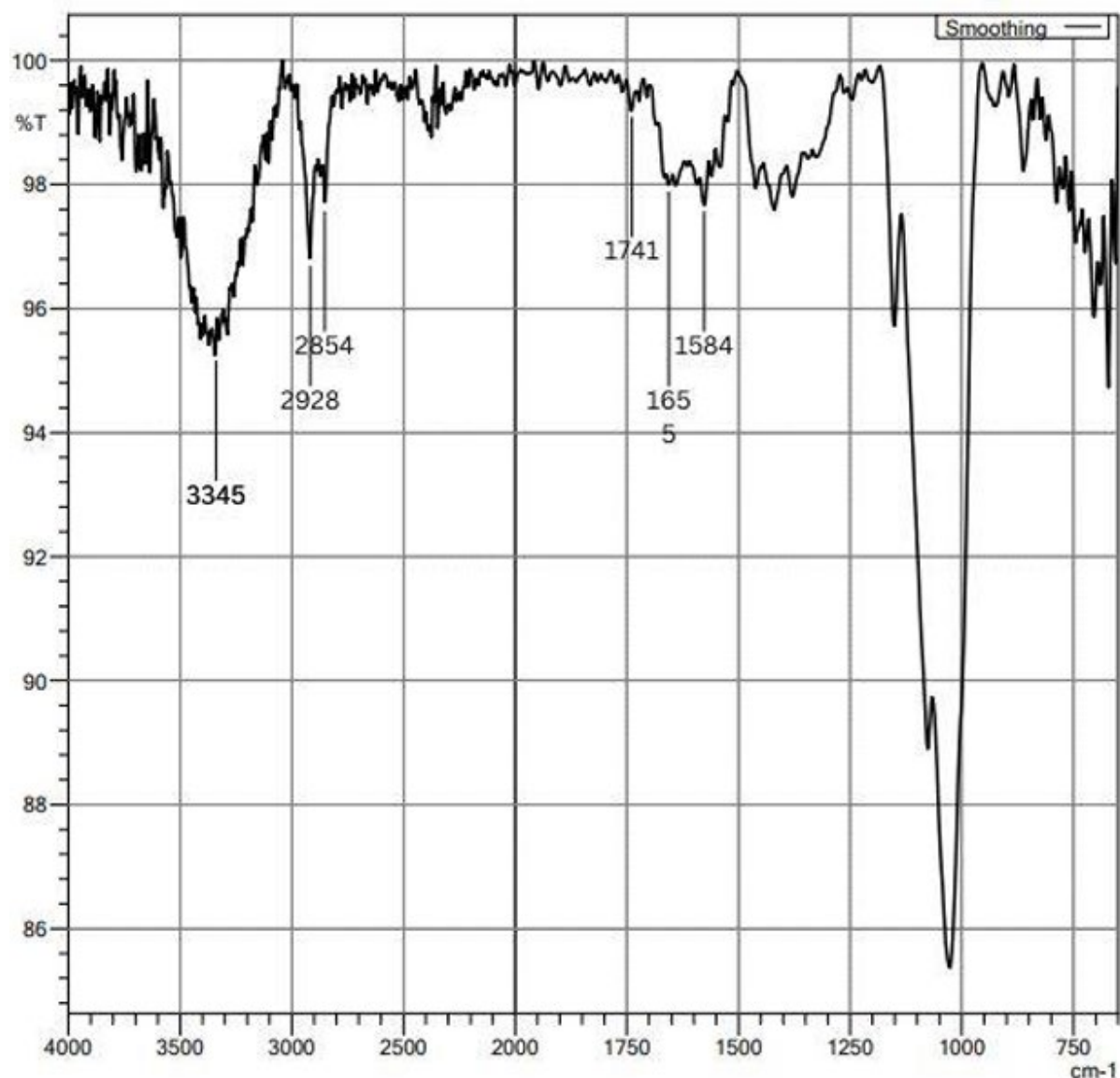


Figure 1. FTIR graph for 2:1 glycerol to chitosan, chitosan-starch composite film

A broad band at 3345 cm^{-1} indicated the presence of O-H stretching vibrations from chitosan, starch and glycerol. Peaks at 2928 cm^{-1} and 1655 cm^{-1} suggested C-H stretching vibrations and the presence of a carbonyl group, respectively. A shift in the amino peak at 1584 cm^{-1} suggested interactions between chitosan and starch [1]. Additionally, new peaks at 2854 cm^{-1} and 2872 cm^{-1} indicated the incorporation of glycerol. These findings offer valuable insights into the composition and interactions within the composite film.

3.2 DSC Studies

showed that increased glass transition temperature (T_g) reduces the biodegradability of the material due to reduced water diffusion [2]. Table 3.2.1 shows the T_g for all three samples.

Table 1: Tg of respective samples

| Sample | Glass transition temperature (°C) |
|----------------------------------|-----------------------------------|
| 2:1 glycerol to chitosan ratio | 70 |
| 1:1 glycerol to chitosan ratio | 75 |
| 0.5:1 glycerol to chitosan ratio | 105 |

As the glycerol content increases, the glass transition temperature (Tg) decreases. This is because glycerol's hydrophilic groups enhance water interaction with the polymer through hydrogen bonds, leading to higher moisture absorption and increased water content in the film [3].

3.3 FESEM and EDX

The morphology of the films generally has smooth texture. Fig. 2 has the smoothest surface, while Fig. 3 and Fig. 4 have rougher textures with some visible cracks, indicating possible voids. The EDX spectra in Fig. 3.3.4 revealed that carbon and oxygen are the core elements, with an additional gold peak from the coating used for testing.

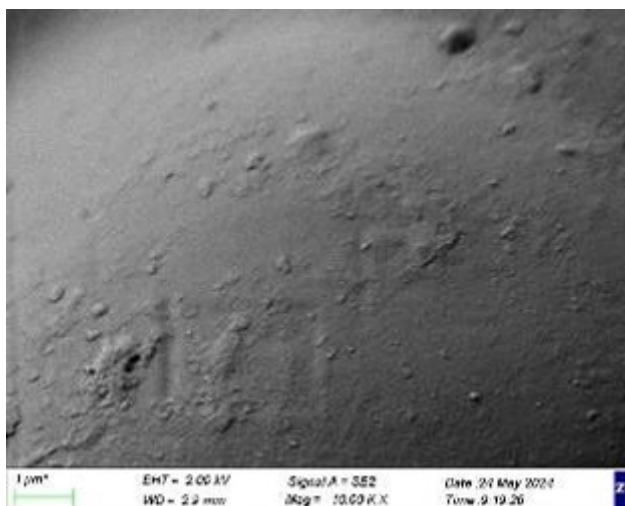


Figure 2. FESEM of 2:1 glycerol to chitosan, chitosan-starch composite film

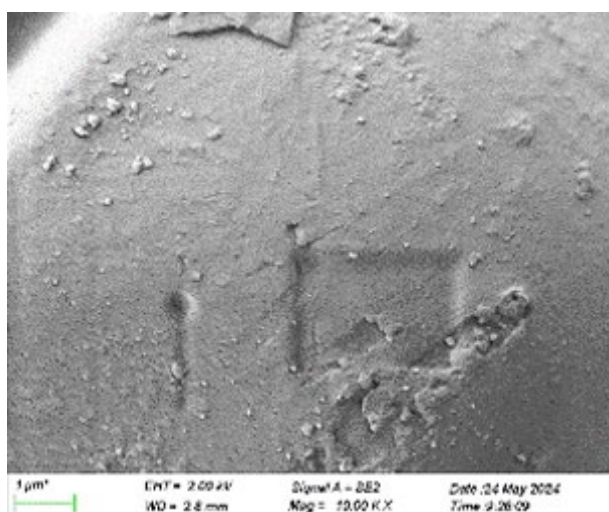


Figure 3. FESEM of 1:1 glycerol to chitosan, chitosan-starch composite film

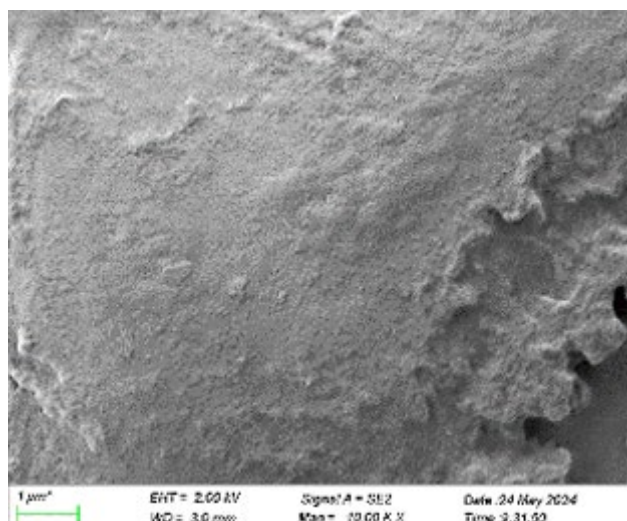


Figure 4. FESEM of 0.5:1 glycerol to chitosan, chitosan-starch composite film

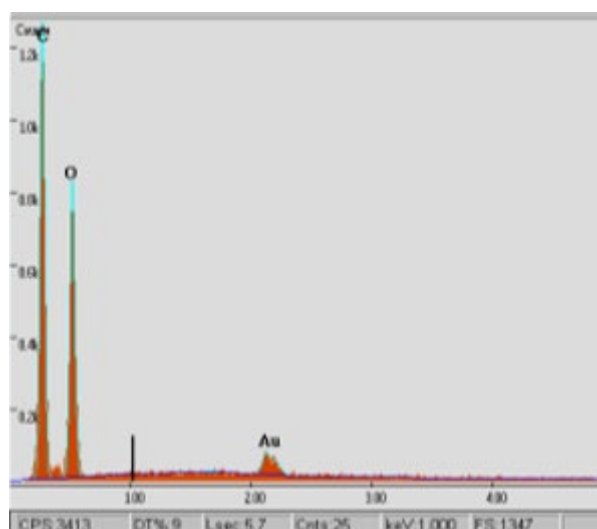


Figure 5. EDX spectra of 2:1 glycerol to chitosan, chitosan-starch composite film with gold coating

3.4 Soil biodegradation

The soil biodegradation was done according to ASTM D 5988 standards [4]. The weight loss percentage of each sample is presented in Fig. 6. Bioplastic samples with a higher glycerol to chitosan ratio degraded faster. The 2:1 ratio degraded completely by week 4, the 1:1 ratio had over 92% weight loss and the 0.5:1 had about 74% weight loss. This indicates that glycerol enhances the biodegradation efficiency of chitosan starch bioplastics by increasing the water content, which promotes microbial growth.

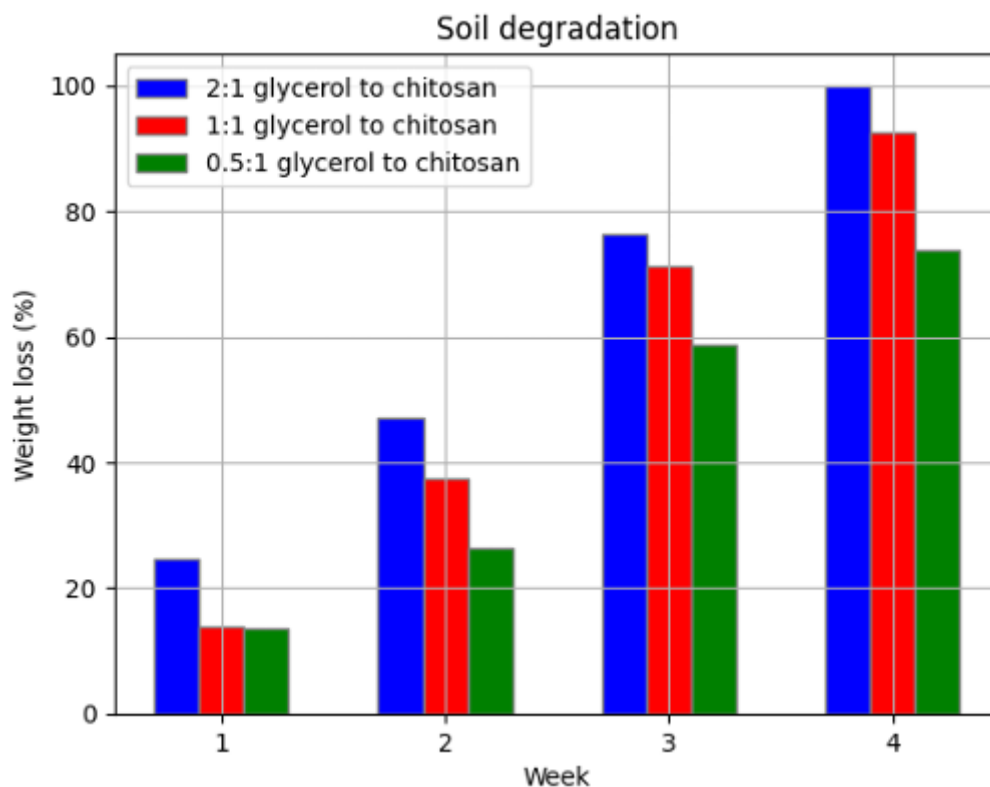


Figure 6. Weight loss percentage of bioplastics

4. CONCLUSION

In conclusion, bioplastic films made from chitosan, starch, and glycerol were fabricated using solution casting. These films exhibited properties, with favorable glass thermal transition temperatures affected by glycerol levels, indicating its role as a plasticizer. FESEM and EDX analyses showed a smooth, homogeneous surface, indicating effective integration of the components. The soil biodegradation test revealed that films with a 2:1 glycerol to chitosan ratio degraded fastest, completely breaking down by week 4, suggesting that higher glycerol content enhances microbial activity and accelerates biodegradation.

REFERENCES

- [1] Meenakshi, P., Noorjahan, S. E., Rajini, R., Venkateswarlu, U., Rose, C., & Sastry, T. P. (2002). Mechanical and microstructure studies on the modification of CA film by blending with PS. *Bulletin of Materials Science*, 25(1), 25-29. <https://doi.org/10.1007/BF02704590>
- [2] Chandra, D. K., Kumar, A., & Mahapatra, C. (2024). Fabricating Chitosan Reinforced Biodegradable Bioplastics from Plant Extract with Nature Inspired Topology. *Waste and Biomass Valorization*, 15(4), 2499-2512. <https://doi.org/10.1007/s12649-023-02293-3> Follow the APA referencing style (same style as your full report).
- [3] Rivero, S., Damonte, L., García, M. A., & Pinotti, A. (2016). An Insight into the Role of Glycerol in Chitosan Films. *Food Biophysics*, 11(2), 117-127. <https://doi.org/10.1007/s11483-015-9421-4>
- [4] Chan, M. Y., & Koay, S. C. (2019). Biodegradation and thermal properties of crosslinked chitosan/corn cob biocomposite films by electron beam irradiation. *Polymer Engineering & Science*, 59(S1), E59-E68. <https://doi.org/https://doi.org/10.1002/pen.24854>

Development of Poly (Ethylene Oxide) Based Solid Polymer Electrolytes Thin Films for Sodium Battery

Nur Farzana binti Jaafar^a and Suriani binti Ibrahim^{b*}

Department of Mechanical Engineering,
Faculty of Engineering, Universiti Malaya,
50603, Kuala Lumpur, Malaysia

Email: ^a farzanajaafar12@gmail.com, ^b sue_83@um.edu.my

*Corresponding author

ABSTRACT

Four solid polymer electrolyte (SPE) thin films with varying NaNO₃ and K₂SO₄ concentrations (100 PEO: x NaNO₃: y K₂SO₄, where x = 0, 20 wt% and y = 0, 10, 20 wt%) were prepared via solution casting. FTIR analysis investigated the chemical composition changes upon salt addition. Electrochemical impedance spectroscopy (EIS) evaluated ionic conductivity, with the highest conductivity observed at 2.9810×10^{-9} S/cm for the 100PEO:20Na:10K wt% system and the lowest at 1.7901×10^{-9} S/cm for pure PEO at room temperature. The sample with the highest and lowest conductivity underwent morphology and thermal property analysis via FESEM-EDX and DSC, respectively, to understand the relationship between NaNO₃ – K₂SO₄ addition and SPE conductivity.

Keywords: Electrochemical impedance; Ionic conductivity; Polyethylene oxide; Solid polymer electrolyte; Sodium-ion battery

1. INTRODUCTION

Solid polymer electrolytes (SPEs) are essential for advancing sodium-ion batteries (SIBs), which are a cost-effective and abundant alternative to lithium-ion batteries. SPEs enhance safety and flexibility compared to liquid electrolytes. This study focuses on synthesizing and characterizing poly(ethylene oxide) (PEO) based SPEs with sodium nitrate (NaNO₃) and potassium sulfate (K₂SO₄). The objective is to examine how these salts affect the structural, thermal, and ionic conductivity properties of PEO to improve SPE performance for SIBs.

2. METHODOLOGY

2.1. Preparation of PEO – NaNO₃ – K₂SO₄ SPEs thin film.

PEO with a molecular weight of 600,000 is dissolved in acetonitrile, stirred, and heated at 40°C until homogeneous. The solution is cast into a petri dish, dried in an oven, then set in a drying cabinet to form a thin film. This process is repeated with varying NaNO₃ – K₂SO₄ concentrations added to the PEO system.

2.2 Characterization method of PEO – NaNO₃ – K₂SO₄ SPEs thin film

The films underwent Fourier-transform infrared spectroscopy (FTIR) for chemical composition analysis and electrochemical impedance spectroscopy (EIS) using the LCR meter GW INSTEK LCR-8101G model across a frequency range of 20 Hz to 5 MHz at 20 mV amplitude and room temperature. Ionic conductivity (σ) was calculated using the formula:

$$\sigma = \frac{1}{R_b} \times \frac{t}{A} \quad (1)$$

Where σ is ionic conductivity, t is thickness of SPE sample, R_b is bulk resistance and A is sample area. Field emission scanning electron microscopy with energy dispersive X-ray (FESEM-EDX) for morphology and elemental analysis and differential scanning calorimetry (DSC) enables to study thermal properties of the SPEs.

3. RESULTS AND DISCUSSION

3.1 Electrochemical Impedance Spectroscopy (EIS) – Ionic Conductivity

After EIS testing with the GW INSTEK LCR-8101G model, Nyquist plots were obtained for each sample to measure bulk resistance (R_b) of the SPEs. The x- intercept of these plots in Fig. 1 provides the bulk resistance values, which will be used to calculate the ionic conductivity of the synthesized SPEs using Equation (1).

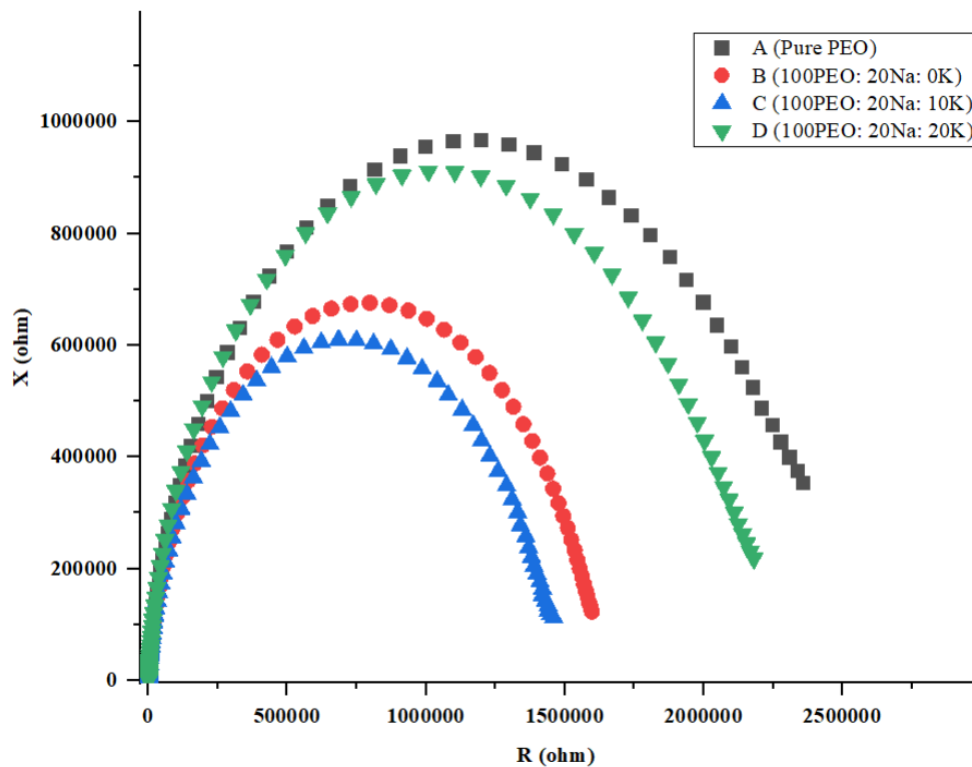


Figure 1. Nyquist fitting plot for all SPEs samples

Table 1 reveals that sample A (pure PEO SPE) has the lowest conductivity (1.7901×10^{-9} S/cm), while sample C (100PEO: 20Na: 10K wt%) exhibits the highest. Conductivity initially increases with salt concentration up to 20 wt% Na: 10 wt% K, then decreases. Amorphous regions introduced by salt enhance ion mobility and chain flexibility [2], while 20 wt% Na: 20 wt% K reduces conductivity due to increased ion interactions hindering Li^+ mobility [1][4]. Sample A and C undergo DSC and FESEM analysis to examine thermal behavior and morphology.

Table 1. Conductivity of SPEs thin film

| Sample | A | B | C | D |
|--|-------|--------|--------|--------|
| Ionic Conductivity, σ (S/cm) ($\times 10^{-9}$) | 1.790 | 2.8912 | 2.9810 | 2.5541 |

3.2 FTIR spectrum analysis

In Fig. 2, the FTIR spectrum of pure PEO (Sample A) displays characteristic peaks: 2870-2960 cm^{-1} for methylene (-CH₂-) group stretching, 1465 cm^{-1} for C-H bending, 1100-1140 cm^{-1} for C-O-C stretching of ether linkages, and 840-960 cm^{-1} for C-H rocking. These peaks denote PEO's crystalline structure, indicating no significant interactions. Introducing Na⁺ ions (Sample B) shifts the C-O-C peak and introduces new peaks in the 600-800 cm^{-1} region, suggesting complexation with ether oxygens. Samples C and D, with additional K⁺ ions, exhibit an extra peak at 620 cm^{-1} and broader peaks in the C-H and C-O-C stretching regions, indicating increased ionic interactions and coordination with PEO, altering its structure and properties.

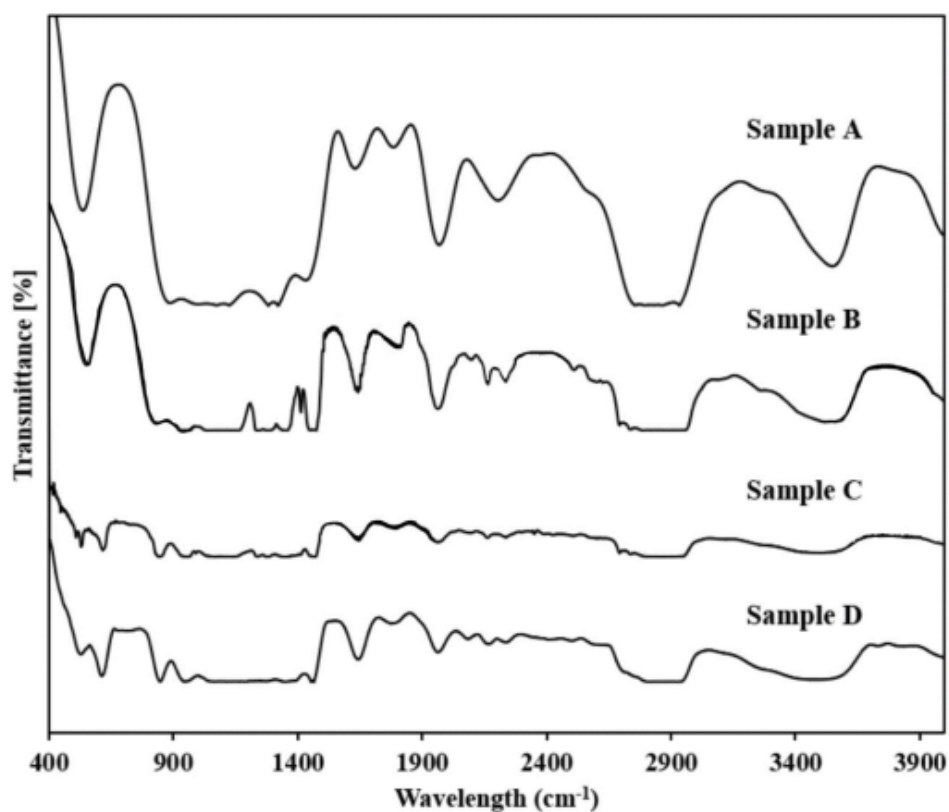


Figure 2. FTIR spectrum of all SPEs samples

3.3 Field Emission Scanning Electron Microscope with energy dispersive X-ray (FESEM-EDX) – Morphology Study

Figure 3 a) and b) show that adding NaNO_3 and K_2SO_4 alters the SPEs' surface morphology. Pure PEO has a rougher surface compared to sample C, which is smoother, though small rough regions remain. As discussed, the salts reduce PEO crystallinity, affecting ionic conductivity. Further surface analysis was conducted at a $2\ \mu\text{m}$ scale with 5000X magnification.

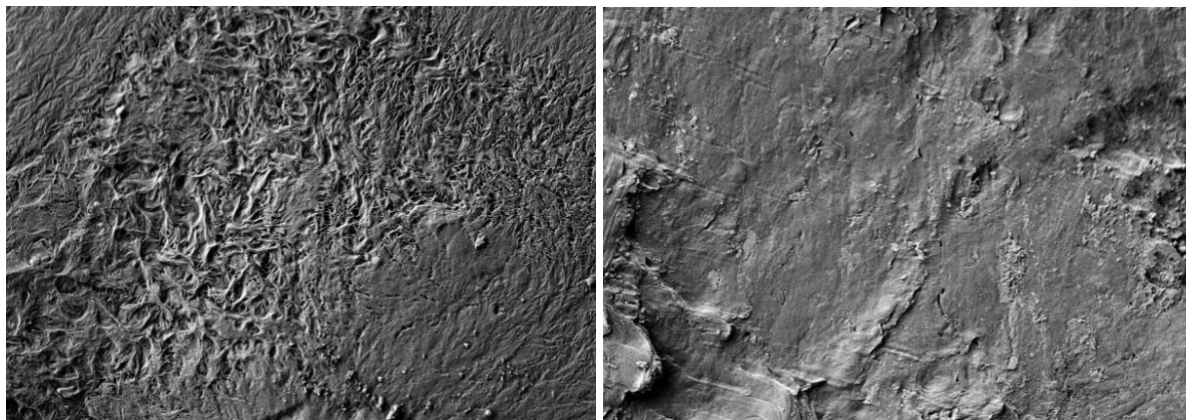


Figure 3. Surface structure a) Sample A-pure PEO b) Sample C-20 wt% Na: 10 wt% K thin film.

Fig. 4 a) shows micropores on pure PEO due to rapid acetonitrile evaporation during solution casting, as commonly reported [5]. This rough, crystalline structure restricts ion movement and reduces conductivity. Fig 4 b) illustrates how adding 20 wt% NaNO_3 and 10 wt% K_2SO_4 smooths the PEO surface and decreases crystallinity, thereby enhancing ionic conductivity. Na^+ and K^+ ions interact with ether oxygens, modifying the crystalline structure and facilitating ion hopping through the amorphous phase of PEO. This coordination improves the interchain mobility of ions, contributing to better conductivity. This also has been confirmed through the elemental analysis through EDX that there is presence of Na and K element with similar wt% of salt added when synthesizing.

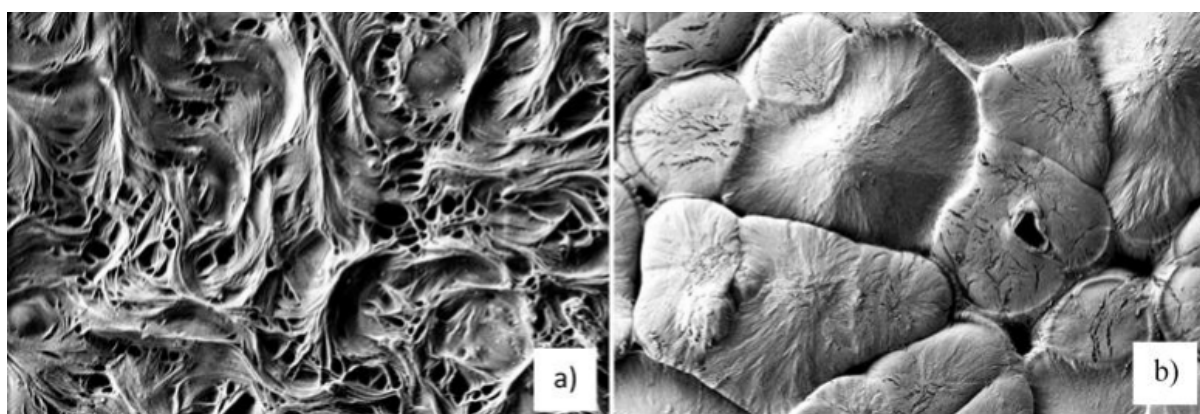


Figure 4. Surface structure a) Sample A-pure PEO b) Sample C-20 wt% Na: 10 wt% K thin film at 5000X magnification.

3.4 Differential Scanning Calorimetry (DSC) – Thermal Properties

Fig. 5 and 6 present the thermograms of sample A (pure PEO) and sample C thin films. Pure PEO shows a melting temperature (T_m) of 72.0°C and a glass transition temperature (T_g) of 54.0°C , aligning with the typical melting range of 68.0°C to 75.0°C [3]. In contrast, sample C exhibits a T_m of 69.0°C and a T_g of 43.0°C , indicating a decrease in T_g by approximately 11°C .

The slight shift in T_g and T_m to lower temperatures in sample C indicates that adding NaNO_3 and K_2SO_4 salts promotes Na^+ and K^+ ion coordination within the PEO matrix. This ionic coordination disrupts the PEO's crystal structure, reducing crystallinity and altering thermal properties, which correlates with increased ionic conductivity.

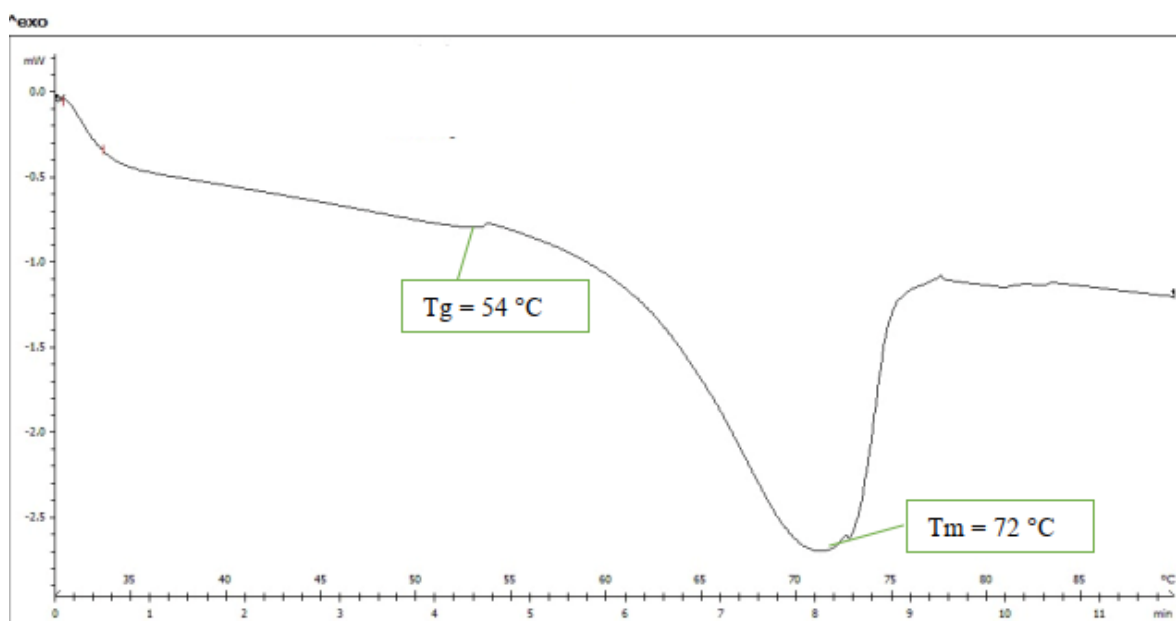


Figure 5. DSC thermograms of sample A (pure PEO) SPE

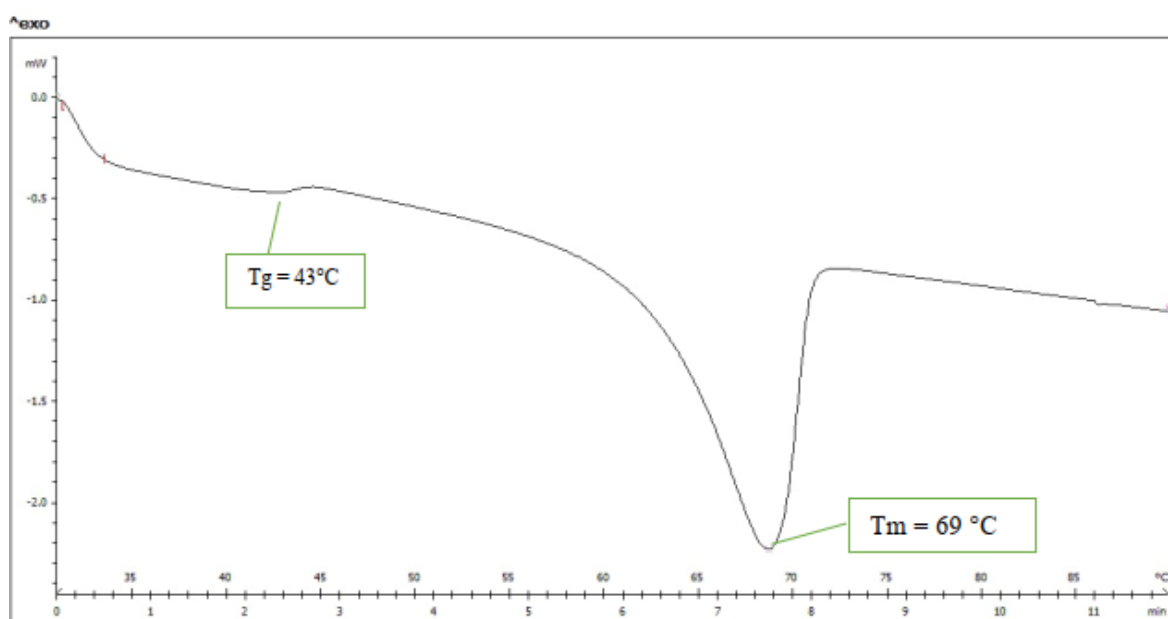


Figure 6. DSC thermograms of sample C (20Na: 10K wt%) SPE.

4. CONCLUSION

In conclusion, the pure PEO and PEO – NaNO₃ – K₂SO₄ has successfully synthesized through solution casting method. The objectives of this research fulfilled by conducting FTIR spectrum analysis to investigate the interaction of Na⁺ and K⁺ with the polymer matrix. The addition of higher concentration of NaNO₃ – K₂SO₄ has increase the ionic conductivity by altering the regular crystal structure of PEO. This can be proven through the EIS data obtained. On the further study FESEM imaging of sample C shown that the surface structure of PEO smoothened resulting in higher ionic conductivity. The glass transition temperature of PEO also reduced when salt is introduced to the system. Lowering the glass transition temperature can also enhance the mobility of polymer segments, thereby facilitating the transport of ions through the material. This improved mobility allows ions to move more freely within the polymer matrix, contributing to higher conductivity. It can be concluded suitable higher concentration of salt increase the ionic conductivity of SPE.

REFERENCES

- [1] Cameron, G. G. (1993). Solid polymer electrolytes: Fundamentals and technological Applications. Fiona M. Gray. VCH Publishers Inc., New York 1991. pp. x + 245, price £44.00. ISBN 0–89573–772–8. Polymer International, 32(4), 436-436.
- [2] Klongkan, S., & Pumchusak, J. (2015). Effects of Nano Alumina and Plasticizers on Morphology, Ionic Conductivity, Thermal and Mechanical Properties of PEO-LiCF₃SO₃ Solid Polymer Electrolyte. *Electrochimica Acta*, 161, 171–176. <https://doi.org/10.1016/j.electacta.2015.02.074>
- [3] Ravindar Reddy, M., Subrahmanyam, A. R., Maheshwar Reddy, M., Siva Kumar, J., Kamalaker, V., & Jaipal Reddy, M. (2016). X-RD, SEM, FT-IR, DSC Studies of Polymer Blend Films of PMMA and PEO. *Materials Today: Proceedings*, 3(10, Part B), 3713-3718
- [4] Shanmukaraj, D., & Murugan, R. (2005). Characterization of PEG: LiClO₄ + SrBi₄Ti₄O₁₅ nanocomposite polymer electrolytes for lithium secondary batteries. *Journal of Power Sources - J POWER SOURCES*, 149, 90-95.
- [5] Xi, J., Qiu, X., Cui, M., Tang, X., Zhu, W., & Chen, L. (2006). Enhanced electrochemical properties of PEO- based composite polymer electrolyte with shape-selective molecular sieves. *Journal of Power Sources*, 156(2), 581-588.

Recycled Aluminium Alloy Casting Process: An Investigation on the Effects of Annealing Parameters

Nur Sakinah binti Zainol^a and Tuan Zaharinie binti Tuan Zahari^{b*}

Department of Mechanical Engineering,
Faculty of Engineering, Universiti Malaya,
50603, Kuala Lumpur, Malaysia

Email: ^a sakinahzainol111@gmail.com, ^b tzaharinie@um.edu.my

*Corresponding author

ABSTRACT

This research aimed to produce recycled aluminium alloy from machining chip waste via conventional casting, investigating annealing parameters and comparing resulting hardness and microstructure. The process involved melting waste with an oxyfuel cutting torch, casting in a graphite mold, and annealing samples at 243°C, 343°C, and 443°C for 30 minutes and 2.5 hours. SEM analysis focused on average grain size, grain structure, pore size, and Mg wt%. Higher temperatures increased grain size and reduced hardness due to higher atomic diffusion. Early recrystallization resulted in equiaxed grains, while further annealing led to uniform grain growth. Increased temperatures also led to larger pores and decreased Mg wt% due to diffusion. The optimal annealing condition was identified as 343°C for 2.5 hours, balancing ductility and hardness with moderate void sizes, corroborated by Vickers hardness testing. This condition aligns with standard heat treatment recommendations.

Keywords: Aluminium alloy; Annealing; Grain size; Hardness; Recycled materials

1. INTRODUCTION

By 2030, a 40% increase in global aluminium demand is expected. Switching to recycling is advisable, as it consumes only 5% of the energy required for primary production. The Annealing process was done to enhance ductility of material. Most research papers only study annealing parameters for primary produced Al Alloy. But the importance of research on annealing parameters for recycled alloy shouldn't be neglected as many big companies such as Alcoa already use recycled aluminium as base materials for products. It was recommended to use annealing temperature of 343°C at 2 to 3 hours holding time [1] but there is no research was done to justify this.

2. METHODOLOGY

Machining chip waste was melted using an oxyfuel cutting torch and cast in graphite molds. Seven samples were prepared, with six undergoing annealing at specified temperatures (243, 343 and 443°C) and holding times (30 minutes and 2.5 hours). To prepare samples for testing, all samples are molded in resin then grind with sandpaper grit 400 until 2000. Then, finishing process using Diamond solution 1 and 3 micro. Etchant used is Keller's reagent (2ml HF (40%) + 3ml HCl (32%) + 5ml HNO₃ (65%) + 190ml Water) [2]. SEM analysis was conducted to assess microstructural changes, while hardness tests were performed using Vickers hardness testing of 1kgf and 10s pressure [3].

3. RESULTS AND DISCUSSION

The average grain size is crucial in microstructure analysis, at Table 1 increasing with higher annealing parameters due to elevated atomic diffusion and grain boundary migration. Larger grains reduce overall energy and barriers, softening the material by easing dislocation movement [4]. Literature indicates hardness decreases with increased annealing time, shown by grain structure changes. Early recrystallization forms new equiaxed grains (samples 1(a) and 1(d)), which grow and mix with deformed grains (sample 1(b)) as recrystallization progresses [5]. Grain growth phase develops larger, more uniform grains with preferred orientations (samples 1(c)(e)(f)), with the most pronounced grain size difference. Pore size is also important in microstructural analysis. High temperatures increase diffusion rates, forming larger gas-filled pores and voids from secondary phase decomposition [6]. Large pores reduce hardness by acting as stress concentrators.

As annealing parameters rise, Mg wt% concentration decreases as Mg atoms diffuse out more rapidly. Mg distribution affects hardness: before annealing, the high standard deviation of 1.168% indicates non-uniform distribution and solution strengthening, distorting the lattice and hardening dislocations. After annealing, a lower standard deviation ($<1\%$) indicates a more uniform distribution [7].

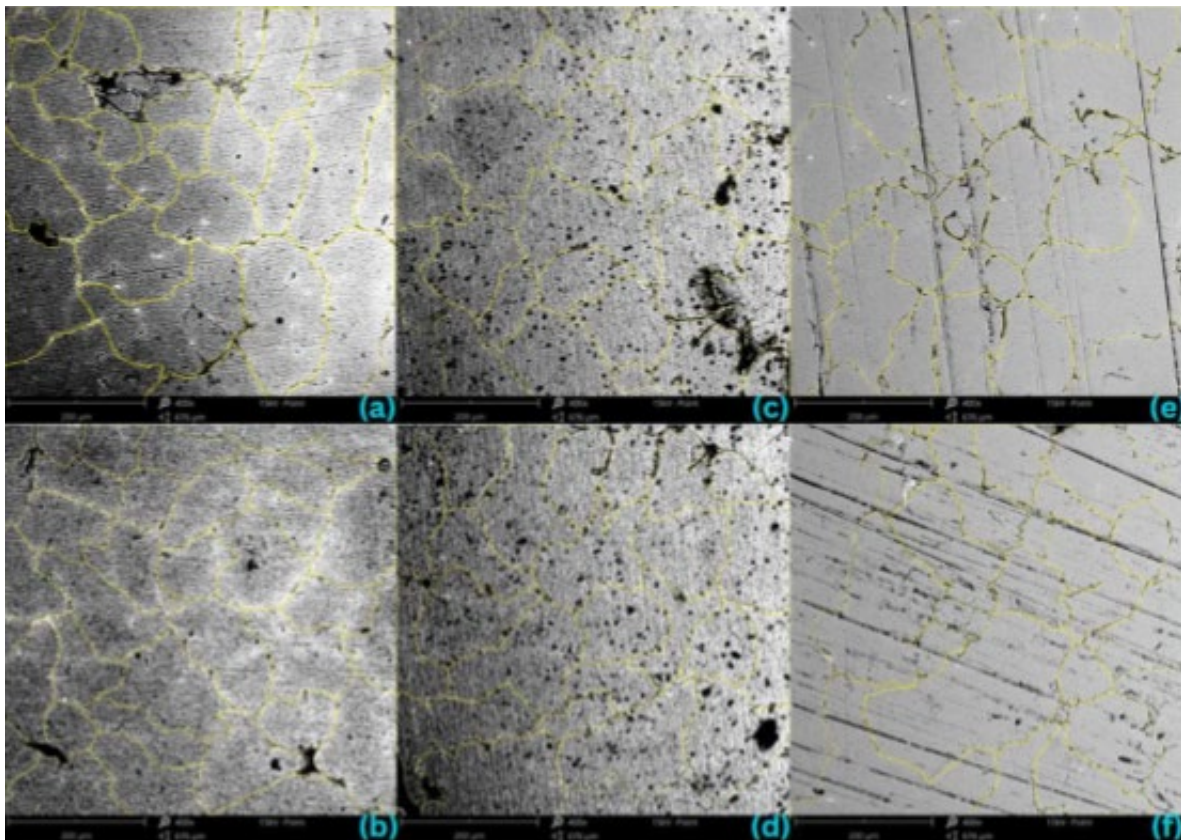


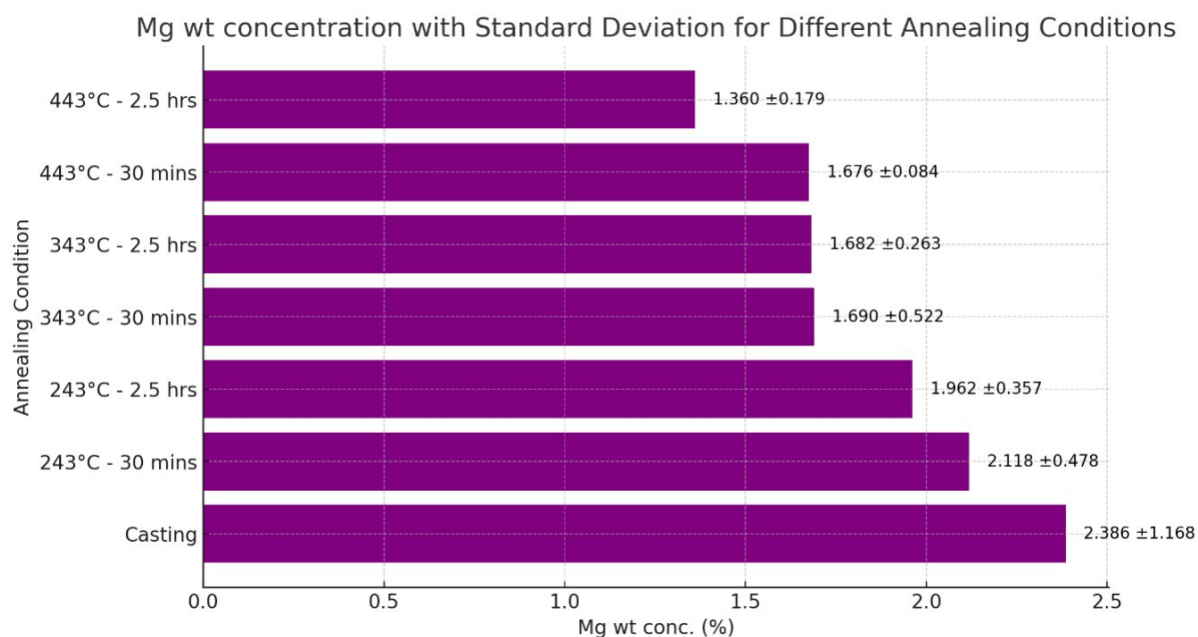
Figure 1. SEM microstructure for (a) 243°C-30 mins (b) 343°C-30 mins (c) 443°C-30 mins (d) 243°C-2.5 hrs (e) 343°C-2.5 hrs (f) 443°C-2.5 hrs

Table 1: Average grain and pore surface area size

| Sample | Grain Surface Area (μm^2) | Average pore surface area (mm^2) |
|--------------------|--|---|
| Original | 7173.42 | 0.00746 |
| 243 °C- 30 mins | 12431.53 | 0.00933 |
| 243 °C - 2.5 hours | 15349.98 | 0.01302 |
| 343 °C - 30 mins | 16235.6 | 0.0144 |
| 343 °C - 2.5 hours | 17968.82 | 0.01764 |
| 443 °C - 30 mins | 18497.64 | 0.02333 |
| 443 °C - 2.5 hours | 20373.47 | 0.02555 |

Table 2: Vicker's hardness value (HV1)

| Sample | Hardness value (HV1) |
|--------------------|----------------------|
| Original | 68.00 \pm 1.20 |
| 243 °C- 30 mins | 61.10 \pm 0.87 |
| 243 °C - 2.5 hours | 60.21 \pm 0.90 |
| 343 °C - 30 mins | 57.68 \pm 1.01 |
| 343 °C - 2.5 hours | 51.13 \pm 0.79 |
| 443 °C - 30 mins | 39.35 \pm 0.98 |

**Figure 2:** Mg wt% concentration with standard deviation for different annealing conditions

Lastly, as annealing temperature and holding time increases, hardness Vicker's (HV1) decreases which indicates increased in ductility.

4.0 CONCLUSION

The study identified that annealing recycled aluminium alloys at 343°C for 2.5 hours has great balance between ductility and hardness. This condition resulted in moderate void sizes and a refined grain structure, enhancing mechanical performance. Higher annealing temperatures and durations increased grain size and porosity, reducing hardness due to the Hall-Petch relationship and atomic diffusion. Mg

content influenced hardness, with higher temperatures reducing Mg concentration and standard deviation, leading to uniform distribution and lower hardness. Vickers' Testing confirmed these trends, showing decreased hardness with increased annealing. The recycled alloy's hardness was comparable to primary AA5052, proving the recycling process's effectiveness.

REFERENCES

- [1] (ASTM), A. S. f. T. a. M. (2009). Standard practice for heat treatment of wrought aluminum alloys (B 918/B 918M – 09). A. International. <https://www.astm.org/Standards/B918.htm>
- [2] Şahbaz, M. (2021). Effect of Artificial Aging and Cooling Rate on Microstructure and Mechanical Properties of AA6082. *European Journal of Science and Technology*, 2021, 300-305. <https://doi.org/10.31590/ejosat.998077>
- [3] Zhang, P., Li, Y., Liu, Y., Zhang, Y., & Liu, J. (2019). Analysis of the microhardness, mechanical properties and electrical conductivity of 7055 aluminum alloy. *Vacuum*, 171, 109005–109005. <https://doi.org/10.1016/j.vacuum.2019.109005>
- [4] Zhang, D. D., Wang, H., Zhang, J. Y., Xue, H., Liu, G., & Sun, J. (2021). Achieving excellent strength-ductility synergy in twinned NiCoCr medium-entropy alloy via Al/Ta co-doping. *Journal of Materials Science & Technology*, 87, 184–195. <https://doi.org/10.1016/j.jmst.2021.01.060>
- [5] Wang, Y. (2014). Fundamentals of Recrystallization in Titanium Alloys. The University of Manchester (United Kingdom).
- [6] Bykov, Y.V., Egorov, S.V., Eremeev, A.G. *et al.* Evidence for microwave enhanced mass transport in the annealing of nanoporous alumina membranes. *Journal of Materials Science* 36, 131–136 (2001). <https://doi.org/10.1023/A:1004893104413>
- [7] Wang, G., Peng, C., Zhang, B., Xu, Z., Li, Q., Liu, K., & Lu, P. (2022). Effect of the Annealing Process on the Microstructure and Performance of 5056 Aluminum Alloy Wires. *Metals*, 12(5), 823. <https://doi.org/10.3390/met12050823>

New Way of Sustaining Paintings on The Wall at The Engineering Faculty

Muhammad Faris bin Mohd Anuar^a and Bushroa binti Abd Razak^{b*}

Department of Mechanical Engineering,
Faculty of Engineering, Universiti Malaya,
50603, Kuala Lumpur, Malaysia

Email: ^a farisxanuar@gmail.com, ^b bushroa@um.edu.my

*Corresponding author

ABSTRACT

The Engineering Faculty faces challenges in maintaining building aesthetics due to recurring fungus and mildew growth on freshly painted surfaces, compromising longevity and posing health risks. Frequent repainting escalates costs and labor. This research explores Cold Atmospheric Plasma (CAP) technology as an eco-friendly solution for microbial control. CAP pre-treats walls, creating a barrier against fungal colonization before painting. The study involves preparing samples of *Aspergillus niger*, *Mucor*, and *Trichoderma*, treating them with CAP generated by a Tesla coil and helium gas. Results demonstrate CAP's effectiveness in microbial mitigation. The goal is to develop a portable, user-friendly CAP tool for on-site use, reducing maintenance costs and supporting sustainable building management. The project addresses fungal issues, aligns with sustainability goals, and supports government climate initiatives, offering a proactive solution for building maintenance. This research pioneers a cost-effective, health-conscious approach to maintaining painted surfaces, benefiting institutions facing similar challenges.

Keywords: Cold Atmospheric Plasma; Fungal control; Microbial mitigation; Plasma treatment; Sustainable maintenance.

1. INTRODUCTION

The Engineering Faculty faces a persistent challenge: fungal and mildew invasions compromise freshly painted surfaces, posing health risks. The repetitive repainting cycle consumes significant time and resources. To address this, the project explores Cold Atmospheric Plasma (CAP) technology as a sustainable solution. CAP is a unique form of plasma that operates at room temperature that neutralizes microorganisms without chemical residue, unlike traditional plasma, which requires high temperatures. The project aims to use CAP for pre-painting treatment, preventing microbial growth and maintaining aesthetic and health standards. Additionally, it focuses on developing a portable CAP tool for efficient on-site use. This innovation promises to reduce maintenance costs, support sustainability, and ensure the long-term preservation of the faculty's buildings, promoting environmental and health benefits.

2. METHODOLOGY

Samples are prepared by cultivating *Aspergillus niger*, *Trichoderma*, and *Mucor* on Sabouraud Dextrose Agars (SDA) using aseptic techniques. Small quantities of each strain are transferred onto SDA plates

under a laminar flow hood to ensure sterility. The plates are then incubated at 25-30°C to promote colony growth and regularly monitored for purity, with any contaminants addressed by transferring healthy colonies to fresh plates. The effectiveness of CAP technology in mitigating microbial growth is assessed by treating *Aspergillus niger*, *Trichoderma*, and *Mucor* on SDA with plasma generated using a Tesla coil and helium gas. Samples are divided, with half undergoing a 4-minute plasma treatment, allowing for a direct comparison between treated and untreated sections. Post-treatment observations are made to assess the impact of CAP technology. The development of the portable CAP prototype followed a structured approach. Initially, four sketch designs were evaluated, with the most promising concept chosen for further refinement. Using SolidWorks, a detailed 3D model was created to visualize and simulate the prototype. Simultaneously, the electrical circuitry was designed and integrated, while mechanical components were developed with precision engineering. The final phase involved assembling all components into a functional prototype, followed by rigorous testing and refinement. This systematic approach ensured the prototype met project objectives effectively.

3. RESULTS AND DISCUSSION

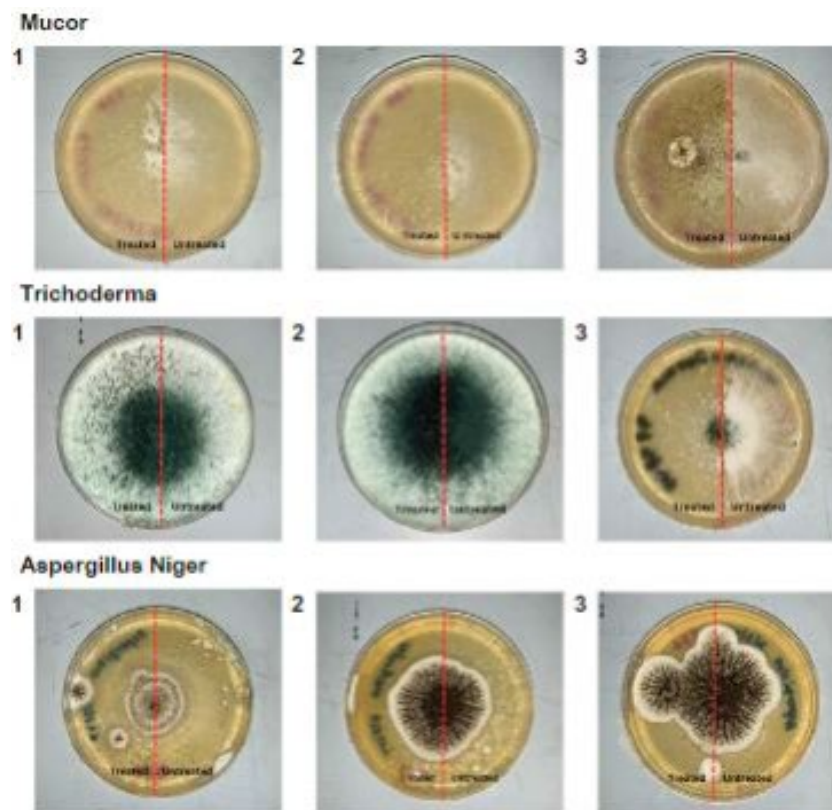


Figure 1. Comparison before and after the Cold Atmospheric Plasma (CAP) Treatment

The results indicate varying degrees of microbial mitigation effectiveness across different parameter settings. For samples 1, where the helium gas pressure was 15 Bar, flow rate of helium gas was 1 L/min, Tesla coil power 10 W, and frequency 5.0 Hz, the efficacy of microbial mitigation was relatively low, suggesting insufficient plasma state generation for effective microorganism elimination. For samples 2, with increased parameters of 20 Bar pressure, 2 L/min flow rate, 65 W power, and 27.5 Hz frequency, there was a noticeable improvement in microbial mitigation, indicating that higher intensity settings enhanced the cold plasma treatment's effectiveness. The most promising results were observed in samples 3, with parameters set at 25 Bar pressure, 3 L/min flow rate, 120 W power, and 50.0 Hz

frequency. This configuration demonstrated the highest efficacy in eliminating microbial colonies, likely due to the more intense and sustained plasma discharge achieved with these elevated settings.

The final design of the portable Cold Atmospheric Plasma (CAP) tool offers a lightweight and maneuverable solution for microbial mitigation in building maintenance. Weighing just 4.5 kg, it runs on battery power for flexible usage in diverse areas. Its high coverage efficiency targets various surfaces effectively, while the innovative back-carrying design enhances portability. Equipped with metal columns for safety, the tool prioritizes user protection during operation.

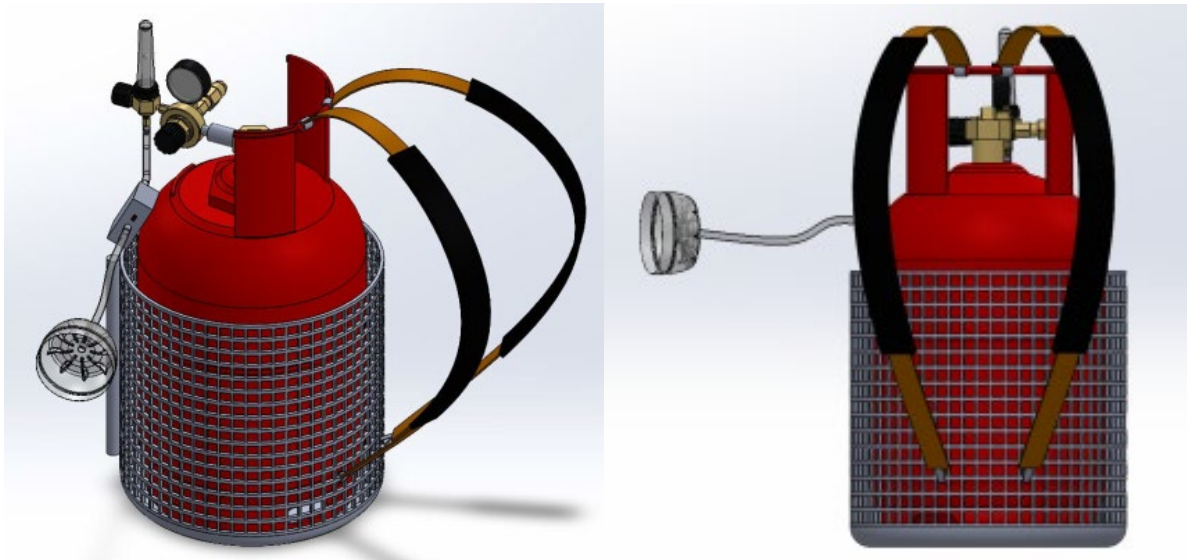


Figure 2. 3D Design of Portable CAP Tool

4. CONCLUSION

The project demonstrates the effectiveness of Cold Atmospheric Plasma (CAP) in reducing microbial growth on building surfaces. Systematic testing and varied parameter configurations reveal CAP as a viable solution to fungal and mildew issues on painted surfaces. Higher intensity settings notably improve efficacy. These findings support eco-friendly and sustainable maintenance practices. CAP technology reduces the need for frequent repainting and associated costs, and the development of a portable CAP tool enhances on-site treatment efficiency.

REFERENCES

- [1] Reema, R. R. K., Heremba Bailung & Kamatchi Sankaranarayanan. (2022). Review of the cold atmospheric plasma technology application in food, disinfection, and textiles: A way forward for achieving circular economy. Retrieved November 8, 2023, from <https://www.frontiersin.org/articles/10.3389/fphy.2022.942952/full>

Breaking Barriers in Solar Cells: Synthesis of Mesoporous Titanium Dioxide using Template Free Method

Lew Sheau Wenn^a and Tan Chou Yong^{b}*

Department of Mechanical Engineering,
Faculty of Engineering, Universiti Malaya,
50603, Kuala Lumpur, Malaysia

Email: ^a sheauwenn.lew@gmail.com, ^b chouyong@um.edu.my

*Corresponding author

ABSTRACT

Increasing energy demands accelerate the need for affordable and efficient renewable solutions, particularly solar energy. Studies proved that mesoporous material could improve efficiency of Dye Sensitized Solar Cells (DSSCs). In this research, mesoporous titanium dioxide (TiO₂) are studied, focusing on synthesizing mesoporous TiO₂ using template free method and determining the effects of calcination temperature on the TiO₂ structure and efficiency of DSSC. Mesoporous TiO₂ with small pore size and high specific surface area has been synthesized successfully with precipitation method. XRD confirmed presence of anatase TiO₂ in all samples and rutile TiO₂ in sample synthesized at 650°C while FESEM indicated improved crystallinity with higher calcination temperature. BET analysis showed decreased surface area and pore volume, with larger pores at higher temperatures. The photovoltaic performance of DSSCs revealed that higher calcination temperatures enhance FF, VOC, JSC and η of DSSC up to certain temperature as JSC and η were reduced when TiO₂ is calcinated at 650°C. TiO₂ calcinated at 450°C showed best DSSC performance with η of 5.91 %, JSC of 12.43 mA/cm², VOC of 0.71 V, FF of 0.67 % and RCT1 of 244 Ω.

Keywords: Calcination, Dye Sensitized Solar Cells, Mesoporous, Synthesis, Titanium Dioxide.

1. INTRODUCTION

Statistical Review of World Energy 2023 revealed a 2.8% increase in primary energy use in 2022 from 2019 and record-high carbon dioxide emissions of 39.3 billion tonnes. Oil, coal, and natural gas remain as primary energy sources, but renewable energy's share rose to 7.5% in 2022, with solar energy accounting for 72% of the new capacity [1]. Goal 7 of SDGs targets universal access to sustainable energy by 2030, with focus on solar energy to enhance efficiency, reduce emissions, and provide energy access in remote areas. However, despite various solar cell technologies, achieving higher efficiency at lower costs remains a challenge. 3rd generation solar cells, like DSSCs, offer lower processing costs, environmental benefits and good low-light performance but lower in efficiency. Thus, mesoporous TiO₂ is crucial for DSSCs development due to its high surface area, enhancing dye molecule adsorption essential for photoelectron generation. The synthesis method and parameter of significantly mesoporous impacts the cost TiO₂ and efficiency of solar cells, so template-free precipitation method, synthesized successfully by [2] that is simple, cost and time effective were chosen to be studied at various calcination temperature to see relationship of calcination temperature with TiO₂ structure and DSSC efficiency.

2. METHODOLOGY

2.1 Synthesis of Mesoporous TiO₂

TTIP is added to ethanol with dropwise addition of KCl solution under stirring. The mixture is then centrifuged, dried and calcinated at 250°C, 450°C and 650°C [2].

2.2 Working Electrode Preparation

Cleaned FTO is spin-coated with P90 TiO₂ and sintered. 2nd layer of synthesized TiO₂ is applied with doctor blade method, sintered and immersed in N719 dye.

2.3 Dye Preparation

N917 dye, chenodeoxycholic acid and ethanol is mixed under continuous stirring in aluminium foil covered glass container.

2.4 Electrolyte Preparation

A mixture of poly(acrylo nitrile), ethylene carbonate, propylene carbonate, 1-methyl-3 propylimidazolium iodide, sodium iodide and iodine was stirred to form a gel polymer electrolytes (GPEs) [3].

2.5 Counter Electrode Preparation

Chloroplatinic acid with ethanol slurry was drop-casted onto FTO glass and sintered, repeating to achieve desired thickness.

2.6 DSSC Fabrication

The working electrode is sandwiched to counter electrode with electrolyte in between and secured with clips. Alligator clips were clipped onto the FTO glass and connected to Metrohm Autolab potentiostat (PGSTAT128N) and placed under the ABET technologies solar simulator, measured with NOVA software.

3. RESULTS AND DISCUSSION

3.1 FESEM

Based on Fig.1, it is seen that higher calcination temperatures promote particle growth and agglomeration, consequently reducing the surface area of the synthesized TiO₂ material.

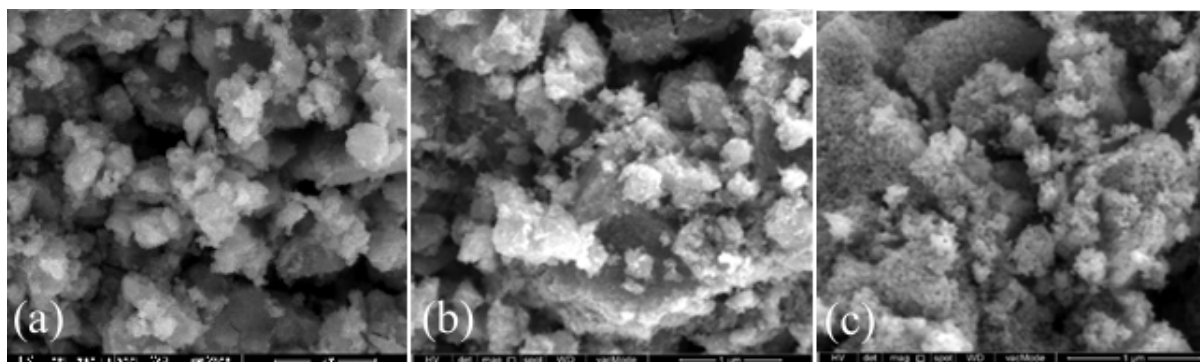


Figure 1. FESEM images of TiO₂ synthesized at (a) 250°C (b) 450°C (c) 650°C

3.2 XRD

From Fig 2, the intensity of anatase peaks increase with calcination temperature, likely due to improved crystallinity, which further reduces the scattering of X-rays within the material, further leading to narrower peaks. Rutile phase appeared with TiO_2 is calcinated at 650°C .

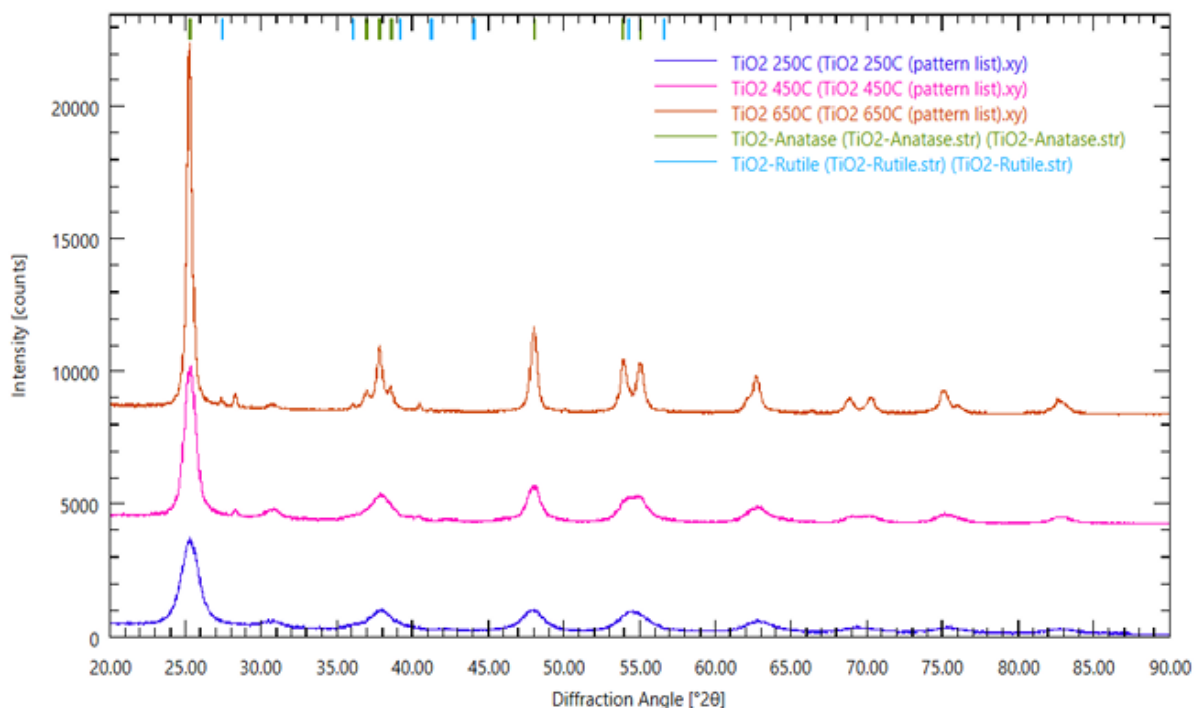


Figure 2. XRD graphs of TiO_2 synthesized

3.3 BET

The isotherm plots are classified as Type IV isotherm and samples are mesoporous based on IUPAC scheme. The hysteresis loop appears at higher relative pressures as calcination temperature increases. Surface area and pore volume decreases with increasing calcination temperature, indicating sintering effects and pore collapse at higher temperatures. The pore size increases with higher calcination temperatures, suggesting the growth and merging of pores.

Table 1. BET result for all TiO_2 synthesized

| | 250°C | 450°C | 650°C |
|--|--------|-------|-------|
| Surface Area (m^2/g) | 171.61 | 87.95 | 35.59 |
| Pore Size (nm) | 6.64 | 12.30 | 26.95 |
| Pore Volume (cm^3/g) | 0.28 | 0.27 | 0.24 |

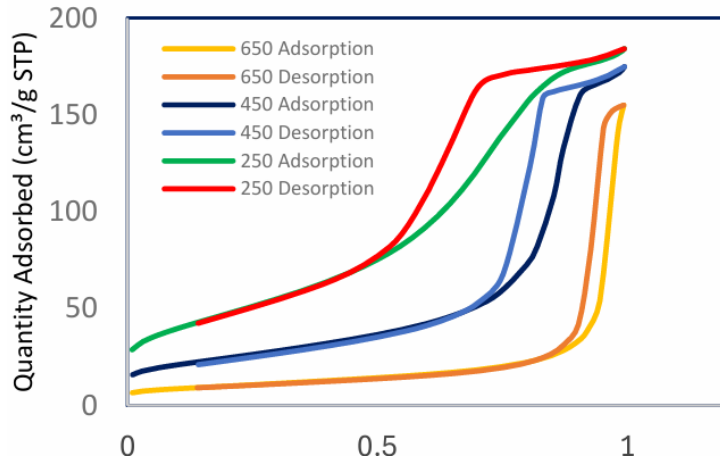


Figure 3. Isotherm plots of TiO₂

3.4 Photovoltaic Performance

As calcination temperature increases, RCT1 increases, indicating harder charge transfer at the TiO₂/electrolyte interface. Lower JSC of all sample compared to [3] suggest that the surface area and pore structure are not optimal for high dye loading and light absorption [4]. Bode plot with lower maximum phase angle indicates reduced recombination rate across the TiO₂/electrolyte interface due to improved electron life [5].

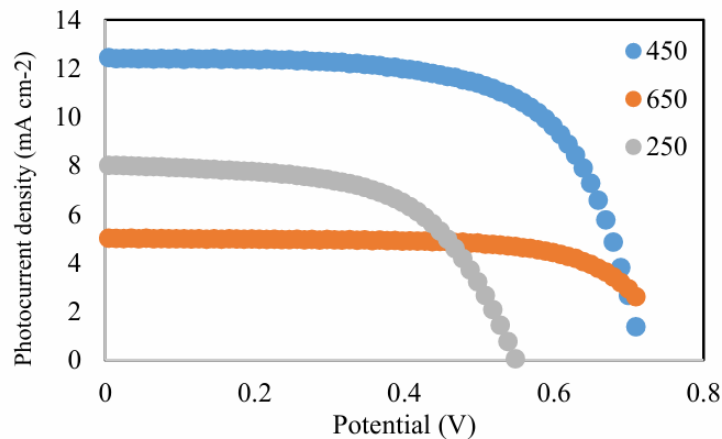


Figure 4. J-V curves of DSSCs

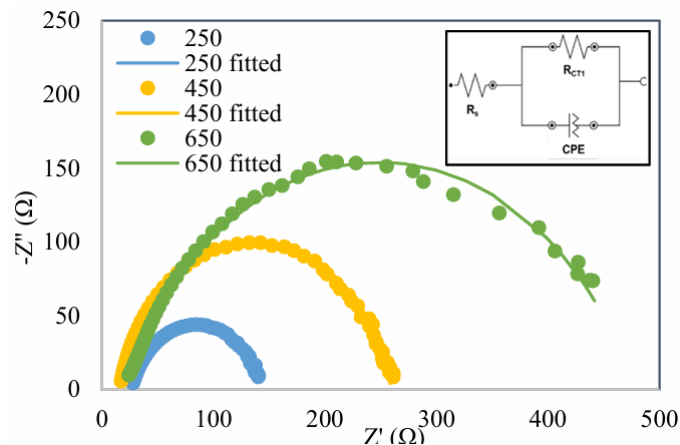


Fig. 5: EIS of DSSCs

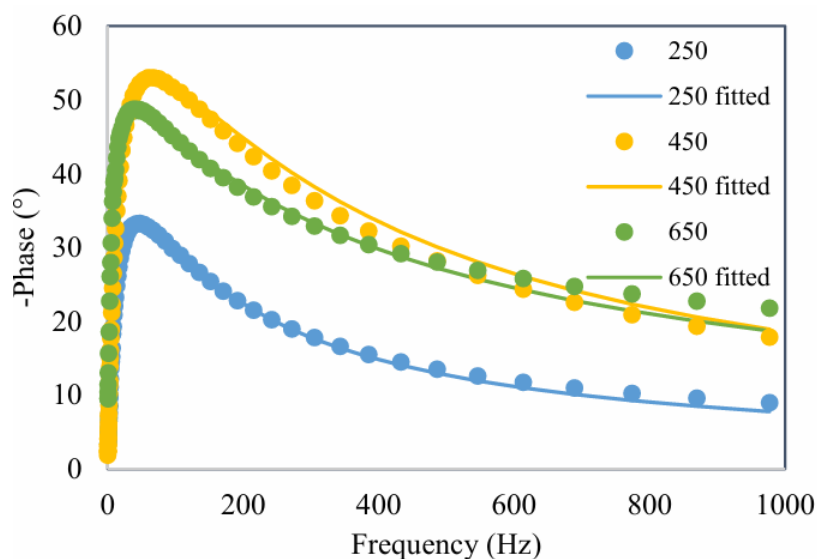


Figure 6. Bode plot of DSSCs

Table 2: J-V parameters for all the DSSCs

| TiO ₂ | JSC (mA cm ⁻²) | VOC (V) | FF (%) | η (%) | R _s (Ω) | R _{CT1} (Ω) |
|------------------|-------------------------------|------------|-----------|---------------|--------------------------------|----------------------------------|
| Commercial P25 | 15.60 | 0.65 | 0.64 | 6.47 | - | - |
| 250°C | 8.00 | 0.55 | 0.59 | 2.57 | 26.8 | 116 |
| 450°C | 12.43 | 0.71 | 0.67 | 5.91 | 15.5 | 244 |
| 650°C | 5.01 | 0.71 | 0.74 | 2.64 | 21.1 | 455 |

4. CONCLUSION

Mesoporous TiO₂ was successfully synthesized with template free precipitation method. From the characterizations, it was found that higher calcination temperature leads to improved crystallinity with greater pore size but reduce in surface area and pore volume. Rutile phase appeared when TiO₂ is calcinated at 650 °C.

The photovoltaic performance of DSSCs using TiO₂ calcinated at different temperatures demonstrates that while higher calcination temperatures enhance FF and VOC due to improved crystallinity, JSC and overall efficiency will reduce when the calcination temperature exceed 650 °C possibly due to rutile phase formation, altering the charge dynamics and reduced surface area, which further reduce the active sites for dye adsorption. TiO₂ calcinated at 450°C provides the best DSSC performance with η of 5.91 %, JSC of 12.43 mAcm⁻², VOC of 0.71 V, FF of 0.67 % and RCT1 of 244 Ω

REFERENCES

- [1] Institute, E. (2023). Statistical Review of World Energy.
- [2] Lakshminarasimhan, N., Bae, E., & Choi, W. (2007). Enhanced Photocatalytic Production of H₂ on Mesoporous TiO₂ Prepared by Template-Free Method: Role of Interparticle Charge Transfer. The Journal of Physical Chemistry C, 111(42), 15244-15250. doi:10.1021/jp0752724
- [3] Saidi, N. M., Goh, Z. L., Arif, H. M., Farhana, N. K., Ramesh, S., & Ramesh, K. (2021). Consolidation of ion promoters into quasi solid state (QSS) polymer electrolytes for dye-sensitized solar cells (DSSCs). Solid State Ionics, 363, 115592. doi:https://doi.org/10.1016/j.ssi.2021.115592

- [4] Kim, H., Choi, Y., Park, Y., Pawar, R. C., Choa, Y.-H., & Lee, C. S. (2017). Improved efficiency of dye-sensitized solar cell based on randomly ordered pore structure fabricated by dry deposition method. *Current Applied Physics*, 17(4), 433-441. doi:<https://doi.org/10.1016/j.cap.2017.01.007>
- [5] Balakrishnan, M., & John, R. (2021). Impact of Ni metal ion concentration in TiO₂ nanoparticles for enhanced photovoltaic performance of dye sensitized solar Cell. *Journal of Materials Science: Materials in Electronics*, 32. doi:10.1007/s10854-020-05100-0

Enhancing Supercapacitor Performance with Hydrothermally Synthesized Mesoporous Nickel-Based Nanostructure

Leong Sze Xun ^a and Tan Chou Yong ^{b*}

Department of Mechanical Engineering,
Faculty of Engineering, Universiti Malaya,
50603, Kuala Lumpur, Malaysia

Email: ^a szexun.leong@gmail.com, ^b chouyong@um.edu.my

*Corresponding author

ABSTRACT

Mesoporous nickel oxide nanostructure was fabricated through hydrothermal synthesis method. Hydrothermal method includes the preparation of precursor solution using nickel chloride and urea, hydrothermal treatment, drying and calcination. The samples were labelled according to calcination temperature of 250°C, 350°C and 450°C. The results of FESEM, XRD, BET, TGA and CV of the synthesized sample is presented in this research. The effect of parameters like calcination temperature on material morphology and electrochemical properties like specific capacitance was studied. The XRD pattern generated reflects the mesoporous nickel oxide is successfully synthesized. NiO-250 consists of numerous thin and well-defined nanopetals and diminished gradually with the increase in calcination temperature. NiO-250 have the highest BET volume of $30.6543\text{m}^2/\text{g}$. A maximum specific capacitance of 159 F/g was achieved by Ni-250 at low scan rate of $10\text{mV}/\text{s}$.

Keywords: Mesoporous Nickel Oxide; Hydrothermal Synthesis; Calcination Temperature; Nanopetal Morphology; Specific Capacitance

1. INTRODUCTION

Supercapacitor is an advanced energy storage system with high power density and fast charging; nevertheless, supercapacitor does not prove to have large energy storage when compared to other. Supercapacitors can be divided into two main types based on their storage mechanism which are electrostatic double-layer capacitors (EDLCs) and pseudo capacitors (PCs). PCs store energy through fast and reversible oxidation-reduction reactions or known as Faradaic charge process which electron transfer happens across the electrode surface through redox reaction. Transition metal oxides are the choice of material that made up the electrode for PCs as it has reactive electronic transitions, high dielectric constants, wide bandgaps and good electrical characteristics. (Ashik, 2018). Studies have been done and proved that that mesoporous metal oxides can be used as electrode material in supercapacitor due to their large surface area and better structural stability. NiO and are non-toxic TMOs that have considerably high theoretical specific capacitance which are 2584 F/g in a potential window of 0.5 V make itself a promising material for supercapacitor.

2. METHODOLOGY

2.1 Synthesis

1 mol/L of NiCl₂ solution is prepared and mixed 2 mol/L of urea solution. The urea solution is added dropwise in NiCl₂ solution and vigorous stirring is done. The mixture is hydrothermally heated at 110°C for 6 h in Teflon-lined autoclaves. The solution from the autoclave is washed 5 times with deionized water and then 3 times with ethanol. The precipitate is transferred to crucible to be dried at 70°C for 12 h in the oven at a heating/cooling rate of 5°C. The dried powder is calcinated at different temperature 250°C, 350°C, 450°C for 3 h in the furnace at a heating/cooling rate of 5°C. The samples are then named after their calcination temperature which are NiO-250, NiO-350 and NiO-450.

2.2 Characterization

Chemical composition and crystal structure of the samples were characterized by powder X-ray diffraction (Rigaku MiniFlex 600, XRD) using Cu K β radiation. Thermogravimetric analysis (TGA) was carried out on PerkinElmer TGA4000 to observe the thermal decomposition process of the samples. The field emission scanning electron microscopy (FESEM, QUANTA FEG 450) was used to observe the morphologies of the samples. Brunauer-Emmett-Teller (BET, TriStar II 3020) analysis was used for further quantitative analysis of the samples' microstructure, such as specific surface area, pore diameter, distribution and isothermal absorption/desorption.

2.3 Electrochemical Measurement

A mixed slurry composed of 70 wt% NiO, 20 wt% carbon black and 10 wt% polytetrafluoroethylene (PTFE) was coated on a 316L stainless steel and then dried in vacuum at 80°C. After the coated stainless steel was pressed, the working electrode was prepared. The mass of the active material coated was measured. The cyclic voltammetry test (CV) was conducted in three-electrode system with Autolab potentiostat. 1M of sodium hydroxide (NaOH) solution was prepared as electrolyte, platinum sheet electrode is used as the counter electrode, the silver/silver chloride electrode is used as the reference electrode. CV at different scan rates were conducted. The specific capacitance of the NiO samples was determined using the equation below.

$$C_s = \frac{1}{v \times 2m \times (V_a - V_c)} \int_{V_a}^{V_c} I dV$$

Where v is the sweep rate, $\int I dV$ is area of the CV curve, m is the mass of NiO sample coated, $V_a - V_c$ is the potential window.

3. RESULTS AND DISCUSSION

3.1 FESEM

Figure 1 showed that NiO-250 consists of numerous thin and well-defined nanopetals grow in a spherical shape forming a flower-like microballs. However, the distinctive shape of the nanopetals diminished gradually with the increase in calcination temperature. NiO-350 showed less pronounced nanopetals due to early stage of agglomeration where small particles grow on the petals while NiO-450 illustrate relatively larger agglomeration which lead to the loss of nanopetals structure.

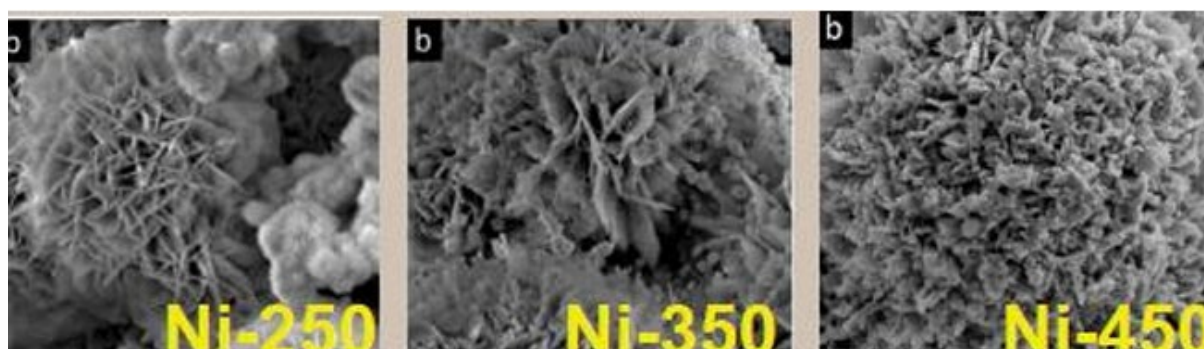


Figure 1. FESEM images of Ni-250, Ni-350 and Ni-450 nanostructures

3.2 XRD

The characteristic diffraction peaks were observed around 37°, 43°, 62°, 75° and 79° which is corresponded to NiO. Thus, NiO is successfully synthesized on the NiO-350 and NiO-450 samples. NiO 250 sample differs from other samples as there are diffraction peaks on 33° and 59° which are only compatible to the peaks of beta Nickel hydroxide (β -Ni(OH)₂). β -Ni(OH)₂ is known to be the unreacted compound throughout the calcination and drying process as β -Ni(OH)₂ is not visible when the calcination temperature elevated. For NiO-350, it showed peaks with higher intensity with slightly broader full width at half maximum (FWHM) compared to 450°C, this indicates that NiO-350 samples have more well-ordered crystalline domains but in smaller sizes.

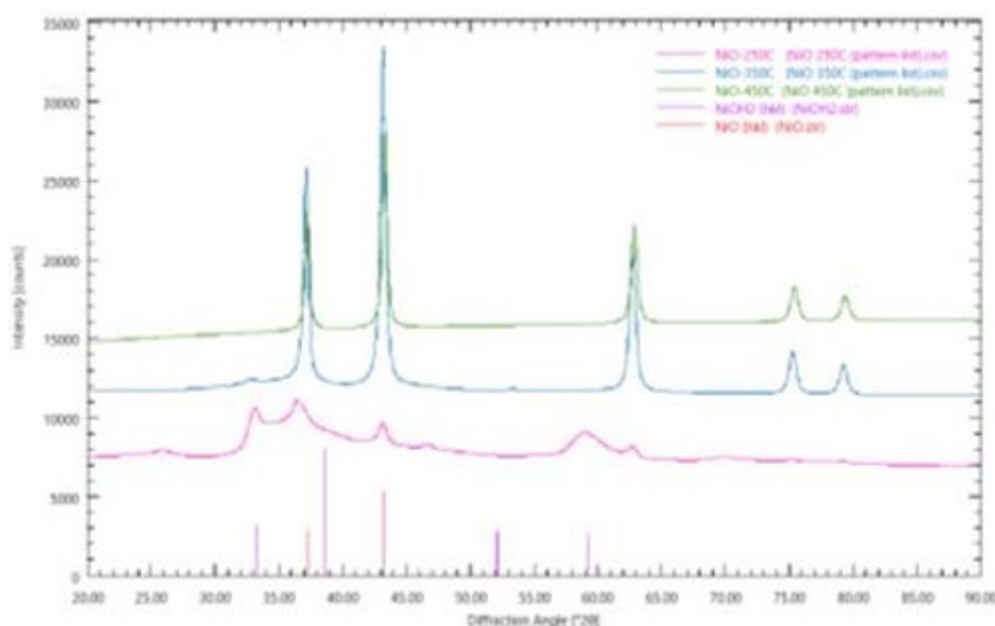


Figure 2. XRD patterns for NiO samples

3.3 BET

The NiO nanostructures were studied using the nitrogen adsorption/desorption measurements at 77 K. All the isotherm plots were identified as type IV isotherm with an H1-type loop hysteresis) which is characteristics of a mesoporous nanostructure. NiO-250 showed the highest absorption quantity at high relative pressure region followed by NiO-350 and then NiO 450. The higher adsorption quantity at this region indicates a higher overall pore volume or surface area, thus NiO-250 have the highest BET volume of 30.6543m²/g as shown in Table 1. BET surface area and pore volume decrease as the

calcination temperature increase. This is because of the high calcination temperature promote higher degree of crystallization which lead to removal of pores and agglomeration.

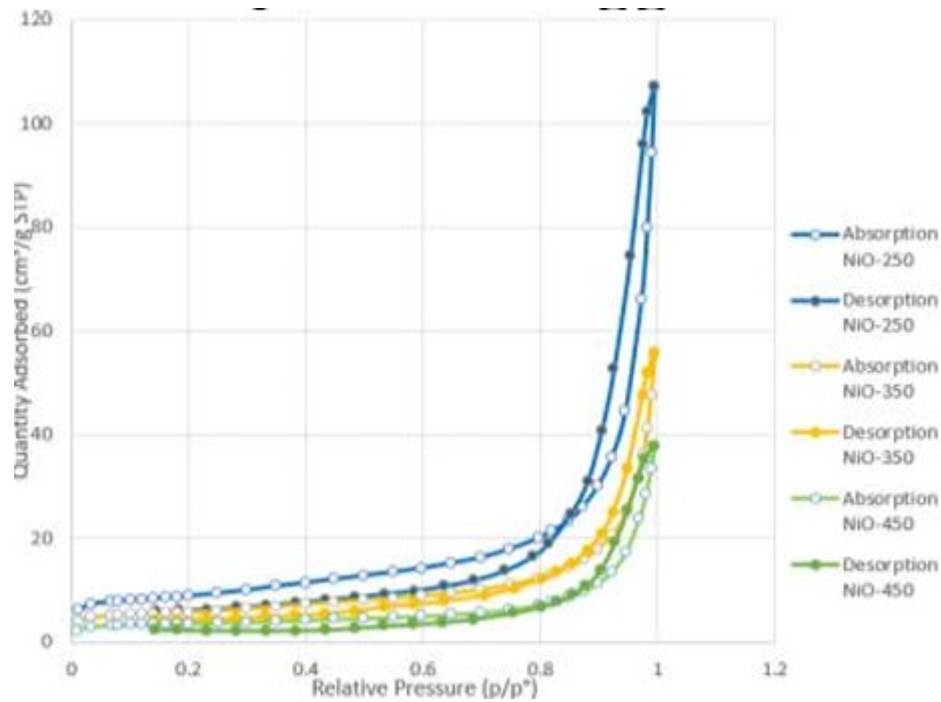


Figure 3. Isotherm Plot for NiO samples

Table 1. BET results for NiO samples

| Sample | BET surface area (m^2/g) | Average pore diameter (nm) | Average pore volume (cm^3/g) |
|---------|---------------------------------|-----------------------------------|-------------------------------------|
| NiO-250 | 30.6543 | 21.62123 | 0.165696 |
| NiO-350 | 19.8596 | 17.33168 | 0.086050 |
| NiO-450 | 12.3250 | 18.94504 | 0.058374 |

3.4 CV

Based on Figure 4, all CV curves of NiO samples exhibited reduction peaks around 0.1V to 0.2V while most of oxidation peaks are unclear which does not indicate the presence of redox reaction. From Figure 5, specific capacitance decreases with increasing scan rate for all samples. This is typical in supercapacitors where higher scan rates limit the ability of the material to fully interact with the electrolyte. At low scan rates, ions in the electrolyte have sufficient time to diffuse into the electrode material leading to higher specific capacitance. NiO-250 which is having the highest specific capacitance at 10mV/s experience the most significant drop in specific capacitance. This significant drop might due to the presence of low conductivity of $Ni(OH)_2$ (Kim et al., 2013).

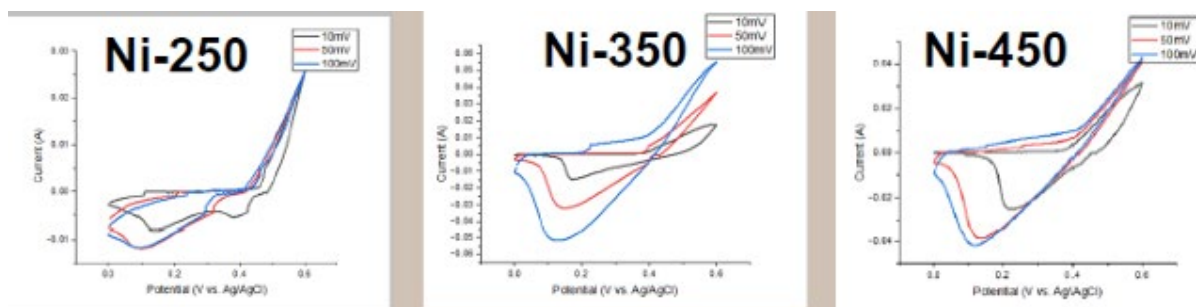


Figure 4. CV curve for NiO samples

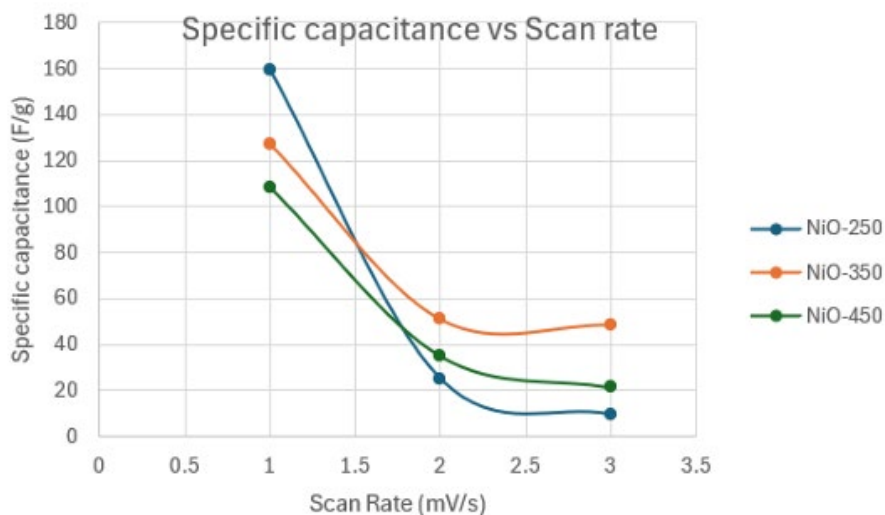


Figure 5. Specific capacitance for NiO samples

4. CONCLUSION

The mesoporous flowerlike NiO with nanopetals was successfully fabricated using hydrothermal synthesis method. NiO 250 consists of numerous thin and well defined nanopetals, the distinctive shape diminished gradually as calcination temperature increases. BET surface area and pore volume decrease as the calcination temperature increase, thus NiO-250 have the highest BET volume of $30.6543 \text{ m}^2/\text{g}$ followed by NiO-350 and NiO-450 with surface area of $19.8596 \text{ m}^2/\text{g}$ and $12.3250 \text{ m}^2/\text{g}$ respectively. Most of oxidation peaks are not seen clearly hence no clear representation the pseudocapacitance of NiO. A maximum specific capacitance of 159 F/g was achieved by Ni-250 at 10 mV/s , note the importance of surface area in the charge storing mechanism. Hence it can be concluded that lower calcination temperature leads to higher surface area and contribute to higher specific capacitance at low scan rates.

REFERENCES

- [1] Ashik, U. P. M., Kudo, S., & Hayashi, J. I. (2018). An Overview of Metal Oxide Nanostructures. In Synthesis of Inorganic Nanomaterials: Advances and Key Technologies (pp. 19-57): Elsevier.
- [2] Kim, B. K., Chabot, V., & Yu, A. (2013). Carbon nanomaterials supported Ni(OH)₂/NiO hybrid flower structure for supercapacitor. Electrochimica Acta, 109, 370-380. doi:<https://doi.org/10.1016/j.electacta.2013.07.119>

Warpage Analysis of Flip Chip Semiconductor Packages

Sam Yong Pin^a and Wong Yew Hoong^{b*}

Department of Mechanical Engineering,
Faculty of Engineering, Universiti Malaya,
50603, Kuala Lumpur, Malaysia

Email: ^a sampin1213@gmail.com, ^b yhwong@um.edu.my

*Corresponding author

ABSTRACT

Flip chip semiconductor packages are renowned for their advancements in miniaturization, yet warpage poses a significant challenge during the heated packaging process. This research investigates the warpage behaviours of flip chip semiconductor packages during and after the post-mold cure process. Conducted entirely through simulations with Ansys Workbench, the study evaluated various curing temperatures (165°C, 175°C, and 185°C) and durations (1 hour and 4 hours). Results indicate that warpage deformation increases with higher curing temperatures, while duration has minimal impact. Additionally, residual stress raised after the post-mold cure, with higher temperatures leading to greater stress. These findings demonstrate that flip chip packages experience similar post-mold cure deformation trends as conventional semiconductor packages, emphasizing the need for careful control of curing parameters to prevent deformation and stress-related issues in semiconductor packaging.

Keywords: Deformation; Flip Chip; Residual Stress; Semiconductor; Warpage

1. INTRODUCTION

Flip chip packages (FCPs) feature the active side facing the substrate, unlike conventional packages. This orientation introduces bump technologies, replacing wire bonding and reducing assembly time. FCPs enable miniaturization and increase connection density, improving electrical performance and signal integrity for high-frequency applications.

Warping, an irregular bending, or twisting is a common issue due to factors like mismatched coefficients of thermal expansion (CTE) and temperature changes during fabrication. Warpage can lead to solder joint failures, cracks, and electrical issues, necessitating research on mitigating this problem. The molding process in FCP manufacturing uses epoxy molding compound (EMC), requiring an additional post-mold cure (PMC) to complete curing. However, PMC induces residual stress, causing warpage. Thus, studying warpage behaviours during and after PMC is crucial for developing reliable FCPs.

2. METHODOLOGY

The methodology of this research is divided into four parts: 'Define Components & Material Properties', 'Create Simulation Model', 'Apply Loads & Boundary Conditions', 'Assess Validity, and Run Simulations'. Firstly, the essential parts of FCPs, including the EMC, bump, die, and substrate, were identified as key components. Material properties of these components were researched and

inputted into the ANSYS library for simulations. To avoid complex geometry and a high number of elements not supported by the ANSYS student version, a simple 2D model consisting of four rectangular layers was created. This 2D-model approach was based on existing research [2].

Transient thermal and transient structural analyses were then conducted. For the transient thermal analysis, the ambient temperature was set at 25°C, with convection applied to the model's outer edges. Three cases were analysed: varying temperatures (165°C, 175°C, 185°C) for 14,180 seconds, 175°C for 4,400 seconds and 14,180 seconds, and an additional half-hour post-PMC assessment. The FCP temperatures were then imported into the transient structural analysis. The left vertex was fixed along both axes, while the right vertex was fixed along the x-axis and free along the y-axis. Gravitational force was ignored, eliminating the need for bottom support. Total deformation and equivalent stress were measured to record warpage deformation and residual stress.



Fig. 1: Vertices of FCPs model

Lastly, validation was based on previous studies [1] and [2]. The simulation approach is deemed accurate if the warpage behaviours match existing results and the difference in PMC warpage value between the model and existing result is less than 8%.

3. RESULTS AND DISCUSSION

The maximum deformation at the final second of the PMC process was recorded as 2.3778 mm, compared to 2.22 mm from existing paper [2]. The validation result differs by only 7.108%, which falls within the acceptable range of 8%, indicating the simulation approach is successful.

The positive deformation values presented in the Table 1 illustrate that the FCPs exhibited a smiling shape warping at the end of the PMC process. Higher PMC temperatures correlated with elevated warpage deformation values. At higher PMC temperatures, a greater degree of crystallization occurred, resulting in greater substrate deformation compared to the EMC. Moreover, the curing duration varied while maintaining the same temperature gradient, thus, no significant impact was observed.

Table 1. Warpage deformation values under different PMC conditions

| PMC Conditions | Warpage Deformation Value (mm) | |
|----------------|--------------------------------|--------------------|
| | 200s of PMC Process | End of PMC Process |
| 165 °c | 1.9396 | 2.2956 |
| 175 °c | 2.1394 | 2.3778 |
| 185 °c | 2.3088 | 2.4743 |
| 1 hour | 2.1394 | 2.3746 |
| 4 hours | 2.1394 | 2.3778 |

The negative warpage deformation values tabulated in Table 2, indicate a shift from smiling to frowning warpage shapes due to thermal shrinkage effects after PMC process. Greater temperature differentials between PMC and ambient temperature lead to more severe warpage and residual stress levels within FCPs, as substrate was shrunk at a faster rate than EMC.

Table 2. Warpage deformation values & residual stress induced values after PMC process

| PMC Temperature (°c) | Warpage Deformation Values (mm) | Residual Stress Induced Values (MPa) |
|-----------------------------|--|---|
| 165 | -0.0413 | 10.5749 |
| 175 | -0.1747 | 13.1181 |
| 185 | -0.4971 | 16.2798 |

4. CONCLUSION

The FCPs model accurately predicted warpage behaviours during and after PMC, with a 7.108% discrepancy with existing results. Higher PMC temperatures induced increased smiling shape deformation, while PMC duration variations had minimal impact. After PMC, a shift to frowning shape was observed due to thermal shrinkage, with higher PMC temperatures resulting in greater warpage values. Varying PMC temperatures significantly influenced residual stress levels, particularly concentrated at the semiconductor die body. These findings emphasise the importance of precise PMC process parameter control in semiconductor packaging to prevent undesirable deformation and stress effects.

REFERENCES

1. Baek, J., Park, D., Oh, G., Kawk, D., Park, S. S., & Kim, K. H. (2022). Effect of cure shrinkage of epoxy molding compound on warpage behavior of semiconductor package. *Materials Science in Semiconductor Processing*, 148, 106758. <https://doi.org/10.1016/j.mssp.2022.10.6758>
2. Chuang, W., & Chen, W. (2022). Study on the strip warpage issues encountered in the Flip-Chip process. *Materials*, 15(1), 323. <https://doi.org/10.3390/ma15010323>

Development of Fire-Retardant Nanocomposite Thin Films for Building Applications

Tan Wei Kang^a and Wong Yew Hoong^{b*}

Department of Mechanical Engineering,
Faculty of Engineering, Universiti Malaya,
50603, Kuala Lumpur, Malaysia

Email: ^a weikang0365@gmail.com, ^b yhwong@um.edu.my

*Corresponding author

ABSTRACT

Majority of the fire retardant in the current market contains halogen which are detrimental to the environment. The focus of this paper will be to develop environmental friendly nanocomposite fire retardant thin film using polyactic acid (PLA) and carbon nanotube (CNT). A simulation model of the nanocomposite thin film was built in the ANSYS simulation software to study the effect of the thin film on the mechanical properties and thermal properties of concrete. The model was validated through similar reference paper with percentage of difference below 10% before the boundary conditions being applied. Load of 6000N to 14000N were applied on the concrete structure with thin film, without thin film and without CNT in the thin film. Lower deformation, stress and strain when comparing structure with and without thin film showed that thin film can increase the strength of structure. Temperature of 200°C to 1000°C were applied on the top surface of concrete with and without thin film. Concrete with thin film has significant lower surface temperature and heat flux showed the effectiveness of the thin film in dissipating the heat and maintain the integrity of the structure when exposed to heat but has higher thermal stress due to the difference in coefficient of thermal expansion.

Keywords: Fire-Retardant; Nanocomposite; Polyactic Acid; Simulation; Thermal Properties.

1. INTRODUCTION

Halogenated FR, particularly brominated fire retardant is among the most used FR but its combustion could bring adverse effects to human 'health and environmental [1]. PLA is made from the lactic acid through fermentation of the renewable sources. However, it has low thermal resistance, fragility and mechanical properties compared to synthetic polymer. CNT has tubular nanostructures with small diameters and high length-to-diameter ratios with high thermal conductivity, robust mechanical strength, and excellent electrical properties.

Unmodified polymer materials have weak FR properties. Common plastics like polyethylene exhibiting a LOI of only 17.0- 18.0%, making them vulnerable to highly flammable or combustible [2]. Unmodified polymers need to enhance their flame retardancy. According to the Fire and Rescue Department, half of the 8,638 buildings nationwide classified as "high- risk" failed to meet fire safety standards [3]. This issue is particularly critical for older buildings at Universiti Malaya, where fire safety and sustainability have emerged as pressing concerns.

The current research in the market for nanocomposite fire retardant are focusing on experimental approach and lack of simulation. In this research, nanocomposite simulation model will be built on the ANSYS workbench. Mechanical and thermal properties of the thin film will be simulated and discussed.

The resulting simulation model in ANSYS will be validated using similar reference paper before begin the simulation process.

2. METHODOLOGY

2.1 Nanocomposite modelling

The materials used in this experiment is SWCNT and PLA. The validation will be carried out by applying the simulation approach for the previous studies and considered valid if the difference between both approaches is less than 10%. The dimension of the concrete structure is 0.3m x 0.1m with thickness 0.1m and thickness of PLA is 25nm and CNT of length 80nm on it for mechanical analysis. The PLA/CNT/PLA laminate thin film with and without CNT will be analysed to determine the effect of CNT on the strength of structure. The thickness of PLA is $0.5\mu\text{m}$ and length of CNT is $1\mu\text{m}$ on $10\mu\text{m} \times 10\mu\text{m} \times 5\mu\text{m}$ thickness concrete structure are used in thermal analysis.

2.2 Boundary condition and solutions

Thermal properties and mechanical properties of the resulting nanocomposite thin film will be tested on concrete. To determine the mechanical properties, both sides of the nanocomposite are set to fixed support and a total of 6000N-14000N force is applied at the centre of the concrete structure. Comparison will be made between concrete with thin film and without thin film on the desired mechanical properties.

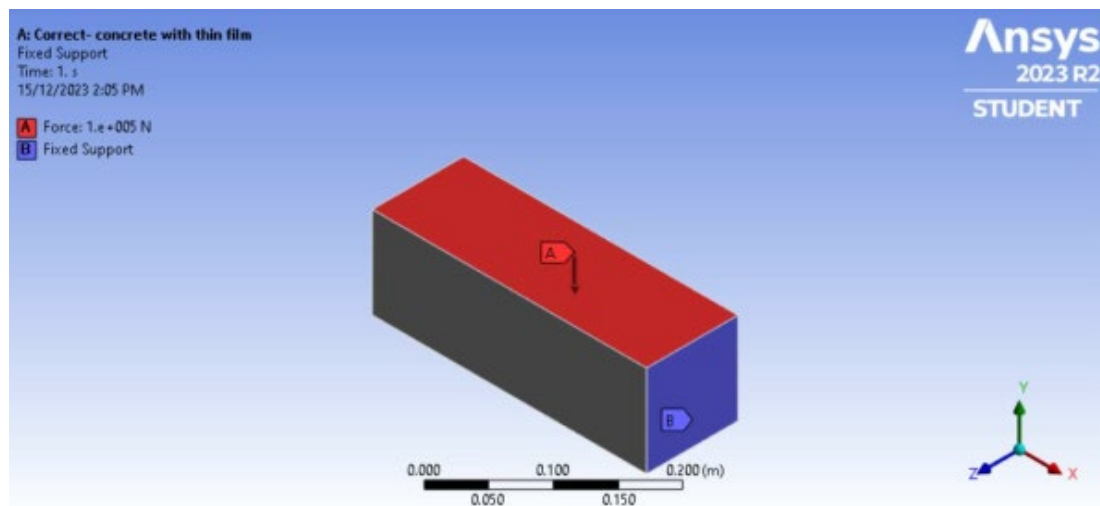


Figure 1. 100000N of force is exerted in the negative y- axis and side surfaces as fixed support

For the thermal properties, the temperature of concrete equal to the room temperature (26°C) and the temperature of the top surface will be set at 1000°C with $20\text{W}/\text{m}^2\text{K}$ heat convection. The resulting temperature distribution, heat flux and thermal stress of the layers will be determined.

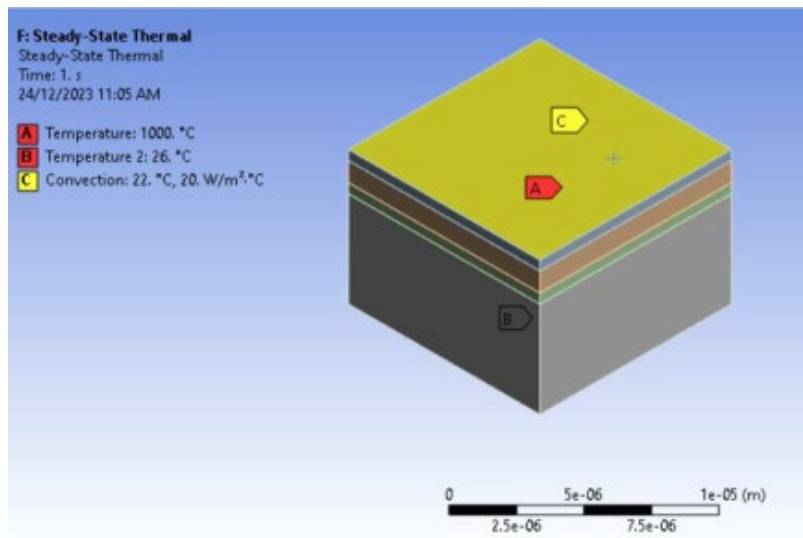


Figure 2. Boundary condition for thermal analysis

3. RESULTS AND DISCUSSION

Thin film is able to reduce the maximum stress acting along the structure by 160kPa. Since the percentage of difference between the current approaches and the reference paper is less than 10%, the current approaches is validated.

3.1 Mechanical properties of concrete block coated with and without nanocomposite thin film

When the force applied increase, the total deformation, equivalent stress and equivalent strain will increase. However, the deformation, stress and strain of the concrete with thin film show slightly lower values compared to the concrete with thin film. The ultimate tensile strength of the concrete is 5MPa. Research [4] shows that crack will start to form when the ultimate strength is exceeded. In the simulation for the 14000N of force applied on the structure, the maximum stress is 4.1496MPa and the value is close to the ultimate strength. Thin film with PLA/CNT/PLA has a lower stress, deformation and strain than thin film with PLA only due to the effect of adding SWCNT to increase the strength of PLA that has low strength. Research [5] shows that the strength of the PLA/CNT nanocomposite increases rapidly when the CNT content increases from 0wt% to 5wt%.

3.2 Thermal properties of the concrete coated with nanocomposite thin film

The top surface of the structure is exposed to different temperature ranging from 200 °C to 1000 °C . The temperature of concrete surface is almost half of the temperature of the exposed surface shows the effectiveness of the thin film in dissipating the heat. The presence of CNT increase the thermal stability of thin film as it provides a thermally conductive path for energy dispersion which can be seen from the temperature of concrete with (458.89 °C) and without thin film of concrete (1000°C). The thin film is able to reduce the total heat flux of the structure where a large difference is observed between concrete with thin film ($1.2752e7 \text{ Wm}^{-2}$) and without thin film ($4.383e8 \text{ Wm}^{-2}$) at 1000 °C. Without the insulation provided by the thin film, the concrete structure is directly exposed to the heat sources such as fire. The interfacial thermal resistance between PLA/CNT, CNT/PLA create resistance to the transfer of thermal energy that hinder the movement of phonons that transfer thermal energy.

When the top surface temperature increases, the thermal stress increases. The maximum thermal stress is still far lower than the ultimate strength of the structure (5MPa) that could cause catastrophic failure that occur suddenly. However, concrete without thin film shows a low thermal stress (358.48Pa) compared to concrete with thin film (20741Pa) for 1000 °C. This is due to the relative lower coefficient of expansion of concrete that expand more than the rest of layer. Constraint of thin film will affect the thermal expansion of the concrete structure and it leads to higher stresses within the concrete as the expansion or contraction will be restrained by the thin film [6].

4. CONCLUSION

First objective is achieved. Environmentally friendly nanocomposite was developed in ANSYS. Both PLA and CNT were chosen due to the biodegradability, mechanical properties and fire retardancy. Second objective is achieved. The simulation model was validated as the percentage of discrepancy was lower than 10%.

Third objective is achieved. CNT has been proven to increase the strength of the thin film and the structure as it decreases the amount of stress, deformation and strain acting on the concrete. In terms of the thermal properties of the thin film, it is able to reduce the peak temperature of the concrete temperature. The large difference of the temperature of concrete with and without the thin film shows the ability of the thin film in delaying the onset of peak temperature. Without the thin film, the concrete will be exposed to the flame directly and result in higher heat flux. Concrete with no thin film shows a relative lower stress than concrete with thin film due to the difference in the thermal expansion.

REFERENCES

- F. Teles, G. Martins, and F. Antunes, "Fire retardancy in nanocomposites by using nanomaterial additives," *Journal of Analytical and Applied Pyrolysis*, vol. 163, p. 105466, 2022.
- D. Gao et al., "Flame retardant effect and mechanism of nanosized NiO as synergist in PLA/APP/CSi-MCA composites," *Composites Communications*, vol. 17, pp. 170-176, 2020.
- NewStraitTimes. "Fully occupied for disaster - thousands of 'high- risk' buildings" (accessed 30 November 2023).
- Y. Zheng, M. Xie, Z. Liu, Y. Zhang, and X. Ding, "Performance of high strength steel bar splice with novel grouted deformed sleeve under tensile load," *Construction and Building Materials*, vol. 403, p. 133092, 2023.
- Y. Zhou, L. Lei, B. Yang, J. Li, and J. Ren, "Preparation and characterization of PLA, CNT nanocomposites," *Polymer Testing*, vol. 68, pp. 34-38, 2018.
- J.-H. Kim, K.-L. Jang, K. Ahn, T. Yoon, T.-I. Lee, and T.-S. Kim, "Thermal expansion behavior of thin films expanding freely on water surface," *Scientific Reports*, vol. 9, no. 1, p. 7071, 2019.

INDEX

Aquaponics & Agriculture

| | Page |
|----------------------------|------|
| Aquaponic system | 1,8 |
| Automated aquaponic system | 8 |
| Ball valve | 8 |
| Urban farming | 13 |

Biomaterials & Bio-based Products

| | |
|-----------------------|-----------------------|
| Bio-based lubricants | 21 |
| Biochar | 189, 194 |
| Bioplastic | 234 |
| Chitosan | 234 |
| Nano additives | 21 |
| Palm oil | 16, 21, 189, 194, 229 |
| Prawn shell waste | 234 |
| Sustainable additives | 221 |

Corrosion & Material Degradation

| | |
|-------------------------------------|------------------|
| Alkaline environment | 216, 221 |
| Andrographis paniculata extract | 216, 221 |
| Carbon steel | 216, 221 |
| Corrosion inhibition | 216, 221 |
| Corrosion test | 16, 21, 216, 221 |
| Cyclic potentiodynamic polarization | 221 |
| Epoxy coating | 221 |
| Immersion test | 18, 216 |

Energy & Sustainability

| | |
|-------------------------|-----------------|
| Energy efficiency | 91, 96, 194 |
| Energy harvesting | 77, 159 |
| In-pipe water turbine | 64 |
| Renewable energy | 47, 64, 77, 159 |
| Solar thermal collector | 91 |
| Sustainable behaviour | 115 |

| | |
|-------------------------|---------|
| Sustainable development | 115 |
| Thermoelectric cooling | 96 |
| Wind-wave turbine | 77, 159 |

Manufacturing Processes & Materials

| | |
|--------------------------------|--------------------------------|
| 3D printing | 97 |
| Additive manufacturing | 118 |
| Composite materials | 175, 234 |
| Defect prevention | 118 |
| Electrospinning | 128, 175 |
| Fire retardant materials | 266 |
| Hydraulic press | 144 |
| Mechanical properties | 128, 175, 179, 198, 212, 266 |
| Metal chip recycling | 144 |
| Microstructure | 179, 198, 229, 245, 258 |
| Nanofiber reinforced composite | 175 |
| Optimization | 45, 58, 69, 118, 134, 159, 189 |
| Polyvinylidene fluoride (PVDF) | 175, 224 |
| Selective laser melting (SLM) | 118 |
| Thermal properties | 204, 234, 239, 266 |
| Ti-6Al-4V | 118 |

Mechanical Systems & Design

| | |
|-----------------------------------|----------|
| Coil spring optimization | 58 |
| Particle swarm optimization (PSO) | 58 |
| Genetic algorithm (GA) | 58 |
| Firefly algorithm (FA) | 58 |
| Mechanical jet fans | 101 |
| Ventilation system | 43, 101 |
| Fire simulation | 101 |
| Linkage-based suspension | 69 |
| Vehicle suspension | 69 |
| Simulink model | 69 |
| Robotics | 164, 170 |

Measurement & Analysis

| | |
|--|---|
| BET analysis | 252 |
| Bomb calorimeter | 189, 194 |
| Computational fluid dynamics (CFD) | 101,112 |
| Electrochemical impedance spectroscopy (EIS) | 239 |
| Energy dispersive X-ray spectroscopy (EDX) | 198, 234, 239 |
| Finite element analysis (FEA) | 81, 212 |
| Fourier transform infrared spectroscopy (FTIR) | 21, 180, 184, 221,224, 229, 234, 239 |
| ICP-OES | 224 |
| Image processing | 170 |
| Scanning electron microscopy (SEM) | 16, 21, 175, 179, 189, 194, 245, 252, 258 |
| Thermogravimetric analysis (TGA) | 184, 258 |
| Vickers hardness testing | 198, 245 |
| X-ray diffraction (XRD) | 179, 184, 224 |
| YOLOv8 | 122, 170 |

Software & Applications

| | |
|------------------------|--|
| ANSYS | 43, 81, 101, 106, 112, 128, 204, 212, 263, 266 |
| Database system | 53 |
| HoloLens | 164 |
| IoT platform & sensors | 1,32,38 |
| MATLAB | 8, 38, 58, 69, 118 |
| MySQL | 53 |
| Python | 53, 73, 170 |
| RobotDK | 164 |
| SolidWorks | 43, 64, 77, 81, 96, 106, 140, 144, 151, 204, 249 |
| ThingSpeak | 1 |
| Unity 3D | 164 |
| Website application | 53, 151 |

Other Relevant Topics

| | |
|------------------------------|---|
| Environmental impact | 1, 21, 47, 77, 91, 96, 115, 189, 194, 207, 224, 229, 234, 249, 252, 266 |
| Human factors & Ergonomics | 81, 140 |
| Public health | 224 |
| Sustainable waste management | 189, 207 |

e ISBN 978-967-2182-45-0



9 789672 182450